

Numerical Simulation of non-isothermal Complex Fluid Mixtures in Deep Geothermal Systems

Zur Erlangung des akademischen Grades eines

DOKTORS DER INGENIEURWISSENSCHAFTEN (Dr.-Ing.)

von der KIT-Fakultät für

Bauingenieur-, Geo- und Umweltwissenschaften
des Karlsruher Instituts für Technologie (KIT) genehmigte

DISSERTATION

von

M.Sc. Morteza Esmaeilpour
aus dem Iran

Tag der mündlichen Prüfung: 17. Mai, 2023

Referent: Prof. Dr.-Ing. Thomas Kohl
Korreferent: Prof. Dr.-Ing. Olaf Kolditz

Karlsruhe 2023

Abstract

Global warming profoundly impacts our environment, causing ice melting, rising sea levels, extreme weather events, ocean acidification, and habitat destruction. These changes threaten biodiversity and require immediate action to mitigate their effects. Renewable energy sources, such as geothermal energy, have the potential to reduce the emissions that contribute to global warming significantly. Geothermal projects harness the Earth's natural heat, generating electricity without producing greenhouse gas emissions. Additionally, geothermal power plants have a small footprint and can be located in various areas, reducing the reliance on fossil fuel-based power generation. Investing in renewable energy sources such as geothermal energy can help alleviate the negative impacts of global warming while transitioning to a sustainable energy future.

Wellbores are a critical component of geothermal energy production. They are drilled deep into the earth's surface to expose a working fluid to hot formation or tap into natural geothermal reservoirs, which contain hot water and steam that can be used to generate heat and electricity. The design and construction of wellbores are essential to ensure efficient heat transfer and prevent contamination of the geothermal resource. Moreover, proper maintenance of wellbores is vital to ensure the continued operation of the geothermal power plant.

Numerical modeling of fluid flow, heat transfer, and mechanical behavior in the wellbore and surrounding geologic formations provides a means to optimize system performance, predict issues, and identify risks such as thermal damage or wellbore instability. Nonetheless, The accurate mathematical description of the wellbore system is highly challenging due to the complex interplay between several factors, including fluid flow inside the wellbore, conductive and convective heat transfer within different components (such as the working fluid, cement, casing, annulus, and formation), pressure fluctuations caused by gravitational forces and friction, as well as mass exchange between the wellbore and reservoir. Dealing with two-phase multicomponent flows can further escalate this complexity, as it requires accounting for phase change, varying velocities of the phases, gas and salt solubility in the aqueous phase, and transport of multiple components (i.e., solving more partial differential equations).

The iterative algorithm for computing gas components' solubility in the aqueous phase is computationally expensive for modeling two-phase multicomponent flows in geothermal wellbores. Therefore, Chapter 3 of the thesis aims to develop a precise and efficient machine-learning-based equation of state (EOS) for two-phase geofluids. A robust fugacity-activity model is preliminarily implemented to provide accurate solubility data based on pressure, enthalpy, and composition. This data is then fed into a gene expression programming model to generate highly-precise explicit formulas for output computation, which are validated using one million input sets. The new EOS, GENEOS, can compute gas solubility in brine with almost no iteration and can also calculate other properties such as density, viscosity, and thermal conductivity. Developing a wellbore simulator that incorporates advanced equations of state and couples continuity, momentum, and energy equations with eight other partial differential equations for transporting (H_2O , CO_2 , CH_4 , N_2 , H_2S , NaCl , KCl , CaCl_2 , and MgCl_2) is one of the main contributions of this study to the existing literature.

Chapters 4 and 5 present novel deep closed-loop geothermal (CDG) systems that generate a significant amount of thermal power without contaminating subsurface water or triggering seismic activity. The main focus of Chapter 4 is to quantify the thermosiphon flow in CDG systems and to assess its stability under various scenarios over time. The findings of this study indicate that a CDG system with a depth and horizontal length of 4 km can generate about 2 MW of thermal power through thermosiphon flow for a period of 100 years. The next study (chapter 4) aims to quantify the power generation per meter of multilateral CDG (MCDG) systems possessing several parallel injection and horizontal wellbores. Characterization of common features of successful MCDG systems and prediction of their long-term performance as a function of their short-term behavior are the most important findings of this study. The successful implementation of these insights can significantly improve the design and contribution of MCDG systems to green energy generation.

Chapter 6 focuses on the development of a predictive model for CO_2 -induced corrosion, which is a significant threat to the structural integrity of geothermal wellbores. Most existing models for predicting this type of corrosion are only valid for CO_2 partial pressures below 10 bar, which is applicable for deep geothermal wellbores. As such, the primary aim of this study is to present an innovative predictive model for high-pressure CO_2 -induced corrosion that accurately matches the available experimental data. The R^2 -coefficient of 0.99 obtained from fitting the experimental test dataset indicates that the developed model has been successful in accurately predicting high-pressure CO_2 -induced corrosion.

KURZFASSUNG

Die globale Erwärmung hat tiefgreifende Auswirkungen auf unsere Umwelt. Sie verursacht Eisschmelze, den Anstieg des Meeresspiegels, extreme Wetterereignisse, die Versauerung der Meere und die Zerstörung von Lebensräumen. Diese Veränderungen bedrohen die biologische Vielfalt und erfordern sofortige Korrekturmaßnahmen. Erneuerbare Energiequellen wie die Geothermie haben das Potenzial, die Emissionen, die zur globalen Erwärmung führen, erheblich zu reduzieren. Geothermische Projekte nutzen die natürliche Wärme der Erde zur Stromerzeugung, ohne dabei Treibhausgasemissionen zu erzeugen. Außerdem haben geothermische Kraftwerke einen geringen Platzbedarf und können in einer Vielzahl von Gebieten errichtet werden. Investitionen in erneuerbare Energiequellen wie die Geothermie können dazu beitragen, die negativen Auswirkungen der globalen Erwärmung abzuschwächen und gleichzeitig den Übergang zu einer nachhaltigen Energiezukunft zu schaffen.

Bohrlöcher sind ein kritischer Bestandteil der geothermischen Energieerzeugung. Sie werden tief in die Erdoberfläche gebohrt, um eine Arbeitsflüssigkeit in die heiße Formation zu leiten oder natürliche geothermische Reservoirs anzuzapfen, die heißes Wasser und Dampf zur Erzeugung des Stroms und der Wärme enthalten. Planung und Bau der Bohrlöcher sind von entscheidender Bedeutung, um eine effiziente Wärmeübertragung zu gewährleisten und eine Verunreinigung der geothermischen Ressource zu verhindern. Darüber hinaus ist eine ordnungsgemäße Wartung der Bohrlöcher für den kontinuierlichen Betrieb des geothermischen Kraftwerks unerlässlich.

Die numerische Modellierung von Flüssigkeitsströmung, Wärmeübertragung und mechanischem Verhalten im Bohrloch und den umgebenden geologischen Formationen ermöglicht die Optimierung der Systemleistung, die Vorhersage von Problemen und die Erkennung von Risiken wie thermische Schäden oder Instabilität des Bohrlochs. Die genaue mathematische Beschreibung des Bohrlochsystems ist jedoch aufgrund des komplexen Zusammenspiels verschiedener Faktoren, einschließlich der Flüssigkeitsströmung innerhalb des Bohrlochs, der konduktiven und konvektiven Wärmeübertragung innerhalb verschiedener Komponenten (wie Arbeitsflüssigkeit, Zement, Verrohrung, Ringraum und Formation), der durch Schwerkraft und Reibung verursachten Druckschwankungen sowie des Massenaustauschs zwischen Bohrloch und Lagerstätte, äußerst schwierig. Die Komplexität kann bei zweiphasi-

gen Mehrkomponentenströmungen noch zunehmen, da Phasenwechsel, unterschiedliche Geschwindigkeiten der Phasen, die Löslichkeit von Gasen und Salzen in der wässrigen Phase und der Transport mehrerer Komponenten berücksichtigt werden müssen (d. h. mehrere partielle Differentialgleichungen gelöst werden müssen).

Der iterative Berechnungsalgorithmus für die Löslichkeit der Gaskomponenten in der wässrigen Phase ist für die Modellierung zweiphasiger Mehrkomponentenströmungen in geothermischen Bohrlöchern sehr rechenintensiv. Daher zielt Kapitel 3 der Dissertation darauf ab, eine präzise und effiziente, auf Maschinelernen basierende Zustandsgleichung für zweiphasige Geofluidе zu entwickeln. Ein robustes Fugazitäts-Aktivitäts-Modell wird vorläufig implementiert, um genaue Löslichkeitsdaten auf der Grundlage von Druck, Enthalpie und Zusammensetzung zu erhalten. Diese Daten werden dann in ein Genexpressionsprogrammierungsmodell eingespeist, um hochpräzise explizite Formeln für die Berechnung des Outputs zu generieren, die anhand von einer Million Eingabesätzen validiert werden. Das neue EOS, GENEOS, kann die Gaslöslichkeit in Sole fast ohne Iteration berechnen und andere Eigenschaften wie Dichte, Viskosität und Wärmeleitfähigkeit ermitteln. Entwicklung eines Bohrlochsimulators, der fortschrittliche Zustandsgleichungen enthält und Kontinuitäts-, Impuls- und Energiegleichungen mit acht anderen teilweisen Differentialgleichungen für den Transport von (H_2O , CO_2 , CH_4 , N_2 , H_2S , NaCl , KCl , CaCl_2 , and MgCl_2) koppelt, ist einer der wichtigsten Beiträge dieser Studie zur bestehenden Literatur.

In den Kapiteln 4 und 5 werden neuartige geothermische Tiefensysteme mit geschlossenem Kreislauf (CDG) vorgestellt, die eine beträchtliche Menge thermischer Energie erzeugen, ohne das unterirdische Wasser zu verunreinigen oder seismische Aktivitäten auszulösen. Der Schwerpunkt von Kapitel 4 liegt auf der Quantifizierung des Thermosiphonflusses in CDG-Systemen und der Bewertung seiner Stabilität unter verschiedenen Szenarien im Zeitverlauf. Die Ergebnisse dieser Studie zeigen, dass ein CDG-System mit einer Tiefe und horizontalen Länge von 4 km über einen Zeitraum von 100 Jahren etwa 2 MW thermische Leistung durch Thermosiphonströmung erzeugen kann. Die nächste Studie (Kapitel 4) zielt darauf ab, die Stromerzeugung pro Meter von multilateralen CDG-Systemen (MCDG) zu quantifizieren, die mehrere parallele Injektions- und Horizontalbohrungen aufweisen. Die Charakterisierung gemeinsamer Merkmale erfolgreicher MCDG-Systeme und die Vorhersage ihrer langfristigen Leistung in Abhängigkeit von ihrem kurzfristigen Verhalten sind die wichtigsten Ergebnisse dieser Studie. Die erfolgreiche Umsetzung dieser Erkenntnisse kann das Design und den Beitrag von MCDG-Systemen zur grünen Energieerzeugung erheblich verbessern.

Kapitel 6 befasst sich mit der Entwicklung eines Vorhersagemodells für CO_2 -induzierte Korrosion, die eine signifikante Bedrohung für die strukturelle Integrität der geothermischen Bohrlöcher darstellt. Die meisten bestehenden Modelle zur Vorhersage dieser Art von

Korrosion sind nur für CO₂-Partialdrücke unter 10 Bar gültig, was für tiefe geothermische Bohrungen gilt. Das Hauptziel dieser Studie ist es daher, ein innovatives Vorhersagemodell für CO₂-induzierte Hochdruckkorrosion vorzustellen, das den verfügbaren experimentellen Daten genau entspricht. Der R²-Koeffizient von 0,99, der bei der Anpassung des experimentellen Testdatensatzes erzielt wurde, zeigt, dass das entwickelte Modell bei der genauen Vorhersage der CO₂-induzierten Hochdruckkorrosion erfolgreich war.

Acknowledgements

I would like to express my sincere gratitude to my supervisor Prof. Thomas Kohl for granting me the opportunity to conduct my research under his guidance. His invaluable support and constructive suggestions during the planning and development stages of this research work have been instrumental in its successful completion.

My heartfelt thanks go to Dr. Maziar Ghomali Korzani, who has been a constant source of guidance and encouragement throughout my PhD journey. His insightful advice, patience, and generous support have been instrumental in overcoming many numerical challenges, and I am truly grateful for his contributions.

I also want to acknowledge Dr. Fabian Nitschke and Dr. Emmanuel Gaucher for their invaluable guidance and support during my research. Their contributions have been crucial to the completion of this work.

I would also like to acknowledge the Geothermal Working Group for creating an inspiring working atmosphere that has motivated me, even in the face of difficult times. Their scientific discussions have been fruitful and influenced the progress of my research. I extend special thanks to Silke for her administrative support and for navigating the complexities of the KIT bureaucracy.

Furthermore, I would like to express my gratitude to my parents for their unconditional support throughout my journey.

Finally, I would like to extend my heartfelt appreciation to my wife, Ghazaleh, for her unwavering support and motivation throughout my PhD. Her encouragement and belief in me have been instrumental in my success, and I am truly grateful for her presence in my life.

Table of contents

List of figures	xv
List of tables	xxi
Nomenclature	xxiii
1 INTRODUCTION	1
1.1 Motivation	4
1.2 Thesis structure	6
2 FUNDAMENTAL PROCESSES IN GEOTHERMAL WELLBORES	9
2.1 Relevant physical processes	9
2.1.1 Lateral heat exchange between wellbore and formation	9
2.1.2 Pressure loss due to friction	10
2.1.3 Change of flow regime	10
2.1.4 Mineral and gas dissolution	10
2.1.5 Variation of thermo-physical properties	11
2.1.6 Mass exchange between wellbore and reservoir	11
2.2 Governing equations	11
2.2.1 Conservation equations	12
2.2.2 Friction force	12
2.2.3 Drift flux model	14
2.2.4 Lateral heat model	17
2.2.5 Equation of state	21
2.3 Numerical scheme	22
2.3.1 Finite element method	22
2.3.2 MOOSE	22
2.3.3 MOSKITO	23

3	DEVELOPMENT OF EQUATION OF STATE	25
3.1	Introduction	26
3.2	Methodology	29
3.2.1	Thermodynamic algorithm based on the iterative F-A model	30
3.2.2	Gene expression programming	35
3.3	Results and discussion	36
3.3.1	Comparing fast GEP-based EOS to iterative method	38
3.3.2	GenEOS calculation scheme for fluid properties	42
3.4	Conclusion	54
3.5	Acknowledgment	56
4	THERMOSIPHONING IN CLOSED-LOOP GEOTHERMAL SYSTEMS	57
4.1	Introduction	58
4.2	Methodology	61
4.2.1	Governing equations	61
4.2.2	Model validation	63
4.2.3	Numerical modeling	63
4.3	Evaluation of the CDG system long-term behavior	68
4.3.1	Impacts of flow rates on the produced temperature and energy	68
4.3.2	Impacts of wellbore diameter on the produced power	71
4.3.3	Impacts of wellbore diameter on the produced power	71
4.4	Thermosiphon flow assessments	74
4.4.1	Impacts of surface facilities pressure losses	75
4.4.2	Impacts of wellbores diameters and geometrical configurations	75
4.4.3	Controlling thermosiphon flow	77
4.5	Discussion	78
4.5.1	The CDG system geometry	78
4.5.2	System's longevity and sustainability	81
4.5.3	Thermosiphoning and drilling costs	82
4.5.4	Production pressure and operational energy	82
4.5.5	Production well diameter impacts	82
4.6	Conclusion	83
4.7	Acknowledgment	87
5	MULTILATERAL CLOSED DEEP GEOTHERMAL SYSTEMS	89
5.1	Introduction	90
5.2	System description	92

5.2.1	General description of MCDG system	92
5.2.2	Applied geological setting and geometrical configuration	93
5.3	Methodology	95
5.3.1	Governing equations	95
5.3.2	Numerical modeling	96
5.4	Stochastic analysis of the MCDG system's long-term behavior	97
5.5	Results	102
5.5.1	General behavior of MCDG systems	102
5.5.2	Suggestion of appropriate operation plans	106
5.6	Conclusion	110
5.7	Acknowledgment	112
6	HIGH-PRESSURE CO₂ CORROSION IN GEOTHERMAL WELLBORES	113
6.1	Introduction	114
6.2	Methodology	117
6.2.1	Overview of Gene Expression Programming	117
6.2.2	Data collection	117
6.2.3	Development of corrosion model	118
6.3	Results and discussion	119
6.3.1	Prediction accuracy	119
6.3.2	Relevant parameters	123
6.4	Conclusion	126
7	CONCLUSIONS	129
7.1	Major findings of the research	130
7.2	Outlook	132
	References	135
	Appendix A C++ Codes	151
	Appendix B Training and test datasets for the corrosion model	159
	Appendix C Immiscible displacement flows	161

List of figures

1.1	Change of global surface temperature in comparison with the long-term average from 1951 to 1980 [1].	1
1.2	Carbon dioxide atmospheric concentration over time [2].	2
3.1	Flow chart for the conventional iterative calculation of temperature and equilibrium constants as functions of pressure, enthalpy, and two-phase fluid composition.	35
3.2	The flowchart of gene expression algorithm. Pressure, enthalpy, and two-phase fluid composition are assumed inputs, while the R-squared in calculating temperature and equilibrium constants is considered as a fitness function.	37
3.3	The R-squared and relative error of the GEP equation in the calculation of fluid temperature when (a-b) pressure > 10 MPa and (c-d) pressure <10 MPa	39
3.4	Accuracy of calculated temperatures after the first iteration when the GEP equation is used as the initial guess in the Fugacity-activity algorithm (Fig. 3.1).	40
3.5	The relative error in calculating the equilibrium constant of a) Methane b) Carbon dioxide c) Nitrogen d) Hydrogen sulfide. The orange columns display the outcomes obtained from the F-A model after the first iteration, using GEP equations as the initial guess.	41
3.6	Calculation and validation of enthalpy of a) single gas [CH ₄ , $P = 10 \text{ MPa}$] b) pure liquid water and brine [$P = 10 \text{ MPa}$, mole fraction of NaCl = 0.1]. The red line is solely included to illustrate the behavior of brine enthalpy. c) non-boiling water in NaqP ($T = 70 \text{ }^\circ\text{C}$)	45
3.7	Calculation and validation of density of a) single gas [CO ₂ , $P = 10 \text{ MPa}$] b) H ₂ O-CaCl ₂ solution [$b = 1 \text{ mol Kg}^{-1}$], experimental data are taken from Al Ghafri <i>et al.</i> [3] c) non-boiling water in NaqP [$T = 70 \text{ }^\circ\text{C}$] d) CO ₂ -saturated water [$T = 70 \text{ }^\circ\text{C}$]	48

3.8	Calculation and validation of viscosity of a) binary H ₂ O-CaCl ₂ brine [$b = 1 \text{ mol Kg}^{-1}$], the experimental data are taken from Laliberte' [4] b) single gas (CO ₂)	52
3.9	Calculation and validation of thermal conductivity of a) a single gas [$P = 10 \text{ MPa}$] b) pure water and binary H ₂ O-CaCl ₂ brine (mass fraction = 20 %, $P = 10 \text{ MPa}$), experimental data are taken from Akhmedova-Azizova and Abdulagatov [5]	54
4.1	Comparison between temperature profiles along the system after 20 years of operation. The same style of the reference paper is used for this figure. The pink double arrow shows the variation of calculated temperature in the production wellbore after including the equation of state. The inclusion of the EOS has a negligible impact on the calculated temperature in the injection wellbore.	64
4.2	Schematic illustrating geometrical features of the reference model. $b_1, b_2, b_3,$ and b_4 stand for borehole diameters where the wellbore structure is in direct contact with the formation. $c_1, c_2,$ and c_3 also represent casings' inner diameters. ($b_1 = 0.5588 \text{ m}, c_1 = 0.473075 \text{ m}, b_2 = 0.4318 \text{ m}, c_2 = 0.346075 \text{ m}, b_3 = 0.31115 \text{ m}, c_3 = 0.244475 \text{ m}, b_4 = 0.212725 \text{ m}$). Δz and Δl show the depth of vertical wells and total horizontal length, respectively. The horizontal section is directly exposed to hot formation.	65
4.3	a) Impact of insulation of production wellbore on the total absorbed energy per meter of the CDG system after 100 years of operation (insulation layer is highlighted by red color). The corresponding lines for the presented cases overlap up to the insulation section. b) Ideal insulation of production wellbore c) practical insulation of production wellbore.	67
4.4	Extraction temperatures over time for different flow rates. The short-term behavior of the extraction temperature is caused by the displacement of residual hot fluid, while its long-term behavior is controlled by the lateral heat exchange.	68
4.5	Temperature distribution in each section of the system (I, II, and III) for a) flow rate = 1 L/s b) flow rate = 5 L/s c) flow rate = 10 L/s. The difference between temperature profiles along the wellbores and formation temperature (dashed line) can be used for the determination of the locations requiring insulation.	69

4.6	Cumulative extracted energy over time for different flow rates. After 100 years of operation, the absorbed energy with the flow rate of 10 L/s is 6 times of heat absorption with the flow rate of 1 L/s	70
4.7	Flow rate impact on: a) generated powers in vertical wells b) net generated power and produced power in the horizontal section over time. For each flow rate, the variation of net power over time is like the transient behavior of produced power in the horizontal wellbore.	72
4.8	Impact of wellbore diameter (case 1-4" smaller and case 2-4" larger diameter than the reference model) on: a) generated powers in vertical wells b) net generated power and produced power in the horizontal section over time. . .	73
4.9	Comparison between the impacts of injection temperature increment and system enlargement ($\Delta Z = \Delta L = 5$ km) on the extraction temperature of the reference model (RM and T stand for reference model and temperature, respectively). System enlargement is superior to the injection temperature increment to enhance the extraction temperature.	74
4.10	Impact of pressure loss at surface facilities on the thermosiphon flow rate over time. In all the cases, the thermosiphon flow rate is stable over time. Even in the worse case, with the surface pressure loss of 900 kPa , the thermosiphon flow rate is higher than 11 L/s	76
4.11	Impact of wellbore diameter on the thermosiphon flow rate over time (case 1 - 4" smaller and case 2 - 4" larger diameter than the reference model). The case 2 setup (larger diameter) generates a thermosiphon flow being twice as high as case 1 (smaller diameter).	77
4.12	Thermosiphon flow rates for various CDG configurations over time ($\Delta Z =$ depth of vertical wellbores, $\Delta l =$ length of horizontal section). The total length of both systems is 12 Km	78
4.13	a) Corresponding extraction temperatures for the flow rates of Fig. 4.10 and b) calculated extraction temperature for the valve-controlled flow rate of 6.6 L/s and surface pressure loss of 900 KPa	79
4.14	Impact of subsurface temperature gradient on the cumulative absorbed energy per meter of the CDG system after 100 years of operation. The locations with negative absorbed energy should be insulated to avoid heat loss. The jumps of the absorbed energy at different points are explained in Section 4.2.3 and Fig. 4.3.	80

4.15	Impact of formation thermal conductivity on the total absorbed energy per meter of the CDG system after 100 years of operation. Thermal conductivity of the upper layer is $2 \text{ Wm}^{-1}\text{K}^{-1}$, and Thermal conductivities of the lower layer for case 1, 2, and 3 are 2, 3, and $4 \text{ Wm}^{-1}\text{K}^{-1}$, respectively. The locations with negative absorbed energy should be insulated to avoid heat loss. The jumps of the absorbed energy at different points are explained in Section 4.2.3 and Fig. 4.3.	81
4.16	Comparison between the effects of inlet temperature increment and system enlargement ($\Delta Z = \Delta L = 5 \text{ km}$) on the extraction pressure of the reference model (RM stands for reference model). System enlargement is superior to the injection temperature increment to enhance thermosiphoning.	83
4.17	Impact of decreasing production wellbore diameter on the production temperature over time. The smaller wellbore diameter leads to a higher extraction temperature over time.	84
4.18	Impact of decreasing production wellbore diameter on the production pressure over time. The smaller wellbore diameter leads to a higher pressure difference between injection and extraction points.	84
5.1	Schematics illustrating a) depth of MCDG systems, length of horizontal section, doglegs and manifolds structure, and wellbores configuration b) casing program of a simple CDG system ($b_1 = 22"$, $c_1 = 18 \text{ } 5/8"$, $b_2 = 17"$, $c_2 = 13 \text{ } 5/8"$, $b_3 = 12 \text{ } 1/4"$, $c_3 = 9 \text{ } 5/8"$, $b_4 = 8 \text{ } 3/8"$). $b, c, \Delta z$, and Δl stand for borehole diameter, casing inner diameter, depth of vertical wells, and total horizontal length, respectively. The horizontal section is directly exposed to hot formation. The same casing program is used for MCDG systems. The area highlighted by red color shows insulation.	94
5.2	The transient behavior of a) extraction temperature b) extraction pressure, for a simple CDG system with a depth of 4.1 km , horizontal length of 4 km , and flow rate of 5 L/s . ΔP is defined by ($\Delta P = P_{\text{extraction}} - P_{\text{injection}}$).	98
5.3	Behavior of extraction temperature over time while operating with a simple CDG system. The flow rate is 10 L/s and other initial/boundary conditions and casing program are mentioned in Sections 5.2 and 5.3. Points 1, 2, and 3 correspond to extraction temperatures after 1, 30, and 100 years, respectively.	99
5.4	Correlations between extraction temperatures of MCDG systems after 1 year, 30 years, and 100 years of operation	100

5.5	Correlations between extraction temperatures of MCDG systems after 1 year and extracted energy per liter of working fluid over 100 years of operation. The provided colormap shows the maximum allowed flow rate for the calculation of thermal power.	101
5.6	Ranges of generated thermal power (P), average extraction temperature over 100 years of operation ($T_{Extraction}$), and specific power (P_S) for each flow rate. The boxplots show the impact of wellbore configurations at each flowrate. .	104
5.7	Ranges of generated thermal power (P), average extraction temperature over 100 years of operation ($T_{Extraction}$), and specific power (P_S) for wellbore configuration. The domain of boxplots shows the impact of flow rate on outputs. The first and second indexes of each configuration show the number of injection and horizontal wellbores, respectively.	105
5.8	Average values of extraction temperature over 100 years of operation ($T_{Extraction}$), specific power (P_S), and total generated power (P) of each case. The plotted lines show the filtering criteria (average extraction temperature > 60 °C and specific power > 70.81 W/m). The points located in the gray region are successful cases.	107
5.9	Flow rates and corresponding configurations of successful cases. The first and second indexes of each configuration show the number of injection and horizontal wellbores, respectively.	108
5.10	Correlation between flow rates per lateral/injector and a) specific power b) average extraction temperature over 100 years of operation c) total flow rate (L/s)	109
5.11	Success rate of designed MCDG systems for each flow rate (success rate=(number of successful cases at each flow rate)/16)	111
6.1	The flowchart of gene expression algorithm. Pressure, temperature, pH, and velocity are assumed inputs, while the R-squared in calculating corrosion rate is considered as a fitness function.	120
6.2	Generated expression tree for the GEP corrosion model. It is constructed from a set of genes, which are the building blocks of the program. These genes are represented as strings of characters, and they encode the operators and operands that will be used to construct the tree.	121
6.3	Comparing the corrosion rates predicted by mathematical models with the experimental test dataset.	122
6.4	The absolute error of GEP and NN models in predicting test dataset.	122
6.5	The relative error of GEP and NN models in predicting test dataset.	123

6.6	Calculated corrosion rates by mathematical models against experimental data.	124
6.7	Experimental corrosion rate versus temperature plot for all the training/test datasets.	125
6.8	Calculated corrosion rates by the developed GEP model for a) pH=4.5 b) pH=5.5 c) pH=6.5	126
6.9	Pressure impact on the corrosion rate [$P = 10 \text{ MPa}, U = 2 \text{ m/s}$]	127

List of tables

2.1	K_u value as a function of dimensionless pipe diameter	17
2.2	The values of the Ramey time function $f(t)$ for time periods less than one week	19
3.1	Range of input parameters for training GEP functions (mf stands for mole fraction in two-phase mixture)	38
3.2	GEP settings for the calculation of Temperature	39
3.3	settings for the calculation of equilibrium constant	41
3.4	The median relative error of GEP equations in computing equilibrium constants	41
4.1	Thermo-physical properties of formation, casing, and cement layer	65
6.1	Statistics of the CO ₂ corrosion data	118
6.2	GEP settings for the calculation of corrosion rate	119
6.3	Comparing the accuracy of mathematical models in predicting experimental test dataset	128
B.1	Training Dataset.	159
B.2	Test Dataset.	160

Nomenclature

Roman Symbols

c_0	Profile parameter
cm	Gas-dependent volume shift factor
d	Hydraulic diameter, m
f_g	In-situ gas volume fraction
g	Gravitational acceleration, $m\ S^{-2}$
H	Enthalpy, $J\ kg^{-1}$
K	Equilibrium constant
k	Thermal conductivity, $W\ m^{-1}\ K^{-1}$
K_B	Boltzmann's constant, $J\ kg^{-1}$
K_H	Henry's constant, $Pa\ m^3\ mol^{-1}$
K_u	critical Kutateladze number
M	Molar mass, $kg\ mol^{-1}$
m	Molality, $mol\ kg^{-1}$
M_w	Molecular weight, $kg\ mol^{-1}$
N_A	Avogadro's number
n^v	Mole fraction of non-aqueous phase
N_w	Number of moles per kilogram of water

P	Pressure, Pa
R	Gas universal constant, $J mol^{-1} k^{-1}$
σ_{gl}	gas/liquid interfacial tension, $N m^{-1}$
T	Temperature, K
U_{to}	Overall heat transfer coefficient, $W m^{-2} K^{-1}$
V	Specific volume, $m^3 kg^{-1}$
V_{H_2O}	Average partial molar volume of the water, $m^3 mol^{-1}$
v	Velocity, $m S^{-1}$
w	Mass fraction
x	Mole fraction in the liquid phase
y	Mole fraction in the gas phase
Z	Compressibility factor

Greek Symbols

α	Formation thermal diffusivity, $m^2 S^{-1}$
ε	Thermal expansion coefficient, K^{-1}
η	Viscosity, $Pa S$
γ	Activity coefficient
λ	Second-order interaction parameter
μ	Chemical potential, $J mol^{-1}$
v	Molar volume, $m^3 mol^{-1}$
ω	Acentric factor
Ω	Collision integral
π	$\simeq 3.14 \dots$
ϕ	Fugacity coefficient

ρ	Density, $kg\ m^{-3}$
σ	Lennard-Jones size parameter, m
θ	Temperature, $^{\circ}C$
ζ	Third-order interaction parameter

Superscripts

<i>AqP</i>	Aqueous phase
<i>NaqP</i>	Non-aqueous phase
<i>l</i>	Brine mixture with dissolved gases
<i>sl</i>	Saturated liquid water
<i>sv</i>	Saturated vapor water

Subscripts

0	Reference condition
A	Anion
C	Cation
g	Gas
l	Liquid
<i>sat</i>	Saturation
<i>solution</i>	Brine mixture without dissolved gases

Acronyms / Abbreviations

CDG	Closed-loop Deep Geothermal
EGS	Enhanced Geothermal system
EOS	Equation Of State
FEM	Finite Element Method
GEP	Gene Expression Programming

MCDG Multilateral Closed Deep Geothermal

MOOSE Multiphysics Object-Oriented Simulation Environment

NCG Non-Condensable Gas

Chapter 1

Introduction

Global warming is a significant threat to our environment. Recent data from NASA's Goddard Institute for Space Studies (GISS) has conveyed alarming news about the increase in temperature in recent years [1]. Fig. 1.1 illustrates the variation of global surface temperature in comparison with the long-term average from 1951 to 1980. The year 2020 statistically tied with 2016 as the hottest year on record since the commencement of record-keeping in 1880. Despite the cooling impact of the La Niña climate pattern in the tropical Pacific, every month of 2022 ranked among the top ten warmest for that month. The coolest month of this year (November), was 0.75 °C warmer than the average [6]. This rise in temperature contributes to rising sea levels, melting glaciers and ice caps, more frequent and intense weather events such as hurricanes and heat waves, changes in precipitation patterns, and loss of biodiversity.

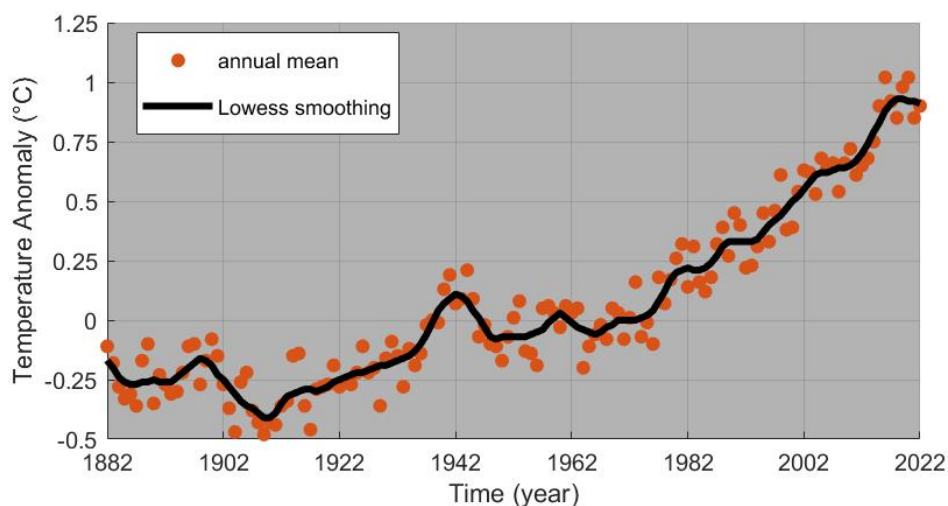


Fig. 1.1 Change of global surface temperature in comparison with the long-term average from 1951 to 1980 [1].

Human activities such as burning fossil fuels are the primary cause of global warming. These activities release greenhouse gases, including carbon dioxide, into the atmosphere, trapping heat from the sun and resulting in an increase in Earth's temperature. Other human activities like deforestation, industrial processes, and agriculture also contribute to greenhouse gas emissions. Based on the analysis conducted by NOAA's Global Monitoring Lab [2], the global average atmospheric carbon dioxide reached 418.56 parts per million (ppm) in 2022, setting a new record, despite the negative economic impact of the COVID-19 pandemic. Fig. 1.2 depicts the modern record of atmospheric carbon dioxide levels that began with observations recorded at the Mauna Loa Observatory in Hawaii [2]. The graph highlights that the more we exceed the natural processes' capacity to remove carbon dioxide in a given year, the quicker the atmospheric concentration of carbon dioxide rises. The rate of the annual increase in atmospheric carbon dioxide over the past sixty years is approximately 100 times greater than previous natural increases, such as those observed at the end of the last ice age between 11,000-17,000 years ago.

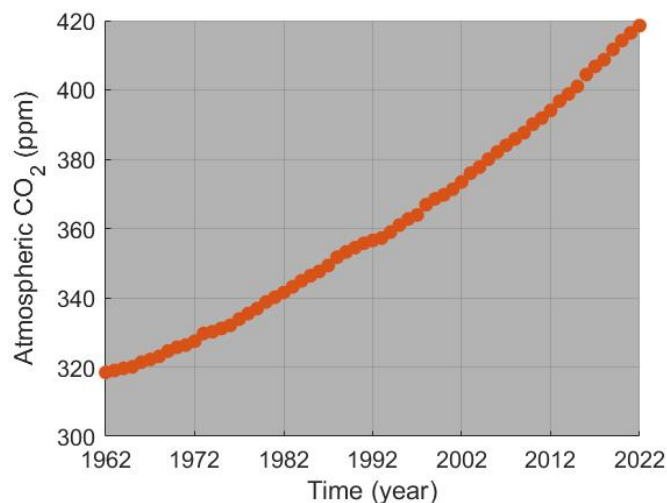


Fig. 1.2 Carbon dioxide atmospheric concentration over time [2].

The Earth's climate has already undergone substantial changes due to the rise in greenhouse gases, and if we fail to reduce emissions, the consequences could be catastrophic. Urgent action is, therefore, necessary to reduce greenhouse gas emissions and shift towards a sustainable, low-carbon economy to alleviate the impacts of global warming. Renewable energy sources such as hydroelectric, solar, wind, geothermal, and biomass play a significant role in reducing CO₂ emissions. In contrast to fossil fuels, renewable energy technologies produce electricity without emitting greenhouse gases that contribute to climate change. The International Energy Agency (IEA) estimates that renewable energy sources contributed to

nearly 80% of the increase in global electricity generation in 2020 [7]. Indeed, renewable energy was the sole energy source that experienced an increase in demand in 2020, whereas the demand for fossil fuels decreased.

The 2050 net-zero plan is a global effort to reach a balance between greenhouse gas emissions and removals, with the aim of limiting global warming to below 2 °C above pre-industrial levels and pursuing efforts to limit the increase to 1.5 °C. The plan involves transitioning to renewable energy, improving efficiency, and implementing carbon capture technologies to achieve net-zero emissions by 2050. Combining various renewable energy sources is crucial in achieving the goals of the 2050 net-zero plan. This is because no single renewable energy source can provide all the energy needed to replace fossil fuels entirely. By combining different sources such as solar, wind, hydro, geothermal, and biomass, it is possible to create a more reliable and consistent energy supply that can meet the needs of society while also reducing greenhouse gas emissions. Additionally, a mix of renewable energy sources can help to address regional variations in energy resources and ensure a more resilient energy system.

Geothermal energy is a critical component of the energy mix for several reasons. Firstly, it is a renewable and sustainable energy source that is constantly replenished by the Earth's natural heat, making it a clean and reliable energy source. Unlike some other renewable energy sources like wind and solar, geothermal energy is available 24/7, which makes it a predictable and consistent source of power. Secondly, geothermal energy is cost-effective, versatile, and possesses a substantially lower carbon footprint than conventional fossil fuels. It can be utilized for various purposes, including electricity generation, heating, and cooling, making it a versatile energy source that can be employed in homes, buildings, and industries. As of year-end 2022, the total installed geothermal power generation capacity stood at 16,127 MW, which is an increase of 286 MW over 2021 [8]. However, the annual electric production of 86 TWh reported for 2017 is still far from the 2050 goal of 1000 TWh per year [7].

Geothermal energy faces several barriers to increasing its contribution to renewable capacity, including high upfront costs, limited availability, technical challenges, environmental impacts, and policy and regulatory challenges. Overcoming these barriers requires a combination of technological innovation, supportive policies and regulations, and investments in infrastructure, research, and development. To make geothermal energy more accessible and cost-effective, governments and industry stakeholders must work together to reduce the costs of drilling and exploration, increase the efficiency of geothermal plants, and create more favorable policies and incentives to support geothermal energy development. With these measures in place, geothermal energy has the potential to become an increasingly important contributor to renewable energy portfolios worldwide.

1.1 Motivation

An ideal geothermal system would have stable and predictable heat output, low environmental impact, and a favorable regulatory environment. Such a system would be able to produce reliable, low-cost, and sustainable energy while minimizing its environmental impact and complying with local regulations and laws. Closed-loop geothermal installations can be an ideal geothermal system in certain circumstances. There are numerous advantages associated with them, such as a reduced environmental impact, decreased operating expenses, and a diminished risk of contamination or alterations to the subsurface stress field. Additionally, it is feasible to use them in a wider range of geographic locations than open-loop systems, making them more accessible to a broader range of consumers. Nevertheless, Closed-loop geothermal installations have lower efficiency than open-loop systems, as they have less direct access to the geothermal resource. This is because their heat exchange surface is limited to the lateral area around the wellbore structure, making it challenging to scale up the power output to meet larger energy demands. These systems require electricity to operate the circulation pump, which reduces their net energy output and can increase overall energy costs.

In light of the limitations of closed-loop geothermal systems mentioned earlier, the need to operate within an ideal framework, and the importance of wellbore modeling for both safety and efficient energy production, the primary objectives of this study are:

- (i) To gain a comprehensive understanding of non-isothermal, multiphase, and multi-component flow in geothermal wellbores by developing a robust and fast numerical tool
- (ii) To apply the acquired knowledge in the previous step in designing innovative geothermal frameworks that prioritize wellbore integrity and optimize energy absorption through wellbore systems

Backed by these motivations, the study is conducted in four parts:

1. Modeling of non-isothermal multiphase and multicomponent flows

Numerical modeling of multicomponent flows in geothermal wellbores is crucial for optimizing energy production, improving accuracy, and enhancing safety. Geothermal energy is a renewable source of energy, but to make it cost-effective, it is essential to optimize its production. Numerical modeling allows us to simulate complex systems accurately, providing insights into how fluids behave in geothermal wellbores, which leads to more efficient energy extraction. Additionally, numerical modeling helps predict potential safety hazards and design safer and more reliable geothermal energy systems.

Modeling multiphase multicomponent flows in geothermal wellbores is a highly complex task due to the presence of multiple phases and components in geothermal fluids. This complexity stems from the need to accurately capture interfacial phenomena and the thermodynamic behavior of the fluid, such as surface tension, viscosity, mass transfer, phase behavior, and temperature and pressure effects. Researchers employ various methods, including computational fluid dynamics simulations, analytical models, and empirical correlations, to address these challenges. These methods require sophisticated numerical algorithms and high-performance computing resources to simulate fluid behavior accurately. Overall, modeling multiphase multicomponent flows in geothermal wellbores demands a deep understanding of underlying physics, advanced computational tools, and expertise in numerical modeling and simulation.

2. Intelligent design of deep closed-loop geothermal systems

The intelligent design of closed-loop geothermal systems plays a vital role in optimizing the efficient and sustainable utilization of geothermal energy. To maximize the system's efficiency, it is essential to consider several factors during the design phase. The thermal and physical characteristics of the underground structure are vital in assessing the viability of the project. The petrophysical characteristics and tectonic situation of the site are essential factors in determining the required depth and type of borehole for the geothermal energy system. For example, the thermal properties of the subsurface play a crucial role in dictating the heat extraction capacity and sizing of the heat exchanger. Therefore, a thorough understanding of these site-specific factors is necessary to optimize the system's performance and achieve the desired energy output.

Design and operational parameters of the closed-loop geothermal system are also essential to ensure maximum efficiency and sustainability. The size and layout of the loop, the type of heat transfer fluid used, and the operating temperature range are factors that significantly influence the system's energy efficiency. The design of the heat exchanger, as well as the pump and piping system, can also have a significant impact on the system's performance. Therefore, it is crucial to consider these factors during the design phase to optimize the system's efficiency, reduce operational costs, and minimize the environmental impact of the system. By using an intelligent design approach, closed-loop geothermal systems can provide sustainable and efficient heating and cooling solutions, reduce greenhouse gas emissions, and promote the transition to a low-carbon energy future.

3. Assessment of wellbore integrity with an emphasis on corrosion risk

Geothermal wellbore integrity is of paramount importance for the efficient and safe operation of geothermal systems. A compromised wellbore can lead to a number of issues, such as the

release of harmful fluids and gases, loss of production, and potential environmental damage. Contributory factors affecting well integrity include corrosion, scale deposition, mechanical damage, thermal stresses, and chemical reactions between the geothermal fluids and well materials. Corrosion is a probable occurrence in geothermal wellbores due to several factors such as the presence of highly corrosive minerals and gases in geothermal fluids, the high temperature and pressure conditions, thermal stresses, and the presence of microorganisms.

CO₂-induced corrosion in geothermal wellbores occurs when carbon dioxide reacts with water to form carbonic acid, which can then corrode the metal components in the wellbore. This can result in the thinning of metal components, which may eventually lead to leaks or failures. Additionally, metal carbonates formed during the corrosion process can cause fouling or scaling in the wellbore, reducing the efficiency of geothermal power plants. To mitigate the impact of CO₂-induced corrosion, it is crucial to predict the corrosion rate using mathematical models. These models can help identify the factors that influence corrosion, such as temperature, pressure, and fluid chemistry. By predicting the corrosion rate, operators can make informed decisions about material selection, maintenance schedules, and other mitigation strategies to minimize the effects of corrosion. Furthermore, accurate predictions of corrosion rates can help extend the lifespan of geothermal wellbores, reduce maintenance costs, and optimize the efficiency of geothermal power plants.

1.2 Thesis structure

This thesis is divided into three main parts. The first part focuses on modeling non-isothermal multiphase and multicomponent flows. The second part explores the intelligent design of deep closed-loop geothermal systems. Lastly, the third part assesses wellbore integrity, with a particular emphasis on the risk of corrosion. These investigations comprise four papers that have been published in or submitted to international journals.

Chapter 2 provides an introduction to the basic physical phenomena, governing and constitutive equations, and underlying assumptions used in this thesis. Additionally, a brief overview of the finite element method (FEM) and its applications, MOOSE and MOSKITO, is included. The following four chapters present the papers in accordance with the outline below. Finally, Chapter 7 provides concluding remarks.

GENEOS: An accurate equation of state for the fast calculation of two-phase geofluids properties based on gene expression programming

Chapter 3 presents a fast equation of state (EOS) for computing two-phase multicomponent fluid properties. The EOS, called GENEOS, utilizes an artificial intelligence technique

called gene expression programming and is capable of computing fluid properties using pressure, enthalpy, and two-phase composition as inputs. Unlike other EOSs available in the literature, GENEOS can calculate fluid properties almost without iteration, making it an ideal choice for fast modeling of multicomponent transport in geothermal wellbores. GENEOS is unique among other EOSs in that it balances accuracy, computation speed, applicability, and transparency. While fast computation is a primary objective, care has been taken to ensure that accuracy in predicting fluid properties is not compromised. Fluid properties calculated by GENEOS are validated against experimental data, accurate numerical studies, and international standards such as IAPWS and NIST. Including the nine primary components of H₂O, CO₂, CH₄, N₂, H₂S, NaCl, KCl, CaCl₂, and MgCl₂ and transparent presentation of all the equations and algorithms as simple C++ codes facilitated the implementation of GENEOS in other codes and software. GENEOS is now successfully coupled to mass, momentum, energy, and transport equations in MOSKITO.

Impact of thermosiphoning on long-term behavior of closed-loop deep geothermal systems for sustainable energy exploitation

Chapter 4 of the study focuses on quantifying thermosiphon flow and assessing thermal power production in closed-loop deep geothermal (CDG) systems. Typically closed installations face several disadvantages, including a rapid decline in production temperature, low generated thermal power, and difficulties in deepening. Thus, the study evaluates several scenarios to identify practical ways of maximizing thermal power generation, decreasing pumping energy, and avoiding production temperature drawdown. The designed CDG system comprises two vertical wellbores connected through an extended long horizontal well. Based on the results of the study, a CDG system with a vertical depth and horizontal extension of 4 km can produce approximately 2 MW of thermal power while operating with thermosiphon effect. The study also demonstrates that the thermosiphon flow triggered in this system is stable for at least 100 years of operation. The stability of the thermosiphon flow rate and extraction temperature provides clear evidence of the system's longevity.

Stochastic performance assessment on long-term behavior of multilateral closed deep geothermal systems

Chapter 5 puts emphasis on the design of a novel multilateral framework that outperforms simple closed-loop geothermal systems in terms of power absorption per meter of wellbores. A multilateral closed deep geothermal (MCDG) system comprises several vertical injection wellbores connected through doglegs (a manifold) at a specific depth. These parallel wellbores must be sufficiently far apart to avoid any thermal interaction. The injected fluids in the vertical wellbores are initially collected at the doglegs and then redistributed through hor-

horizontal wellbores. The total injected fluid is ultimately extracted through a single production wellbore. 160 scenarios were analyzed to evaluate the performance of MCDG systems by varying the number of wellbores (i.e., system configuration) and flow rate. The study found that the heat absorption per meter of MCDG systems can be much higher than that of simple CDG installations. It was also discovered that the long-term performance of MCDG systems could be predicted as a function of their short-term behavior through stochastic analysis. Interestingly, this correlation is independent of the number of wellbores and flow rate. We were successful in filtering high-performance MCDG systems and identifying their common features, which are of great importance for increasing the contribution of closed geothermal systems to green energy production.

Development of a machine learning-based model to predict high-pressure CO₂ corrosion in carbon steel pipelines

With a particular attention to wellbore integrity, chapter 6 is dedicated to the development of a predictive model for CO₂-induced corrosion in geothermal installations. The occurrence of this type of corrosion can have a significant impact on the longevity and performance of geothermal wellbores. However, it is a complex process that involves various physical, chemical, and electrochemical phenomena, which make it difficult to be accurately described through mathematical models. The complexity of describing high-pressure CO₂ corrosion in geothermal wellbores is compounded by the changes in thermodynamics and kinetics of reactions, increased transport rates, and fluid flow patterns. Despite this complexity, most existing corrosion models are only valid for CO₂ partial pressures below 20 bar and do not assume that water wetting will always occur. On the other hand, while microscopic corrosion models are accurate for small-scale systems, they cannot be directly applied to macro-scale environments like long geothermal wellbores. The complex interactions and macroscopic factors, including fluid dynamics, temperature gradients, and material properties, necessitate the development of specialized corrosion models tailored to these larger systems. Regarding these limitations, a machine learning-based model was developed in this study to provide a good fitting for experimental corrosion data as a function of pressure, temperature, pH, and flow rate. Compared to existing corrosion models, the newly-developed model demonstrated superior performance in accurately fitting experimental data. This improved model can contribute to the mitigation of corrosion-related risks and extend the operational lifespan of geothermal installations.

Chapter 2

Fundamental processes in geothermal wellbores

The main purpose of this chapter is to highlight and explore the most significant physical phenomena that occur in geothermal wellbores. Through this discussion, we aim to deepen our understanding of the complex thermal, mechanical, and chemical processes that take place in the wellbore environment, and the impact they have on the performance and longevity of geothermal systems. By identifying and examining these phenomena, we can develop more effective strategies for designing, operating, and maintaining geothermal wells.

2.1 Relevant physical processes

Geothermal wellbores are complex systems that are subject to a range of physical phenomena that influence their performance and longevity. Some of the most significant phenomena that occur in geothermal wellbores include:

2.1.1 Lateral heat exchange between wellbore and formation

Lateral heat exchange plays a vital role in geothermal energy extraction by enabling the transfer of heat between the wellbore and the surrounding formation. The primary mechanisms of heat transfer are conduction and convection, where heat is transferred from the geothermal fluid flowing within the wellbore to the rock formations or vice versa. Several factors influence the heat transfer rate, including the thermal properties of the wellbore components, rock, and working fluid, the temperature difference between the working fluid and the surrounding area, and the fluid velocity. The efficiency of the geothermal system is directly influenced by the lateral heat exchange rate, as a higher rate of heat transfer results in increased energy gain in injection wellbores and higher heat loss in production wellbores.

2.1.2 Pressure loss due to friction

Frictional pressure losses in geothermal wellbores result from the resistance of the geothermal fluid flowing through the wellbore, which causes a drop in pressure along the length of the well. The frictional losses depend on the fluid velocity, fluid properties such as viscosity, and the wellbore geometry, such as the diameter and roughness. These factors create resistance to fluid flow, resulting in a decrease in pressure along the length of the well. Pressure losses due to friction in geothermal wellbores can significantly impact the overall efficiency of the system, and it is essential to consider these losses when designing and optimizing wellbore operations to decrease pumping energy.

2.1.3 Change of flow regime

The flow regime in geothermal wellbores can change due to variations in fluid properties and velocity, wellbore geometry, and the presence of a two-phase fluid mixture. Understanding the impact of changes in flow regime on heat transfer rate and pressure drop is critical for designing and optimizing geothermal wellbores to ensure efficient energy production and well longevity. Two-phase flow regimes, including bubbly flow, slug flow, churn flow, and annular flow, can also affect heat transfer rate and pressure drop in the wellbore. To ensure efficient and sustainable geothermal energy production, it is vital to optimize the flow regime and manage associated risks.

2.1.4 Mineral and gas dissolution

Pressure and temperature are two critical factors that can influence the processes of gas dissolution and mineral scaling in geothermal wellbores. The solubility of gases in fluids typically decreases with reducing pressure, meaning that as geothermal fluids are brought to the surface, gases that were previously dissolved may start to come out of solution, leading to degassing. On the other hand, as the temperature of the fluids decreases, minerals may start to precipitate out of solution, leading to scaling on the wellbore surfaces. Understanding the relationship between pressure, temperature, and these processes is important from a scientific standpoint as it can provide insights into the conditions of the subsurface reservoirs and the behavior of the geothermal fluids. Additionally, it can inform the design and operation of geothermal wellbores and systems to optimize energy production and minimize environmental impacts.

2.1.5 Variation of thermo-physical properties

The thermo-physical properties of fluids, such as density, viscosity, thermal conductivity, and specific heat capacity, can vary depending on pressure, temperature, phase, and composition of the fluid. In geothermal wellbores, these properties are important as they can impact the efficiency and sustainability of geothermal energy production. For example, variations in fluid density and viscosity can affect the flow rate and pressure drop in the wellbore, while variations in thermal conductivity and specific heat capacity can impact the rate of heat transfer between the fluid and the surrounding rock formations. Understanding the thermo-physical properties of single- and multi-phase, as well as multicomponent fluids, is critical for the design and operation of geothermal wellbores and systems to maximize energy output and minimize environmental impacts.

2.1.6 Mass exchange between wellbore and reservoir

The mass exchange between a geothermal wellbore and reservoir is crucial for efficient geothermal energy production. Mass exchange determines the rate at which fluids can be injected into the reservoir for heat extraction, and therefore affects the energy efficiency of the system. Effective mass exchange ensures a constant pressure gradient, enhances injectivity, and reduces the risk of clogging and blockage of the wellbore. However, mass exchange can also lead to unwanted leakage of fluids from the wellbore into surrounding formations, reducing the efficiency of the system and potentially causing environmental risks. Therefore, understanding and managing mass exchange is critical for optimizing geothermal energy production while minimizing the risk of leakage.

2.2 Governing equations

To achieve accurate numerical modeling of wellbores, a thorough comprehension of the underlying physical processes is imperative. This includes a detailed description of energy exchange between the wellbore and the surrounding formation, heat transfer in the formation, and transient processes within the wellbore. The fluid flow inside the inner casing is subject to several coupled physical processes, including pressure loss due to friction, changes in kinetic energy, temperature variation due to heat exchange with the surrounding formation, velocity changes that influence the pressure and temperature fields, and the buoyancy effect due to variations in fluid density. The equations governing these coupled processes are addressed in the next section.

2.2.1 Conservation equations

The following equations govern the non-isothermal transient flow in a wellbore:

Continuity equation

The principle of mass conservation, also known as continuity, is governed by:

$$\frac{\partial}{\partial t}(\rho) = -\frac{\partial}{\partial z}(\rho v) + m \quad (2.1)$$

In this equation, ρ and v respectively denote the fluid density and velocity, while m represents the mass sink/source term per unit volume and time.

Momentum equation:

The equation for momentum describes the pressure drop that occurs along tubing or an annulus, taking into account the effects of gravity, friction, and kinetic energy. According to the law of conservation of momentum, the total forces acting on the fluid are equal to the rate of change of momentum. These forces can include pressure, friction, and gravity:

$$\frac{\partial P}{\partial z} = \rho g \cos(\theta) \pm \frac{f\rho v^2}{2d} \pm \left(\frac{\partial}{\partial t}(\rho v) + \frac{\partial}{\partial z}(\rho v^2) \right) \quad (2.2)$$

where P , g , θ , f , and d represent fluid pressure, gravitational acceleration, the inclination of the well, friction factor, and wellbore hydraulic diameter, respectively. The sign of the terms on the right-hand side of the momentum equation can vary depending on the flow direction and the direction of gravity.

Energy equation:

The energy equation is expressed as:

$$\frac{\partial}{\partial t} \left[\rho \left(h - \frac{P}{\rho} + \frac{1}{2}v^2 \right) \right] = -\frac{\partial}{\partial z} \left[\rho v \left(h + \frac{1}{2}v^2 \right) \right] + \rho v g \cos(\theta) - \frac{q}{A} + Q \quad (2.3)$$

in which, h , q , and Q denote enthalpy, radial heat flow, and heat source/sink terms, respectively.

2.2.2 Friction force

Moody's friction factor [9] is widely used in fluid mechanics to calculate the pressure drop or head loss in a pipe due to frictional losses. It is a dimensionless quantity that characterizes the frictional losses in a pipe and is determined by the flow regime, pipe roughness, and Reynolds

number. Moody's diagram [10] provides a graphical representation of the friction factor as a function of the Reynolds number and pipe roughness, allowing engineers to estimate the friction factor for a given flow regime, pipe roughness, and diameter. The friction factor is used in the Darcy-Weisbach equation [11] to calculate the head loss due to friction in a pipe, which is an important parameter in many engineering applications involving fluid flow. Moody's diagram allows for the identification of four distinct regions:

1. Laminar region where the friction factor remains unaffected by the roughness of the pipe.
2. The transition zone is an intermediate region between the smooth and rough zones, where the friction factor values depend on both the relative roughness of the pipe and the Reynolds number.
3. The hydraulic smooth flow regime, which is characterized by a moderate degree of roughness, in which the pipe behaves similarly to a smooth duct.
4. The fully developed turbulence region where the friction factor is no longer dependent on the Reynolds number.

Hagen-Poiseuille's law is a commonly used equation for single-phase, fully developed internal laminar flows. It can be expressed as:

$$f = 64/Re \quad (2.4)$$

On the other hand, the friction factor for turbulent flows can be determined using the Serghides solution [12]. This solution provides a description of the friction factor for turbulent flows in smooth pipes, given by:

$$f = 0.184Re^{-2} \quad (2.5)$$

The friction factor for rough pipes is determined by:

$$f = \left(\frac{1}{d}\right)^2 \quad (2.6)$$

where

$$d = a - (b - a)^2 / (c - 2b + a) \quad (2.7)$$

and

$$a = -2 \log_{10} \left(\frac{\varepsilon}{3.7} + \frac{12}{Re} \right) \quad (2.8)$$

$$b = -2\log_{10} \left(\frac{\varepsilon}{3.7} + \frac{2.51a}{Re} \right) \quad (2.9)$$

$$c = -2\log_{10} \left(\frac{\varepsilon}{3.7} + \frac{251b}{Re} \right) \quad (2.10)$$

2.2.3 Drift flux model

The drift-flux model is a widely used approach in the analysis of multiphase flow in pipes, particularly in industries such as oil and gas. This model focuses on understanding the velocity difference between different phases, such as gas and liquid, as they flow together. By studying the behavior of these phases, the drift-flux model provides valuable insights into the dynamics of multiphase flow systems. One of the key assumptions of the drift-flux model is the concept of homogeneous flow. It treats the multiphase mixture as a single, homogeneous fluid with averaged properties. This simplification allows for a more straightforward analysis of the overall behavior of the combined phases. Instead of considering each phase separately, the model examines the collective behavior of the phases as they interact and move through the pipe.

The model also assumes local equilibrium, which means that the forces acting on each phase are in balance at each point in the flow. This assumption is reasonable under normal flow conditions where the flow velocities are relatively low to moderate. It implies that the forces driving the phases, such as pressure gradients and gravitational effects, are distributed in such a way that they maintain equilibrium between the phases. In terms of accuracy, the drift-flux model provides reasonable predictions for flows with moderate interfacial velocities and volume fractions. It is suitable for analyzing typical flow scenarios encountered in many practical applications. However, in highly complex or extreme flow regimes, such as slug flow or dispersed flow with large concentration gradients, the model's accuracy may diminish. In these cases, more advanced models or correlations may be necessary to capture the intricate behavior of the multiphase flow.

Despite its simplifications, the drift-flux model offers several advantages. Firstly, it allows for efficient computation, striking a balance between accuracy and computational complexity. This computational efficiency is particularly beneficial when analyzing large-scale systems or when multiple flow scenarios need to be evaluated. Secondly, the model provides valuable insights into the distribution of phases along the pipe, including their velocity profiles and volumetric fractions. This information is crucial for designing and optimizing multiphase flow systems, as it helps in determining factors such as pressure drop, flow regime transitions, and phase separation.

For two-phase flow, ρ and v in Eqs. (2.1) to (2.3) refer to the mixture density and velocity, respectively. The mixture density ρ can be calculated by:

$$\rho = \rho_g f_g + \rho_L (1 - f_g) \quad (2.11)$$

where ρ_g and ρ_L represent gas density and liquid density, respectively. f_g , the in-situ gas volume fraction, is a function of superficial velocity (v_{sg}), drift velocity (v_d), and mixture velocity (v):

$$f_g = \frac{v_{sg}}{c_0 v + v_d} \quad (2.12)$$

The profile parameter (c_0) and drift velocity can be estimated by the so-called drift-flux model. This method is based on the assumption that the two phases move at different velocities (i.e., slip phenomenon) due to differences in their densities, viscosities, and other physical properties. There are two primary factors that contribute to the gas phase moving faster than the liquid phase within a pipe. Firstly, the gas phase has a tendency to accumulate in the center of the pipe, resulting in a higher velocity compared to the surrounding liquid phase. Secondly, gas buoyancy causes the gas to rise vertically upwards through the liquid phase, further accelerating its velocity. The gas velocity (v_g) of two-phase flow in a vertical pipe is given by:

$$v_g = c_0 v + v_d \quad (2.13)$$

The mixture velocity is also expressed as:

$$v = v_{sg} + v_{sL} = f_g v_g + (1 - f_g) v_L \quad (2.14)$$

Including the definition of superficial velocity ($v_{sg} = f_g v_g$ and $v_{sL} = (1 - f_g) v_L$) in Eq. (2.14), the liquid velocity (v_L) can be derived as:

$$v_L = \frac{1 - f_g c_0}{1 - f_g} v - \frac{f_g}{1 - f_g} v_d \quad (2.15)$$

Using the method proposed by Shi *et al.* [13, 14], the profile parameter is computed by:

$$c_0 = \frac{A}{1 + (A - 1)\gamma^2} \quad (2.16)$$

The term γ in Eq. (2.16) is an adjusting parameter to keep c_0 close to 1.0 when mixture velocity or in-situ steam volume fraction is high. It is defined by:

$$\gamma = \frac{\beta - B}{1 - B} \quad (0 \leq \gamma \leq 1) \quad (2.17)$$

where β is given as:

$$\beta = \max \left(f_g, F_v \frac{f_g |v|}{v_{sgf}} \right) \quad (2.18)$$

The "flooding velocity" (v_{sgf} in Eq. (2.18)) refers to the minimum velocity at which the gas phase can support and sustain the liquid flow at an equal velocity to the gas flow. This indicates that the velocity is sufficient to prevent the liquid phase from separating from the gas phase. Once the flooding velocity is reached, the flow regime within the pipe transitions to an annular flow pattern. It is computed by:

$$v_{sgf} = v_g (v_L = 0) = K_u \sqrt{\frac{\rho_L}{\rho_g}} v_c \quad (2.19)$$

The term k_u in Eq. (2.19) is the critical Kutateladze number. Characteristic velocity (v_c) is calculated as a function of gas/liquid interfacial tension (σ_{gl}):

$$V_c = \left(\frac{\sigma_{gl} g (\rho_l - \rho_g)}{\rho_l^2} \right)^{1/4} \quad (2.20)$$

Eqs. (2.16) to (2.18) include the variables A , B , and F_v , which are used to fit experimental data. The parameter A represents the profile in a slug or bubble flow regime and has a default value of (1.2). Parameter B reflects the in-situ gas volume fraction (f_g) or the mixture velocity ratio to the flooding velocity and has a default value of (0.3). The term F_v represents the sensitivity of the profile parameter c_0 to the flooding velocity. Modifying the value of F_v will make c_0 more or less sensitive to changes in velocity. The profile parameter calculation must meet the following conditions:

$$\frac{\partial}{\partial f_g} (f_g c_0) > 0 \text{ and } \frac{\partial}{\partial v} (v c_0) > 0 \quad (2.21)$$

or alternatively:

$$B < (2 - A)/A \quad (2.22)$$

The drift velocity (v_d) can be calculated using the following formula:

$$v_d = \frac{(1 - f_g c_0) c_0 K(f_g) v_c}{f_g c_0 \sqrt{\frac{\rho_g}{\rho_l}} + 1 - f_g c_0} \quad (2.23)$$

where

$$\begin{aligned} K(f_g) &= 1.53/C_0, \text{ when } f_g \leq a_1 \\ K(f_g) &= K_u, \text{ when } f_g \geq a_2 \end{aligned} \quad (2.24)$$

Linear interpolation is applied between the two values mentioned in Eq. (2.24) when ($a_1 \leq f_g \leq a_2$). The default values for a_1 and a_2 are 0.2 and 0.4, respectively. The critical Kutateladze number (K_u) is related to the dimensionless pipe diameter as follows:

$$D = \left[\frac{g(\rho_l - \rho_g)}{\sigma_{gl}} \right]^{1/2} d \quad (2.25)$$

The K_u value varies with changes in the dimensionless pipe diameter, as shown in Table 2.1:

Table 2.1 K_u value as a function of dimensionless pipe diameter

Dimensionless pipe diameter (D)	Critical Kutateladze number (K_u)
≤ 2	0
4	1
10	2.1
14	2.5
20	2.8
28	3
≥ 50	3.2

When dealing with two-phase flows in inclined pipelines, it is common to apply the Hasan and Kabir [15] method to correct the drift velocity:

$$V_{d\theta} = V_d|_{\theta=0} (\cos \theta)^{0.5} (1 + \sin \theta)^2 \quad (2.26)$$

Shi *et al.* [13, 14] introduced an alternative approach for adjusting the drift velocity (V_d), which was based on experimental data:

$$m(\theta) = 1.85(\cos \theta)^{0.21} (1 + \sin \theta)^{0.95} \quad (2.27)$$

$$A = 1.0, a_1 = 0.06, a_2 = 0.21$$

2.2.4 Lateral heat model

Heat exchange can occur between the fluid and its surrounding structures (such as casings, cement layers, and geological formations) through two primary mechanisms. The first mechanism involves conductive heat transfer across all layers, while the second mechanism involves convective heat transfer within a fluid film located near the inner tubing wall. The transient heat exchange rate between the outer casing wall and formation can be calculated

using the formula proposed by Ramey [16]:

$$q = \frac{2\pi k_e (T_{co} - T_e)}{f(t)} \quad (2.28)$$

where k_e , T_{co} , and T_e represent the formation thermal conductivity, the temperature of the outside of the casing wall, and the formation temperature, respectively. Additionally, a time-dependent function $f(t)$ is used to model the transient behavior of the system. Ramey [16] proposed an analytical formula to calculate $f(t)$ for time periods exceeding one week:

$$f(t) = \ln \frac{2\sqrt{\alpha t}}{r_{cf}} - 0.29 \quad (2.29)$$

In the above equation, the formation thermal diffusivity is represented by the variable α , while r_{cf} denotes the radius of the interface between the cement and formation. Willhite [17] made enhancements to Ramey's method of determining heat loss by incorporating an overall heat transfer coefficient that accounts for all the thermal resistances of the fluid flow, tubing wall, annulus, casing wall, and cement as a collective factor. As a result, the formula for quantifying heat loss can be expressed as follows:

$$q = 2\pi r_{to} U_{to} (T_f - T_{cf}) \quad (2.30)$$

The variables U_{to} , r_{to} , T_f , and T_{cf} refer to the overall heat transfer coefficient, outside radius of tubing, fluid temperature, and temperature at the cement/formation interface, respectively. Willhite's method for computing the overall heat transfer coefficient can be expressed as follows:

$$\frac{1}{U_{to}} = \frac{r_{to}}{r_{ti} h_f} + \frac{r_{to} \ln(r_{to}/r_{ti})}{K_t} + \frac{r_{to} \ln(r_{ins}/r_{to})}{K_{ins}} + \frac{r_{to}}{r_{ins} (h_c + h_r)} + \frac{r_{to} \ln(r_{co}/r_{ci})}{K_{cas}} + \frac{r_{to} \ln(r_{wb}/r_{co})}{K_{cem}} \quad (2.31)$$

In which r_{ti} , r_{to} , r_{ins} , r_{ci} , r_{co} , and r_{wb} refer to the radii of the inside tubing, outside tubing, insulation tubing, inside casing, outside casing, and cement/formation interface, respectively. Additionally, K_t , K_{ins} , K_{cas} , and K_{cem} denote the thermal conductivities of the tubing wall, insulation tubing, casing wall, and cement, while h_f , h_c , and h_r represent the convective heat transfer coefficient between the fluid film inside the tubing and the tubing wall, and the convective and radial heat transfer coefficients of the fluid inside the annulus.

To determine the overall heat transfer coefficient, Willhite [17] introduced an iterative procedure that is still widely used today. This procedure involves six steps:

1. Calculate an approximate value for the overall heat transfer coefficient U_{to} using the average temperature of the tubing and the annulus.
2. Compute the Ramey time function $f(t)$ using the appropriate method. If the time is less than one week, refer to Table 2.2 to obtain the value of $f(t)$. If the time is greater than one week, use Eq. (2.29) to calculate $f(t)$.

Table 2.2 The values of the Ramey time function $f(t)$ for time periods less than one week

$r_{to}U_{to}/k_e \rightarrow$	0.01	0.02	0.05	0.1	0.2	0.5	1	2	5	10	20	50	100	8
$\alpha t/r^2 \downarrow$														
0.1	0.313	0.313	0.314	0.316	0.318	0.323	0.33	0.345	0.373	0.396	0.417	0.433	0.438	0.445
0.2	0.423	0.423	0.424	0.427	0.43	0.439	0.452	0.473	0.511	0.538	0.568	0.572	0.578	0.588
0.5	0.616	0.617	0.619	0.623	0.629	0.644	0.666	0.698	0.745	0.772	0.79	0.802	0.806	0.811
1	0.802	0.803	0.806	0.811	0.82	0.842	0.872	0.91	0.958	0.984	1	1.01	1.01	1.02
2	1.02	1.02	1.03	1.04	1.05	1.08	1.11	1.15	1.2	1.22	1.24	1.24	1.25	1.25
5	1.36	1.37	1.37	1.38	1.4	1.44	1.48	1.52	1.56	1.57	1.58	1.59	1.59	1.59
10	1.65	1.66	1.66	1.67	1.69	1.73	1.77	1.81	1.84	1.86	1.86	1.87	1.87	1.88
20	1.96	1.97	1.97	1.99	2	2.05	2.09	2.12	2.15	2.16	2.16	2.17	2.17	2.17
50	2.39	2.39	2.4	2.42	2.44	2.48	2.51	2.54	2.56	2.57	2.57	2.57	2.58	2.58
100	2.73	2.73	2.74	2.75	2.77	2.81	2.84	2.86	2.88	2.89	2.89	2.89	2.89	2.9

3. Determine the initial formation temperature (T_e) and the temperature at the cement/formation interface (T_{cf}) through these calculations:

$$T_e = T_{surf} - g_T Z \cos(\theta) \quad (2.32)$$

$$T_{cf} = \frac{r_{to}U_{to}f(t)T_f + k_e T_e}{r_{to}U_{to}f(t) + k_e} \quad (2.33)$$

where T_{surf} denotes the ground surface geothermal temperature, g_T represents a geothermal gradient, Z is the wellbore depth, and θ indicates the local angle between the well and the vertical direction.

4. Compute the casing internal temperature T_{ci} and the tubing external temperature T_{to} :

$$T_{ci} = T_{cf} + \left[\frac{\ln\left(\frac{r_{cf}}{r_{co}}\right)}{k_{cm}} + \frac{\ln\left(\frac{r_{co}}{r_{ci}}\right)}{k_{cas}} \right] r_{to}U_{to} (T_f - T_{cf}) \quad (2.34)$$

$$T_{to} = T_f - \left[\frac{\ln\left(\frac{r_{to}}{r_{ti}}\right)}{k_t} \right] r_{to}U_{to} (T_f - T_{cf}) \quad (2.35)$$

5. Determining the convective heat transfer coefficient (h_c) and the radial heat transfer coefficient (h_r) in the annulus. The radial heat transfer coefficient (h_r) can be obtained

using the Stefan-Boltzmann law:

$$h_r = \sigma F_{tci} (T_{to}^2 + T_{ci}^2) (T_{to} - T_{ci}) \quad (2.36)$$

$$\frac{1}{F_{tci}} = \frac{1}{\epsilon_{to}} + \frac{r_{ti}}{r_{ci}} \left(\frac{1}{\epsilon_{ci}} - 1 \right) \quad (2.37)$$

where the Stefan-Boltzmann constant (σ) is equal to $[1.713 \times 10^{-9} \text{Btu}/(\text{ft}^2 \text{hrR}^4)]$. The emissivity of the outside tubing surface (ϵ_{to}) and the emissivity of the inside casing surface (ϵ_{ci}) are also required for the calculation. To determine the convective heat transfer coefficient (h_c), Willhite [17] used the correlations presented by Dropkin and Somerscales [18]:

$$h_c = k_{hc} / [r_{to} \ln(r_{ci}/r_{to})] \quad (2.38)$$

$$k_{hc}/k_{ha} = 0.049 (G_r P_r)^{0.333} P_r^{0.074} \quad (2.39)$$

$$G_r = \frac{(r_{ci} - r_{to})^3 g \rho_{an}^2 \beta (T_{to} - T_{ci})}{\mu_{an}^2} \quad (2.40)$$

$$P_r = C_{an} \mu_{an} / k_{ha} \quad (2.41)$$

The variables in Eqs. (2.38) to (2.41) are defined as follows: k_{ha} indicates the thermal conductivity of the fluid in the annulus at the average pressure and temperature, while k_{hc} is determined by calculating the equivalent thermal conductivity of the fluid in the annulus based on natural convection effects at the average pressure and temperature. The dimensionless Grashof and the Prandtl numbers are represented by G_r and P_r , respectively. The thermal volumetric expansion coefficient of the fluid in the annulus is represented by β , while C_{an} is used to denote the heat capacity of the fluid in the annulus. Lastly, the viscosity and density of the fluid in the annulus are respectively represented by μ_{an} and ρ_{an} .

6. Compute a fresh estimate of U_{to} using Eq. (2.31) with the values obtained in steps (1) to (5). Compare this newly derived U_{to} value with the original value. If the discrepancy between the new and old U_{to} values surpasses a certain tolerance threshold, utilize the new U_{to} value to repeat steps (2) to (6) until the difference is below the tolerance value.

Once the U_{to} value has reached a state of convergence, it becomes possible to utilize the temperature at the interface between the cement and formation (T_{cf}) for the purpose of calculating heat loss.

2.2.5 Equation of state

Determining the liquid/gas phase composition is crucial in calculating the thermodynamic properties of two-phase mixtures. One approach to identifying phase equilibria, partition coefficients, and vapor-liquid equilibrium in two-phase multicomponent systems is to assume that the chemical potential of each component in the aqueous phase (AqP) is equal to that in the non-aqueous phase (NaqP). This equilibrium condition can be expressed using either the Fugacity-Fugacity (F-F) model or the Fugacity-Activity (F-A) model. The F-F model uses classical cubic equations of state (EOSs) to calculate the chemical potential in both phases, while the F-A model uses an equilibrium constant and ion activity to represent chemical potential in the AqP, and the fugacity coefficients of gas components are calculated using an EOS. The equations used to calculate the chemical potentials of AqP and NaqP in the F-A model are as follows:

$$\mu^{NaqP}(T, P) = \mu_0^{NaqP}(T, P) + RT \ln(f) \quad (2.42)$$

$$\mu^{AqP}(T, P) = \mu_0^{AqP}(T, P) + RT \ln(a) \quad (2.43)$$

in which μ_0 , R , T , and P symbolize chemical potential at the reference temperature, the gas constant, temperature, and pressure, respectively. The fugacity of gas components, denoted as f , is calculated by:

$$f = P\phi y \quad (2.44)$$

where the mole fraction of each component in the NaqP is denoted by y , and ϕ represents the fugacity coefficient. Equating the two chemical potentials (Eqs. (2.42) and (2.43)) results in:

$$\frac{\mu_0^{AqP}(T, P) - \mu_0^{NaqP}(T, P)}{RT} = \ln\left(\frac{a}{P\phi y}\right) = \ln(K^0) \quad (2.45)$$

Using Henry's constant (K_H) and the number of moles per kilogram of water ($N_w = 55.508$) for defining the equilibrium constant ($K^0 = N_w/K_H$), it is possible to re-formulate Eq. (2.45) as:

$$\frac{N_w}{K_H} = \frac{a}{P\phi y} \quad (2.46)$$

Assuming that the solubility of gas species in the liquid phase is negligible, a in Eq. (2.46) can be expressed as ($a = N_w\gamma x$), where γ and x represent the activity coefficient and mole fraction of components in the AqP, respectively [19]. As a result, the new form of Eq. (2.46) for each gas is given as [20, 21]:

$$(P\phi y_i)_{NaqP} = (K_{Hi}\gamma_i x_i)_{AqP} \quad (2.47)$$

The procedure of computing equilibrium constants, fugacity coefficients, Henry's constant, and activity coefficients is elaborately discussed in the next chapter.

2.3 Numerical scheme

2.3.1 Finite element method

Finite element method (FEM) is a numerical technique for solving partial differential equations in a wide range of engineering, science, and mathematical applications. FEM divides the problem domain into smaller, simpler, and connected elements. The unknown variables in the partial differential equation are then approximated by the basis functions over each element. This approximation leads to a system of algebraic equations that can be solved to determine the unknown variables, such as temperature, pressure, velocity, and stress, at each node or vertex. FEM has several advantages over other numerical methods in modeling multiphase multicomponent flows in geothermal wellbores.

Geothermal reservoirs contain a complex mixture of water, steam, and gas, and their behavior is governed by multiple flow phenomena involving fluid dynamics, thermodynamics, and chemical reactions. Accurate simulation of these phenomena is crucial for optimizing geothermal well performance and lifespan. The Finite Element Method (FEM) is a powerful numerical tool that can handle these complexities, offering a flexible and adaptable framework to model various physical phenomena and boundary conditions. This method can accommodate irregular geometries and non-uniform material properties that are typical of geothermal reservoirs. Moreover, FEM can address transient problems, where fluid behavior changes over time due to variations in temperature, pressure, and flow rates. Additionally, the Finite Element Method can handle non-linear and non-ideal fluid behavior, such as non-Newtonian viscosity, compressibility, and phase change. These capabilities make FEM a robust and versatile numerical method for accurately and efficiently simulating complex multiphase multicomponent flows in geothermal wellbores.

2.3.2 MOOSE

Moose is a Finite Element Method (FEM) solver, a software package for simulating complex physical systems, developed at the Idaho National Laboratory (INL) in the United States. This solver is built using object-oriented C++ which is well-suited for scientific computing. Moose is designed to solve large-scale, multi-physics problems using a modular approach, where users can easily add or modify physical models and numerical methods to suit their

needs. It is an open-source software package, meaning it is freely available to anyone to use and modify, and is actively maintained by a team of developers at the INL.

Moose is particularly useful in simulating problems in which multiple physical phenomena interact, such as heat transfer, fluid dynamics, and structural mechanics. By using FEM, Moose can accurately model the behavior of these systems, taking into account geometric complexity and non-linear behavior. The software also includes a variety of numerical methods and algorithms for solving partial differential equations (PDEs), making it a powerful tool for a wide range of applications in engineering, physics, and materials science.

The modular architecture of Moose allows users to quickly build complex simulations by combining pre-existing modules or creating their own. This makes it an efficient and flexible tool for researchers and engineers, who can quickly test and validate their designs or hypotheses. Additionally, Moose includes a graphical user interface (GUI) for creating and visualizing simulations, as well as tools for post-processing and data analysis. These features make Moose a user-friendly and comprehensive package for modeling complex systems in a variety of fields.

2.3.3 MOSKITO

MOSKITO is a powerful and user-friendly wellbore simulator developed by Dr. Maziar Gholami Korzani and the author of this thesis. The acronym MOSKITO stands for **M**ultiphysics **c**oupled **S**imulator **t**ool**KIT** for well**O**res. It is an open-source C++ code developed on the MOOSE Framework that can handle transient non-isothermal multi-phase and multi-component flows.

MOSKITO solves the conservation equations in a fully coupled manner. This numerical tool has been designed to handle the simulation of wellbores with complex configurations, including Multilateral, U-shape, and Coaxial. Additionally, MOSKITO has the unique ability to calculate the thermo-physical properties of two-phase multi-component mixtures, including H₂O, CO₂, CH₄, N₂, H₂S, NaCl, KCl, CaCl₂, and MgCl₂, using a fast equation of state that has been trained through machine learning. The researchers and engineers can use MOSKITO regardless of their preferred operating system as it can be run on macOS, Linux, and Windows.

Chapter 3

GenEOS: An accurate equation of state for the fast calculation of two-phase geofluids properties based on gene expression programming

This chapter is submitted as GenEOS: An accurate equation of state for the fast calculation of two-phase geofluids properties based on gene expression programming, Esmaeilpour M, Nitschke F, Kohl T.

Abstract

Numerical simulation of two-phase multicomponent flows requires solving continuity, momentum, energy, and transport equations. Typically, these conservation equations are solved for computing the main variables of pressure, enthalpy, velocity, and composition. Variation of thermophysical properties (e.g., density, viscosity, etc.) as functions of the main variables necessitates introducing equations of state (EOS) to the modeling scheme, equating the number of unknowns and equations. The problem arises here as almost all the available EOSs in the literature receive temperature as an input, which is not a main variable. Guessing temperature, as an unknown input, imposes more iterations on the already iterative algorithm of the EOS and increases the computational cost. The primary focus of this study is to provide highly-precise, but fast EOS scheme for calculating two-phase fluid properties using artificial intelligence algorithms. In the first step, a Fugacity-Activity model is implemented to supply a supervised learning algorithm with a large dataset. The provided data are fed into a machine-learning (ML) model called gene expression programming (GEP). The outputs of this GEP model are high-preciseness explicit formulas for non-iterative computing of temperature and equilibrium constants. Testing the proposed GEP equations for 1,000,000 arbitrary sets of inputs revealed high accuracy in predicting desired outputs (e.g., < 0.6 % error in calculating temperature). Implementing GEP equations in modeling platforms can result in 90 % reduction in EOS-related computational cost. This ML-based EOS is a

transparent box for computing thermophysical properties of two-phase mixtures containing H_2O , CO_2 , CH_4 , N_2 , H_2S , NaCl , KCl , CaCl_2 , and MgCl_2 .

3.1 Introduction

Control of thermal fluids is essential for producing renewable geothermal energy [22, 23] or storing/extracting solutes in deep reservoirs [24, 25]. Depending on the specific application (e.g., leaching, underground CO_2 storage, heat extraction), the circulated fluid should be engineered to be a proper carrier of energy to maximize the power production rate [26], have high mobility factor (inverse kinematic viscosity) to be easily circulated in the system [27], be a good solvent of target minerals to enhance absorption rate [28], and not cause any environmental hazard. Two-phase conditions may occur under a specific P-T situation, like gas injection into geothermal brines [29] or under production conditions when non-condensable gases (NCG) are released [30]. Injecting CO_2 for carbon capture, utilization, and storage (CCUS) [31] and enhancing oil recovery (EOR) [32, 33] are the most-renown examples of two-phase flows in reservoirs. It is also noteworthy that typically the high pressure of deep geothermal reservoirs avoids water boiling. However, the co-occurring high temperature and low pressure in production wellbores may cause the fluid to enter the two-phase regime [34].

Calculating two-phase geofluids properties is challenging, as they are complex functions of pressure, temperature, and the composition of both liquid and gas phases. The process of calculating these properties poses an enormous challenge to rapidly model fluid flow and heat transfer in large 3D reservoirs due to the highly iterative algorithms required to determine the composition of each phase. The equilibrium condition, when the chemical potential of each component in the aqueous phase (AqP) equals that in the non-AqP (NaqP), can be expressed by either Fugacity–Fugacity (F–F) or Fugacity–Activity (F–A) models. These two methods use different thermodynamic properties for defining the equilibrium state of each component in a two-phase mixture. The F–A model introduces equilibrium constants and ion activities to represent the chemical potentials in the AqP, while the fugacity coefficients of gas components are calculated using an equation of state (EOS). However, The F–F model uses the classical cubic EOSs (e.g., Soave-Redlich-Kwong and Peng-Robinson) to compute the chemical potential in both phases.

Determining the liquid/gas phase composition is essential for calculating two-phase mixture properties. However, the available algorithms for computing gas solubility in the aqueous medium are highly iterative and impose an enormous barrier to the fast modeling of fluid flow and heat transfer in large 3D reservoirs. Assuming that the chemical potential of

each component in the aqueous phase (AqP) equals that in the non-aqueous phase (NaqP), the equilibrium condition can be expressed by either Fugacity–Fugacity (F–F) or Fugacity–Activity (F–A) models. These two methods use different thermodynamic properties for defining the equilibrium state of each compound in a two-phase mixture. The F–A model introduces equilibrium constant and ion activity to represent chemical potential in the AqP, while the fugacity coefficients of gas components are calculated using an equation of state (EOS). However, The F–F model uses the classical cubic EOSs to compute the chemical potential in both phases.

Various numerical software packages apply EOS algorithms to calculate two-phase fluid properties. The TOUGH software family is widely used for modeling non-isothermal multiphase multicomponent flows [35]. These codes contain several equation of state modules that calculate the thermodynamic properties of various fluid systems using F–A and F–F algorithms. The ECO2N [36] and ECO2N V2.0 [37] modules were specifically developed to simulate the flow of CO₂-brine systems at temperatures of up to 110 °C and 250 °C, respectively. Neither of these two modules has the capability to calculate gas-mixture properties. In order to incorporate additional gas components, such as N₂ and CH₄, in the two-phase mixture, Oldenburg *et al.* [38] developed another module called EOS7C. Using a highly-iterative thermodynamic model to solve the mutual solubility of gases in brine makes EOS7C computationally expensive. Pruess and Battistelli [39] proposed TMVOC as a TOUGH2 module to model three-phase systems comprising gas, aqueous, and non-aqueous phase liquids. However, TMVOC was developed to simulate near-surface contamination, characterized by low pressure and temperature conditions. TMGAS is another TOUGH2 module that has been developed based on the TMVOC module to simulate the injection of gas mixtures into deep geological sites [40]. Unlike other modules, TMGAS uses the F–F model to calculate phase equilibrium in gas mixtures and brine systems. It poses a considerable computational cost when included in the numerical modeling of multiphase multicomponent flows, and its accuracy decreases for salinities greater than 2 mol/kg water. EWASG is a TOUGH module developed for modeling non-condensable gas-brine systems with temperatures ranging between 100 and 350 °C [41]. It assumes perfect gas behavior, which simplifies the calculation of gas properties. However, it is important to note that this assumption may not accurately represent the behavior of real gases at extreme pressures or low temperatures.

Further studies have been conducted applying EOS algorithms for determining the phase composition. Numerous non-iterative F–A models have been developed to predict the phase equilibrium of binary systems, such as CO₂-brine [42–46, 19, 47–49], H₂S-brine [50], and CH₄-brine [51]. However, calculating the solubility in two-phase mixtures with several

gas components is iterative as it requires solving the sophisticated Rachford-Rice equation. Ziabakhsh-Ganji and Kooi [52] used this iterative F-A approach to model the thermodynamic equilibrium in brine-gas mixtures containing CO₂, CH₄, N₂, H₂S, and SO₂. In their proposed model, fugacity coefficients of gas components are calculated by Peng-Robinson (PR) EOS, while Pitzer formalism and Henry's law are implemented for computing activity coefficients in the aqueous phase. Appelo *et al.* [53] introduced a more general model for calculating the apparent molar volumes of single ions. While their modifications are now embedded in the F-A algorithm of PHREEQC, the validity of H₂S solubility is still unclear. Francke *et al.* [54] tried to unify Duan's single-gas solubility functions [42, 51, 55] to model the gas dissolution in CO₂-CH₄-N₂-brine mixtures. However, assuming ideal gas behavior (fugacity coefficients equal to unity) makes this model inappropriate for geothermal applications with a high range of pressures/temperatures. Zirrahi *et al.* [56] tried to develop a non-iterative F-A model to describe the phase equilibrium behavior of brine-gas mixtures, including CO₂, CH₄, and H₂S. However, their proposed method cannot accurately predict CO₂ and H₂S solubility in the aqueous phase [57]. In 2015, Li *et al.* [58] formulated an iterative F-F model to calculate the mutual solubility of gas mixtures (CO₂-CH₄-N₂-H₂S-SO₂) in brine. While their suggested model is valid over a wide range of pressures, temperatures, and salinity, the considerable computational costs imposed by iterative solving of the Rachford-Rice equation make it inadequate for implementation in reactive transport simulations. Li *et al.* [59] compared the calculation speed of the F-F and F-A models in predicting the mutual solubility of CO₂-CH₄-H₂S mixtures in brine and confirmed that the F-A models are much faster than the F-F models.

All the EOS algorithms discussed above use pressure, temperature, and two-phase composition as inputs. However, most of the conducted studies on numerical modeling of multiphase multicomponent flows solve continuity, momentum, energy, and transport equations to calculate the main variables of pressure, enthalpy, velocity, and two-phase composition. Using these EOSs in the simulation process of multiphase reactive transports considerably increases the computational cost since temperature, as an unknown, needs to be guessed at the beginning of the algorithm. In other words, considering enthalpy instead of temperature as an input multiplies the iterations required for calculations of gas solubility in the AqP.

The main focus of the current study is to propose a novel EOS, applicable to the fast simulation of multiphase/multicomponent flows. This work is distinguished from the existing body of knowledge with the following novelties:

1. For the first time, an artificial intelligence (AI) technique, called gene expression programming (GEP), is implemented to propose a new formulation for the non-iterative calculation of thermodynamic properties.
2. Unlike other thermodynamic algorithms, GenEOS takes enthalpy as an input, making it suitable for fast numerical modeling of multiphase and multicomponent transport.
3. Focusing mainly on geothermal applications, GenEOS is developed for two-phase mixtures of H_2O , CO_2 , CH_4 , N_2 , H_2S , NaCl , KCl , CaCl_2 , and MgCl_2 .
4. In contrast to some other EOSs (e.g., TMGAS), GenEOS presents a transparent box for the fast computation of fluid properties.

Accuracy, computation speed, applicability, and transparency are the key characteristics that make an EOS suitable for implementation in reactive transport modeling. Since it is challenging to achieve all of these targets simultaneously, most studies tend to prioritize some of these targets at the expense of others. However, the four aforementioned points serve as compelling evidence that we have achieved our primary goal of developing a suitable EOS without compromising any of its desired characteristics. The development of this novel calculation scheme is organized in three steps: 1) using the F-A model to provide large datasets for training the GEP model, 2) assessing the accuracy of GEP equations in predicting target outputs, and 3) discussing the methods/equations for computing other thermophysical properties.

3.2 Methodology

While the F-A algorithm is less time-expensive than the F-F model in calculating gas solubility, it still imposes a considerable computational cost when implemented in the numerical modeling of two-phase multicomponent flows. The primary suggestion of this study for accelerating the computation process is to use an artificial intelligence technique called gene expression programming, GEP. This method can generate highly precise and easy-to-implement explicit formulas for predicting target outputs that bypass the iterative algorithm of the thermodynamic model.

The following sections provide detailed explanations of both, the conventional thermodynamic and the novel GEP algorithms. Primarily, the calculation procedure of the major components of the F-A model is outlined in detail to clarify why it requires an iterative approach. Despite the absence of sufficient experimental data, this time-consuming conventional thermodynamic method can provide substantial and reliable inputs for machine

learning. Therefore, in the subsequent section, the GEP model is fed by the outputs of the F-A model. The developed GEP equations are indeed the main contribution of the current study to the existing body of knowledge. For the ease of implementation, they are presented as user-friendly C++ codes in Appendix A.

3.2.1 Thermodynamic algorithm based on the iterative F-A model

- Chemical potential

The F-A model used in this study [52] is capable of describing thermodynamic equilibrium between a NaqP in gas/supercritical/condensed conditions and an AqP including water and dissolved gases/solids. In this model, the chemical potentials of each component in the AqP and NaqP are assumed to be equal to each other and calculated by the following equations:

$$\mu^{NaqP}(T, P) = \mu_0^{NaqP}(T, P) + RT \ln(f) \quad (3.1)$$

$$\mu^{AqP}(T, P) = \mu_0^{AqP}(T, P) + RT \ln(a) \quad (3.2)$$

Where μ_0 , R , T , and P represent the chemical potential at the reference temperature, the gas constant, temperature, and pressure, respectively. f , the fugacity of gas components, is calculated by:

$$f = P\phi y \quad (3.3)$$

In which y is the mole fraction of each component in the NaqP and ϕ denotes the fugacity coefficient. Equating the two chemical potentials (Eqs. (3.1) and (3.2)) results in:

$$\frac{\mu_0^{AqP}(T, P) - \mu_0^{NaqP}(T, P)}{RT} = \ln\left(\frac{a}{P\phi y}\right) = \ln(K^0) \quad (3.4)$$

Given that the equilibrium constant ($K^0 = N_w/K_H$) can be defined by Henry's constant (K_H) and the number of moles per kilogram of water ($N_w = 55.508$), it is possible to re-express Eq. (3.4) as:

$$\frac{N_w}{K_H} = \frac{a}{P\phi y} \quad (3.5)$$

Assuming that the solubility of gas species in the AqP is small, a in Eq. (3.5) can be defined by $a = N_w\gamma x$, where γ and x indicate the activity coefficient and mole fraction of components in the AqP [19]. Hence, the new form of Eq. (3.5) for each gas is [20, 21]:

$$(P\phi_i y_i)_{NaqP} = (K_{Hi} \gamma_i x_i)_{AqP} \quad (3.6)$$

Similar to Battistelli and Marcolini [40], the binary interaction between different dissolved gases in the AqP is disregarded, which allows for the non-iterative calculation of activity coefficients. The procedure of calculating $K_i = \frac{y_i}{x_i}$, ϕ_i , K_{Hi} , and γ_i in Eq. (3.6) are explained in the following.

- Equilibrium constant ($K_i = \frac{y_i}{x_i}$)

While the equilibrium constants of CO₂, CH₄, N₂, and H₂S can be calculated by Eq. (3.6), the more straightforward and accurate approach of Spycher *et al.* [47] is chosen for computing the water equilibrium constant:

$$K_{\text{H}_2\text{O}} = \frac{f_{\text{H}_2\text{O}}(g)}{a_{\text{H}_2\text{O}}(l)} = K_{\text{H}_2\text{O}}^0(T, P_0) \exp \left[\frac{(P - P_0) V_{\text{H}_2\text{O}}}{RT} \right] \quad (3.7)$$

Where $V_{\text{H}_2\text{O}}$ represents the average partial molar volume of the water in the AqP (18.1) and P_0 is the reference pressure (1 bar). $K_{\text{H}_2\text{O}}^0(T, P_0)$, the equilibrium constant of water at reference pressure is obtained by:

$$\log(K_{\text{H}_2\text{O}}^0) = -2.209 + 3.097 \times 10^{-2} \theta - 1.098 \times 10^{-4} \theta^2 + 2.048 \times 10^{-7} \theta^3 \quad (3.8)$$

Where θ is the temperature in °C. Combining Eqs. (3.3) and (3.7) results in:

$$y_{\text{H}_2\text{O}} = \frac{K_{\text{H}_2\text{O}}^0 a_{\text{H}_2\text{O}}}{\phi_{\text{H}_2\text{O}}} \exp \left[\frac{(P - P_0) V_{\text{H}_2\text{O}}}{RT} \right] \quad (3.9)$$

Because of the low solubility of gases, water activity can be approximated by its mole fraction in the AqP. Consequently, the equation for the equilibrium state of H₂O in the two-phase system can be written as:

$$K_{\text{H}_2\text{O}}^0 \exp \left[\frac{(P - P_0) V_{\text{H}_2\text{O}}}{RT} \right] x_{\text{H}_2\text{O}} = \phi_{\text{H}_2\text{O}} P y_{\text{H}_2\text{O}} \quad (3.10)$$

- Fugacity coefficient (ϕ_i)

Calculating the fugacity coefficient of gas components as a function of compressibility necessitates solving the classical cubic EOS of Peng-Robinson:

$$Z^3 - (1 - B)Z^2 + (A - 2B - 3B^2)Z - (AB - B^2 - B^3) = 0 \quad (3.11)$$

Parameters A and B are functions of temperature and pressure:

$$A = \frac{a(T)P}{(RT)^2} \quad (3.12)$$

$$B = \frac{bP}{RT} \quad (3.13)$$

In which

$$a(T) = 0.45724 \frac{R^2 T_c^2}{P_c} \alpha(T) \quad (3.14)$$

$$b = 0.07780 \frac{RT_c}{P_c} \quad (3.15)$$

$$\alpha(T) = \left[1 + (0.37646 + 1.4522\omega - 0.26992\omega^2) \left(1 - \sqrt{\frac{T}{T_c}} \right) \right]^2 \quad (3.16)$$

In the above equations, ω , P_c , and T_c stand for acentric factor, critical pressure, and critical temperature, respectively. For a gas mixture, the parameters of a and b can be calculated by the following mixing rules:

$$a = \sum_i \sum_j y_i y_j a_{ij}, \quad a_{ij} = \sqrt{a_i a_j} (1 - k_{ij}), \quad b = \sum_i b_i y_i \quad (3.17)$$

It is noteworthy that in these calculations (Eq. (3.17)), the mole fraction of water in the gas phase is neglected, which allows for the non-iterative computation of solubility in binary systems (e.g., brine-CO₂, brine-CH₄). However, to accurately determine the compressibility factor, the interaction coefficient (k_{ij}) between water and other gases are modified [52]. The other interaction coefficients are taken from the study conducted by Li and Yan [60]. Finally, the fugacity coefficient can be determined by:

$$\ln(\phi_i) = \frac{B_i}{B}(Z-1) - \ln(Z-B) + \frac{A}{2.828B} \left[\frac{B_i}{B} - \frac{2\sum_j y_j a_{ij}}{a} \right] \ln \left[\frac{Z+2.414B}{Z-0.414B} \right] \quad (3.18)$$

• Henry's constant (K_h)

Henry's constant and activity coefficient are the remaining unknowns on the right-hand side of Eq. (3.6). The virial-type equation established by Akinfiev and Diamond [20] can be used for calculating thermodynamic properties of the AqP species at infinite dilution. This model gives Henry's constant by:

$$\ln(K_h) = (1 - \eta) \ln(f_{\text{H}_2\text{O}}^0) + \eta \ln \left(\frac{RT}{M_w} \rho_{\text{H}_2\text{O}}^0 \right) + 2\rho_{\text{H}_2\text{O}}^0 \Delta B \quad (3.19)$$

Where

$$\Delta B = \tau + \Gamma P + \beta \sqrt{\frac{10^3}{T}} \quad (3.20)$$

For more information about the calculation procedure of fugacity and density of pure water, $f_{\text{H}_2\text{O}}^0$ and $\rho_{\text{H}_2\text{O}}^0$, as well as adjustable parameters of η , τ , Γ , and β refer to Fine and Millero [61] and Ziabakhsh-Ganji and Kooi [52].

- Activity coefficient (γ_i)

The reduction of the activity coefficient, caused by the interaction between solutes in the brine, is determined by a virial expansion of Gibbs excess energy. This expansion is derived using the Pitzer model [62]:

$$\ln(\gamma_i) = \sum_C 2m_C \lambda_{i-C} + \sum_A 2m_A \lambda_{i-A} + \sum_C \sum_A m_A m_C \zeta_{i-A-C} \quad (3.21)$$

Where i refers to the dissolved gases of CH₄, CO₂, N₂, and H₂S. The calculated activity factors will be used for computing the equilibrium constants Eq. (3.6). m_C and m_A in Eq. (3.21) denote cations and anions molality in the AqP. The second (λ) and third-order (ζ) interaction parameters are calculated by:

$$\text{Par}(T, P) = c_1 + c_2 T + \frac{c_3}{T} + c_4 P + \frac{c_5}{P} + c_6 \frac{P}{T} + c_7 \frac{T}{P^2} + \frac{c_8 P}{630 - T} + c_9 T \ln(P) + c_{10} \frac{P}{T^2} \quad (3.22)$$

In Eq. (3.22), $\text{Par}(T, P)$ can be either λ or ζ . Following Duan and Sun [42] and Ziabakhsh-Ganji and Kooi [52], we assumed that ($\lambda_{i-A} = 0$, $\lambda_{i-C} = \lambda_{i-Na}$, and $\zeta_{i-A-C} = \zeta_{i-Na-Cl}$). For the other constant factors and the procedure of calculating the molality of the ions, refer to Ziabakhsh-Ganji and Kooi [52]. As an example, in a system of sodium (Na), calcium (Ca), potassium (K), and magnesium (Mg) salts, the activity coefficient is given by:

$$\ln(\gamma_i) = 2\lambda_{i-Na}(m_{Na} + 2m_{Ca} + m_K + 2m_{Mg}) + \zeta_{i-Na-Cl} m_{Cl}(m_{Na} + m_K + m_{Mg} + m_{Ca}) \quad (3.23)$$

- H₂O-CO₂ binary mixture

Since the fugacity of a gas component in a binary gas-brine system does not depend on the composition, its solubility in the AqP can be non-iteratively determined. For a binary mixture of H₂O-CO₂, the mole fraction of water in the NaqP and the CO₂ solubility in AqP can be

calculated by the following equations:

$$y_{\text{H}_2\text{O}} = \frac{\left(1 - \frac{P\phi_{\text{CO}_2}}{K_{\text{H}_2\text{O}}\gamma_{\text{CO}_2}}\right)}{\left(\left(\frac{1}{\phi_{\text{H}_2\text{O}}P} \exp\left[\frac{(P-P_0)V_{\text{H}_2\text{O}}}{RT}\right]\right) - \frac{P\phi_{\text{CO}_2}}{K_{\text{H}_2\text{O}}\gamma_{\text{CO}_2}}\right)} \quad (3.24)$$

$$x_{\text{CO}_2} = \frac{P\phi_{\text{CO}_2}}{K_{\text{H}_2\text{O}}\gamma_{\text{CO}_2}} \left(1 - \frac{\left(1 - \frac{P\phi_{\text{CO}_2}}{K_{\text{H}_2\text{O}}\gamma_{\text{CO}_2}}\right)}{\left(\left(\frac{1}{\phi_{\text{H}_2\text{O}}P} \exp\left[\frac{(P-P_0)V_{\text{H}_2\text{O}}}{RT}\right]\right) - \frac{P\phi_{\text{CO}_2}}{K_{\text{H}_2\text{O}}\gamma_{\text{CO}_2}}\right)}\right) \quad (3.25)$$

Eqs. (3.24) and (3.25) are provided by combining Eqs. (3.6) and (3.10) and following the rule:

$$\sum_{i=\text{CO}_2, \text{H}_2\text{O}} x_i = 1, \quad \sum_{i=\text{CO}_2, \text{H}_2\text{O}} y_i = 1 \quad (3.26)$$

- Flash calculation and general iterative algorithm

Nevertheless, vapor-liquid flash calculations are required to compute the gas mixture mutual solubility. In this case, the total pressure, temperature, and mole fraction of each component in the two-phase mixture (z_i) are received as inputs. Then, the Rachford–Rice equation is implemented to calculate the mole fraction of NaqP (n^v):

$$\sum_{i=1}^N \frac{Z_i(K_i - 1)}{1 + (K_i - 1)n^v} = 0 \quad (3.27)$$

Where K_i is defined as:

$$K_i = \frac{y_i}{x_i}, i = \text{H}_2\text{O}, \text{CO}_2, \text{CH}_4, \text{N}_2, \text{H}_2\text{S} \quad (3.28)$$

Using the formerly derived equations (Eqs. (3.6) and (3.10)), the k-value of water and other components can be alternatively calculated by:

$$K_{\text{H}_2\text{O}} = \frac{K_{\text{H}_2\text{O}}^0}{P\phi_{\text{H}_2\text{O}}} \exp\left[\frac{(P-P_0)V_{\text{H}_2\text{O}}}{RT}\right] \quad (3.29)$$

$$K_i = \frac{K_{Hi}\gamma_i}{P\phi_i}, i = \text{CO}_2, \text{CH}_4, \text{N}_2, \text{H}_2\text{S} \quad (3.30)$$

With the known values of Z_i , K_i , and n^v , it is now possible to compute the composition of each phase:

$$x_i = \frac{Z_i}{1 + (K_i - 1)n^v}, \quad y_i = \frac{Z_i K_i}{1 + (K_i - 1)n^v} \quad (3.31)$$

Using pressure, temperature, and two-phase composition as inputs makes this F-A algorithm an unattractive option to be included in the numerical simulation of two-phase multicomponent flows. Indeed, most of the conducted studies on modeling of two-phase flows in reservoirs solve the partial differential equations of continuity, momentum, and energy to calculate the main variables of pressure, enthalpy, and velocity. Therefore, the fluid temperature cannot be provided as input to the F-A model. As shown in Fig. 3.1, using enthalpy instead of temperature as an input multiplies the required iteration for calculating solubility. This iterative F-A algorithm is highly precise in predicting the mutual solubilities of gas mixtures in brine. Therefore, it is suitable for producing a large dataset to train a new ML-based equation of state that can perform this calculation without the need for iteration. Gene expression programming is the artificial intelligence technique employed by this study to develop the new EOS. This method is elaborately introduced in the next section.

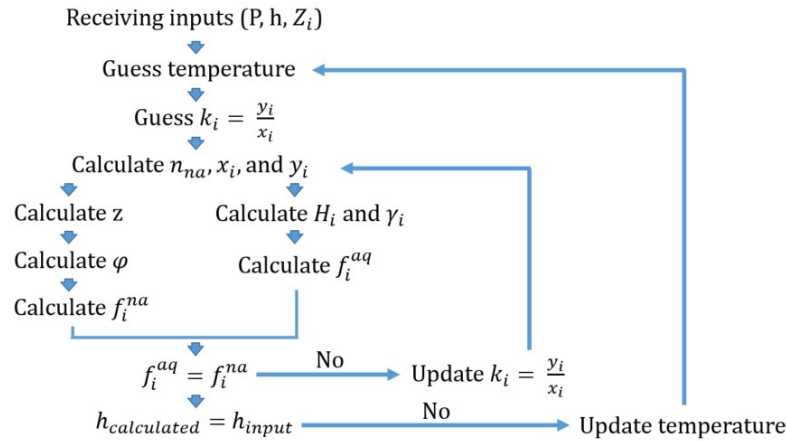


Fig. 3.1 Flow chart for the conventional iterative calculation of temperature and equilibrium constants as functions of pressure, enthalpy, and two-phase fluid composition.

3.2.2 Gene expression programming

The GEP method is known as an extension of genetic programming (GP). Ferreira [63] introduced this evolutionary AI technique to improve the older GP approach performance and overcome some of its constraints, such as the poor exploration of the research area, the limited regression strategies, and the low convergence rate. This method is chosen for the

development of the equation of state as it is capable of generating high-preciseness explicit formulas for the non-iterative prediction of target outputs. The new formulation can be easily implemented in other codes and software systems, eliminating the need for iteration in conventional F-A and F-F algorithms.

The operators employed by the GEP method are all inspired by the biological evolution in nature. They range from fundamental genetic operators (e.g., mutation, crossover, selection) to some advanced operators like transposition, insertion, and recombination. Each GEP model uses the three primary components of chromosomes, genes, and expression trees (ET) in the optimization process. Chromosomes are composed of one or several genes. They possess a fixed length and mimic candidate solutions within the code. Genes themselves consist of terminals (tails) which can be either some variables (e.g., pressure and temperature) or functions (heads) such as (+, -, /, ×, *tan*, *log*). The expression trees also represent the real candidate expressions. A general GEP framework is established by setting control parameters like population size, gene length, and mutation rate and then creating an initial population set of random potential solutions encoded as chromosomes. Each individual chromosome is assessed by a fitness function, and the fittest (best) solutions are selected for reproduction in the new population. The genetic operators are subsequently applied to the chosen individuals to generate new offspring. As shown in Fig. 3.2, the processes of selection, replication, mutation, inversion, transposition, and recombination are reiterated until a stopping criterion is fulfilled. This study utilized GeneXproTools v5.0, a gene expression algorithm software, to generate precise formulas that correlate input and output parameters. For more details about the implementation process alongside with code examples, refer to Ferriera [63] and Gao *et al.* [64].

3.3 Results and discussion

Although not favoring fast computation of fluid properties, the iterative algorithm of the F-A model shows high accuracy in the reproduction of experimental data [52]. Herein, we use this thermodynamic scheme can be used for generating numerous reliable solubility data, which is required for training the GEP model. In the next step, the GEP functions can entirely replace the time-consuming iterative F-A algorithm or at least decrease the number of iterations for determining each phase composition. This study introduces two sets of GEP functions to calculate fluid temperature and equilibrium constants. The presented GEP equations can predict the fluid temperature as a function of pressure, enthalpy, and two-phase composition. Nevertheless, even using these functions, the algorithm is still iterative as computing equilibrium constant as a function of temperature requires some iterations.

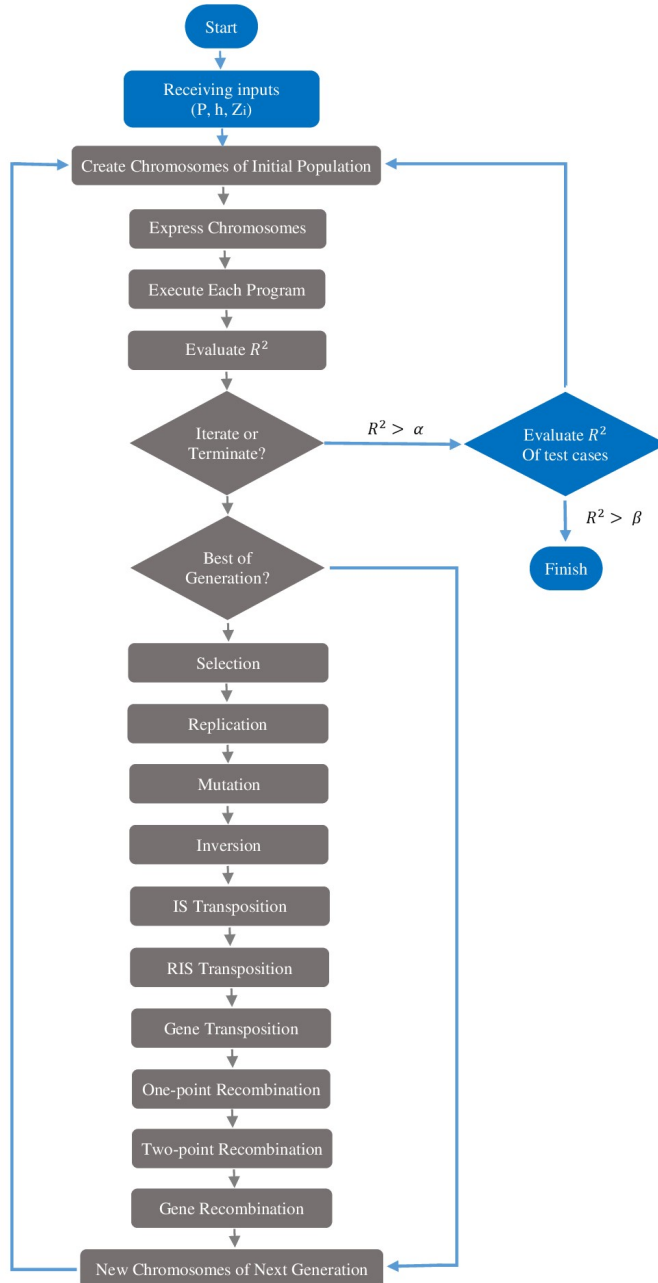


Fig. 3.2 The flowchart of gene expression algorithm. Pressure, enthalpy, and two-phase fluid composition are assumed inputs, while the R-squared in calculating temperature and equilibrium constants is considered as a fitness function.

Therefore, a new set of straightforward GEP functions are developed to directly calculate the equilibrium constants as functions of pressure, temperature, and two-phase composition and bypass the iterations. The following section discusses the precision and computational speed of the new GEP-based EOS.

The predicted temperatures derived from the GEP are compared to those calculated by the iterative F-A algorithm for 1,000,000 arbitrary sets of [pressure, enthalpy, two-phase composition]. The same comparison is conducted for the equilibrium constant values, with the difference that the inputs were [pressure, temperature, two-phase composition]. The range of input values is mentioned in Table 3.1. The accuracy of suggested GEP equations in predicting target values is elaborately discussed in the next sections.

Table 3.1 Range of input parameters for training GEP functions (mf stands for mole fraction in two-phase mixture)

Variable	Min	Max
Pressure (<i>MPa</i>)	1	50
Enthalpy (<i>MJ Kg⁻¹ K⁻¹</i>)	-13	114
mf (H ₂ O)	0.5	0.93
mf (CH ₄)	0	0.27
mf (CO ₂)	0	0.26
mf (N ₂)	0	0.32
mf (H ₂ S)	0	0.28
mf (NaCl)	0	0.027
mf (KCl)	0	0.026
mf (CaCl ₂)	0	0.025
mf (MgCl ₂)	0	0.026

3.3.1 Comparing fast GEP-based EOS to iterative method

• Temperature

In our approach, 10,000 data sets are used for training the GEP equations with the settings addressed in Table 3.2. Then, the precision of developed equations in predicting 1,000,000 other data points (i.e., validation cases) is meticulously evaluated. The GEP method shows a better performance in predicting fluid temperature when it is normalized by enthalpy. Therefore, the presented GEP function is trained to calculate the value of temperature/enthalpy (displayed as T/H in Fig. 3.3). Since fluid enthalpy is assumed to be a known input, it is easy to subsequently compute the fluid temperature ($T = T/H \times H$). The strong nonlinear behavior

of T/H as a function of pressure does not allow for developing a single high-preciseness equation for predicting temperature over the whole range of $1 \text{ MPa} < P < 50 \text{ MPa}$. Therefore, two GEP equations are suggested for calculating temperature in the pressure ranges of $1 \text{ MPa} < P \leq 10 \text{ MPa}$ and $10 \text{ MPa} < P < 50 \text{ MPa}$. Fig. 3.3 shows the R-squared and relative error of these two equations in computing the temperature of validation cases (the 1,000,000 data sets). Both equations can predict the fluid temperature with the R-squared of ≈ 0.998 and the median relative error of less than 0.6 %, which indicates their reliability for accurate computation of fluid temperature.

Table 3.2 GEP settings for the calculation of Temperature

Number of chromosomes	30	Head size	10
Linking function	/	Fitness function	R2
IS Transposition	0.00546	RIS Transposition	0.00546
One-point Recombination	0.00277	Two-point Recombination	0.00277
Constants per gene	10	Range of constants	-10 to +10
Number of genes	4	Mutation	0.00138
Inversion	0.00546	Gene Transposition	0.00277

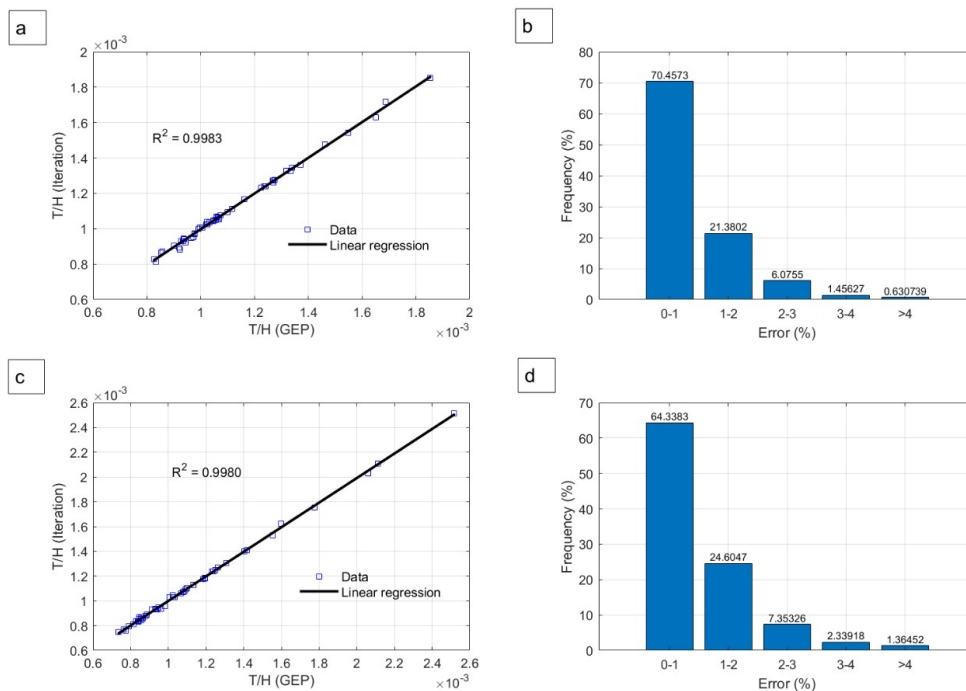


Fig. 3.3 The R-squared and relative error of the GEP equation in the calculation of fluid temperature when (a-b) pressure $> 10 \text{ MPa}$ and (c-d) pressure $< 10 \text{ MPa}$

Even this small error may be unacceptable in some applications. In this case, the proposed GEP equations can be used as an initial guess for temperature in the F-A algorithm shown in Fig. 3.1. It is guaranteed that, after the first iteration, the error will be almost zero (Fig. 3.4).

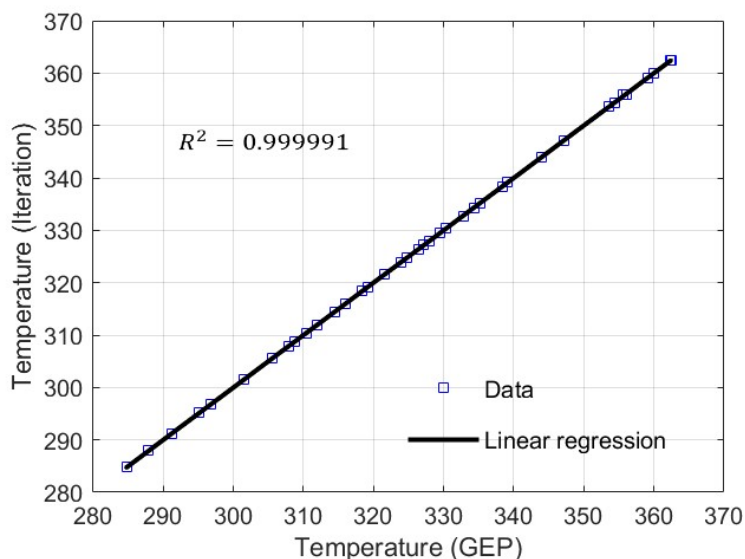


Fig. 3.4 Accuracy of calculated temperatures after the first iteration when the GEP equation is used as the initial guess in the Fugacity-activity algorithm (Fig. 3.1).

For ease of implementation, the GEP functions are provided as simple C++ codes in Appendix A.

• Equilibrium constants

The new GEP equations for calculating equilibrium constants are developed with the settings mentioned in Table 3.3. The extremely nonlinear behavior and broader value range of the equilibrium constant (0.1 - 10000) compared to the temperature domain (10 - 100 °C) impose an enormous hurdle for developing high-preciseness functions. Nevertheless, the herein introduced GEP equations by this study can compute the equilibrium constants of the 1,000,000 (validation) data set with a median relative error of $\approx 6\%$ (Fig. 3.5 and Table 3.4). Using these equations as an initial guess for solving the Rachford-Rice equation (Fig. 3.1) is highly recommended as it results in a median relative error of only $\approx 1\%$ after the first iteration.

The F-A algorithm typically needs nine iterations for the simultaneous calculation of fluid temperature and equilibrium constants as functions of enthalpy, pressure, and two-phase composition. However, using the developed GEP functions as initial guesses for temperature and equilibrium constant can yield accurate results in only one iteration. This leads to an 89%

Table 3.3 settings for the calculation of equilibrium constant

Number of chromosomes	30	Head size	10
Linking function	/	Fitness function	R2
IS Transposition	0.00546	RIS Transposition	0.00546
One-point Recombination	0.00277	Two-point Recombination	0.00277
Constants per gene	10	Range of constants	-10 to +10
Number of genes	8	Mutation	0.00138
Inversion	0.00546	Gene Transposition	0.00277

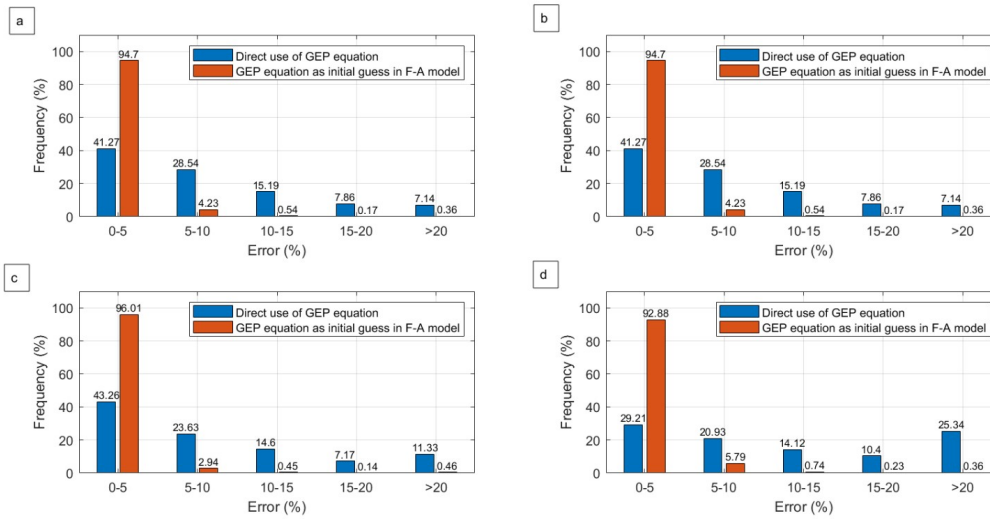


Fig. 3.5 The relative error in calculating the equilibrium constant of a) Methane b) Carbon dioxide c) Nitrogen d) Hydrogen sulfide. The orange columns display the outcomes obtained from the F-A model after the first iteration, using GEP equations as the initial guess.

Table 3.4 The median relative error of GEP equations in computing equilibrium constants

Component	Relative error (%)	
	GEP equation	After first iteration
CH ₄	6.2	0.8
CO ₂	5.6	1.4
N ₂	6.1	0.5
H ₂ S	10	1.1

reduction ($8/9 \times 100$) in the number of iterations, which now makes GenEOS an exciting option to be included in the fast simulation of two-phase multicomponent flows.

3.3.2 GenEOS calculation scheme for fluid properties

After having determined temperature and phase composition by the non-iterative GEP algorithm, it is also possible to calculate the thermophysical properties of these fluids. This section presents the GEP scheme for calculating fluid properties, with three main objectives: 1) to enhance the transparency of GenEOS as an EOS, 2) to demonstrate its accuracy through validation against international standards, experimental data, and numerical methods, and 3) to show that its capabilities are beyond computing gas solubility in brine.

• Enthalpy

◦ Liquid phase

For the pressure range of ($1 \text{ MPa} < P < 50 \text{ MPa}$) and temperature domain of ($10 \text{ }^\circ\text{C} < T < 100 \text{ }^\circ\text{C}$), the enthalpy of pure liquid water can be calculated by:

$$H_{H_2O}^{Aq}(T, P + \Delta P) - H_{H_2O}^{SL}(T, P) = V[1 - \varepsilon T]\Delta P \quad (3.32)$$

In which $H_{H_2O}^{SL}$, V , and ε represent the enthalpy of saturated liquid (reference condition), specific volume, and thermal expansion coefficient, respectively. These parameters are defined as:

$$H_{H_2O}^{SL}(T, P) = d_1 + d_2T + d_3T^2 + d_4T^3 + d_5T^4 + d_6T^5 \quad (3.33)$$

$$V = \frac{V^0 - V^0P}{B + A_1P + A_2P^2} \quad (3.34)$$

$$\varepsilon = r_1 + r_2T + r_3T^{1.5} + r_4T^2 \quad (3.35)$$

More details about the constant factors of $d_1 - d_6$, $r_1 - r_4$, and the equations for computing V^0 , A_1 , A_2 , and B can be found in Fine and Millero [61] and Popiel and Wojtkowiak [65].

The enthalpy of Water+NaCl solution is computed through a model developed by Driesner [66].

$$H_{\text{solution}}(T, P, X_{NaCl}) = H_{H_2O}^{Aq}(T_h^*, P) \quad (3.36)$$

This simple model declares that the enthalpy of brine mixture (H_{solution}) at a specific pressure, temperature, and salinity equals pure water enthalpy at another temperature (T_h^*), calculated by:

$$T_h^* = q_1 + q_2T \quad (3.37)$$

Where q_1 and q_2 are functions of pressure and temperature [66]. Calculation of enthalpy of a brine mixture containing other salts (i.e., KCl, CaCl₂, MgCl₂) is conducted using a model

developed by Nusiaputra [67]:

$$H_{\text{solution}}(P, T) = w_{\text{H}_2\text{O}}^{\text{Aq}} H_{\text{H}_2\text{O}}^{\text{Aq}} + \sum_{N_i} \frac{w_i^{\text{Aq}}}{M_i} h_i^{\phi} \quad (3.38)$$

Where w , M , and h_i^{ϕ} stand for mass fraction, molar mass, and apparent molar enthalpy, respectively.

$$h_i^{\phi} = g_{01} + g_{02}b_i + g_{03}(\theta + 273.15) + g_{04}(\theta + 273.15)^2 + (b_i^{c_1} + c_2) \left(c_3(\theta + 273.15) - c_4 \ln \left(1 - \frac{\theta + 273.15}{c_5} \right) \right) \quad (3.39)$$

b in Eq. (3.39) denotes salt molality in the liquid phase. For other constants, refer to Nusiaputra [67]. The enthalpy of the dissolved gases in the AqP can be expressed by the summation of gas enthalpy at the corresponding total pressure (h_j) and dissolution enthalpy ($h_{\text{sol},j}^{\phi}$). Therefore, the AqP enthalpy after gas dissolution (H'_{solution}) is governed by [67]:

$$H'_{\text{solution}}(P, T) = H_{\text{solution}}(P, T) + \sum_{N_j} w_j^{\text{Aq}} \left(h_j + \frac{h_{\text{sol},j}^{\phi}}{M_j} \right) \quad (3.40)$$

Where M_j represents gas molar mass. The dissolution enthalpy (i.e., the enthalpy change associated with the dissolution of gas in water at constant pressure resulting in infinite dilution) can be computed by using the first derivative of the standard chemical potential $\left(\frac{\partial}{\partial T} \left(\mu_j^{1(0)} / RT \right) \right)$. Following Pitzer *et al.* [62], the standard chemical potential can be calculated by:

$$\frac{\mu_j^{1(0)}}{RT} = s_1 + s_2T + s_3/T + s_4T^2 + s_5/(630 - T) + s_6P + s_7P \ln(T) + s_8P/T + s_9P/(630 - T) + s_{10}P^2/(630 - T)^2 + s_{11}T \ln(P) \quad (3.41)$$

The constant parameters of $s_1 - s_{11}$ can be found in studies conducted by Duan *et al.* [42, 50, 51, 55].

○ Gas phase

The classic Peng-Robinson EOS is employed for computing gas enthalpy [68]:

$$H^{\text{Naq}} - H_0^{\text{Naq}} = RT(Z - 1) + \left(\frac{a - T \left(\frac{da}{dT} \right)}{2\sqrt{2}b} \right) \ln \left(\frac{Z - 0.414B}{Z + 2.414B} \right) \quad (3.42)$$

Where H_0^{Naq} represents ideal gas enthalpy. For a gas mixture, the term of (da/dT) is calculated by:

$$\frac{da}{dT} = \frac{1}{2} \sum_i \sum_j w_i w_j (1 - K_{ij}) \sqrt{(a_i a_j)} \left[\frac{1}{a_i} \frac{da_i}{dT} + \frac{1}{a_j} \frac{da_j}{dT} \right] \quad (3.43)$$

Where

$$\frac{da(T)}{dT} = -ka(T_c) \sqrt{\frac{a(T)}{TT_c}} \quad (3.44)$$

The PR EOS cannot describe the behavior of non-boiling water in NaqP. As reported by Pan *et al.* [69], the small water content of the NaqP behaves like a mixture of "vapor-like" and "liquid-like" components. The gas phase pressure increment plays an essential role in deviating its properties from "vapor-like" to "liquid-like". The proposed equation by Pan *et al.* [69] for computing water enthalpy is:

$$h_{H_2O} = (1 - X_L) u_{sv} + X_L u_{sl} + \frac{P_{H_2O}}{\rho_{H_2O}} \quad (3.45)$$

Where

$$X_v = 1 - X_L = \begin{cases} 1 & \text{if } P_{H_2O} \leq P_{sat} \\ \frac{P_{sat}}{P_{H_2O}} & \text{if } P_{H_2O} > P_{sat} \end{cases} \quad (3.46)$$

$$P_{H_2O} = y_{H_2O} P \quad (3.47)$$

$$P_{sat} = P_C \exp \left\{ \left[\frac{T_c}{273.15 + \theta} \right] \left(a_1 + a_2 Y^{1.5} + a_3 Y^3 + a_4 Y^{3.5} + a_5 Y^4 + a_6 Y^{7.5} \right) \right\} \quad (3.48)$$

In Eq. (3.45), u_{sv} and u_{sl} denote the specific enthalpies of water vapor and liquid water, respectively. The constant factors of $a_1 - a_6$ for a binary mixture of H_2O - CO_2 are addressed in the reference paper. In this case, the enthalpy of NaqP can be computed by:

$$H^{Naq} = y_{H_2O} h_{H_2O} + (1 - y_{H_2O}) h_{CO_2} + w_{H_2O} \left(\frac{P}{\rho^{Naq}} - \frac{P_{H_2O}}{\rho_{H_2O}} \right) \quad (3.49)$$

The procedure of calculating water/NaqP density will be elaborately discussed later.

o Two-phase mixture

The mass-average two-phase enthalpy (H) is calculated through [67]:

$$H = w^{Aq} H'_{\text{solution}} + w^{Naq} H^{Naq} \quad (3.50)$$

The calculated enthalpies by GenEOS are validated against accurate numerical studies, experimental data, and international standards like IAPWS [70] and NIST [71]. Some validation cases are addressed in Fig. 3.6.

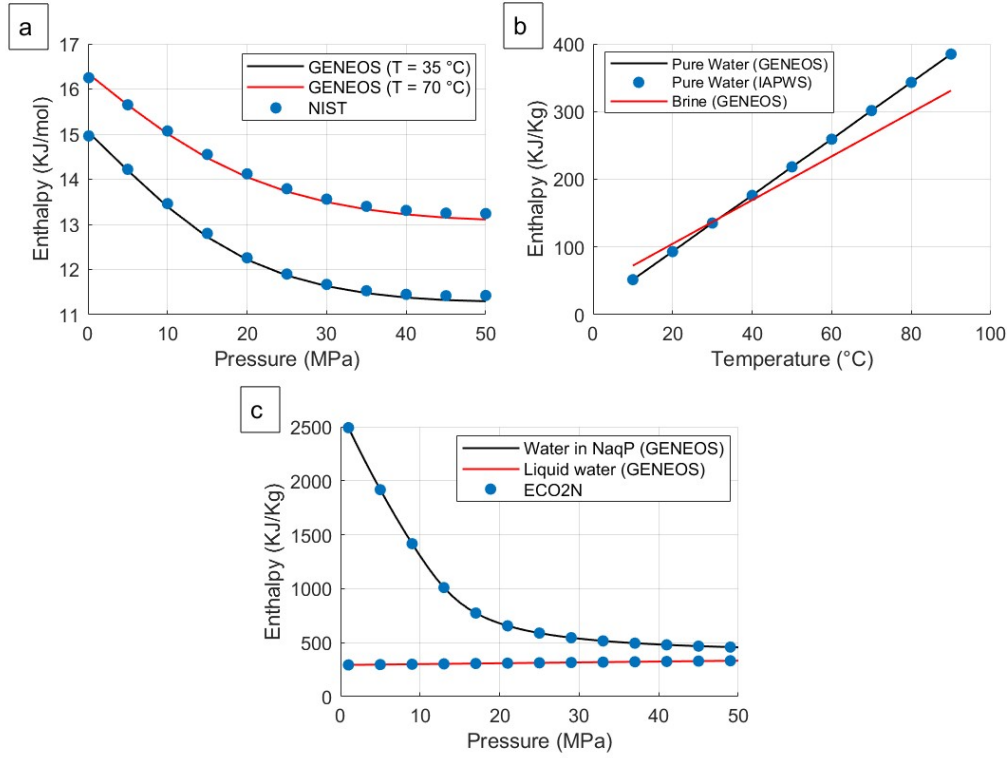


Fig. 3.6 Calculation and validation of enthalpy of a) single gas [CH_4 , $P = 10 \text{ MPa}$] b) pure liquid water and brine [$P = 10 \text{ MPa}$, mole fraction of NaCl = 0.1]. The red line is solely included to illustrate the behavior of brine enthalpy. c) non-boiling water in NaqP ($T = 70 \text{ }^\circ\text{C}$)

• Density

○ Liquid phase

Al Ghafri *et al.* [3] performed a series of experiments with a vibrating-tube densimeter to measure the density of brine containing various salts (i.e., MgCl_2 , CaCl_2 , KI, NaCl, KCl, and AlCl_3). Their proposed correlations for calculating density are very accurate for pressures up to 68.5 MPa , temperature range of ($10 \text{ }^\circ\text{C}$ to $200 \text{ }^\circ\text{C}$), and salt molality of ($b < 5$). This model is implemented in GenEOS and expresses the brine density as:

$$\rho(T, P, b) = \rho_{\text{ref}}(T, b) \left\{ 1 - C(b) \ln \left[\frac{B(T, b) + P}{B(T, b) + P_{\text{ref}}(T)} \right] \right\}^{-1} \quad (3.51)$$

Where

$$\rho_{\text{ref}}(T, b) - \rho_0(T) = \sum_{i=1}^{i=3} \alpha_{i0} b^{\frac{i+1}{2}} + \sum_{i=1}^{i=3} \sum_{j=1}^{j=3} \alpha_{ij} b^{\frac{i+1}{2}} (T/T_c)^{\frac{j+1}{2}} \quad (3.52)$$

$$C(b) = \gamma_0 + \gamma_1 b + \gamma_2 b^{3/2} \quad (3.53)$$

$$B(T, b) = \sum_{i=0}^{i=1} \sum_{j=0}^{j=3} \beta_{ij} b^i (T/T_c)^j \quad (3.54)$$

$$\ln \left(\frac{P_{\text{ref}}(T)}{P_c} \right) = (T_c/T) \left(\sigma_1 \varphi + \sigma_2 \varphi^{1.5} + \sigma_3 \varphi^3 + \sigma_4 \varphi^{3.5} + \sigma_5 \varphi^4 + \sigma_6 \varphi^{7.5} \right) \quad (3.55)$$

In Eq. (3.55), ($T_c = 647.10 \text{ K}$) and ($P_c = 22.064 \text{ MPa}$) stand for critical temperature and pressure of pure water. φ is defined by ($\varphi = 1 - T/T_c$) and ρ_0 , the density of saturated liquid water, is given by the auxiliary equation of Wagner and Kretzschmar [70]:

$$\rho_0(T)/\rho_c = 1 + n_1 \varphi^{1/3} + n_2 \varphi^{2/3} + n_3 \varphi^{5/3} + n_4 \varphi^{16/3} + n_5 \varphi^{43/3} + n_6 \varphi^{110/3} \quad (3.56)$$

In which ($\rho_c = 322 \text{ kg m}^{-3}$) denotes the critical density of water. The density of a brine mixture containing various salts can be computed by:

$$\rho_{\text{solution}}(T, P, b) = \left[\sum_i x_i (1 + bM_i) \right] \times \left[\sum_i \frac{x_i (1 + bM_i)}{\rho_i(T, P, b)} \right]^{-1} \quad (3.57)$$

Here, x_i and M_i represent the mole fraction of electrolyte i in the mixed salt and the molar mass of salt i . ρ_i is the density of the single electrolyte solution at the pressure, temperature, and molality of the mixed electrolyte solution. For the constant factors used in Eqs. (3.51) to (3.57) refer to Al Ghafri *et al.* [3].

Laliberte' [4] and Francke *et al.* [54] introduced a mixing rule that converts the apparent molar volume into AqP density. Using this model, brine density after gas dissolution (ρ'_{solution}) can be written as:

$$\rho'_{\text{solution}}(T, P, b) = \left(\left(1 - \sum_j w_j^{Aq} \right) \rho_{\text{solution}}(T, P, b) + \sum_j \frac{w_j^{Aq}}{M_j} V_j^\varphi \right)^{-1} \quad (3.58)$$

Where the apparent molar volume of dissolved gases is computed by [67]:

$$V_j^\varphi = g_1 f_1 + f_2 \quad (3.59)$$

$$g_1 = \sum_{n=1}^4 c_{0n} T^{(n-1)} \quad (3.60)$$

$$f_1(T) = (1 + \exp((T - T_{ps}) / (c_1 T_{ps})))^{-1} \quad (3.61)$$

$$f_2(T) = c_{21} \exp(c_{22} \cdot |(T - T_{ps}) / T_{ps}|^{c_{23}}) \quad (3.62)$$

In Eqs. (3.61) and (3.62), T_{ps} denotes the pseudocritical temperature of 395 °C. The gas-dependent constants used in Eqs. (3.58) to (3.62) are addressed in the study conducted by Nusiaputra [67].

○ Gas phase

The density of a gas mixture is given as:

$$\rho = \frac{MW_g}{v_g + cm} \quad (3.63)$$

Where

$$v_g = \frac{Z_g RT}{P} \quad (3.64)$$

In these equations, Z_g is the compressibility factor computed by the PR EOS, v_g represents molar volume, and MW_g denotes the molecular weight of the gas phase. cm , the gas-dependent volume shift factor, is introduced by Shabani and Vilc ez [72] to increase the accuracy of these equations in calculating gas density.

As mentioned before, the PR EOS cannot be used for determining non-boiling water density in the NaqP. The suggested empirical equation by Pan *et al.* [69] for computing water density is:

$$\rho_{H_2O}(P, T) = \rho_v(P, T) + (1 - X_v)^{1.8} \rho_l(P, T) \quad (3.65)$$

In which vapor density (ρ_v) is given by:

$$\rho_v(P, T) = \begin{cases} \frac{P}{P_{H_2O}} \rho_{sv}(P_{H_2O}, T) & \text{if } P_{H_2O} \leq P_{sat} \\ \frac{P}{P_{H_2O}} \rho_{sv}(P_{sat}, T) & \text{if } P_{H_2O} > P_{sat} \end{cases} \quad (3.66)$$

In Eq. (3.66), ρ_{sv} represents the vapor density. For a binary mixture of H₂O-CO₂ the density of NaqP is written as [69]:

$$\rho^{Naq} = y_{H_2O} \rho_{H_2O} + (1 - y_{H_2O}) \rho_{CO_2} \quad (3.67)$$

○ Two-phase mixture

The mass-average two-phase density (ρ) is calculated through:

$$\rho = w^{Aq} \rho'_{\text{solution}} + w^{Naq} \rho^{Naq} \quad (3.68)$$

Some validated/calculated densities by GeneOS are shown in Fig. 3.7.

• Viscosity

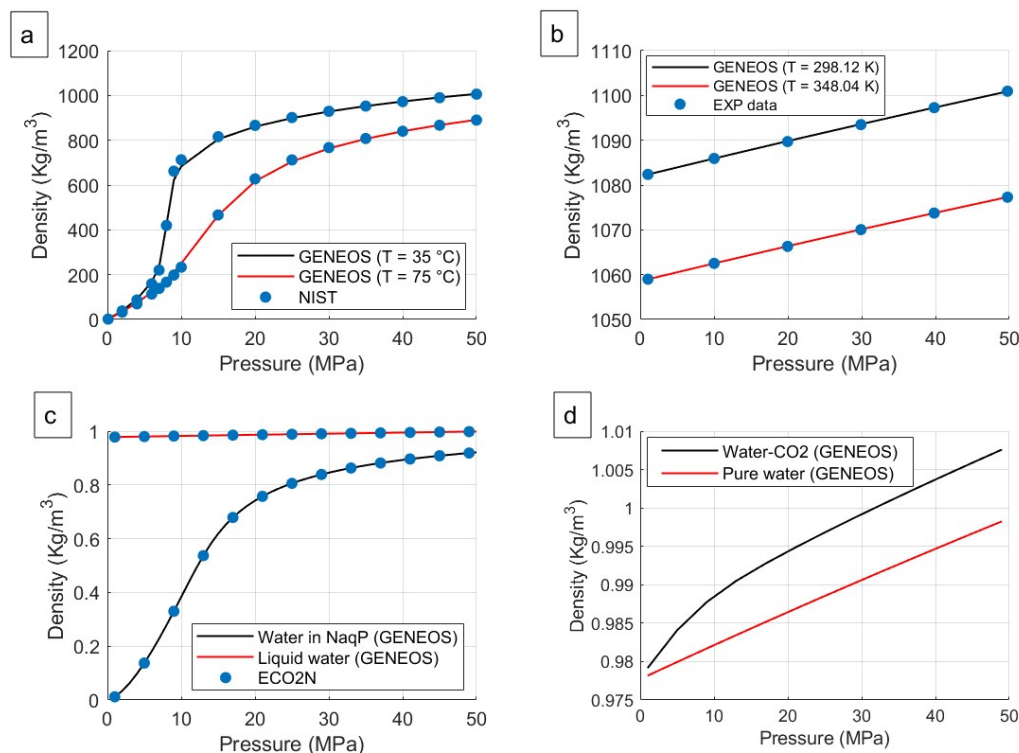


Fig. 3.7 Calculation and validation of density of a) single gas [CO_2 , $P = 10 \text{ MPa}$] b) $\text{H}_2\text{O}-\text{CaCl}_2$ solution [$b = 1 \text{ mol Kg}^{-1}$], experimental data are taken from Al Ghafri *et al.* [3] c) non-boiling water in NaqP [$T = 70 \text{ }^\circ\text{C}$] d) CO_2 -saturated water [$T = 70 \text{ }^\circ\text{C}$]

○ Liquid phase

Laliberte' [4] introduced an experimental correlation for computing brine viscosity:

$$\eta^{Aq} = \eta_w^{w_w} \prod \eta_i^{w_i} \quad (3.69)$$

In Eq. (3.69), η_w and η_i are water and salt viscosities, respectively. These properties are defined by:

$$\eta_w / \text{mPa} \cdot \text{s} = \frac{T / ^\circ\text{C} + 246}{(0.05594T / ^\circ\text{C} + 5.2842) T / ^\circ\text{C} + 137.37} \quad (3.70)$$

$$\eta_i / mPa \cdot s = \frac{e^{\left(\frac{v_1(1-w_w)^{v_2+v_3}}{v_4(T/^\circ C)+1} \right)}}{v_5(1-w_w)^{v_6} + 1} \quad (3.71)$$

Where $v_1 - v_6$ are salt-dependent constants. The average relative error of Eq. (3.69) in predicting an experimental viscosity database with 1700 points is reported to be 2.7 % [4].

○ Gas phase

To the best of our knowledge, there is no single high-preciseness equation for calculating the viscosities of all the gases included in GenEOS (i.e., CO₂, CH₄, N₂, and H₂S). Therefore, various models are employed for computing gas viscosities. Subsequently, a mixing rule is used to compute gas mixture viscosity.

- Carbon dioxide

Fenghour and Wakeham [73] proposed an empirical equation for computing CO₂ viscosity, which is valid for pressures up to 300 MPa and temperatures below 1000 K. according to this model, CO₂ viscosity is decomposed into three separate terms:

$$\eta(\rho, T) = \eta_0(T) + \Delta\eta(\rho, T) + \Delta\eta_c(\rho, T) \quad (3.72)$$

Where η_0 , $\Delta\eta$, and $\Delta\eta_c$ stand for viscosity in the zero-density limit, the viscosity increase at elevated density over the dilute gas value, and the viscosity alteration in the immediate vicinity of the critical point. The term η_0 is given by:

$$\eta_0(T) = \frac{1.00697T^{1/2}}{\rho_\eta^*(T^*)} \quad (3.73)$$

In which

$$\ln(\rho_\eta^*(T^*)) = \sum_{i=0}^4 a_i (\ln(T^*))^i \quad (3.74)$$

$$T^* = kT/\varepsilon \quad (3.75)$$

The energy scaling parameter (ε/k) in Eq. (3.75) is 251.196 K. The term ($\Delta\eta$) is Eq. (3.72) is defined as a function of density (ρ):

$$\Delta\eta(\rho, T) = d_{11}\rho + d_{21}\rho^2 + \frac{d_{64}\rho^6}{T^{*3}} + d_{81}\rho^8 + \frac{d_{82}\rho^8}{T^*} \quad (3.76)$$

The ratio of $\Delta\eta_c(\rho, T)/\eta(\rho, T)$ may be greater than 0.01 only within 1% (≈ 5 K) of the critical temperature. For more information about the calculation of $\Delta\eta_c$ as well as the constant parameters in Eqs. (3.72) to (3.76) refer to Vesovic *et al.* [74] and Fenghour and Wakeham

[73].

- Methane

The viscosity of methane is calculated using a simple empirical equation suggested by Tadashi *et al.* [75]:

$$\eta = \sum_{i=0}^4 B_{0i}T^i + P \sum_{i=0}^2 B_{1i}T^i + P^2 \sum_{i=0}^3 B_{2i}T^i + P^3 \sum_{i=0}^3 B_{3i}T^i + P^4 \sum_{i=0}^2 B_{4i}T^i \quad (3.77)$$

- Nitrogen

Stephan and Krauss [76] developed a model that splits the viscosity of Nitrogen into two contributions of zero-density limit (dilute-gas function, η_0) and residual part (excess function, $\Delta\eta_R$):

$$\eta(\rho, T) = \eta_0(T) + \Delta\eta_R(\rho) \quad (3.78)$$

η_0 in Eq. (3.78) is expressed as:

$$\eta_0(T) = 5/16 [MkT / (\pi N_A)]^{0.5} / [\sigma^2 \Omega(T^*)] \quad (3.79)$$

Here M , k , and N_A denote molecular weight, Boltzmann's constant, and Avogadro's number, respectively. The constant parameters of π and σ are assumed to be 3.14159 and 0.36502496 nm. Furthermore, the function $\Omega(T^*)$ is written as:

$$\ln(\Omega(T^*)) = \sum_{i=0}^4 A_i (\ln(T^*))^i \quad (3.80)$$

In which T^* is the normalized temperature (Eq. (3.75)) by the energy scaling parameter of ($\epsilon/k = 100.01654$ K). The residual part of viscosity ($\Delta\eta_R$) in Eq. (3.78) is given by:

$$\frac{\Delta\eta_R(\rho)}{\eta_c} = \frac{C_1}{(\chi - C_2)} + \frac{C_1}{C_2} + \sum_{i=3}^5 C_i \chi^{i-2} \quad (3.81)$$

Where η_c represents the critical viscosity of Nitrogen, and χ stands for normalized density ($\chi = \rho / (\rho_c = 314.0 \text{ kg m}^{-3})$). For all the constant parameters used in Eq. (3.78) to (3.81), refer to Stephan and Krauss [76].

- Hydrogen sulfide

An empirical correlation proposed by Giri *et al.* [77] is employed by GenEOS for computing

H₂S viscosity:

$$\frac{\eta}{\mu Pas} = a_0 + a_1 \left(\frac{T}{K} \right) \exp \left[\left(a_2 + \frac{a_3}{(T/K)} + \frac{a_4}{(T/K)^2} \right) \cdot \left(\frac{\rho(T,P)}{(kgm^{-3})} \right) \right] \quad (3.82)$$

This model is valid for pressures up to 100 MPa and temperatures below 483 K.

○ Gas mixture

A mixing rule developed by Wilke [78] is used for computing the gas mixture viscosity:

$$\eta^{Naq} = \sum_{i=1}^n \frac{\eta_i}{1 + \frac{1}{x_i} \sum_{\substack{j=1 \\ j \neq i}}^n x_j \phi_{ij}} \quad (3.83)$$

where ϕ_{ij} is defined as:

$$\phi_{ij} = \frac{\left[1 + (\eta_i/\eta_j)^{1/2} (M_j/M_i)^{1/4} \right]^2}{(4/\sqrt{2}) \left[1 + (M_i/M_j) \right]^{1/2}} \quad (3.84)$$

M in Eq. (3.84) denotes the molecular weight of each component.

○ Two-phase mixture

The mass-average two-phase viscosity (ρ) is written as:

$$\eta = w^{Aq} \eta^{Aq} + w^{Naq} \eta^{Naq} \quad (3.85)$$

Fig. 3.8 depicts some validated/calculated viscosities by GenEOS.

• Thermal conductivity

○ Liquid phase

The following equation can be used for calculating the thermal conductivity of multicomponent electrolyte solutions [79]:

$$\lambda^{Aq} = \lambda_0 \left(1 + \sum_{i=1}^k \beta_i c_i \right) \quad (3.86)$$

Where β , c , and k denote the gas-dependent constant, mass content of electrolyte in the solution, and the number of components, respectively. λ_0 , the thermal conductivity of pure

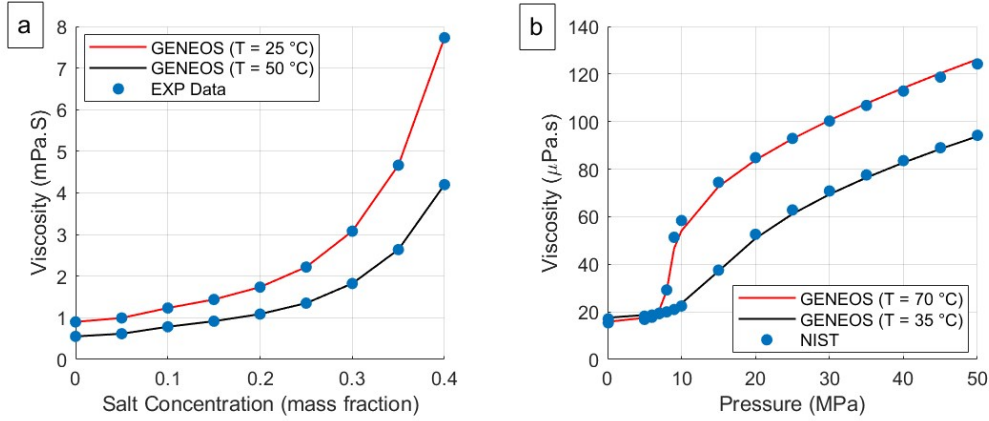


Fig. 3.8 Calculation and validation of viscosity of a) binary $\text{H}_2\text{O}-\text{CaCl}_2$ brine [$b = 1 \text{ mol Kg}^{-1}$], the experimental data are taken from Laliberte' [4] b) single gas (CO_2)

water, is written as:

$$\lambda_0 = 10^{-3} \left(L_0 + L_1 \Psi + L_2 \Psi^{1.5} + L_3 \Psi^{2.5} + L_4 \Psi^3 \right) \quad (3.87)$$

Eq. (3.87) is valid for the temperature range of ($0 \text{ }^\circ\text{C} < T < 135 \text{ }^\circ\text{C}$), and Ψ is given by ($\Psi = 0.01 \times T \text{ (}^\circ\text{C)}$).

o Gas phase

The thermal conductivity of each gas is described by a specific model, and subsequently, a mixing rule is implemented for computing the gas mixture thermal conductivity.

- Carbon dioxide

Amooy [80] developed a model that computes the CO_2 thermal conductivity as a function of density and temperature:

$$\lambda = \frac{A_1 + A_2 \rho + A_3 \rho^2 + A_4 \rho^3 T^3 + A_5 \rho^4 + A_6 T + A_7 T^2}{\sqrt{T}} \quad (3.88)$$

The constant factors of $A_1 - A_7$ are calibrated to cover the thermal conductivity in the temperature range of ($290 \text{ K} < T < 800 \text{ K}$) and densities below 1200 Kg m^{-3} .

- Methane

Prasad *et al.* [81] proposed a correlation for calculating CH_4 thermal conductivity, which is valid for the temperature range of ($120 \text{ K} < T < 400 \text{ K}$) and pressure domain of ($2 \text{ MPa} < P < 70 \text{ MPa}$). According to this model, the total thermal conductivity is composed of two

primary terms:

$$\lambda = \lambda_1 + \Delta\lambda_e \quad (3.89)$$

In which λ_1 , the thermal conductivity at low pressures, is calculated by:

$$\lambda_1 = \sqrt{T_r} / \sum_{k=0}^n \left(a_k / T_r^k \right) \quad (3.90)$$

And the excess value of thermal conductivity in high-density regions ($\Delta\lambda_e$) is given by:

$$\Delta\lambda_e = \sum_{i=0}^m \sum_{j=0}^n b_{ij} T_r^i \rho_r^j \quad (3.91)$$

In Eqs. (3.90) and (3.91), T_r and ρ_r are temperature and density, normalized by the critical value of the corresponding property. For the constant factors of a_k and b_{ij} refer to the reference paper.

- Nitrogen

Lemmon and Jacobsen [82] proposed a model for computing the Nitrogen thermal conductivity as a function of temperature and density:

$$\lambda = \lambda_0(T) + \lambda_r(\tau, \delta) + \lambda_c(\tau, \delta) \quad (3.92)$$

Where $\tau = T_c/T$ and $\delta = \rho/\rho_c$. The dilute gas thermal conductivity (λ_0) can be computed by:

$$\lambda_0(T) = N_1 \left[\frac{\eta_0(T)}{1 \mu Pa \cdot s} \right] + N_2 \tau^2 + N_3 \tau^3 \quad (3.93)$$

In which η_0 represents the dilute gas viscosity, described by:

$$\eta_0(T) = \frac{0.0266958 \sqrt{MT}}{\sigma^2 \Omega(T^*)} \quad (3.94)$$

In Eq. (3.94), σ stand for the Lennard-Jones size parameter (0.3656 nm), and Ω is the collision integral given by Eq. (3.80). The energy scaling parameter of Nitrogen is ($\epsilon/k = 98.94 K$). The residual contribution to the thermal conductivity (λ_r) is expressed as:

$$\lambda_r(\tau, \delta) = \sum_{i=4}^n N_i \tau^{t_i} \delta^{d_i} \exp\left(-\gamma_i \delta^{l_i}\right) \quad (3.95)$$

Where γ_i is zero when l_i is zero and one when l_i is not zero. For all the coefficients of N_i , t_i , d_i , l_i , and the calculation procedure of λ_c refer to the reference paper.

○ Gas mixture

The thermal conductivity of a gas mixture can be computed by [83]:

$$\lambda^{Naq} = \sum \frac{y_i \lambda_i}{\sum y_i A_{ij}} \quad (3.96)$$

Where the interaction parameter (A_{ij}) is defined by:

$$A_{ij} = \left(\frac{MW_j}{MW_i} \right)^{0.5} \quad (3.97)$$

○ Two-phase mixture

The mass-average two-phase thermal conductivity (λ) is calculated through:

$$\lambda = w^{Aq} \lambda^{Aq} + w^{Naq} \lambda^{Naq} \quad (3.98)$$

Some validated/calculated thermal conductivities by GenEOS are exhibited in Fig. 3.9.

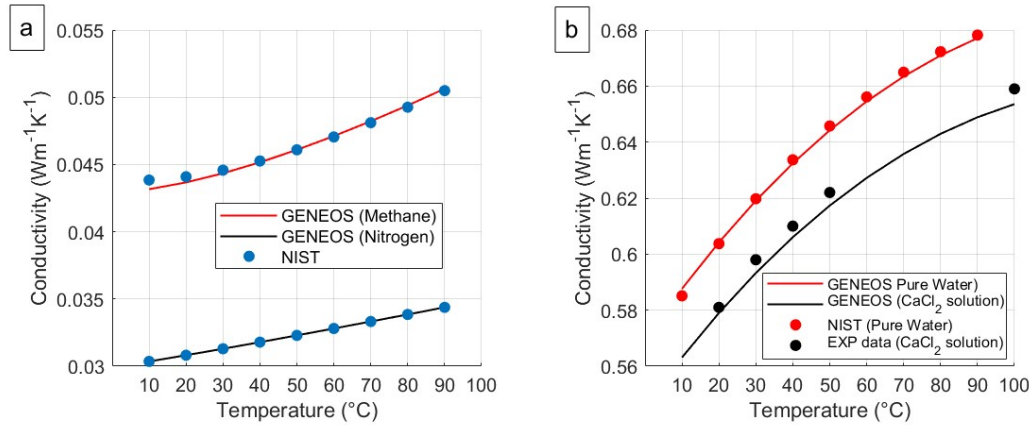


Fig. 3.9 Calculation and validation of thermal conductivity of a) a single gas [$P = 10 \text{ MPa}$] b) pure water and binary $\text{H}_2\text{O}-\text{CaCl}_2$ brine (mass fraction = 20 %, $P = 10 \text{ MPa}$), experimental data are taken from Akhmedova-Azizova and Abdulagatov [5]

3.4 Conclusion

Determining the phase composition plays an essential role in the accurate computation of two-phase mixtures properties. Fugacity-Fugacity and Fugacity-Activity are popular thermodynamic models to quantify the impact of gas dissolution on phase composition. However,

their iterative algorithms make them computationally expensive. GenEOS is a novel approach to overcome the limitations of conventional Fugacity-Fugacity and Fugacity-Activity models. Using a unique AI approach allows for the application of highly sophisticated and precise EOS methods even on large-scale problems. The scope of applications can encompass even the most challenging environments, such as those found in the reservoir domain, which may involve high pressure, high temperature, and high salinity conditions. Gene expression programming is used in this study to provide explicit equations for the prediction of target outputs and support this fast calculation of fluid properties. Developing high-preciseness GEP functions requires a lot of accurate data for the training process. Hence, in the first step of this study, a large database is provided by employing a robust Fugacity-Activity method. The generated data points are fed into established GEP models to non-iteratively anticipate the fluid temperature and equilibrium constants as functions of enthalpy, pressure, and two-phase composition. The introduced EOS in this study (GenEOS) uses these novel GEP equations to quickly calculate fluid properties. GenEOS shows benefits in terms of:

→ Accuracy: The average relative error of 0.6 % in predicting fluid temperature for 1,000,000 arbitrary sets of [pressure, enthalpy, two-phase composition] indicates the high accuracy of introduced GEP functions in calculating target outputs. This error reduces to zero after the first iteration when the GEP function is used as an initial guess in the F-A algorithm. Accounting for the highly-nonlinear pressure-dependent thermodynamic behavior of non-boiling water in the NaqP phase and quantifying the impact of gas dissolution on the AqP composition makes GenEOS very accurate in predicting fluid properties.

→ Computation speed: The F-A algorithm typically needs three iterations for calculating equilibrium constants as functions of temperature. However, in the numerical modeling of two-phase flows, the conservation equations are solved for computing velocity, pressure, enthalpy, and two-phase composition. Therefore, temperature, as an input for the EOS, should be guessed at the beginning of the algorithm. It can increase the total number of iterations to nine. Using the proposed GEP equations as initial guesses leads to convergence in only one iteration and considerably reduces the EOS-related computational costs.

→ Applicability: Focusing on geothermal applications, the nine primary components of water, carbon dioxide, methane, nitrogen, hydrogen sulfide, sodium chloride, potassium chloride, magnesium chloride, and calcium chloride are included in GenEOS. This C++ code can work stand-alone, without coupling to any other chemical solver. Consequently, it can be easily implemented in other modeling platforms while avoiding the complexity of calling multiple linked codes/software. GenEOS is also provided as an object in a multi-physics object-oriented simulation environment called MOOSE [84]. Therefore, all MOOSE-based

applications can now benefit from this open-access UserObject. So far, GenEOS is included in a MOOSE-based wellbore simulator called MOSKITO [85–88].

→ Transparency: GenEOS is a transparent box for computing fluid properties. All the new GEP equations for computing fluid temperature and equilibrium constants are presented as simple C++ codes in Appendix A. Thus, they can directly and freely be used or converted to any other programming language. Moreover, the implemented equations for calculating other properties and corresponding references are clearly addressed in the context of the paper.

The development of GenEOS has opened up new avenues for the accurate and efficient computation of fluid properties in two-phase mixtures, with broad applications in various fields. In the numerical modeling of two-phase fluid flow, GenEOS's ability to quickly calculate fluid properties using novel GEP equations provides a significant advantage over traditional EOS methods, enabling more precise simulations of complex flow phenomena. Furthermore, the application of GenEOS can extend to the forecasting of complex processes in pipes, where the accurate prediction of fluid properties is critical for optimizing pipeline design and operation.

Another promising area of application for GenEOS is in carbon capture and storage, where it can be used to accurately predict the behavior of fluids under varying pressure and temperature conditions, facilitating the design of efficient and cost-effective carbon capture and storage systems. In the field of geothermal reservoirs, GenEOS's ability to accurately calculate fluid properties can aid in the prediction of reservoir behavior, improving reservoir management and maximizing energy production.

3.5 Acknowledgment

The study is part of the subtopic "Geoenergy" in the program "MTET - Materials and Technologies for the Energy Transition" of the Helmholtz Association.

Chapter 4

Impact of thermosiphoning on long-term behavior of closed-loop deep geothermal systems for sustainable energy exploitation

This chapter is published in Renewable Energy, <https://doi.org/10.1016/j.renene.2022.06.014>

Abstract

Circulation of working fluid in closed geothermal loops is an alternative environmentally friendly approach to harvest subsurface energy compared to open hole geothermal doublet systems. However, the rapid decline of production temperature, low generated thermal power, and difficulties in deepening the system are major limitations. Herein, synthetic studies are presented to investigate the system's performance and improve its longevity for better use of this clean baseload power. The investigations are conducted by implementing appropriate equations of state to model state-of-the-art thermal and hydraulics processes in wellbores and considering various geometrical configurations to adopt proper design strategies. They provide insight for maximizing the generated thermal power, decreasing pumping energy, and avoiding production temperature drawdown. The results indicate that a stable thermal condition could be reached in which not only the temperature breakthrough is avoidable, but also the generated thermal power and production temperature continuously enhance over the project lifetime of one century. Analysis of the thermosiphon effect in the designed systems revealed that even with the pressure loss of 900 *kPa* at surface installations, the triggered natural flow rate is larger than 11 *L/s*. This thermosiphon flow rate yields the thermal power production of 2 *MW* and Cumulative extracted energy of 15 *PJ* over the project lifetime of 100 years. Restriction of this flow rate to 5 *L/s* leads to an average extraction temperature of 80 °C. It is also found that a change in the subsurface temperature gradient does not affect the optimal 2 *km* isolation length of the production well.

4.1 Introduction

The possibility to continually extract heat from different geological systems (e.g., hydrothermal [89, 90], geo-pressurized [91], EGS systems [92], hot dry rock [93], and magma [94]) makes geothermal energy an exciting option responding to the increase of global energy demand and mitigating harmful environmental impacts of fossil fuels [95]. However, seismic events induced by hydraulic fracturing and excess pressure, subsurface water contamination, uncertainties in geothermal field characterization [96], and the considerable drilling costs are significant barriers to the spread of open geothermal systems [97–99]. Borehole heat exchangers (BHEs) equipped with heat pumps can sustainably harvest geothermal energy without the aforementioned hazards [100–107]. Despite the power consumption of the heat pump, they are economically beneficial and are successfully implemented by large numbers for single dwellings [108]. Their worldwide installed capacity has increased from 1.8 GW in 1995 to 50 GW in 2015 [109], and the total number of installed systems in Europe exceeds 1.9 million units [110]. The typical thermal power generation of BHE systems is approximately 50 W/m [111]. Moreover, retrofitting abandoned wells [112–114], as so-called “Deep BHE” [115, 116], have recently received particular attention. The existence of 20–30 million abandoned wells [113] promotes the global tendency to retrofit them as geothermal systems and to produce a considerable amount of cost-effective energy by cutting the drilling cost.

Several studies have been conducted to improve the performance of BHEs by extending the heat exchange surface. Based on these studies, the BHEs can be categorized into four main groups: coaxial BHE [117], single U-tube BHE [118], double U-tube BHE [119], and helical BHE [120–122]. The double U-tube BHE comprises two connected U-tubes inside one borehole requires rather large wellbore diameters. Similarly, the coaxial BHE consists of a small “upflow” production pipe wrapped in a larger “downflow” injection pipe, forming an annular cross-section, which requires a relatively large wellbore diameter to maintain suitable fluid velocities in the inner and outer pipes. Although the heat exchange area of helical BHE is more extensive than the other BHEs, helical pipe, which is made of special flexible materials, should be installed on a reinforced frame to strengthen its structure. In conclusion, the helical BHE system also suffers from large overall diameter which restricts its application in geothermal energy utilization. Furthermore, the economic viability of this system at high temperatures is a controversial issue since this thermal condition can deform its structure, which is commonly made of polyethylene (PE) and polyvinyl chloride (PVC) [123]. Nowadays, double U-tube and helical BHEs are installed as prefabricated structures with large overall diameters, which can be an obstacle to deepening these systems.

Recent development in drilling technologies [124–127] made drilling of deep inclined boreholes (i.e., the dip angle of greater than 90 deg. at several km depths) with complex

trajectories feasible [128]. It allows for employing a rather new closed-loop deep geothermal (CDG) systems with a lengthy horizontal extension to exploit geothermal energy from both hydrothermal systems and hot dry rock. This CDG system consists of two vertical wellbores connected through an extended long horizontal well. Based on the geometrical configuration of this system, it is expected to obtain higher production temperature and thermal power compared to the conventional BHEs due to its operating depth and extended heat exchange surface area. To the best of our knowledge, the performance of a similar system possessing relatively shorter vertical and horizontal wellbores is experimentally evaluated in the north of Canada [129], and few studies have investigated its heat extraction mechanism numerically.

After having conducted a systematic literature review on the design and heat transfer of deep closed systems, Budiono *et al.* [130] finally identified 38 relevant publications with most articles published in the period of 2016-2021. This shows that researchers have recently started to consider the potential of these geothermal systems for sustainable energy exploitation. However, most studies focus on coaxial systems. Although CDG systems are superior to deep coaxial systems in terms of power production and extraction temperature [130], only few papers [131–137] are related to analyzing their heat extraction mechanisms. The systematic work of Budiono *et al.* [130] is combined with our literature review to provide a comprehensive overview of the conducted studies and the research gap.

In 2018, Song *et al.* [131] used a synthetic model to evaluate the impact of operational parameters (e.g., flow rate and inlet temperature) on the performance of the CDG system. With respect to the evolution of the production temperature, they distinguished possible decreasing, transition, and stable production scenarios. However, they set up a single stratigraphic structure and assumed the physical properties of water to be constant despite temperature and pressure alteration. In 2018, Sun *et al.* [132] repeated their study using carbon dioxide as a circulating fluid, and proposed new concepts for the evaluation of the geothermal recovery performance. In 2020, Chen *et al.* [138] used temperature-dependent equation of state for a limited four months operation period but neglecting the impact of well completion (casings and cement layers) on heat exchange. Yuan *et al.* [134] evaluated the geothermal energy recovery on an idealized CDG system identifying reservoir thermal conductivity as most important parameter determining the system's energy recovery potential. However, they assumed constant properties for the working fluid without accounting on thermal resistance by convective fluid flow within the wellbores, the steel tube wall, casing, and cement ring. Sun *et al.* [133] analyzed the geothermal energy production by supercritical CO₂ circulation in CDG systems. They have conducted a sensitivity analysis to demonstrate the effects of injection parameters, heat transmission fluid, and wellbore properties on the temperature field. However, the short production time (10000 h) and high subsurface

temperature gradient ($50\text{ }^{\circ}\text{C}/\text{km}$) may lead to an unrealistic estimation of the long-term heat production. Fallah *et al.* [136] introduced a novel concept of integrating an automated managed pressure operation (MPO) system with a CDG system for scalable power generation. They analyzed the generated thermal power for operation scenarios accounting for vertical depth and horizontal length, openhole or cased-hole lateral completions, heat insulation or lack thereof of the return flow, and changing pump rates. With depth and horizontal length of the system assumed to be each 7 km and a maximum rock temperature of $250\text{ }^{\circ}\text{C}$ the parametrization precedes current drilling technology. Ghavidel *et al.* [135] studied the transient heat transfer in CDG systems. Their investigation is different from other reviewed literature as they only focused on heat absorption in the horizontal wellbore. Nevertheless, ignoring the power production in the injection wellbore can result in a notable underestimation of the CDG system's heat extraction potential.

The above-mentioned studies focused on describing the general behavior of CDG systems and suffer from some oversimplifications or unrealistic assumptions. Furthermore, practical proposals to make the CDG system a strong competitor to other conventional geothermal systems are still lacking. The main purpose of this study is to develop novel concepts with relevance to the economic efficiency of CDG systems, which is one of the main barriers to their wider use, based on state-of-the-art simulation techniques:

1. Using thermosiphon effect to decrease the pumping energy, thus reducing the pumping costs. Being not yet numerically analyzed for CDG systems, the magnitude and stability (transient behavior) of thermosiphon flow rate under different geometrical configurations and surface pressure losses will be quantitatively assessed.
2. Valve-controlled thermosiphon flow is suggested by this study to stabilize the extraction temperature and to improve system's longevity. This will result in optimizing flow rate considering thermal power production, extraction temperature stability, and internal energy consumption.
3. Defining new criteria for the calculation of optimum insulation length by addressing a specific absorbed energy. Therewith, the energy absorption of the system is maximized as function of temperature gradient and thermal conductivity.
4. Sectional analysis of power production in CDG systems in vertical and horizontal wellbores are providing quantitative insights for the future design of multi-lateral structures.

To achieve these goals, thermal interactions between different components of the system (i.e., cement, casing, formation, and working fluid) are analyzed. A pressure and temper-

aturedependent equation of state (EOS) is included to consider the buoyancy force in the thermosiphoning evolution. A fully coupled mathematical and physical model, including continuity, momentum, and energy equations, the EOS, and an analytical lateral heat transfer approach, is employed and presented. Finally, the sectional performance of the system is thoroughly evaluated to avoid production temperature drawdown, which is a severe problem in dealing with closed geothermal systems, and the impact of suggested scenarios on the net generated thermal power, insulation strategy, and pumping energy are further discussed. It should be noted that the CDG system is designed for district heating purposes. Therefore, the word "power" in the next chapters refers to "thermal power", and it is also explicitly mentioned when the system is producing electric power.

4.2 Methodology

4.2.1 Governing equations

To model the CDG systems, three major components, including energy exchange between wellbore and formation, heat transfer in formation, and transient processes in wellbores, should be considered. Fluid flow in tubing undergoes several coupled physical processes, such as pressure change balanced by friction loss, gravity and kinetic energy alteration [139, 140], temperature variation due to heat exchange with surrounding formation, and velocity change influencing pressure and temperature fields. In order to appropriately simulate these physical processes, a finite element code, called MOSKITO [86, 141], is developed in the MOOSE Framework [84, 142] environment to consider such complex physical processes. MOOSE is a multiphysics object-oriented simulation environment that is written in C++. This open-access code can be used for solving a wide variety of partial differential equations.

While the temperature of the circulating fluid may significantly increase, because of its high pressure, the fluid doesn't experience a two-phase state. A non-isothermal transient flow in a pipe is described as [143]:

Continuity equation:

$$\frac{\partial}{\partial t}(\rho) = -\frac{\partial}{\partial z}(\rho v) + m \quad (4.1)$$

where ρ and v are the density and velocity of fluid, and m is the mass sink/source term in unit volume and unit time.

Momentum equation:

$$\frac{\partial P}{\partial z} = \rho g \cos(\theta) \pm \frac{f\rho v^2}{2d} \pm \left(\frac{\partial}{\partial t}(\rho v) + \frac{\partial}{\partial z}(\rho v^2) \right) \quad (4.2)$$

where f , g , θ , d and P are the friction factor, gravitational acceleration, the inclination of the well, wellbore hydraulic diameter, and fluid pressure, respectively. Depending on flow and gravity directions, the sign of the right hand side (RHS) terms in the momentum equation can change.

Energy equation:

$$\frac{\partial}{\partial t} \left[\rho \left(h - \frac{P}{\rho} + \frac{1}{2}v^2 \right) \right] = -\frac{\partial}{\partial z} \left[\rho v \left(h + \frac{1}{2}v^2 \right) \right] + \rho v g \cos(\theta) - \frac{q}{A} + Q \quad (4.3)$$

where h , q and Q are the enthalpy, lateral heat flow, and heat sink/ source terms, respectively.

Based on Eqs. (4.1)-(4.3), main variables are the velocity, pressure, and enthalpy of the fluid. This set of coupled partial differential equations (PDEs) will be bounded by transient Dirichlet boundary condition type. To solve these equations, some constitutive relationships/ empirical equations, including the viscosity, the density, and the friction factor, are required. The viscosity is calculated by Vogel Equation [144]. An empirical equation of state (EOS) [145] is used to calculate the density as a function of pressure, temperature, and salinity of the fluid (saline water).

The fluid can exchange heat by surrounding structure, including casings, cement layers, and geological formation, through two main mechanisms. The first mechanism is the conductive heat transfer through all layers, and the second mechanism is the convective heat transfer within a fluid film in the vicinity of the inner tubing wall. In overall, this heat flow can be calculated by:

$$q = 2\pi r_{to} U_{to} (T_f - T_{cf}) \quad (4.4)$$

where r_{to} , U_{to} , T_f and T_{cf} are the outside radius of the inner tubing, the overall heat transfer coefficient, the fluid temperature, and the temperature at the cement/formation interface, respectively. This lateral heat model updates the temperatures at the interfaces of different layers over time. For a detailed explanation, refer to Willhite [17]. The increase of the casing diameter is accompanied by the enlargement of the heat exchange area leading to losing or absorbing a higher amount of heat. Simulating the thermosiphon flow is one of the main goals. This flow is a self-flowing system driven solely by the density difference at both wellheads due to temperature differences. Therefore, the temperature dependency of the EOS plays a key role since the density monotonically decreases by increasing the temperature. The pressure gradient caused by the density difference acts as the driving force to circulate fluid in the system. However, this pressure gradient should overcome pressure losses in the CDG system (i.e., velocity-dependent) and at surface facilities. Numerical simulation of thermosiphon flow requires special treatment at the boundary. Therefore, a particular type of Dirichlet boundary condition, called velocity postprocessor BC, is designed in this study to

automatically calculate the re-injection velocity using wellheads pressure differences reduced by surface facilities pressure loss at each timestep (see Section 4.4).

4.2.2 Model validation

The presented model on the scale of CDG systems is validated against the results of the study conducted by Song *et al.* [131]. An identical configuration and parameters, i.e., a flow rate of $70 \text{ m}^3 \text{ h}^{-1}$, an injection temperature of $40 \text{ }^\circ\text{C}$, a depth of 3.5 km, and a horizontal extension of 6 km, are assumed. In order to comply with Song *et al.* [131] study, an EOS with a constant density, ignoring the impact of fluid pressure and temperature, is considered.

Fig. 4.1 illustrates a comparison of three models for the temperature field. In the first step of validation, all the physical properties of the fluid are assumed to be constant despite temperature and pressure changes. The obtained result perfectly agrees with the results of Song *et al.* [131] when the simulation is conducted without EOS. Nevertheless, the considerable variations of pressure and temperature in this deep geothermal system can affect the fluid properties. Therefore, in the second step, the temperature and pressure-dependent EOS is used to account for the alterations of density, viscosity, and specific heat capacity. The inclusion of the EOS has no notable impact on the computed temperature profile in the injection wellbore. However, it reduces the calculated temperature in the production wellbore ($\approx 1 \text{ }^\circ\text{C}$) as the fluid experiences larger pressures and temperatures in this section of the system.

4.2.3 Numerical modeling

In the present study, the CDG system is supposed to provide a continuous supply for district heating purposes over the whole year, thus neglecting possible recovering periods. The geometrical configuration of the system comprises of three sections (Fig. 4.2): I) a vertical injection well, II) a horizontal well, and III) a vertical production well. The vertical wells are relatively deep, and they are connected at the bottom hole through the horizontal well, which is relatively long. The vertical wells (sections I and III) are cased to avoid subsurface contamination and maintain wellbore stabilities, while the horizontal extension (section II) is directly exposed to hot formation to maximize energy absorption. It is supposed that the injection of some chemicals seals the lateral area around section II [129]. The heat exchange in sections I and III is regulated by the number of layers around the wellbore, their thicknesses, fluid velocity, pipe roughness, and thermophysical properties of casing, cement, formation, and circulating fluid. However, depending on the pressure difference between circulating fluid and the surrounding environment, we may have lateral inflow or outflow

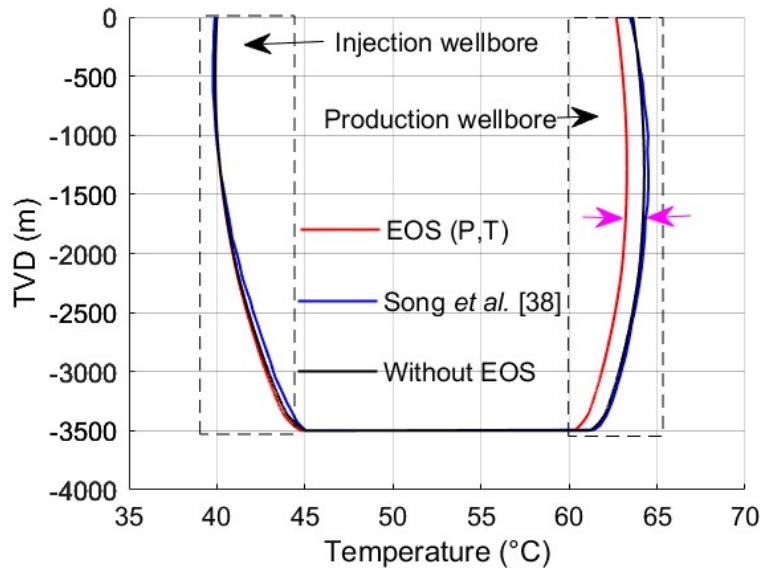


Fig. 4.1 Comparison between temperature profiles along the system after 20 years of operation. The same style of the reference paper is used for this figure. The pink double arrow shows the variation of calculated temperature in the production wellbore after including the equation of state. The inclusion of the EOS has a negligible impact on the calculated temperature in the injection wellbore.

through section II. This direct exposition is necessary since casing the horizontal section, like the lower section of vertical wellbores, increases the total thermal resistivity by 40 %.

A reference model with specific configuration and parameters is introduced below. the configuration and parameters of the reference model are preserved throughout this study unless otherwise noted.

Reference model

In the reference model, both the vertical depth, Δz , and the horizontal length, Δl , are 4 km, as shown in Fig. 4.2. This figure also demonstrates the wellbore diameters, which ranges from 8 3/8" (section II) to 22" (the upper part of section I), as well as casings arrangements. The roughnesses of sections I, II, and III are 10^{-4} m, 2×10^{-4} m, and 10^{-4} m, respectively [146]. The formation surrounded the system consists of two geological units with a depth of 2 km each. The thermal conductivities of the upper and lower layers are 2 and 3 $Wm^{-1}K^{-1}$, respectively. The underground subsurface temperature gradient is assumed to be 30 °C/km, and the temperature at the surface is 10 °C. All thermo-physical properties of the cement layer, casing, and formation are shown in Table 4.1.

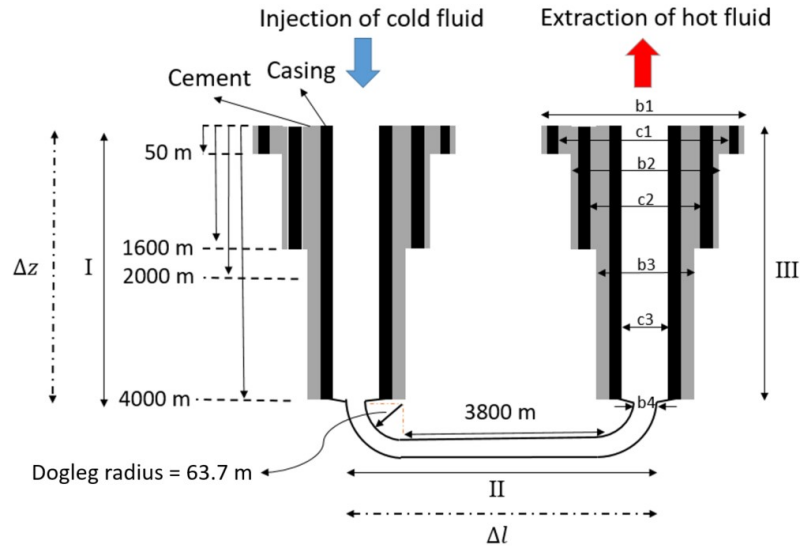


Fig. 4.2 Schematic illustrating geometrical features of the reference model. b_1 , b_2 , b_3 , and b_4 stand for borehole diameters where the wellbore structure is in direct contact with the formation. c_1 , c_2 , and c_3 also represent casings' inner diameters. ($b_1 = 0.5588$ m, $c_1 = 0.473075$ m, $b_2 = 0.4318$ m, $c_2 = 0.346075$ m, $b_3 = 0.31115$ m, $c_3 = 0.244475$ m, $b_4 = 0.212725$ m). Δz and Δl show the depth of vertical wells and total horizontal length, respectively. The horizontal section is directly exposed to hot formation.

Table 4.1 Thermo-physical properties of formation, casing, and cement layer

Formation density	2400 kgm^{-3}	Cement thermal conductivity	$0.7 \text{ Wm}^{-1}\text{K}^{-1}$
Formation heat capacity	$1000 \text{ J kg}^{-1}\text{K}^{-1}$	Casing thermal conductivity	$100 \text{ Wm}^{-1}\text{K}^{-1}$
Formation thermal conductivity (upper layer)	$2 \text{ Wm}^{-1}\text{K}^{-1}$	Subsurface temperature gradient	$30 \text{ }^\circ\text{C km}^{-1}$
Formation thermal conductivity (lower layer)	$3 \text{ Wm}^{-1}\text{K}^{-1}$	Ground surface temperature	$10 \text{ }^\circ\text{C}$

The initial temperature of the circulating fluid is assumed to be the same as the ambient formation temperature considering a thermal equilibrium between the residual fluid and the surrounding formation. The initial pressure condition is hydrostatic. Moreover, Dirichlet boundary conditions with fixed values are applied at the injection point. A constant salinity of 0.25 molal is considered while, using Dirichlet BCs, the injection temperature, pressure, and flow rate are set at 10 °C, 100 kPa, and 5 L/s, respectively.

A sensitivity analysis for three spatial discretizations ($\Delta x = 14\text{ m}$, $\Delta x = 11\text{ m}$; and $\Delta x = 7\text{ m}$) was conducted to confirm that the solution is mesh-independent. Evaluation of pressure and temperature fields over the length of the wellbores revealed the negligible impact of implemented mesh sizes on the results. The maximum relative variation of pressure and temperature values is below $6 \times 10^{-4}\%$ when changing the mesh size from 7 m to 14 m. Even though, the mesh size of 14 m is acceptable for this study, the mesh size of 7 m was used due to the reasonable computational cost. The total simulation time is 100 years which time steps gradually increase from 100 s to one month. While the operation period of 100 years is much longer than the lifetime of conventional geothermal systems (i.e., 30 years), evaluation of the ratio of generated power to the total length of the wellbores revealed that this system requires a long payback period. Additionally, the assessment of the system's long-term performance helps to compare its longevity against other geothermal systems. This long operation period is also suggested by some other companies working on this system [129]. Consequently, all the casing, cement layers, insulation, and pumping should efficiently work for a long period which is a serious issue while operating with this system.

Insulation strategy for production well

Proper insulation of production wellbore is a key aspect of designing CDG systems. The main purpose of insulation is to prevent heat loss at areas in which the temperature of the circulation fluid is higher than those of surrounding areas. However, temperature alteration of the fluid and its adjacent formation leads to the continuous change of insulation length. Since the length of the insulation layer cannot vary over time, this length should be properly estimated to minimize heat loss and to be practical for construction. Hence, the total absorbed energy in each section should be calculated to determine zones in which the total exchanged energy possesses a negative value (i.e., energy loss). The total absorbed energy per meter (TAEM) for different sections after 100 years of operation is plotted in Fig. 4.3.a. The TAEM value of each section depends on lateral exchange area, total thermal conductivity, and temperature difference between circulating fluid and surrounding area (DT) as per Eq. (4.4). Positive values reflect heat absorption from the surroundings, while negative values yield heat losses to the surrounding. The jumps of the TAEM at points β and ζ (in sections I and

III, respectively) originate from the alteration of the formation thermal conductivity at the depth of 2 km as introduced in the previous section. Similarly, the jump of the TAEM at point α is related to the changes of casing and cement layers, as per Fig. 4.2, leading to the reduction of the total thermal resistivity.

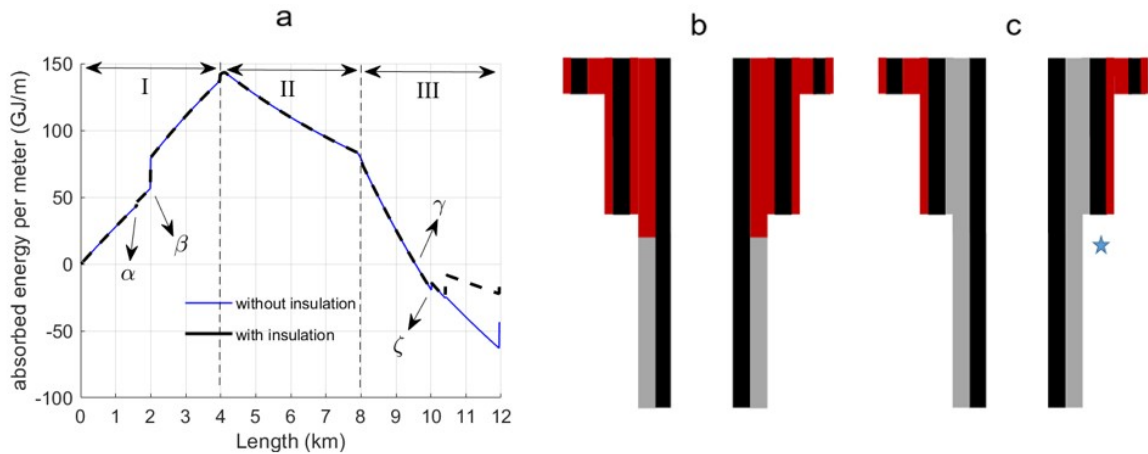


Fig. 4.3 a) Impact of insulation of production wellbore on the total absorbed energy per meter of the CDG system after 100 years of operation (insulation layer is highlighted by red color). The corresponding lines for the presented cases overlap up to the insulation section. b) Ideal insulation of production wellbore c) practical insulation of production wellbore.

Since the lateral exchange area is constant in each section (I, II, and III) and the jumps are explained above, the overall trend of the TAEM is mainly dependent on ΔT . In section I, ΔT grows by the depth leading to increasing of the TAEM. However, the temperature of the circulating fluid approaches the surrounding temperature along section II, leading to the reduction of ΔT resulted in the decline of the TAEM. Similarly, this trend is observed in section III, with the exception that the TAEM changes the sign (from positive to negative) in this section. Point γ in Fig. 4.3a indicates that the circulating fluid is hotter than the surrounding formation, and the fluid is losing heat from this point up to the extraction point. To avoid the cooling of the circulating fluid, proper insulation of section III is necessary from point γ upward as illustrated in Fig. 4.3b. However, the insulation arrangement in Fig. 4.3c is considered in this study to prevent severe complexity in practical well design and drilling plans. The thermal conductivity of the insulation material (urethane fiberglass) is $\lambda = 0.021 \text{ Wm}^{-1}\text{K}^{-1}$ [147]. This insulation configuration prevents 50 GJ/m heat loss at the upper part of section III. It is worth mentioning that the insulation length mainly depends on operation duration and production flow rate. Moreover, operating in highly conductive geothermal fields with a large subsurface temperature gradient may increase the optimum length of the insulation layer.

4.3 Evaluation of the CDG system long-term behavior

4.3.1 Impacts of flow rates on the produced temperature and energy

In this chapter, the system behavior for different flow rates of 1 L/s, 5 L/s, and 10 L/s are evaluated assuming the reference model conditions (Fig. 4.4).

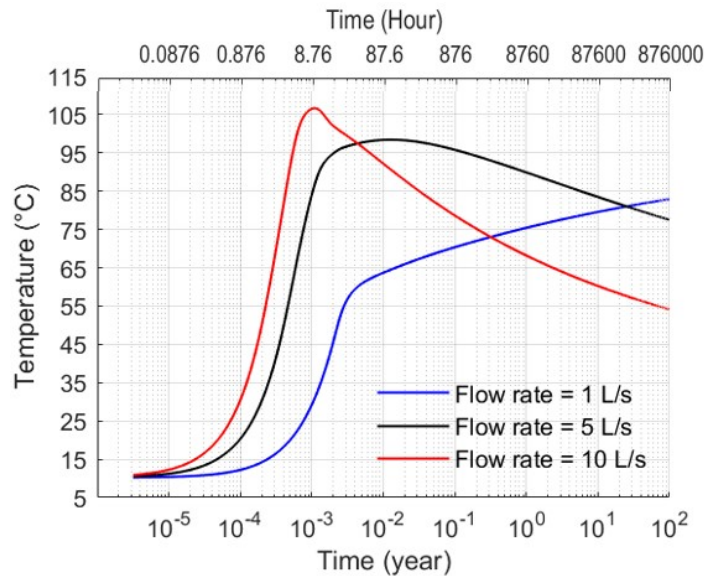


Fig. 4.4 Extraction temperatures over time for different flow rates. The short-term behavior of the extraction temperature is caused by the displacement of residual hot fluid, while its long-term behavior is controlled by the lateral heat exchange.

Fig. 4.4 shows the impact of flow rate on the behavior of production temperature over time. The immediate rise of the extraction temperature in the first few days is due to the residual hot fluid displacement. After this short period, the production temperature tends to decrease (Fig. 4.4, flow rate = 10 L/s and flow rate = 5 L/s), which is a well-known behavior in closed geothermal systems. The rapid decline in the production temperature is the major challenge of the CDG system. However, to guarantee the reliability of the system for district heating purposes, a production temperature of at least 80 °C at a meaningful flow rate is required, which is further analyzed in the following. The system's thermal performance is strongly dependent on flow rate due to the heat exchange rate between the surrounding formation and the circulating fluid. Accordingly, the reduction of the circulating fluid velocity results in reaching a higher temperature along the injection and horizontal wells (sections I and II) but thermal huge temperature loss along the production well (section III). Fig. 4.5 illustrates this behavior for these sections at different flow rates and timings.

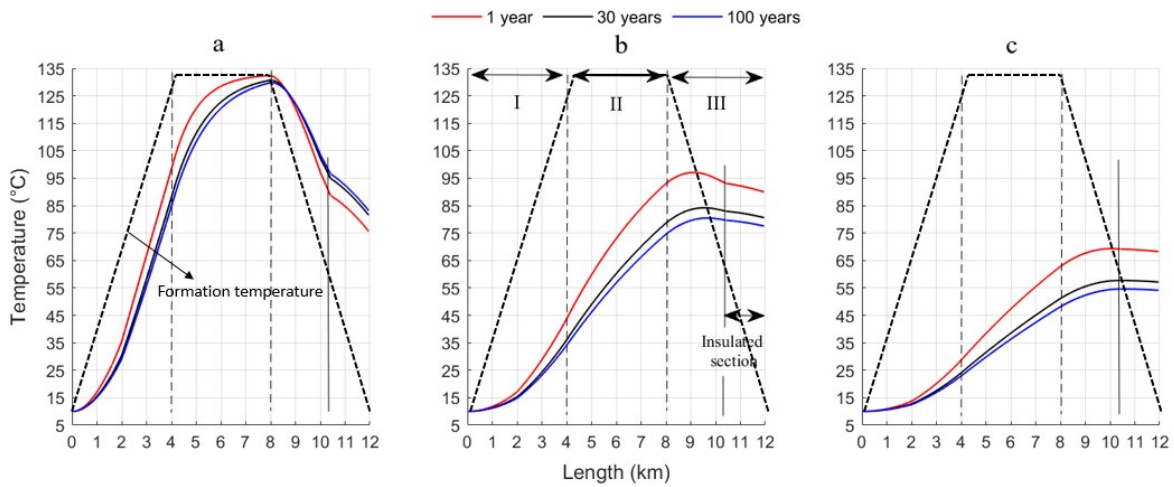


Fig. 4.5 Temperature distribution in each section of the system (I, II, and III) for a) flow rate = 1 L/s b) flow rate = 5 L/s c) flow rate = 10 L/s. The difference between temperature profiles along the wellbores and formation temperature (dashed line) can be used for the determination of the locations requiring insulation.

The duration of heat exchange for a given volume of fluid is longer at smaller flow rates, which plays a key role in regulating the extracted/lost heat in each section of the system. Over time, the fluid temperature in sections I and II is decreasing regardless of the flow rate. In section III, a similar trend is observed except for the flow rate of 1 L/s, when a hotter fluid enters the production wellbore, and it has a longer time to exchange heat with the surrounding formation. Therefore, the circulating fluid loses a lot of energy, represented by a notable temperature drop in the production wellbore. For this flow rate, the circulating fluid heat loss causes the surrounding formation around section III to warm up over time, leading to prevention of the mentioned temperature drop and continuous production temperature rise, as shown in Fig. 4.4. In the other flow rates, such an effect is not observed as 1) the fluid velocity is higher, so the heat loss is lower in section III, and 2) the circulating temperature is closer to the surrounding formation around section III because of low heat gain in section I and II (due to high fluid velocity). This reveals the importance of the heat exchange duration. The energy loss may contradict the idea of maximizing power generation. However, it is useful when a high stable extraction temperature is required for operation. It is also noteworthy that sometimes the increase of extraction temperature compensates for the decrease of flow rate. Therefore the generated power doesn't change significantly.

Aside from the heat exchange duration discussed above, the flow rate can remarkably influence the convective heat transfer factor leading to the variation of the heat exchange rate. This factor is a function of the Reynolds number, friction factor, and Nusselt number, which are all functions of the circulating fluid velocity. For instance, the convective heat

transfer factor in the case of the flow rate of 1 L/s takes values between $91.6 \text{ Wm}^{-1}\text{K}^{-1}$ and $164.5 \text{ Wm}^{-1}\text{K}^{-1}$, while it ranges between $577.8 \text{ Wm}^{-1}\text{K}^{-1}$ and $932.75 \text{ Wm}^{-1}\text{K}^{-1}$ for the flow rate of 10 L/s . Therefore, the interplay between the heat exchange duration and the heat transfer factor, which are strongly functions of the fluid velocity at each section (I, II, and III) and the overall system's flow rate, is the key factor to stabilize the production temperature over time and maintain the longevity of the CDG system.

The produced energy of the reference model can range between 1 PJ and 6 PJ for the simulated flow rates (Fig. 4.6). The generated power and energy production depend on flow rate and the temperature difference between injection and extraction points. As mentioned before, the increase of the flow rate is associated with the extraction temperature decrement. However, there is not a linear relation between variations of extraction temperature and flow rate. As shown in Fig. 4.6, the increase of the flow rate from 1 L/s to 5 L/s can remarkably enhance the cumulative absorbed energy over time. It means the increases of flow rate prevailed over the reduction of extraction temperature. However, further increase of the flow rate from 5 L/s to 10 L/s doesn't considerably enhance the energy absorption. It indicates that the severe reduction of the extraction temperature doesn't allow for a significant improvement of energy absorption. Consequently, the decrease of extraction temperature, generated power, and energy absorption rate are the main barriers to the increase of the operating flow rate.

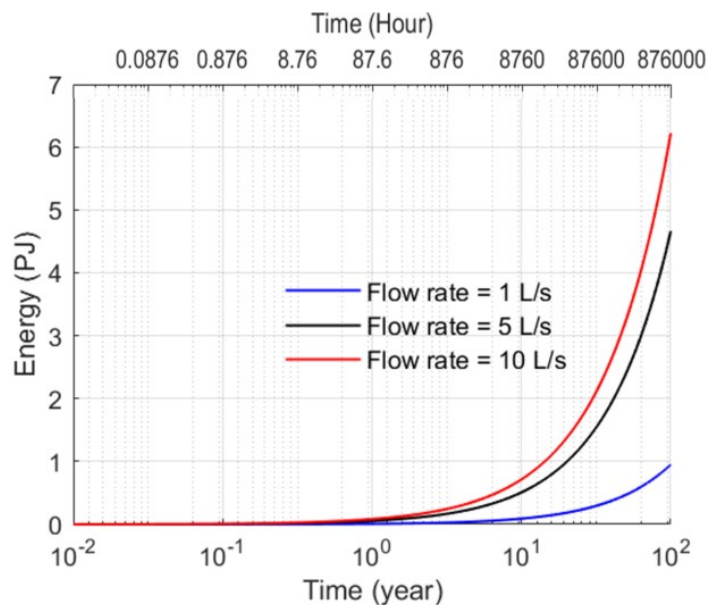


Fig. 4.6 Cumulative extracted energy over time for different flow rates. After 100 years of operation, the absorbed energy with the flow rate of 10 L/s is 6 times of heat absorption with the flow rate of 1 L/s .

To better evaluate the total extracted energy in Fig. 4.6, a sectional (I, II and III) performance of a CDG system is illustrated in Fig. 4.7. Fig. 4.7a shows that the extracted heat in section I is mainly wasted in section III (almost mirrored curves around the power of zero). However, this lost heat in all cases is reduced over time since the warm up bubble around section III get bigger and hotter (it is also explained in Fig. 4.5). Interestingly, the total net power curve in Fig. 4.7b for each flow rate mainly mimics the power behavior of section II which is shifted by the difference of the obtained powers in section I and III. Therefore, the extracted heat in section II and preventing heat loss in section III are of paramount importance in the production temperature sustainability and power longevity.

4.3.2 Impacts of wellbore diameter on the produced power

The friction loss is proportional to the circulating fluid velocity. Hence, reducing wells diameters increases frictional loss, assuming the same flow rate. The following sensitivity study is performed: Case 1 is devised by subtracting 4" from the wellbore diameters of the reference model, while the wellbore diameters of case 2 are 4" larger than those of the reference model. The rest parameters are the same as of the reference model.

As exhibited in Fig. 4.8a and Fig. 4.8b, altering the wellbore diameters does not have a considerable impact on the generated power. Wellbore diameter increment is associated with the enlargement of the lateral heat exchange area. Additionally, the heat exchange duration and the convective heat transfer factor change. These changes and enlarged area are in the favor of the case 2 resulted in higher produced power. Nevertheless, this is a proof of the complex behavior of the system and the demand for an advanced mathematical and physical model. In conclusion, regardless of the negligible changes in the produced power, the feasibility of the drilling cost reduction by decreasing the wellbore diameters is showcased in this section.

4.3.3 Impacts of wellbore diameter on the produced power

As discussed before, the main objective of this study is to better assess the CDG system for district heating purposes. However, the feasibility of the CDG system to be utilized for electricity production is also evaluated in this system. Hence, two cases are designed here to testify the possibility of long-term hotter produced temperature ($>100\text{ }^{\circ}\text{C}$) compared to the case of district heating ($>80\text{ }^{\circ}\text{C}$). These scenarios are: 1) the injection temperature of $70\text{ }^{\circ}\text{C}$, and 2) increasing the depth and the length of the system. For the first case, the reference model is used and only the injection temperature increased from $10\text{ }^{\circ}\text{C}$ to $70\text{ }^{\circ}\text{C}$.

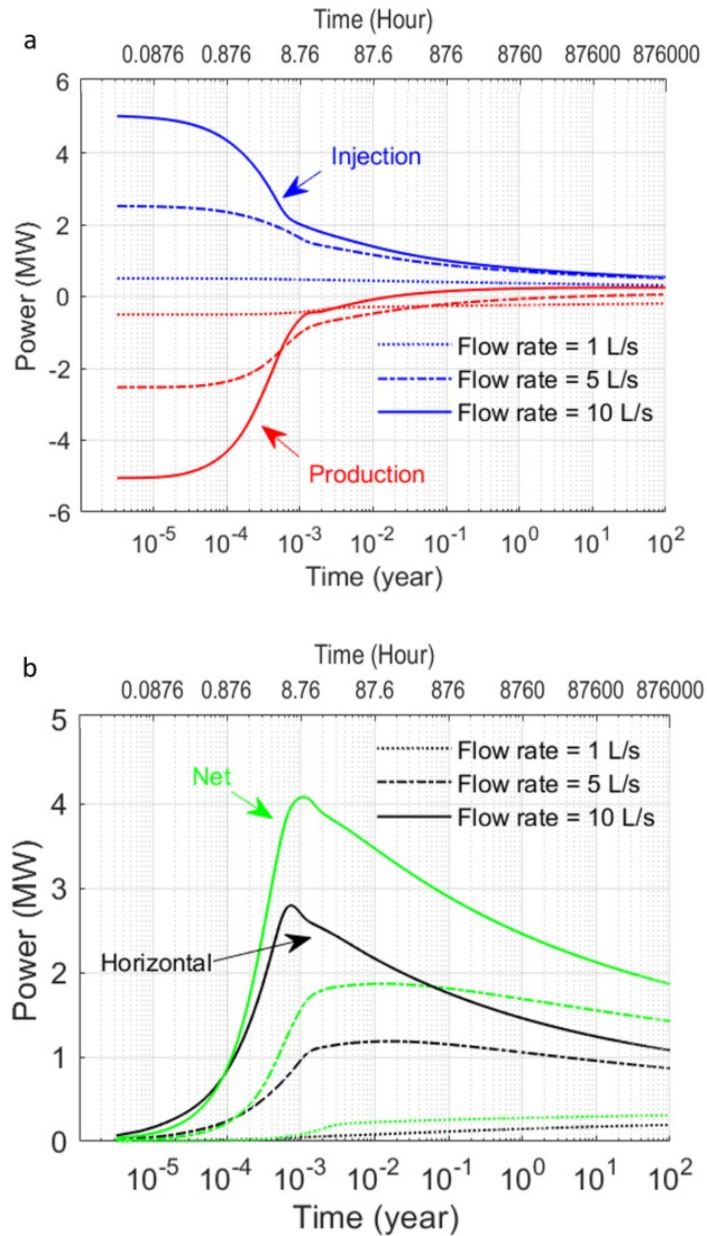


Fig. 4.7 Flow rate impact on: a) generated powers in vertical wells b) net generated power and produced power in the horizontal section over time. For each flow rate, the variation of net power over time is like the transient behavior of produced power in the horizontal wellbore.

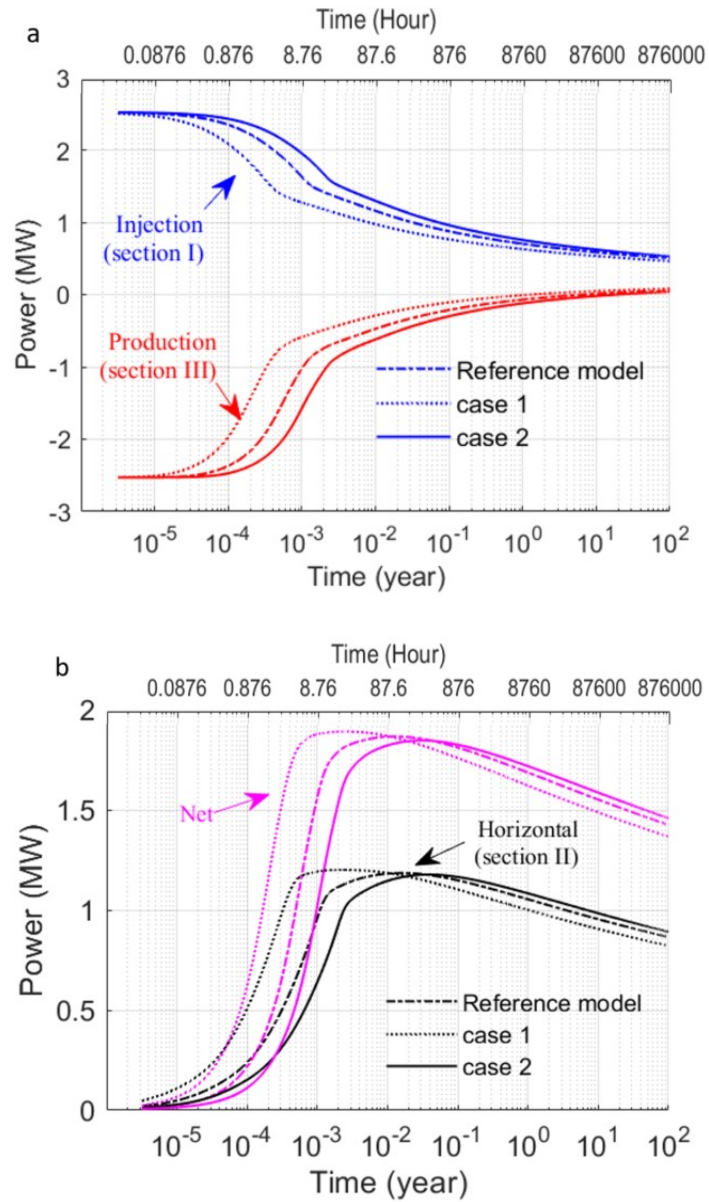


Fig. 4.8 Impact of wellbore diameter (case 1-4" smaller and case 2-4" larger diameter than the reference model) on: a) generated powers in vertical wells b) net generated power and produced power in the horizontal section over time.

For the second case, all sections' length and depth are incremented by 1 km compared to the reference model. Hence, sections I and III are 5 km deep, and section II is 5 km long.

As depicted in Fig. 4.9, even with the increase of the injection temperature (case 1), the extraction temperature is still lower than 100 °C. Meanwhile, raising the injection temperature brings on a lower generated power. However, case 2 (enlarging the CDG system geometry) is successful in maintaining the produced temperature above 100 °C over a period of one century. This success is due to accessing a hotter formation in the depth of 5 km. It is noteworthy that decreasing the flow rate leads to enhancing the produced temperature (as shown in Fig. 4.4) while the generated power reduces.

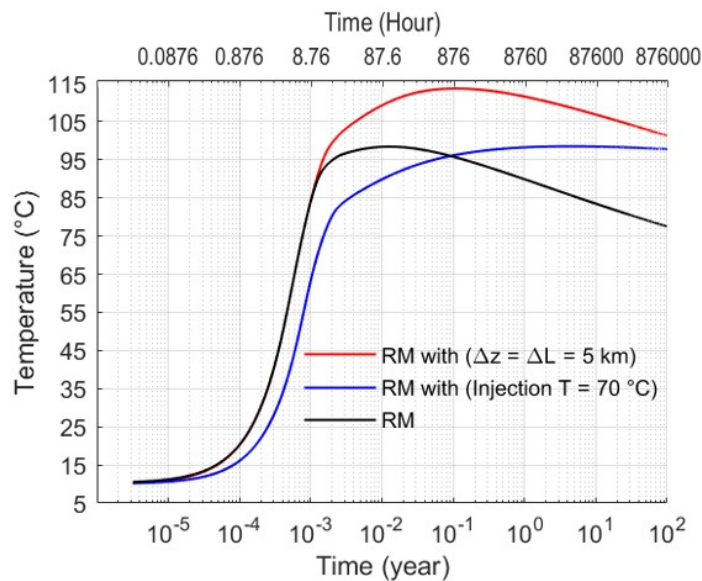


Fig. 4.9 Comparison between the impacts of injection temperature increment and system enlargement ($\Delta Z = \Delta L = 5$ km) on the extraction temperature of the reference model (RM and T stand for reference model and temperature, respectively). System enlargement is superior to the injection temperature increment to enhance the extraction temperature.

4.4 Thermosiphon flow assessments

The temperature difference across a CDG system, particularly wellhead, leads to a density difference since the circulating fluid EOS is temperature-dependent. Consequently, the existence of a heavier fluid in the injection well (section I) compared to a lighter fluid in the production well (section III) triggers the fluid circulation known as thermosiphon flow. This phenomenon can significantly decrease the required pumping power for the fluid circulation

in a CDG system, and it can potentially make the system independent of an external power grid.

Before operation, the temperature field was undisturbed with temperature profiles of injection and production wells being identical. An initial forced circulation is required to displace the residual fluid in the system, to create a temperature difference between sections I and III, and to trigger the thermosiphon flow. Accordingly, an initial period of ten days forced, pump-driven circulation was taken to establish the temperature contrast between the wellheads, necessary to trigger thermosiphoning. This thermosiphon flow is calculated by applying the "velocity postprocessor boundary condition" (see Section 4.2.1) taking the reference model as basis. The sensitivity analysis accounts for various factors that could impact the resistive forces on fluid circulating, such as surface pressure losses and system geometry.

4.4.1 Impacts of surface facilities pressure losses

The thermosiphon effect in CDG systems overcome pressure losses in both subsurface wells and surface facilities (e.g., heat exchangers, piping, etc.). The frictional pressure loss of the surface facilities, ΔP_s , is incorporated as a bulk pressure loss ranging from 0 *kPa* to 900 *kPa*. Fig. 4.10 illustrates that a thermosiphon flow rate of $Q_{TS} > 11$ L/s would be yielded after 100 years of the production even for the extreme case of $\Delta P_s = 900$ *kPa*. Over the lifetime of the system, although the temperature and density contrasts between the wellheads at sections I and III reduce, the thermosiphon effect will not weaken significantly. It is noteworthy that all operating flow rates assumed in Section 4.3 (i.e., 1 L/s, 5 L/s, and 10 L/s) are smaller than the lowest calculated thermosiphon flow rate of 11 L/s.

The optimum flow rate for the operation depends on power production, extraction temperature, and pumping power. The following assessment of thermosiphoning presumes that the pumps are shut-off and no pumping is required to circulate the fluid in the system, thus reducing the corresponding operation cost to zero. In the considered range of 1-10 L/s (Fig. 4.7) the produced thermal power increases with flow rate. Therefore, extraction temperature is the only limiting factor when determining an optimum valve-controlled flow rate. For example, operating with the valve-controlled flow rate of 5 L/s leads to the extraction temperature of ≈ 80 °C after 100 years of operation (Fig. 4.4).

4.4.2 Impacts of wellbores diameters and geometrical configurations

Similar cases of Section 4.3.2 are repeated for the simulation of the thermosiphon flow with $\Delta P_s = 900$ *kPa* (Case 1 is devised by subtracting 4" from the wellbore diameters of the

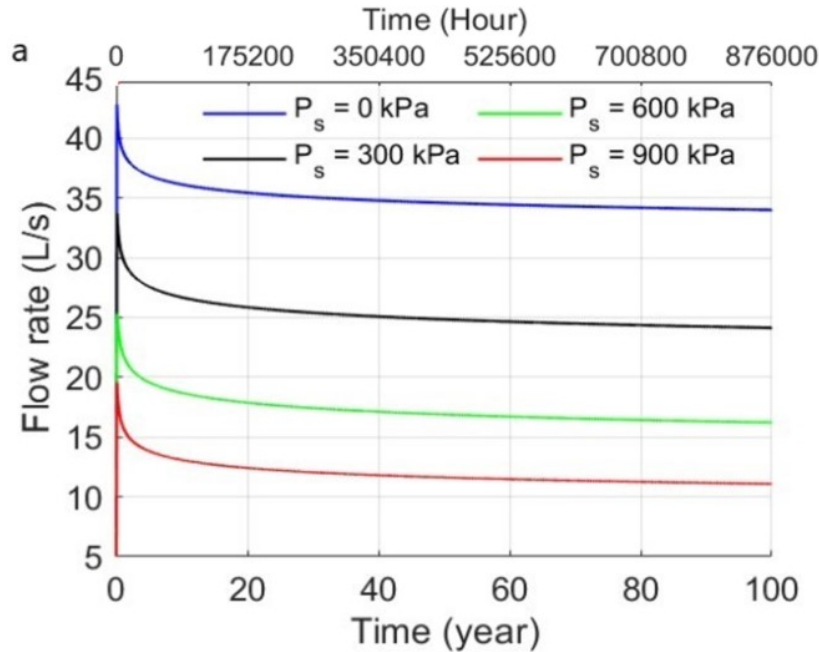


Fig. 4.10 Impact of pressure loss at surface facilities on the thermosiphon flow rate over time. In all the cases, the thermosiphon flow rate is stable over time. Even in the worse case, with the surface pressure loss of 900 kPa, the thermosiphon flow rate is higher than 11 L/s.

reference model (Fig. 4.2), while the wellbore diameters of case 2 are 4" larger than those of the reference model). As illustrated in Fig. 4.11, the case 2 setup generates a thermosiphon flow being twice as high as case 1. Nevertheless, the obtained Q_{TS} for case 1 is still sufficient to produce the desired T_{TS} since the flow rate for the Min $T_{TS} = 80$ °C should be less than 5 L/s (Fig. 4.4). Consequently, case 1 is economically beneficial due to the reliance of drilling cost on wellbore diameter (i.e., smaller wellbore diameter significantly reduces drilling expenses).

Irrespective of the wellbore diameter, the influence of the depth and horizontal length of a CDG system on the thermosiphon flow should be investigated. Hence, two systems with a total length of 12 km are considered to evaluate the impact of geometrical configurations on the thermosiphon flowrate. System 1 owns the same geometry as the reference model, while in system 2, the depth of sections I and III and the length of section II are 3 and 6 km, respectively. All other parameters are the same as the reference model. As depicted in Fig. 4.12, it is more beneficial to deepen the system rather than extending it horizontally because the deeper system gets access to hotter formation for the same subsurface temperature gradient. Operating With a system possessing a longer horizontal section enhances the heat extraction surface and increases the temperature difference between vertical wellbores. However, in the case of a deeper system, not only the heat exchange surface is more extensive, but also

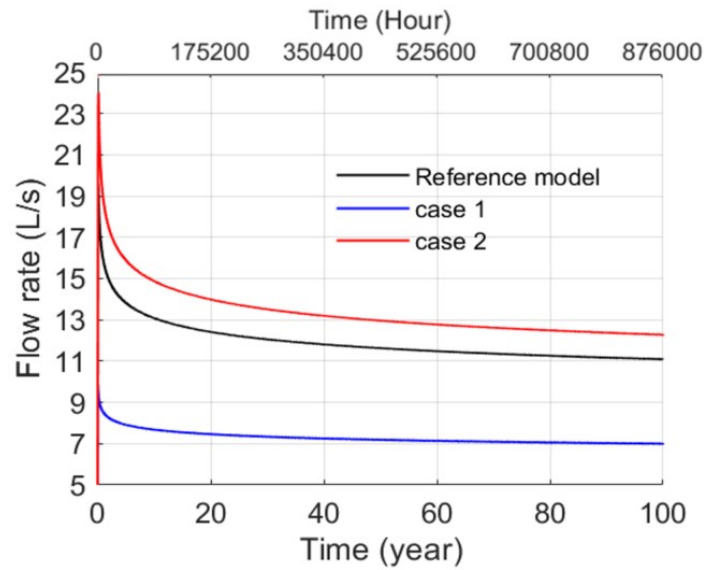


Fig. 4.11 Impact of wellbore diameter on the thermosiphon flow rate over time (case 1 - 4" smaller and case 2 - 4" larger diameter than the reference model). The case 2 setup (larger diameter) generates a thermosiphon flow being twice as high as case 1 (smaller diameter).

the system gets access to hotter formation for the same subsurface temperature gradient. Therefore, the thermosiphon flow rate increases significantly. While the thermosiphon flow rate is mainly influenced by the depth of the system, the magnitude and behavior of total generated power depend on the generated power in the horizontal wellbore (Fig. 4.7). Hence, it is not reasonable to ignore the importance of horizontal extension of the system. It is worth mentioning that in a real situation, the drilling costs/risks of both vertical and horizontal wellbores should also be taken into account to design the system appropriately.

4.4.3 Controlling thermosiphon flow

Operation with a high flow rate results in a low extraction temperature. As shown in Fig. 4.10, the lowest thermosiphon flow rate ($Q_{TS} = 11 \text{ L/s}$) is calculated for the highest surface pressure loss (900 KPa). Nevertheless, even for this small flow rate, the average extraction temperature is approximately 50 °C (Fig. 4.13a). It means the thermosiphon flow rate should be restricted to achieve a higher extraction temperature (T_{TS}). In other words, the thermosiphon flow rate should be controlled by a valve to produce hotter fluid, which is extremely important for dimensioning of a CDG system and identifying economically beneficial operational scenarios. As an example, a valve-controlled thermosiphon flow rate of 6.6 L/s for the case of ($\Delta P_s = 900 \text{ KPa}$) results in producing hot fluid with a temperature of higher than 70 °C over the project lifetime of a century (Fig. 4.13b). In this case, the

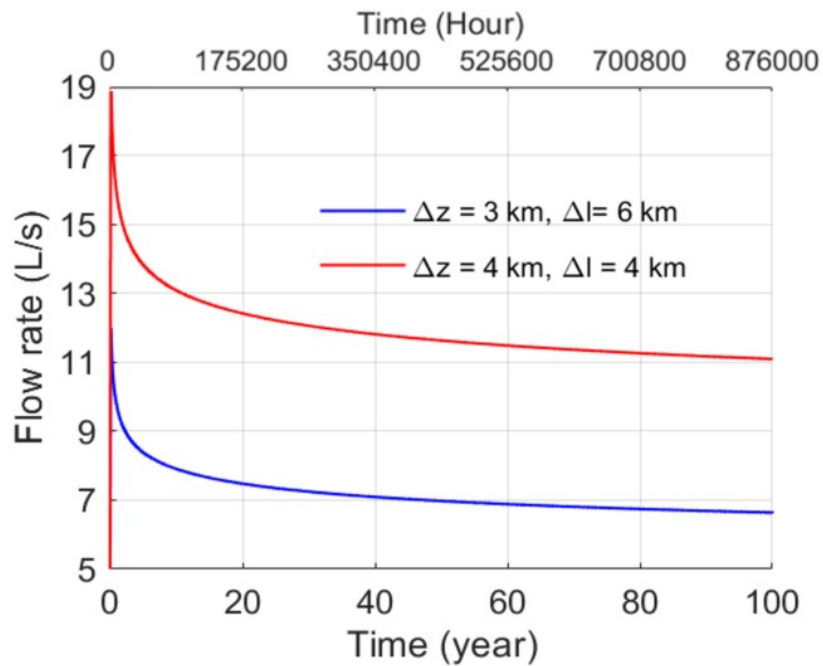


Fig. 4.12 Thermosiphon flow rates for various CDG configurations over time (ΔZ = depth of vertical wellbores, Δl = length of horizontal section). The total length of both systems is 12 Km.

control of the thermosiphon flow rate results in producing hot fluid at a meaningful flow rate and reasonable extraction temperature over a long period.

4.5 Discussion

In the last chapters, the CDG system's behavior for several operational and geometrical cases and the feasibility of the thermosiphoning are extensively presented. In this section, a CDG system is further evaluated and discussed to 1) maximize the generated power, 2) to decrease relative drilling cost, and 3) to enhance thermosiphon flow.

4.5.1 The CDG system geometry

Decreasing the total length and wellbore diameters of a CDG system certainly result in a considerable reduction of relative drilling costs. Based on results, the reduction of wellbores diameters has negligible impacts on the generated power, as well as a sufficient flow rate can still be generated in the case of the thermosiphon flow. However, accessing a hotter underground for the horizontal section through a deeper system is extremely important since the net generated power mimics the behavior of the generated power in the this section.

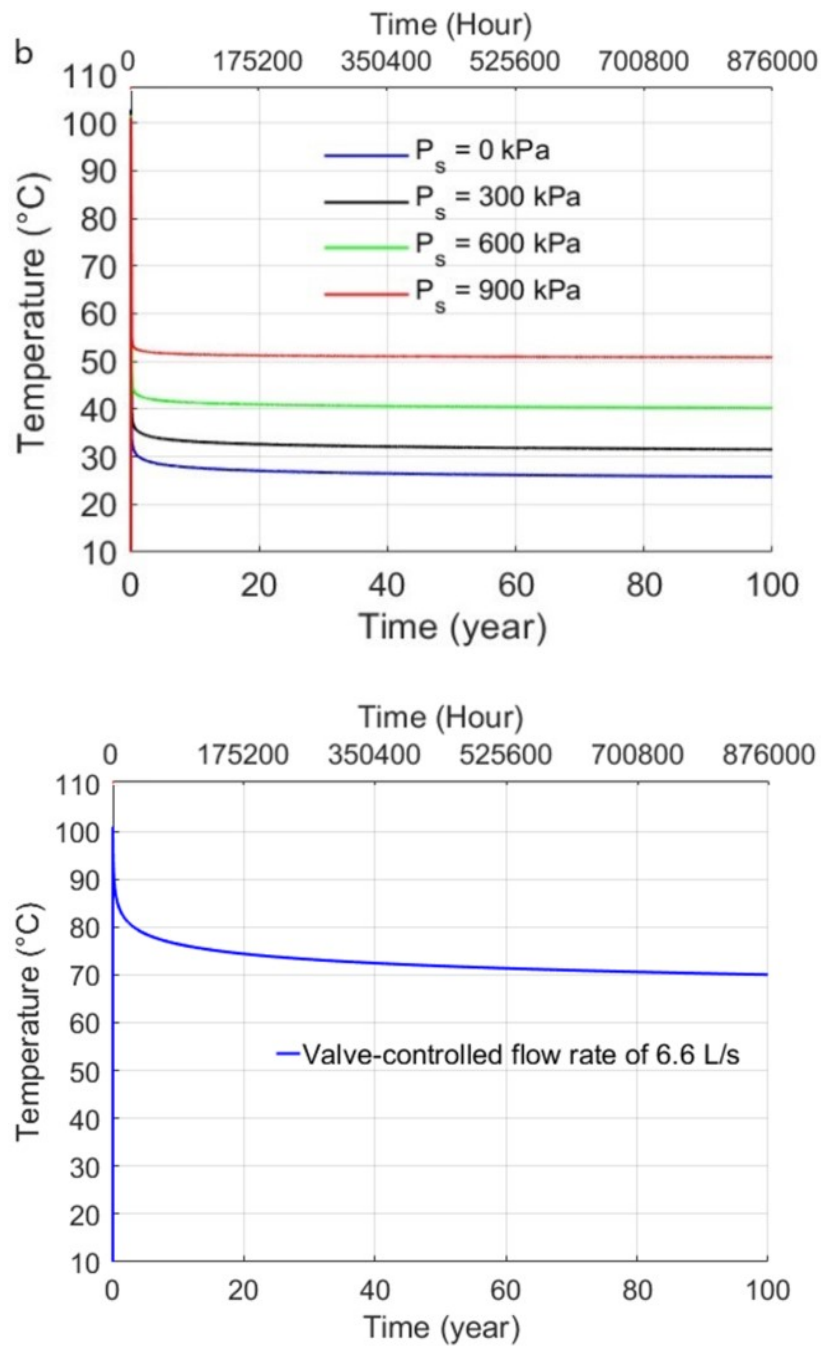


Fig. 4.13 a) Corresponding extraction temperatures for the flow rates of Fig. 4.10 and b) calculated extraction temperature for the valve-controlled flow rate of 6.6 L/s and surface pressure loss of 900 kPa.

Meanwhile, different geometrical configurations should be individually analyzed since it is significantly dependent on geological settings which is unique for every project.

Operating in a region with a higher subsurface temperature gradient is associated with a higher production temperature and generated power. By assuming the reference model conditions, three models with different subsurface temperature gradients of 30, 35, and 40 °C/km are simulated. By increasing the subsurface temperature gradient of the reference model, the circulating fluid temperature is higher at the end of section II (Fig. 4.14). However, the fluid loses/gains in section III higher heat compared to the cases with a lower subsurface temperature gradient. Therefore, this leads to the fact that TAEM changes in section III at the same location in all cases resulted in the independence of the insulation layer's length from the subsurface temperature gradient.

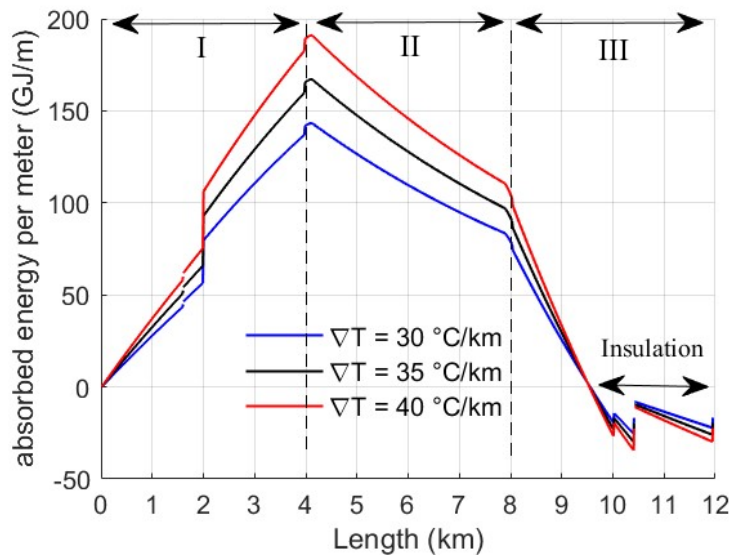


Fig. 4.14 Impact of subsurface temperature gradient on the cumulative absorbed energy per meter of the CDG system after 100 years of operation. The locations with negative absorbed energy should be insulated to avoid heat loss. The jumps of the absorbed energy at different points are explained in Section 4.2.3 and Fig. 4.3.

Similarly, three models (case 1, 2, and 3) with different thermal conductivities of 2, 3, and 4 $Wm^{-1}K^{-1}$ for the lower formation are simulated by assuming the reference model conditions. In contrast to the subsurface temperature gradient, formation thermal conductivity has a major impact on the length of the insulation layer (Fig. 4.15). Operating in a region with a high thermal conductivity necessitates extending the insulation layer. Therefore, geological settings, particularly thermal conductivity, have direct impacts on the insulation layer length, which influences the drilling costs.

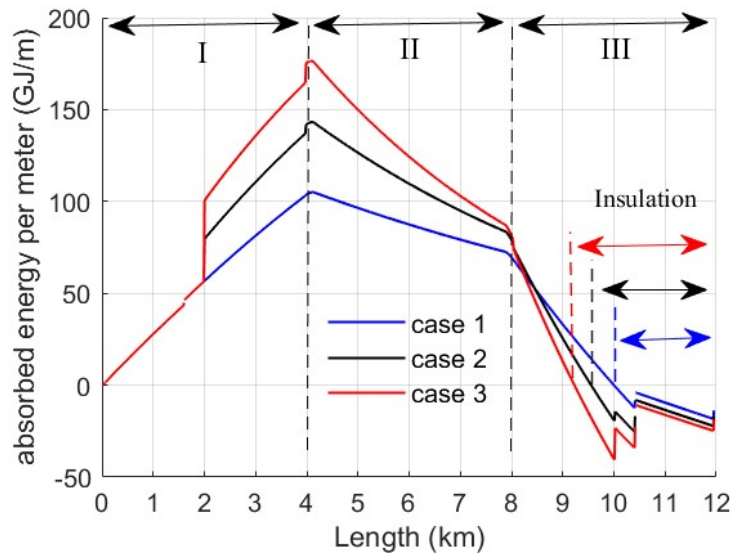


Fig. 4.15 Impact of formation thermal conductivity on the total absorbed energy per meter of the CDG system after 100 years of operation. Thermal conductivity of the upper layer is $2 \text{ Wm}^{-1}\text{K}^{-1}$, and Thermal conductivities of the lower layer for case 1, 2, and 3 are 2, 3, and $4 \text{ Wm}^{-1}\text{K}^{-1}$, respectively. The locations with negative absorbed energy should be insulated to avoid heat loss. The jumps of the absorbed energy at different points are explained in Section 4.2.3 and Fig. 4.3.

In general, decreasing the fluid velocity in the production well (section III) and achieving a higher temperature of the circulating fluid at the end of the horizontal well (section II) increase the insulation layer's length. Accordingly, the following scenarios increase the temperature of the fluid entering the production wellbore and extend the length of the insulation layer:

- Increasing inlet temperature
- Decreasing flow rate
- Deepening the system
- Extending horizontal section

4.5.2 System's longevity and sustainability

Commonly, the scenarios that maximize heat loss in the production wellbore can improve the system's longevity. Although the heat loss in section III decreases the rate of heat extraction from the system, it warms up the surrounding section III, leading to the stabilization of the

production temperature. For example, raising the inlet temperature can prevent the production temperature drop over time (Fig. 4.9), but it decreases the net generated power dramatically.

4.5.3 Thermosiphoning and drilling costs

A proper design of the CDG layout significantly enhances the thermosiphon flow. However, it may increase the drilling costs concurrently. For instance, deepening the CDG system, extending the length of the horizontal well, and enlarging wellbore diameters enhance the thermosiphon flow (Figs. 4.11 and 4.12). Nonetheless, all of these cases result in additional drilling costs. Additionally, the generated thermosiphon flow in this study was always greater than the optimal flow rate required for district heating purposes. For the district heating, both high extraction temperature and high generated power are required. The results of our simulation (Figs. 4.4 and 4.7) revealed that the flow rate of roughly 5 L/s yields approximately 1.5 MW power with the extraction temperature of 80 °C. In the other hand, more effective insulation also results in increasing the thermosiphon flow. Therefore, it is more beneficial to better insulate the system rather than enlarging it to achieve higher thermosiphon flow.

4.5.4 Production pressure and operational energy

As explained in Section 4.3, extending the total length of the system (case 2 in Section 4.3) is more beneficial than re-injection of hot fluid to enhance the production temperature and generated power (Fig. 4.9). Fig. 4.16 proves that case 2 is also advantageous for increasing the pressure gradients between wellheads, and it can enhance the thermosiphon flow. This is highly important when the operating flow is higher than the thermosiphon flow leading to the reduction of the operational energy (cost) because of the less required pumping power.

4.5.5 Production well diameter impacts

Changing wellbore diameter considering a constant flow rate leads to the increase/decrease of the circulating fluid velocity, which influences the heat exchange rate dramatically, as explained in Section 4.3.1. Based on the results, it is expected that larger wellbore diameters in sections I and II and a smaller wellbore diameters in section III should improve the performance of a CDG system. To testify this expectation, the reference model is modified by subtracting 4" from the diameters in section III, while the diameters of sections I and II remained unchanged, and the flow rate of 1 L/s is simulated. Fig. 4.17 and Fig. 4.18 show the impact of decreasing production wellbore diameter on the extraction temperature/pressure.

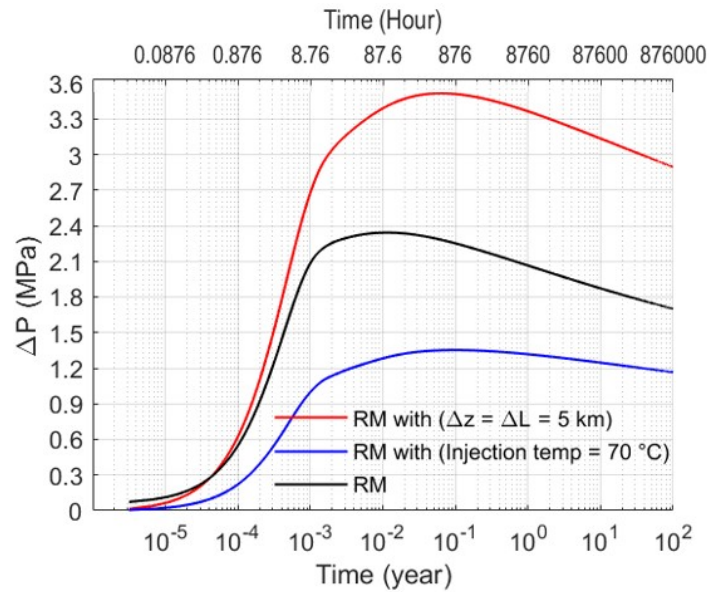


Fig. 4.16 Comparison between the effects of inlet temperature increment and system enlargement ($\Delta Z = \Delta L = 5$ km) on the extraction pressure of the reference model (RM stands for reference model). System enlargement is superior to the injection temperature increment to enhance thermosiphoning.

As expected, the production temperature increased about 5°C , but the production pressure is surprisingly enhanced even considering a higher friction loss due to a higher velocity in section III. Production temperature enhancement escalates the mean temperature difference and density contrast between vertical wells (sections I and III). The difference between weights of vertical water columns increases the extraction pressure, while the pressure loss due to friction reduces it. By decreasing the production wellbore diameter, the larger density contrast prevails the incremented friction loss. Consequently, the extraction pressure enhances. This pressure gradient improvement is also beneficial for the case of the thermosiphon flow since a higher excess pressure is available at the outlet for the fluid circulation.

4.6 Conclusion

Our investigation indicates new insights to forecasting CDG behavior by state-of-the-art numerical simulations considering the coupling of mass, momentum, and energy conservation equations with an appropriate equation of state (EOS) and analytical lateral heat model. Novel approaches were proposed to make the CDG system a strong competitor to other conventional geothermal systems.

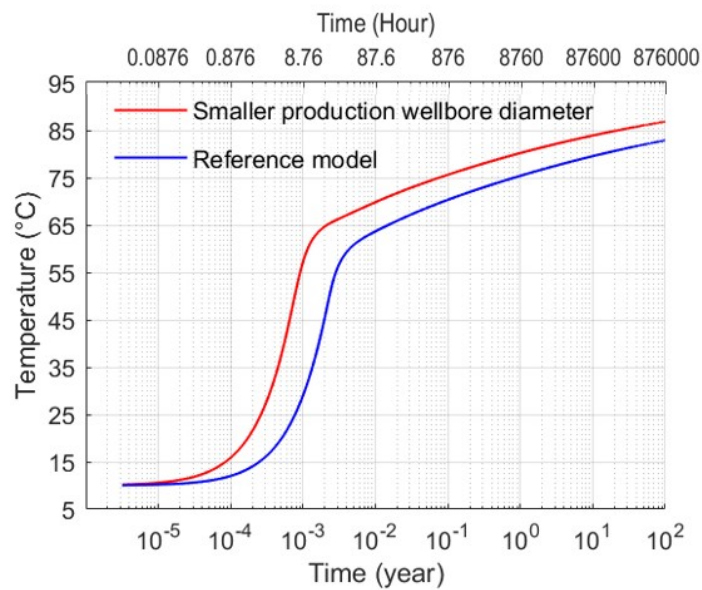


Fig. 4.17 Impact of decreasing production wellbore diameter on the production temperature over time. The smaller wellbore diameter leads to a higher extraction temperature over time.

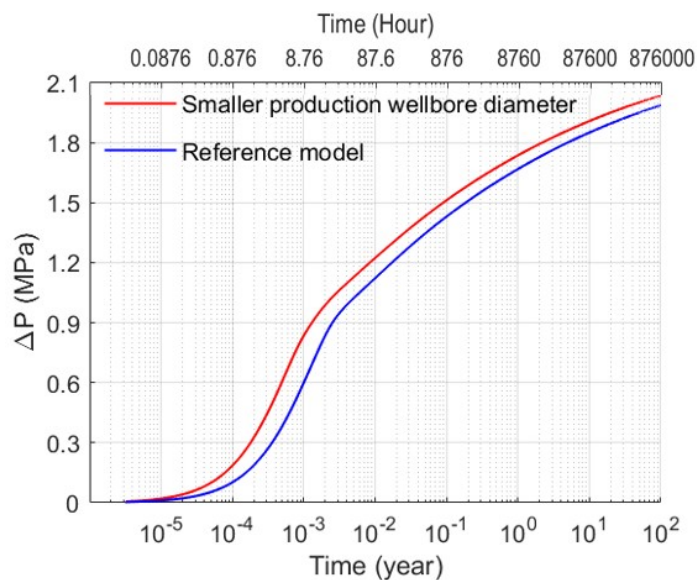


Fig. 4.18 Impact of decreasing production wellbore diameter on the production pressure over time. The smaller wellbore diameter leads to a higher pressure difference between injection and extraction points.

As addressed by Budiono *et al.* [130], drilling cost is the main hurdle limiting the contribution of CDG systems to green energy generation. Our simulations allow to advance this knowledge and to identify beneficial factors for increasing the economic efficiency of CDG systems. One of these novel approaches was the evaluation of natural thermosiphon flow for fluid circulation that will significantly reduce the pumping energy. Also, the conditions for stability of thermosiphon flow under various pressure losses at surface facilities and geometrical configurations are demonstrated for the first time. The results are important as the two factors "high extraction temperature" and "stable thermosiphon flow rate" enable a cost-efficient power generation. Unique contributions are provided to the casing program and to the conceptual scheme to determine an optimum length of insulation.

Operation with CDG systems is associated with a rather stable production temperature over a span of a century. This effect was evaluated under various geometrical configurations (e.g., wellbore diameter) and operational parameters (e.g., flow rate). Also, thermosiphon flow generation can be considered a typical behavior of CDG systems. This flow could even be valve-controlled but has restrictions in geometry. Finally, various operational scenarios, as well as system configurations, are elaborately discussed to enhance the system's longevity, to decrease pumping energy, to increase extracted power, and to diminish drilling costs.

The key findings of this study are summarized as:

1. In general, the CDG system presented in this study is capable of generating thermosiphon flow. Several case studies considering different parameters and configurations were evaluated. Even in the most extreme condition of the pressure loss in surface facilities (900 kPa), the triggered thermosiphon flow rate of the 12 km long reference case is higher than 11 L/s. Operating this flow can result in the production of approx. 2 MW thermal power at an average extraction temperature of 50 °C. Restricting this flow rate to 5 L/s increases the average extraction to approximately 80 °C. Thermosiphon flow rate is highly geometry sensitive. A shallower 3 km depth system (but identical total borehole length) results in 66 % of the thermosiphon flow rate of the 4 km deep reference case. Reduced diameters results in a considerable lower thermosiphon flow rate. As such a reduction of 4" lowers the flow rate by 4 L/s due to higher friction losses.
2. A prolonged thermal exchange duration and a convenient convective heat transfer factor can avoid the huge temperature drop along all wellbores over time, and they also stabilize the extraction temperature. While operating with a flow rate of 10 L/s results in 12 °C extraction temperature drop over the project lifetime (67 °C after the first year, 55 °C after 100 years), the flow rate of 1 L/s yields 9 °C temperature increment

over this period (75 °C after the first year, 84 °C after 100 years). Consequently, it was shown that not only the extraction temperature doesn't reduce considerably over time, but also the generated power and production temperature continuously enhance over a project lifetime of one century. Therefore, an appropriate adjustment of CDG systems results in considerable enhancement of system's longevity and preventing the initial extraction temperature drop, which is the major limitation in utilizing closed geothermal systems.

3. It is demonstrated that the reduction of the production well diameter enhances the extraction temperature through the increase of the circulating fluid velocity and the reduction of heat loss in this section of the CDG system. Subtracting 4" from the production wellbore diameter of the reference case increases the extraction temperature by 5 °C. It is also helpful for the generation of the thermosiphon flow, which is a function of temperature/density contrast between vertical wells. Consequently, the decrease of production wellbore diameter reduces the relative drilling costs, improves power production, and diminishes the energy required for pumping the fluid.
4. It is disclosed that the insulation length in the production well is absolutely dependent on geological settings. The increase of the thermal conductivity of the lower geological layer from 2 to 4 $Wm^{-1}K^{-1}$ raises the optimum insulation length from 2 km to 2.8 km. Nevertheless, insulation extension is independent of the subsurface temperature gradient, assuming the same geometrical configuration and operational parameters (i.e., flow rate, injection temperature, and pressure). For all the subsurface temperature gradients of 30, 35, and 40 °C/km, the optimum insulation length is 2.5 km. Therefore, operating in regions with higher subsurface temperature increases the power production temperature and net generated power without the necessity of extending the insulation layer.

CDG systems certainly have a good perspective in urban areas. They should be considered as a long-term investment, providing energy to domestic heat systems or district heating grids over a period of more than 100 years. CDG systems could be enhanced by multi-lateral structures to scale up the generated power and decrease the ratio of extracted energy to the total length of the system. The herein presented analysis of thermal power production in vertical and horizontal wellbore sections will be further advanced for the design of multilateral CDG systems.

4.7 Acknowledgment

The study is part of the subtopic "Geoenergy" in the program "MTET - Materials and Technologies for the Energy Transition" of the Helmholtz Association.

Chapter 5

Stochastic performance assessment on long-term behavior of multilateral closed deep geothermal systems

This chapter is published in Renewable Energy, <https://doi.org/10.1016/j.renene.2023.03.074>

Abstract

Increasing the contribution of geothermal systems to green energy generation requires designing new innovative systems producing a significant amount of thermal power in a sustainable manner. The focus of this study is the performance evaluation of multilateral closed deep geothermal (MCDG) systems as a novel environmentally friendly approach for energy extraction from earth. The investigations on these synthetic systems assume a probabilistic number of borehole sections with several vertical and horizontal wellbores connected through some manifolds and doglegs. To reduce possible thermal losses, the circulated fluid is extracted through only one production wellbore. The findings of this study demonstrated that the heat absorption per meter of MCDG systems is much higher than for simple closed geothermal systems (CDG). Operating with these systems will not necessarily yield better performance. It is also found that the long-term performance of MCDG systems can be predicted as a function of their short-term behavior through stochastic analysis. This correlation is interestingly independent of the number of wellbores and flow rate. By defining specific criteria, the high-performance MCDG systems can be filtered to demonstrate common features as a specific relation between flow rates per vertical and horizontal wellbores. This characterization of MCDG systems should support the design of future high-performance systems.

5.1 Introduction

Utilizing geothermal energy is a clean and sustainable way of supplying thermal energy required for district heating purposes [138, 148, 137]. In contrast to other renewables (e.g., solar and wind energy), geothermal energy - extracted from the earth through open and closed systems - provides baseload power available throughout the whole year [149]. Open systems are characterized by the direct contact between circulating fluid and hot rock, while faults and fractures provide extensive heat exchange surfaces and enhance the capability of these systems for extracting a large amount of thermal power [92, 90, 99]. These systems need to be managed with care not to harm the environment or to create induced seismic events [150–152]. Fluid circulation in closed geothermal loops prevents the potential hazards [86], but the generated thermal power is much lower, making it difficult to respond to the total heating demand. Increasing the contribution of geothermal energy to the global renewable capacity necessitates developing new innovative systems that combine the advantages of both open and closed systems. Optimizing the generated thermal power of closed systems requires a specific design of possible geometries and wellbore diameters to enhance the lateral heat exchange area and the heat absorption rate. However, these conditions often conflict with economic considerations. Herein, pathways are demonstrated to maximize energy extraction from closed geothermal systems.

In the previous study conducted by the authors of this study [85], the power production feasibility of closed-loop deep geothermal (CDG) systems with a lengthy horizontal extension was assessed. It is disclosed that a CDG system can produce an average thermal power of $2 MW_t$, nearly constantly over 100 years (continually) only supported by the thermosiphon effect. The longevity of this system (i.e., stability of extraction temperature over time) is also much better than those of open geothermal systems [85]. In spite of the relatively large power generation of CDG systems, their economic feasibility suffers from the small ratio of produced thermal power per length of the drilled wellbores. This could extend the payback period and may discourage the interest of investors in these closed systems. Now, this study investigates possible novel solutions for multilateral CDG (MCDG) systems, to increase the ratio of generated thermal power to the total length of the system by introducing several (parallel) injection and horizontal wellbores.

The performance of open multilateral systems has been evaluated in recent studies [131, 153–155]. However, to the best of our knowledge, assessment of the reliability of closed multilateral frameworks for district heating purposes is rarely addressed in the literature. Professional companies are already proposing to install multilateral structures without revealing details of their projects. In 2020, Wang *et al.* [156] investigated the production characteristics of various coaxial closed-loop geothermal systems (CCGS), leading to po-

tential thermal power production of $3.05 MW_t$, which is remarkably higher than those of single vertical and horizontal coaxial systems. Nevertheless, producing roughly $3 MW_t$ power hardly compensates for the drilling expenses of a deep multilateral system possessing a vertical section with a depth of $4500 m$ and several horizontal wellbores with lengths of $2000 m$. In another study [106], they tried to analyze the heat extraction mechanism of the CCGS. Based on their investigations, the reservoir temperature has a considerable effect on the heat extraction process that mainly occurs in the lateral wellbores of a multilateral CCGS. Since they take a formation temperature of $236\text{ }^\circ\text{C}$ at $3750 m$ depth (i.e., assuming temperature gradients of approx. $0.06\text{ }^\circ\text{C}/m$), it is difficult to generalize the results of this study to other thermal situations.

Although few studies evaluated the performance of multilateral closed systems, they only focused on coaxial structures. However, as mentioned before, the required large wellbore diameter, heat absorption by steel connectors, difficulties in the deepening of the wellbores, and the limited range of generated thermal power are the main disadvantages of the multilateral CCGS. Therefore, MCDG systems seem to be more reliable, practical, and efficient rather than the multilateral CCGS. The present investigation of MCDG systems contributes to the existing body of knowledge having a nearly probabilistic number of borehole vertical and horizontal wellbores sections:

1. A total of 160 geometries are taken to identify a meaningful correlation between the long-term performance of MCDG systems and their short-term behavior independent of the number of wellbores and flow rate. The provided stochastic analysis forecasts the probability of various outcomes (i.e., extraction temperature, generated thermal power, and specific power) under different conditions, using random variables. In this analysis, the randomness is attributed to more than one arbitrary variable (i.e., flow rate and the number of wellbores).
2. Several measures, such as the ratio of produced thermal power to the equivalent total length (i.e., simplified/normalized indicator for drilling expenses), are introduced to evaluate the MCDG system's performance compared to CDG systems. The unbiased realistic attitude of this research project toward the concept of multilateral closed loops helps to choose between CDG and MCDG systems for producing a particular amount of thermal power at a specific flow rate.
3. Based on extraction temperature and the ratio of generated thermal power to the equivalent total length, criteria are defined to optimize the operation/construction planning. The successful cases shall facilitate the design of future high-performance MCDG systems.

To achieve these objectives, the thermal transfer between different components of the system (i.e., circulating fluid, cement layer, casing, and formation) is accurately simulated. This advanced numerical modeling comprises of full coupling of mass, momentum, and energy equations, implementing equations of state (to account for variations of fluid density and viscosity as functions of pressure and temperature), modeling conductive heat transfer in a formation with the energy exchange inside the wellbores using an analytical radial heat exchange model, and superposing the lateral wellbores to decrease the computational cost.

5.2 System description

The extraction temperature of CDG is proportional to the heat output produced, but inversely proportional to the flow rate. Based on the previously conducted research by Esmailpour *et al.* [85], the highest possible amount of produced thermal power is smaller than $2 MW_t$, when operating with a CDG system possessing a total length of $12 km$. Nevertheless, a larger heat exchange area can enhance the heat utilization capacity of the system and allows for operating with higher flow rates. Therefore, designing multilateral closed deep geothermal systems could be a suitable alternative to extending lateral heat exchange surfaces. In the following section, the structure of MCDG systems, introduced in this study, is elaborately explained.

5.2.1 General description of MCDG system

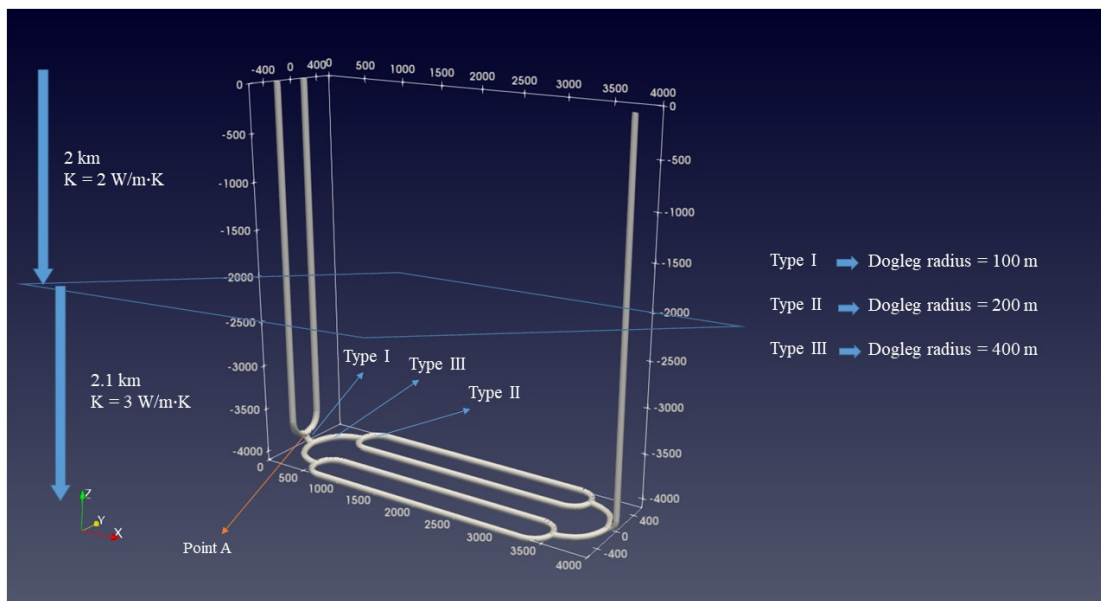
As shown in Fig. 5.1a, MCDG systems can possess several deep injection wellbores, which are joined through doglegs (a manifold) at a particular depth (Fig. 5.1a, point A). In a multilateral framework, it is important to maintain sufficient wellbore separation to prevent thermal interference between the different branches. Thermal interference can occur when the flow of working fluid from one branch of the system affects the temperature of the fluid in another branch, which can reduce the overall efficiency of the system. The optimum distance between these parallel wellbores is a function of time, thermo-physical properties, and temperature difference between wellbore and formation. The injected fluids through vertical wellbores are initially collected at these doglegs and then redistributed in horizontal wellbores. The total injected fluid is finally extracted through only one production wellbore. The uniform alteration of all the wellbores' diameters can change the heat exchange surface, cross-sectional area, fluid velocity, and convective heat transfer factor. However, it doesn't have a significant impact on the extraction temperature and generated thermal power [85]. So, it is reasonable to construct the system with small wellbore diameters ranging between 4" and

12" to decrease the relative drilling expenses. Nevertheless, operating with a smaller wellbore diameter increases the pressure loss due to friction. In order to avoid subsurface water contamination and preserve the system's integrity, the injection and production wellbores (i.e., vertical sections of the system) are equipped with several casings and cement layers. However, horizontal wellbores are sealed with some chemicals and directly exposed to hot formation [129]. Consequently, the circulating fluid experiences a greater pressure loss due to the larger friction factor of this section. However, this special design increases the leakage probability through the horizontal wellbores. Nevertheless, direct exposition to hot formation enhances the heat exchange rate dramatically as the thermal conductivity of the formation is much higher than that of cement. The conductive energy exchange between the circulating fluid and its surrounding area depends on the number of layers around the wellbore and their thermal conductivities. Embedding some cement layers with low thermal conductivity between the wellbore and its adjacent formation restricts thermal interaction severely. Therefore, removing casings and cement layers from the wellbore structure increases the overall thermal conductivity and heat absorption rate. As a result, this new devise of the system makes it feasible to capture a higher extraction temperature and improves thermal power generation. The circulating fluid exchanges energy with the wellbore completion system through convective heat transfer. This type of energy exchange depends on the fluid velocity. A higher fluid velocity increases the Reynolds and Nusselt numbers and considerably enhances the heat extraction rate.

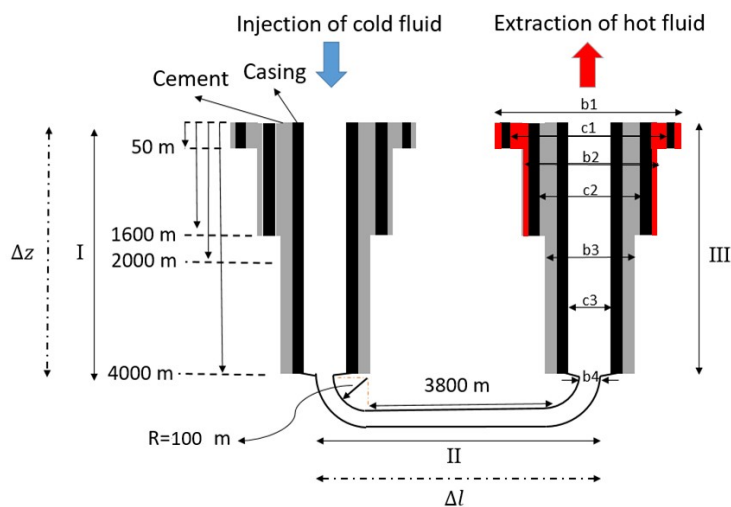
5.2.2 Applied geological setting and geometrical configuration

In all the simulations of this study, the depth of the system is 4.1 km which includes the length of vertical wellbores and the depth of doglegs. The injection and production wellbores are located in two parallel plates, which are 4 km away from each other (Fig. 5.1a). The MCDG system can possess 1, 2, 4, and 8 injection/horizontal wellbores that indicates the range of randomness for the number of wellbores in the stochastic analysis. This randomness is not attributed to the number of production wellbores as in all the simulations of this study only one production wellbore is included in the MCDG systems' structure. In order to preserve the 200 m distance between the parallel wellbores in both vertical and horizontal sections, they are connected to each other through some doglegs with radiuses of 100 m (type I), 200 m (type II), and 400 m (type III). This optimum distance (200 m) is calculated through analytical analysis [16] and some numerical simulations [99]. The casing program of vertical wellbores is addressed in Fig. 5.1b.

The thermal conductivities of casing, cement layer, and insulation material (urethane fiberglass) are $100 \text{ W} \cdot \text{M}^{-1} \cdot \text{K}^{-1}$, $0.7 \text{ W} \cdot \text{M}^{-1} \cdot \text{K}^{-1}$, and $0.021 \text{ W} \cdot \text{M}^{-1} \cdot \text{K}^{-1}$, respectively



(a)



(b)

Fig. 5.1 Schematics illustrating a) depth of MCDG systems, length of horizontal section, doglegs and manifolds structure, and wellbores configuration b) casing program of a simple CDG system ($b_1 = 22''$, $c_1 = 18 \frac{5}{8}''$, $b_2 = 17''$, $c_2 = 13 \frac{5}{8}''$, $b_3 = 12 \frac{1}{4}''$, $c_3 = 9 \frac{5}{8}''$, $b_4 = 8 \frac{3}{8}''$). $b, c, \Delta z$, and Δl stand for borehole diameter, casing inner diameter, depth of vertical wells, and total horizontal length, respectively. The horizontal section is directly exposed to hot formation. The same casing program is used for MCDG systems. The area highlighted by red color shows insulation.

[147]. The formation density is also supposed to be $2400 \text{ kg} \cdot \text{m}^{-3}$. The roughness of the inner casing in vertical wellbores is 10^{-4} m . However, due to the lack of casing in horizontal wellbores, the roughness of this section is assumed to be $2 \times 10^{-4} \text{ m}$ [146]. Two geological units with a depth of 2 km and 2.1 km comprise the formation that surrounded the system (Fig. 5.1a). The thermal conductivities of the upper and lower layers are $2 \text{ W} \cdot \text{M}^{-1} \cdot \text{K}^{-1}$ and $3 \text{ W} \cdot \text{M}^{-1} \cdot \text{K}^{-1}$, respectively. The underground ambient temperature gradient is set to be $30 \text{ }^\circ\text{C}/\text{km}$, and the surface temperature is $10 \text{ }^\circ\text{C}$. Therefore, the undisturbed temperature in the deepest point of the system (4.1 km) is $133 \text{ }^\circ\text{C}$ ($10 \text{ }^\circ\text{C} + 4.1 \text{ km} \times 30 \text{ }^\circ\text{C}/\text{km} = 133 \text{ }^\circ\text{C}$).

5.3 Methodology

Accurate numerical modeling of MCDG systems should include a detailed description of energy exchange between wellbore and formation, heat transfer in formation, and transient processes in wellbores. Fluid flow inside the inner casing undergoes several coupled physical processes, such as pressure loss due to friction, kinetic energy alteration [139, 140], temperature variation due to heat exchange with surrounding formation, velocity changes influencing pressure and temperature fields, and buoyancy effect because of variation of fluid density. In order to appropriately simulate these complex physical processes in a wellbore, a finite element code, called MOSKITO [86, 141], is developed in the MOOSE (Multiphysics Object-Oriented Simulation Environment) Framework [84, 142]. The capability and validity of this solver to model fluid flow and heat transfer in closed deep geothermal systems are assessed in another research project carried out by the authors of this study [85].

5.3.1 Governing equations

A non-isothermal transient flow in a pipe is governed by these equations [143]:

Continuity equation:

$$\frac{\partial}{\partial t}(\rho) = -\frac{\partial}{\partial z}(\rho v) + m \quad (5.1)$$

where ρ and v represent density and velocity of fluid, and m is the mass sink/source term in unit volume and unit time.

Momentum equation:

$$\frac{\partial P}{\partial z} = \rho g \cos(\theta) \pm \frac{f \rho v^2}{2d} \pm \left(\frac{\partial}{\partial t}(\rho v) + \frac{\partial}{\partial z}(\rho v^2) \right) \quad (5.2)$$

where P, g, θ, f , and d refer to fluid pressure, gravitational acceleration, the inclination of the well, friction factor, and wellbore hydraulic diameter, respectively. The sign of the right-hand side terms in the momentum equation depends on flow and gravity directions.

Energy equation:

$$\frac{\partial}{\partial t} \left[\rho \left(h - \frac{P}{\rho} + \frac{1}{2}v^2 \right) \right] = -\frac{\partial}{\partial z} \left[\rho v \left(h + \frac{1}{2}v^2 \right) \right] + \rho v g \cos(\theta) - \frac{q}{A} + Q \quad (5.3)$$

where h, q and Q show the enthalpy, radial heat flow, and heat sink/source terms, respectively.

The main variables (i.e., flow rate, pressure, and enthalpy) are calculated by solving Eqs. 5.1 to 5.3. Some constitutive relationships / empirical equations, including viscosity, density, and the friction factor, are also required to solve these equations. The Vogel Equation [157] is used to calculate viscosity. Additionally, an empirical equation of state (EOS) [145] is implemented to compute the fluid density as a function of pressure, temperature, and salinity of the fluid (saline water).

Using a special radial heat exchange model makes it possible to simulate the heat exchange between the wellbore and its adjacent formation with a low computational cost. Based on this model, the radial heat flow can be calculated by:

$$q = 2\pi r_{to} U_{to} (T_f - T_{cf}) \quad (5.4)$$

where r_{to}, U_{to}, T_f and T_{cf} indicate the outside radius of the inner tubing, the overall heat transfer coefficient, the fluid temperature, and the temperature at the cement/formation interface, respectively. For a detailed explanation, refer to Willhite [17].

5.3.2 Numerical modeling

Modeling several branches of MCDG systems can cause the simulation time to increase significantly. However, it should be taken into account that these lateral wellbores show a similar thermal/hydraulic behavior. Therefore, it is possible to simulate fluid flow and heat transfer for only one branch and assume the same pressure, temperature, and flow rate along other lateral wellbores. In order to apply this kind of superposition, a particular boundary condition is implemented, which receives the main variables at the end of the simulated branch in each time step and imposes the same pressure and temperature at the beginning of the subsequent section in the next time step. The boundary condition for the flow rate is also computed by the total volumetric flow rate divided by the number of branches.

The initial fluid temperature is set to be the same as the formation temperature, believing in an equilibrium thermal condition between residual fluid and its surrounding environment.

The initial pressure condition is hydrostatic. Furthermore, Dirichlet boundary conditions with fixed values are imposed at the injection point for all variables. The injection temperature and pressure are 10 °C and 1 MPa, while the flow rate can take values between 5 and 50 L/s (i.e., range of flow rate randomness in the stochastic analysis), which will be mentioned for each simulation case.

A sensitivity analysis for three spatial discretizations ($\Delta x = 14\text{ m}$, $\Delta x = 11\text{ m}$, and $\Delta x = 7\text{ m}$) was conducted to confirm that the solution is mesh-independent. Evaluation of pressure and temperature fields over the length of the wellbores revealed the negligible impact of implemented mesh sizes on the results. The maximum variation of pressures and temperatures over their absolute values is less than 6×10^{-6} when changing the mesh size from 7 m to 14 m. Therefore the mesh size of 14 m was selected for the simulations to decrease the computational time. It is worth noting that increasing the mesh size to 25 m and 50 m leads to a greater relative variation in the main variables, up to 2×10^{-4} and 3×10^{-3} , respectively. The time steps gradually increase from 100 seconds to one month to provide a better convergence initially ($\Delta t = 100\text{ S}$) and subsequently decrease the simulation time ($\Delta t = 1\text{ month}$). The combination of superposition, reasonable time-stepping, and proper spatial discretization decreases the simulation time. Consequently, it takes less than 20 minutes to simulate 100 years of operation of an MCDG system using a host PC with a 4-core CPU (Intel(R) Core(TM) 2 Quad) at 2.3 GHz.

5.4 Stochastic analysis of the MCDG system's long-term behavior

An accurate stochastic analysis of the system's long-term behavior supports the future design of high-performance MCDG systems and reduces the computational cost. Therefore, the main focus of this section is to find a meaningful correlation between long-term and short-term behaviours (values) of extraction temperature and generated thermal power as primary indicators of the system's performance. For this purpose, the behavior of 160 MCDG systems with 10 different flow rates (i.e., first arbitrary variable) and 16 various wellbore configurations (second arbitrary variable) is evaluated. As mentioned before, the flow rate randomness can range between 5 L/s and 50 L/s, while the number of vertical/horizontal wellbores can be 1, 2, 4, and 8.

Fig. 5.2 illustrates the extraction temperature and pressure in a simple CDG system with a depth of 4.1 km, horizontal length of 4 km, and flow rate of 5 L/s. Comparing Fig. 5.2a and Fig. 5.2b, it is evident that the overpressure ($\Delta P = P_{\text{extraction}} - P_{\text{injection}}$) tracks

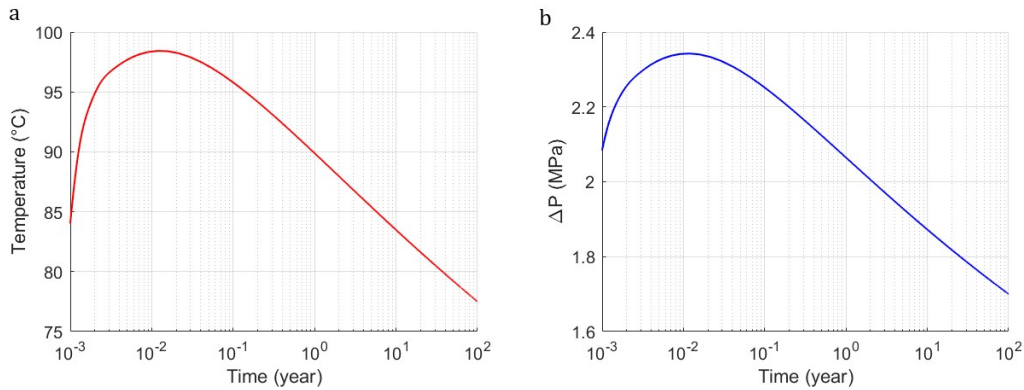


Fig. 5.2 The transient behavior of a) extraction temperature b) extraction pressure, for a simple CDG system with a depth of 4.1 km, horizontal length of 4 km, and flow rate of 5 L/s. ΔP is defined by ($\Delta P = P_{extraction} - P_{injection}$).

the trend of extraction temperature. In an isothermal condition, the extraction pressure is expected to be lower than the injection pressure due to friction loss. However, when fluid temperature is updated in non-isothermal simulations, a significant pressure increase occurs in the production wellbore. This is because the higher temperature of the working fluid in the production wellbore, along with the temperature-dependent density behavior, results in a lighter water column in the production side. This phenomenon, known as the thermosiphon effect, creates a pressure gradient between the vertical wellbores. The overpressure of approximately 2 MPa in Fig. 5.2b clearly indicates that the pressure rise caused by the density difference between the vertical wellbores is much greater than the pressure loss due to friction.

The operating flow rate can significantly influence the extraction temperature of closed-loop system. Fig. 5.3 shows the extraction temperature of a simple CDG system operating with a flow rate of 10 L/s. The immediate increase in extraction temperature was prompted by the displacement of residual hot fluid in wellbores. After this short period, the extraction temperature reduces due to the cooling down of the surrounded formation. For more information about the transient behavior of extraction temperature over time, refer to Esmaeilpour *et al.* [85].

Analogous to Fig. 5.3, the transient behavior of extraction temperature for 160 MCDG systems with various flow rates and wellbore configurations is analyzed. Fig. 5.4 shows the extraction temperatures after 1 year, 30 years, and 100 years. This figure consists of two main sections. Each section contains a parabola fitting of 160 points representing the extraction temperatures of simulated cases. The right curve exhibits the temperature of the produced

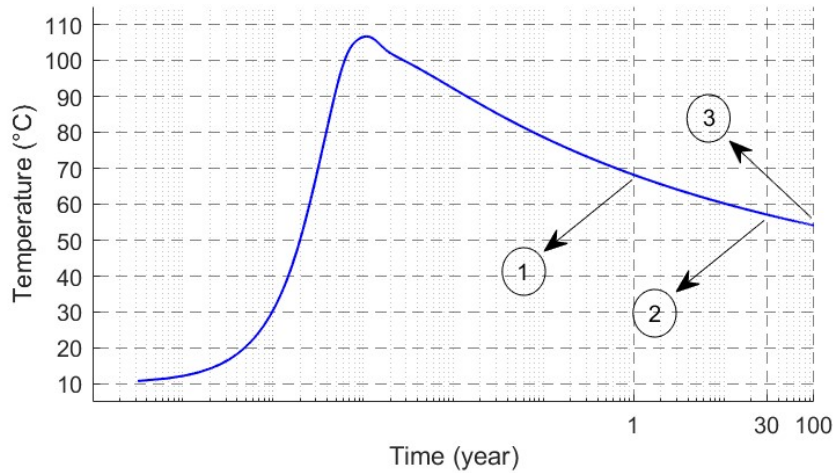


Fig. 5.3 Behavior of extraction temperature over time while operating with a simple CDG system. The flow rate is 10 L/s and other initial/boundary conditions and casing program are mentioned in Sections 5.2 and 5.3. Points 1, 2, and 3 correspond to extraction temperatures after 1, 30, and 100 years, respectively.

fluid after 30 years of operation as a function of the extraction temperature at the end of the first year of the operation. The left curve shows the extraction temperatures after 30 years and 100 years. For example, the extraction temperatures of a simple case with a flow rate of 10 L/s (Fig. 5.3) are marked with arrows in Fig. 5.4 to explain how to use/read the figure. Points 1, 2, and 3 in Fig. 5.4 correspond to the extraction temperatures in Fig. 5.3 for the mentioned operation year (1, 30 and 100) as a temporal instance. Similarly, the extraction temperatures of other MCDG systems are included in this figure. Since the left and right sections share one of their axes (i.e., the axis which indicates the extraction temperature after 30 years), it is also possible to read the temperature of produced fluid after one century of operation based on the extraction temperature after the first year and vice versa.

In contrast to the nonlinear change of T_{30} as a function of T_1 (Fig. 5.4, right side), the relationship between T_{30} and T_{100} (Fig. 5.4, left side) is almost linear. These correlations between extraction temperatures over different periods are in good agreement with the observed trend of extraction temperature in other studies. Esmailpour *et al.* [85] showed that the extraction temperature of CDG systems experiences a huge nonlinear temperature change initially, and then it undergoes a small (linear) variation over time. The provided example in Fig. 5.3 also shows the same behavior that the extraction temperature decreases 11 °C in the period of 1 to 30 years, while its reduction is less than 3 °C in the period of 30 to 100 years. Moreover, the maximum observed reduction of extraction temperature in 30 to 100 years is approximately 4 °C, which shows the longevity of MCDG systems. This remarkable

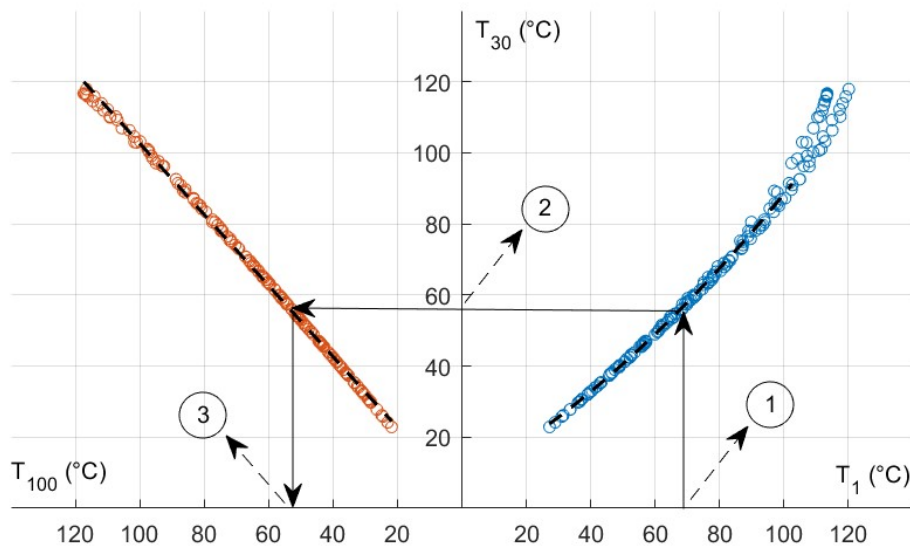


Fig. 5.4 Correlations between extraction temperatures of MCDG systems after 1 year, 30 years, and 100 years of operation

longevity is also represented by the inclination angle of T_{100} over T_{30} (45°), implying that the extraction temperature after 100 years is almost equal its value after 30 years of operation.

It is also worth mentioning that there is no clear relation between the extraction temperatures when T_1 is higher than 105°C . Operating with low flow rates leads to the temperature increment of the working fluid entering the production wellbore. This hot fluid experiences a considerable temperature drop in the production wellbore. Nevertheless, as reported by Esmailpour *et al.* [85], heating the area around the production wellbore prevents the temperature drop along this wellbore and results in extraction temperature enhancement over time. This strange behavior of extraction temperature causes deviation from the parabola fitting.

In Fig. 5.5, the energy density (i.e., extracted energy per liter of circulating fluid) over the project lifetime of one hundred years is plotted versus the extraction temperature after the first year. Using the energy density for the calculation of total generated thermal power (power (MW_t) = energy density (MJ/L) \times flow rate (L/s)) should be treated with care. As shown in Fig. 5.5, only low flow rates can result in high extraction temperature after the first year (T_1). However, small extraction temperatures can be outcomes of either low or high flow rates. Therefore, the provided colormap shows the maximum allowed flow rate for the calculation of thermal power. The provided example in Fig. 5.5 shows the calculation procedure clearly. When the extraction temperature after the first year (T_1) is 84°C , the energy density is 0.26 MJ/L . Calculation of average generated thermal power requires reading the flow rate from the colormap. For the energy density of 0.26 MJ/L , the flow rate

is 40 L/s, leading to the total thermal power production of 10.4 MW_t ($0.26 \text{ MJ/L} \times 40 \text{ L}$). In conclusion, the achieved relation between short-term and long-term values of extraction

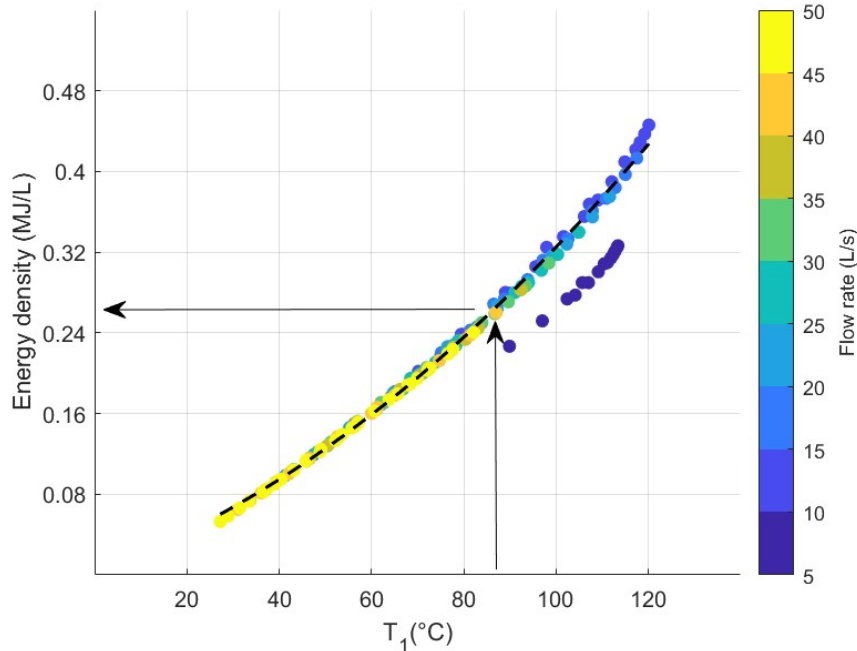


Fig. 5.5 Correlations between extraction temperatures of MCDG systems after 1 year and extracted energy per liter of working fluid over 100 years of operation. The provided colormap shows the maximum allowed flow rate for the calculation of thermal power.

temperature is independent of flow rate and the number of wellbores. It shows the possibility of utilizing these correlations to anticipate the performance of other MCDG systems with various flow rates and wellbore configurations. It should be noted that the depth of the system, length of horizontal wellbore, number of casing/cement layers around wellbores, thermo-physical properties of geological layers, and subsurface temperature gradient can influence the short-term behavior of the system. Nevertheless, the long-term behavior of the system will be again a specific function of its short-term performance. For example, the temperature of extracted fluid after 100 years of operation can still be anticipated as a linear function (different slope) of the extraction temperature after 30 years. The spacing of the lateral wellbores could affect this correlation. If the well spacing is reduced below 400 m (i.e., the distance that ensures no thermal interference), it will inevitably lead to a different correlation. This is because reducing the spacing further will lower production temperatures in long-term behavior. In this study, a well spacing of 400 meters is used to ensure no thermal interaction between parallel wellbores and maximize energy absorption from the reservoir.

5.5 Results

5.5.1 General behavior of MCDG systems

Based on the previous investigations conducted by Esmailpour *et al.* [85], operating with high flow rates reduces the extraction temperature of CDG systems and violates their longevity. On the other hand, the low range of operating flow rates limits the system's power production as the maximum generated thermal power of the designed CDG system was approximately $2 MW_t$. Therefore, the primary purpose of this section is to evaluate the impact of multiple wellbores on the thermal power generation, heat absorption rate, and extraction temperature.

Analogous to Section 5.4, 160 different MCDG systems are designed to perform stochastic analysis with regard to flow rate and system configuration. Their geometrical configuration, parameters and BCs/ICs are addressed in Sections 5.2 and 5.3, respectively. In order to have a meaningful comparison of different cases, an index called specific power (W/m) is defined as the ratio of the generated thermal power to the equivalent total length of the system :

$$\text{specific power} = \frac{\text{generated power}}{\text{equivalent total length}} \quad (5.5)$$

where the equivalent total length is a simplified/normalized indicator of drilling expenses, defined by this equation:

$$\begin{aligned} \text{Equivalent total length} = & \text{total length of vertical wellbores} \\ & + 2 \times \text{total length of horizontal wellbores} \end{aligned} \quad (5.6)$$

It is assumed that the horizontal wellbore's drilling cost is two times that of a vertical wellbore. However, this weighting coefficient can be changed considering the length of the wellbores, their diameters, geological condition, casing program, drilling technology, and other complicated parameters. The calculated specific power of a simple CDG system operating with a flow rate of $5 L/s$ is $70.81 W/m$ [85]. Accordingly, the specific power $> 70.81 W/m$ is an indicator of a more productive system compared to the CDG system, resulted in shortening the relative payback period. Therefore, it is technically reasonable to operate with MCDG systems possessing a specific power of $> 70.81 W/m$. However, this criterion should not be considered a sharp indicator for project decision making.

Fig. 5.6 exhibits the impact of flow rate on the average values of extraction temperature, generated thermal power, and specific power over 100 years of operation. As mentioned before, 16 various configurations are modeled for each flow rate. Therefore, the boxplots

show the impact of multiple wellbores at a specific flow rate. The increment of the flow rate enhances the thermal power generation and the specific power. Although the extraction temperature and the generated thermal power are very sensitive to low flow rates, their sensitivity to high flow rates is negligible. As an example, median, lower / upper quartiles and whiskers of generated thermal powers at the flow rate of 45 L/s are almost the same as those of 50 L/s. It indicates that for the simulated set of system configurations, the decline of extraction temperature compensates for the increment of operating flow rate, leading to a small variation in the generated thermal power spectrum. Consequently, exceeding a critical value of flow rate reduces the extraction temperature and doesn't change the generated thermal power significantly compared to its variation at lower flow rates. However, it should be high enough to exploit the maximum potential of the system. It is also shown that the increase in flow rate is associated with higher uncertainty in the determination of power production. For instance, adding extra wellbores increases the generated thermal power of the system from 3.5 MW_t to 10 MW_t , when the flow rate is 35 L/s. Although operating with multilateral systems can scale up the thermal power production at high flow rates, the increase in the number of wellbores seems to be unreasonable when operating with low flow rates since the generated thermal power doesn't increase significantly (Fig. 5.6, flow rate = 5 L/s). Finally, increasing the flow rate reduces the extraction temperature significantly. Consequently, the reduction of extraction temperature and low sensitivity of generated thermal power to high flow rates are the main barriers to the increase of flow rate.

Fig. 5.7 shows the impact of system configuration on the extraction temperature, generated thermal power, and specific power of various MCDG systems consisting of 10 flow rates ranging between 5 L/s and 50 L/s. Therefore, the boxplots show the impact of flow rates for each system configuration. The first and second indices of each configuration show the number of injection and horizontal wellbores, respectively (e.g. the configuration of 2:4 means 2 injection and 4 horizontal wellbores).

As shown in Fig. 5.7, adding extra horizontal wellbores is more impactful than including additional injection wellbores to enhance power production and extraction temperature. Indeed, the working fluid is directly exposed to the hottest formation in the horizontal wellbore. Hence, this part of the system is very important for heat absorption. This finding is also testified by Esmailpour *et al.* [85], that the magnitude and behavior of net generated thermal power is like the power production in the horizontal wellbore of CDG systems. Nevertheless, the high relative drilling cost is a primary obstacle to increasing the number of horizontal wellbores since it increases the equivalent total length of the system and subsequently reduces the specific power. Therefore, the increment of produced thermal

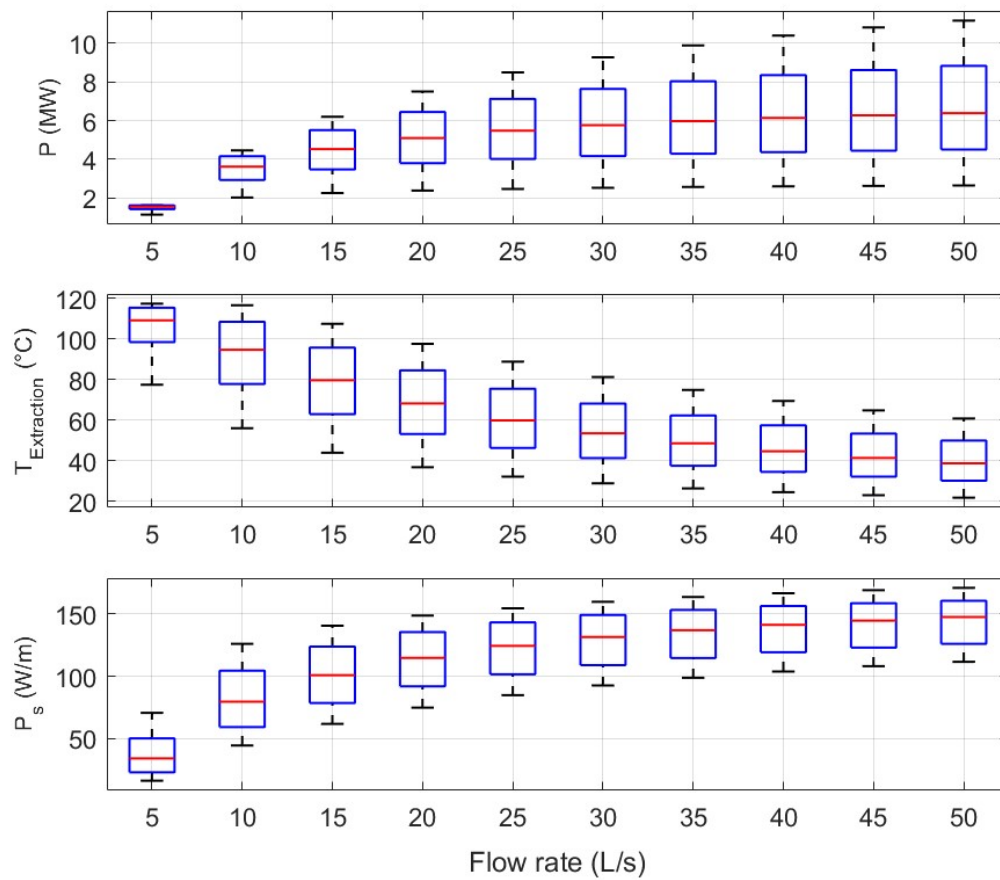


Fig. 5.6 Ranges of generated thermal power (P), average extraction temperature over 100 years of operation ($T_{\text{Extraction}}$), and specific power (P_s) for each flow rate. The boxplots show the impact of wellbore configurations at each flowrate.

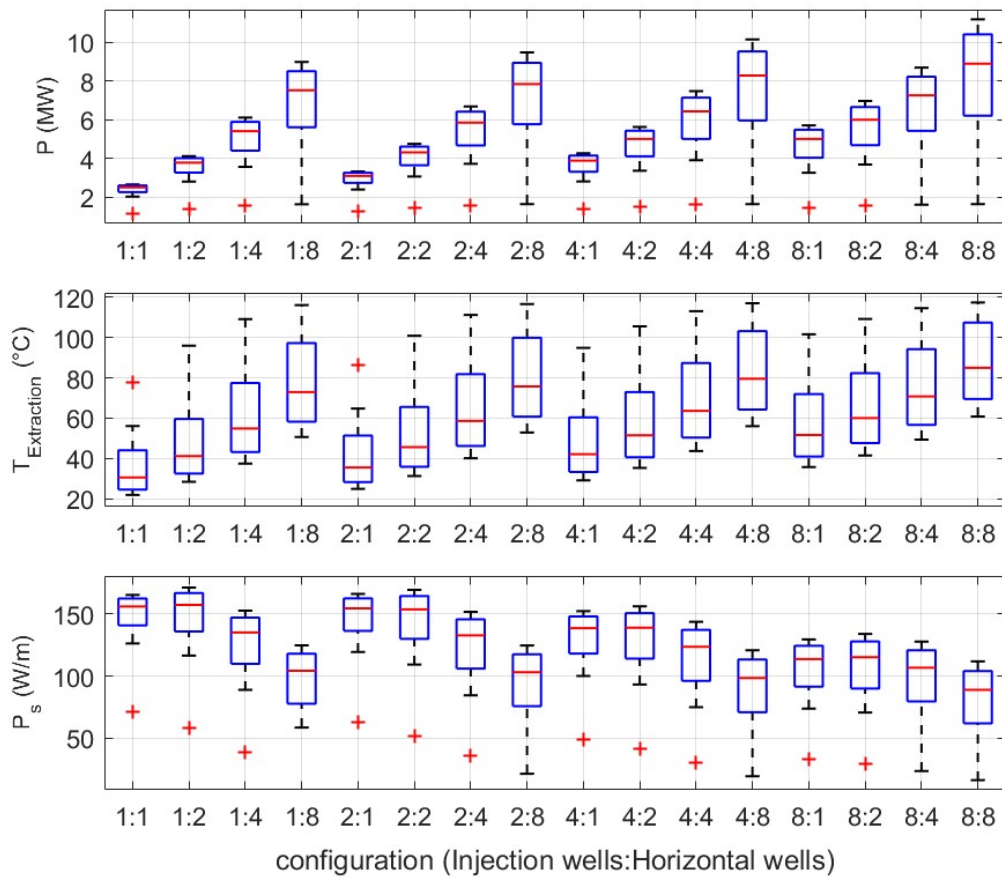


Fig. 5.7 Ranges of generated thermal power (P), average extraction temperature over 100 years of operation ($T_{\text{Extraction}}$), and specific power (P_s) for wellbore configuration. The domain of boxplots shows the impact of flow rate on outputs. The first and second indexes of each configuration show the number of injection and horizontal wellbores, respectively.

power and the excess drilling expenses are the primary criteria that should be considered when adding a new horizontal wellbore to an MCDG system.

5.5.2 Suggestion of appropriate operation plans

Utilizing MCDG systems doesn't guarantee a better performance compared to CDG systems as demonstrated in Section 5.5.1. Finding a high-performance MCDG system is a key issue for a successful project. Therefore, this section is dedicated to filtering out inappropriate cases (from our 160 models) which are not aligned with sustainable and profitable geothermal production. Furthermore, the important outcome will be the identifying of specific shared features in all filtered cases to make the study transferable.

Fig. 5.8 illustrates the total generated thermal power, average extraction temperature over 100 years of operation, and the specific power of each simulated case. Increasing the number of wellbores and the reduction of the total flow rate result in a higher extraction temperature (the top left quarter in Fig. 5.8). However, both factors typically lead to a lower specific power due to either decreasing the generated thermal power or increasing the equivalent total length of a system. As a result, the studied MCDG systems are not capable of producing electric power cost-effectively (it is worth mentioning that a deeper system or longer horizontal section may make electric power generation feasible but it is out of the scope of the current study). Nonetheless, they are potentially reliable for district heating purposes. On the other hand, operating with a higher flow rate increases the generated thermal power and enhances the specific power, but it reduces the extraction temperature (the bottom right quarter in Fig. 5.8). To conclude, it is crucial to set criteria, in which high specific power and extraction temperatures coincide, to choose proper operation/construction plans. In this study, the cases with the extraction temperature $> 60\text{ }^{\circ}\text{C}$ (the min temperature suitable for district heating) and the specific power $> 70.81\text{ W}/m$ (the specific power of the CDG system introduced earlier) are assumed to be convenient for operation and named successful cases. Remarkably, the majority of the selected cases (the gray rectangle in Fig. 5.8) also have higher generated thermal power than the disregarded cases. The MCDG systems with an extraction temperature range of $60\text{ }^{\circ}\text{C}$ to $100\text{ }^{\circ}\text{C}$ (successful cases) are well-suited for use in district heating and local heating applications to provide warmth to buildings. The main difference between these two applications is in the scale of the system and how heat is distributed. Geothermal district heating is a large-scale system that distributes heat to entire neighborhoods or cities through a network of pipes that carry hot water or steam, while local heating is a smaller-scale system that provides heat to individual buildings or homes using boilers or heat pumps. The typical temperature range of geothermal fluids used for district heating is between $70\text{-}120^{\circ}\text{C}$ [158]. The flow rate for district heating systems can

vary widely depending on the size of the system and the demand for heat. According to a report by the international energy agency [7], the flow rate for district heating networks in Europe ranges from less than 1 L/s for small networks to more than 50 L/s for large networks. In contrast, the typical temperature range for local heating systems depends on the type of heating equipment used. According to the U.S. department of energy [159], the temperature range for hot water boilers is typically 40-80°C. The local heating network in Riehen (a municipality in the canton of Basel-Stadt in Switzerland) is a good example of local heating where geofluid with a temperature of 66°C is heated with the help of a heat pump to provide hot fluid with a temperature of 80-90°C to dwellings at a flow rate of 25 L/s . The extraction temperature and flow rate of successful MCDG systems clearly demonstrate their capability to be used for both district heating and local heating applications.

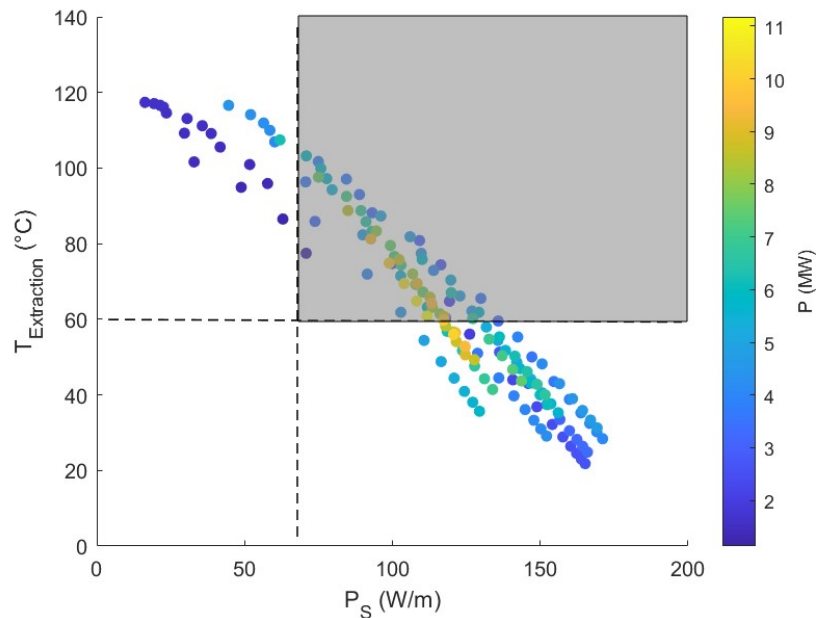


Fig. 5.8 Average values of extraction temperature over 100 years of operation ($T_{\text{Extraction}}$), specific power (P_S), and total generated power (P) of each case. The plotted lines show the filtering criteria (average extraction temperature > 60 °C and specific power > 70.81 W/m). The points located in the gray region are successful cases.

Fig. 5.9 exhibits the total flow rates and wellbore configurations of successful cases highlighted in Fig. 5.8. Clearly, the points are clustered with a specific repeated pattern and oriented toward the right side (of the pattern), where the MCDG system possesses more lateral wellbores. It indicates that by increasing the number of wellbores, it is more likely to have a successful case (this assessment doesn't include drilling difficulties). What are the common features of these repeated patterns? Finding these features in successful cases supports a

better design of high-performance MCDG systems in the future. Therefore, it is tried to find a meaningful correlation between local parameters (flow rates per injection/horizontal wellbores) and global parameters (i.e. specific power, average extraction temperature, and total flow rate of successful cases).

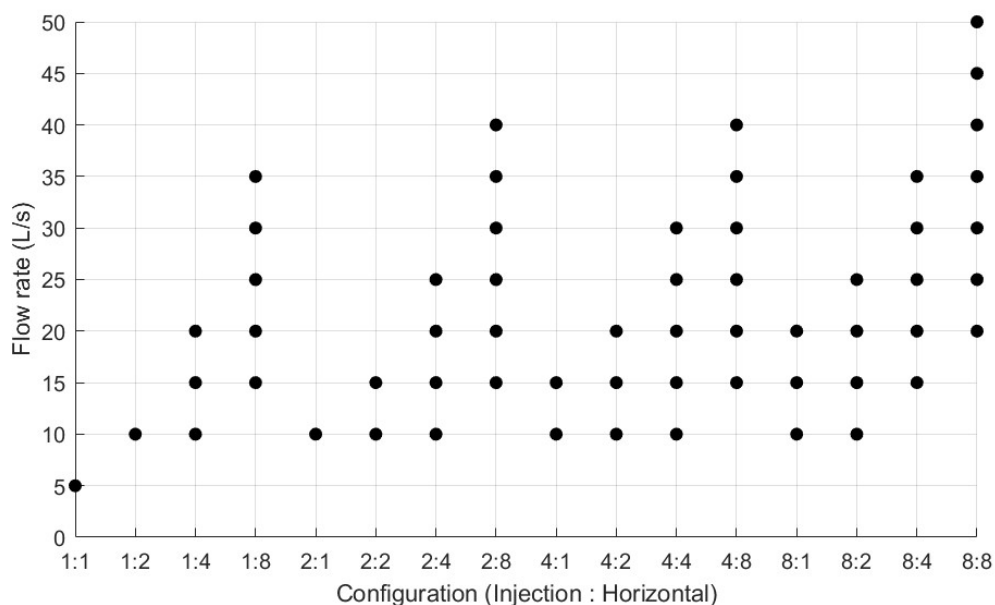


Fig. 5.9 Flow rates and corresponding configurations of successful cases. The first and second indexes of each configuration show the number of injection and horizontal wellbores, respectively.

Fig. 5.10 plots flow rates per injector and lateral for successful cases, and global parameters are shown in each subfigure. Flow rates per injector and lateral are calculated by dividing the total operating flow rate by the number of injection and horizontal wellbores, respectively. The main outcome is that the plotted data has an upper limit (asymptote) which is governed by:

$$\text{flow rate per lateral} < \frac{1}{a \times (\text{flow rate per injector})^2 + b \times (\text{flow rate per injector}) + c} \quad (5.7)$$

where a , b , and c are $-3.16e-4$, $1.69e-2$ and $-3.85e-3$, respectively. These factors are specific to this study, and they vary in different geometrical/geological conditions.

The extraction temperature is decreasing along the arrows shown in Fig. 5.10a and Fig. 5.10b while the specific power is increasing. All plotted points under the curve have an extraction temperature of higher than 60°C , demonstrating that the extraction temperature

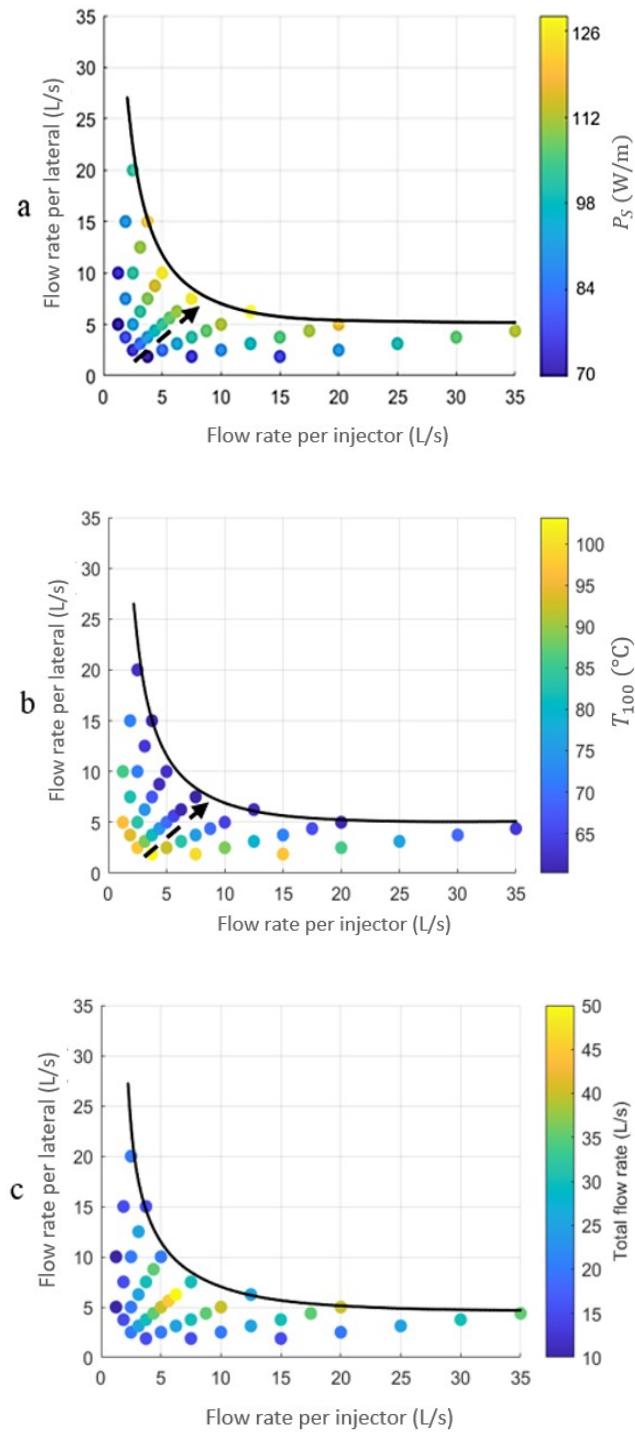


Fig. 5.10 Correlation between flow rates per lateral/injector and a) specific power b) average extraction temperature over 100 years of operation c) total flow rate (L/s)

is the main factor forming Eq. 5.7. Additionally, it is found that high total flow rates are achievable when the flow rate per injector is approximately the same as the flow rate per lateral (Fig. 5.10c). Simultaneous low flow rates per injector and lateral can guarantee a high extraction temperature. However, the points with low flow rates per lateral possess higher extraction temperatures compared to the points with low flow rates per injector. Therefore, horizontal wellbores are preferable to vertical wellbores in terms of extraction temperature enhancement due to the direct exposition of working fluid to hotter formation in the horizontal section. Consequently, to maximize the extraction temperature, the number of horizontal wellbores should be certainly higher than the number of injection wellbores. However, a high extraction temperature cannot guarantee considerable thermal power production. Moreover, the increase in the total flow rate necessitates operating with MCDG systems in which the number of injection wellbores is roughly equal to the number of horizontal wellbores. Hence, contrary to conventional belief, it is not a good idea to construct an MCDG system with only one injection wellbore and many horizontal wellbores. Nonetheless, the number of horizontal wellbores should be higher than the number of injection wellbores.

Fig. 5.11 shows the success rate calculated by dividing the number of successful cases by the total number of simulated cases for each flow rate (i.e., 16 configurations). The highest success rate occurs when the flow rate ranges between 10 L/s and 25 L/s . For instance, the success rate is 75 % when the flow rate is 15 L/s . Small generated thermal power and low extraction temperature make it risky to operate with low and high flow rates in MCDG systems, respectively.

5.6 Conclusion

Designing high-performance MCDG systems makes it feasible to obtain baseload power in an environmentally friendly manner without causing seismic events and contaminating subsurface water. Therefore, the main purposes of this study were to analyze the heat extraction capability of MCDG systems, enhance their performance, and increase their contribution to green energy generation. To achieve these targets, several multilateral systems with various operational parameters and configurations are proposed. In the first step, the system's long-term performance is described as a function of its short-term behavior through stochastic analysis. This way, the short-term outputs (i.e., extraction temperature and generated thermal power) and appropriate operational/configurational parameters can be back-calculated out of the desired long-term performance. Then, the impact of flow rate and wellbore configuration on the system's behavior is assessed. Defining a specific power allows comparing the performance of individual MCDG systems. The ratio of generated thermal

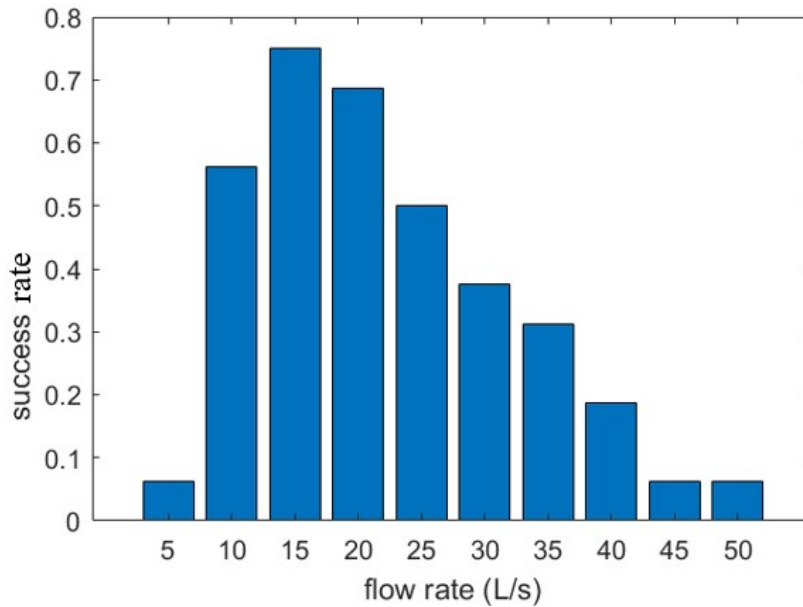


Fig. 5.11 Success rate of designed MCDG systems for each flow rate (success rate= (number of successful cases at each flow rate)/16)

power to the equivalent total length of the system is of key importance for economic analyses. It is concluded that the performance of MCDG systems is not always better than simple CDG systems. Subsequently, some criteria are set to select the best operation/configuration plans. Finally, the common features of successful cases are characterized, which gives insight into designing high-performance MCDG systems.

The key findings of this study are listed below:

1. It is found that the long-term extraction temperature and generated thermal power of MCDG systems can be predicted as functions of their short-term extraction temperature through stochastic analysis. Interestingly, these correlations are independent of the number of wellbores and flow rate.
2. Operating with MCDG systems doesn't always result in better performance than CDG systems. It is also demonstrated that adding horizontal wellbores is more beneficial than including extra injection wellbores in terms of power production.
3. The findings of this study revealed that regardless of technical drilling difficulties, increasing the number of lateral wellbores enhances the heat absorption per meter of the system and the success rate.

4. The cases with appropriate extraction temperate and high ratio of generated thermal power to the equivalent total length can be characterized by a specific relation between flow rates per injection and horizontal wellbores.
5. In contrast to conventional belief, it is not reasonable to operate with only one injection wellbore and many horizontal wellbores since the highest total flow rate is achievable when the flow rate per injector approaches the flow rate per lateral.

The quantitative results of the present work provide a realistic overview of the heat extraction potential of MCDG systems. Nevertheless, the drilling expense is another essential factor that should be taken into account when selecting the best system design. In this study, a specific criterion is defined to give a rough estimation of the ratio of thermal power to relative drilling costs. However, future research should focus more on various drilling technologies and associated costs/risks to improve the defined criterion and provide a comprehensive economic analysis. It is also worth mentioning that the structure of doglegs and manifolds may be more complicated in real MCDG systems. This complexity cannot considerably change the energy absorption of the system as the length of the doglegs is small compared to the total length of the system. Nonetheless, dogleg design is an important topic for future studies concerning the drilling of MCDG systems.

5.7 Acknowledgment

The study is part of the subtopic "Geoenergy" in the program "MTET - Materials and Technologies for the Energy Transition" of the Helmholtz Association.

Chapter 6

Development of a machine learning-based model to predict high-pressure CO₂ corrosion in carbon steel pipelines

This chapter is submitted as Development of a machine learning-based model to predict high-pressure CO₂ corrosion in carbon steel pipelines, Esmaeilpour M, Nitschke F, Kohl T.

Abstract

CO₂-induced corrosion is an essential factor affecting the lifespan and performance of geothermal wellbores as it can cause damage to the well casing and tubing, leading to leaks, reduced well productivity, and increased maintenance costs. The intricate interplay of physical, chemical, and electrochemical phenomena poses a significant challenge in developing precise models for predicting corrosion rates. The mathematical description of high-pressure CO₂ corrosion is even more complex due to the alterations in thermodynamics and kinetics of the reactions, increased transport rates, and changes in fluid flow patterns. Nonetheless, the majority of existing corrosion models are only applicable for CO₂ partial pressures below 20 bar and do not assume that water wetting will always occur. To our knowledge, the most accurate model fitting available experimental data on high-pressure CO₂ corrosion is presented by Abbas *et al.* [160] in 2018. The neural network model they proposed can predict the experimental test dataset with an R²-coefficient of 0.91. However, an average relative error of $\approx 38\%$ in predicting corrosion rate (test dataset) indicates a significant potential for further refinement of the model to enhance its accuracy. Therefore, the main goal of the current study is to employ another artificial intelligence technique, called gene expression programming, to obtain a more accurate estimate of CO₂-induced corrosion in geothermal wellbores. The explicit formulas suggested in this study demonstrate a remarkable degree of precision, as demonstrated by their capability to compute the experimental test dataset with an R²-coefficient of 0.99 and reduce the average relative error to $\approx 21\%$.

6.1 Introduction

Geothermal systems are a vital component of the energy transition. Harnessing the earth's internal heat provides a renewable, emission-free, and baseload-capable source of energy, which can play an important role in decreasing the reliance on fossil fuels [161]. The long-term reliability of geothermal installations depends on the system's integrity. A well-designed and well-operated geothermal system with proper attention to system integrity will result in a long-term safe, efficient, and sustainable energy production. Nevertheless, the adequate operation and maintenance of geothermal systems is a challenging task due to the often very harsh physico-chemical conditions (e.g., high temperatures and pressures and complex chemistry). Corrosion is one of the critical factors that can impact the longevity of geothermal systems, potentially causing leaks, decreasing heat transfer efficiency, and potentially leading to ultimate system failure.

Several types of corrosion can occur in geothermal installations, including general corrosion [162, 163], pitting corrosion [164, 165], galvanic corrosion [166, 167], and erosion-corrosion [168–170]. General corrosion occurs when a corrosive environment causes a uniform loss of material from the surface of a component, while pitting corrosion is the result of localized corrosion that creates deep, narrow holes in the material. Galvanic corrosion occurs when two dissimilar metals are in electrical contact with each other, and the less noble metal corrodes preferentially. Erosion-corrosion occurs when high-velocity fluids erode a material while simultaneously promoting corrosion.

The presence of CO₂ in geo-fluids is one of the primary contributory factors for triggering corrosion in geothermal wellbores, which often manifests as general corrosion. CO₂ dissolves in the liquid medium, forms carbonic acid, and reacts with metal surfaces [171, 172]. The resulting corrosive environment can rapidly degrade the steel casing of geothermal wells. CO₂ corrosion is particularly dangerous because it can occur in small, hard-to-detect amounts, making it difficult to be detected and controlled. Predictive models for CO₂ corrosion potential are of high importance as they allow for identifying the most effective strategies for preventing or controlling CO₂ corrosion, leading to improved reliability and efficiency of geothermal frameworks.

The majority of mathematical models for predicting CO₂ corrosion are developed by oil companies (e.g., Shell's HydroCor [173, 174], Total's Corplus [175], IFE's KSC [176], and BP's Cassandra [177] models). Typically, the corrosion models can be categorized into two primary classes:

- **Mechanistic models:** They possess a robust theoretical approach that outlines the fundamental electrochemical reactions and transport processes. Unfortunately, despite

extensive research over the years, the underlying chemical processes and their interaction with scaling remain elusive and not fully comprehended. Hydrocor, KSC, and Multicorp [178, 179] are some examples of mechanistic corrosion models.

- **Empirical models:** These models are developed by conducting experiments where various system parameters are altered, and the resulting corrosive effects are observed and monitored. The empirical models may produce trustworthy predictions when used within the bounds of existing experimental data, extrapolating beyond these limits is unreliable and potentially hazardous. They possess limited or insufficient theoretical background, and many of the constants employed in these models lack physical meaning. Norsok [180, 181], Waard [182], and Corplus are some examples of empirical corrosion models.

The implementation of these models in geothermal applications should be approached with caution as most of them do not assume that water wetting will always take place and their validity is limited the maximum partial pressure of CO₂ of 20 bars [183, 184]. The nature of high-pressure and low-pressure CO₂ corrosion differs in the rate and pattern of corrosion damage. High-pressure CO₂ corrosion typically causes more severe localized corrosion, such as pitting, due to the higher concentration of dissolved CO₂ in the fluid. Low-pressure CO₂ corrosion, on the other hand, tends to cause more uniform and widespread corrosion over a larger area. The specific mechanism of corrosion also differs between high and low-pressure CO₂ environments. In high-pressure CO₂, the formation of carbonic acid is accelerated by increasing the concentration of dissolved CO₂ in the aqueous phase, leading to more aggressive corrosion. In low-pressure CO₂, the corrosion mechanism is often associated with the presence of surface-active species that promote corrosion by creating pits or promoting uniform corrosion.

Abbas *et al.* [160, 185] conducted a comprehensive study to assess the performance of several widely used models in accurately predicting CO₂-induced corrosion. Based on his report, the 1975 Waard correlation [186] calculates the corrosion rate as a monotonically increasing function of temperature and does not account for a mid-temperature peak observed in experimental data, which corresponds to the temperature where the maximum corrosion rate occurs. The Waard correlations introduced in 1991 [182] and in 1995 [187] both account for the mid-temperature peak, but the former does not explicitly include a velocity term in its function, while the latter incorporates a velocity term as part of its resistance model. The Norsok model's corrosion rate-temperature profiles are similar to those of the Waard models, while also accounting for shear stress in pipe flow. This empirical model was developed using data from the North Sea oil and gas industry, and its accuracy may be limited when

applied to other geological settings or industrial applications. The NPO model [188] is based on mechanistic and electrochemical principles, which can cause it to over-predict corrosion rates, especially at temperatures above 80 °C. It should be noted that while empirical models such as the Waard correlations and the Norsok model may appear to provide more accurate predictions than the mechanistic NPO model, making conclusions based on results outside of their range of applicability problematic. Freecorp [189] is another empirical corrosion model developed by Ohio University for predicting corrosion rates of steel in CO₂-saturated brine environments. This model computes the corrosion rate as a monotonically increasing function of temperature, is restricted to predicting uniform corrosion, and cannot estimate pitting or any other types of localized corrosion.

None of the models mentioned above are capable of accurately predicting high-pressure CO₂ corrosion. Therefore, Abbas opted to develop novel machine-learning-based models that well match experimental data gathered from various references. He implemented Neural Networks (NN) [190, 191], fuzzy [192, 193], statistical [194, 195], and Monte Carlo [196, 197] methods to anticipate the corrosion rate as a function of temperature, CO₂ partial pressure, fluid velocity, and pH. To the best of our knowledge, his proposed NN model offers the most accurate fit for the available experimental data on high-pressure CO₂ corrosion. Nevertheless, the R²-coefficient of 0.91 and average relative error of $\approx 38\%$ in the prediction of corrosion rate (test data set) highlight a striking potential for further refinement of the corrosion model to improve its accuracy. Therefore, the main goal of the current study is to employ an artificial intelligence (AI) technique, called gene expression programming (GEP) to achieve a more precise estimation of CO₂-induced corrosion in geothermal wellbores. This machine learning method utilizes genetic algorithms to evolve computer programs capable of solving complex problems. GEP is a robust technique that can handle noisy and incomplete inputs, making it a suitable choice for developing a corrosion prediction model based on limited experimental data. GEP generates highly precise explicit formulas that can be easily implemented in other software, enabling accurate estimation of CO₂-induced corrosion potential in carbon steel pipelines. This study proposes a new formulation that demonstrates significant improvement in predicting high-pressure CO₂ corrosion, which will be further discussed in the following sections.

6.2 Methodology

6.2.1 Overview of Gene Expression Programming

Gene expression programming (GEP) is an advanced technique in the field of evolutionary artificial intelligence that was developed as an extension of genetic programming (GP) [198, 199]. Its main purpose was to address some of the limitations of GP, including its poor exploration of the research area, limited regression strategies, and low convergence rate. This evolutionary algorithm is designed to generate highly accurate and explicit formulas that can be used to predict target outputs. The resulting solutions can be easily implemented into other software systems and codes.

GEP's genetic operators are all based on biological evolution in nature. They include both fundamental operators like mutation, crossover, and selection, as well as more advanced operators like transposition, insertion, and recombination. GEP models consist of three primary components: chromosomes, genes, and expression trees (ET). Chromosomes are made up of one or more genes, and they mimic candidate solutions within the code. Genes are composed of terminals and functions, which represent variables like pressure or temperature, as well as mathematical functions such as addition, subtraction, division, multiplication, tangent, and logarithm. Expression trees also represent the candidate expressions.

A general framework for implementing GEP involves setting control parameters like population size, gene length, and mutation rate, and creating an initial population of potential solutions encoded as chromosomes. Each chromosome is evaluated using a fitness function, and the best-performing solutions are selected for reproduction in the new population. Genetic operators are applied to the selected individuals to generate new offspring. This process of selection, replication, mutation, inversion, transposition, and recombination is repeated until a stopping criterion is met. For a more detailed explanation of the implementation process, including code examples, refer to Ferreira [200].

6.2.2 Data collection

The inputs of the GEP-based corrosion model are collected from various sources in the open literature. All of these studies utilized weight loss through autoclave experiments to determine corrosion rates:

- (Hesjevik *et al.* [201]): For the experiments of this study, the Hastelloy C-276 (UNS N10276) nickel-alloy was utilized. Their measurements are mainly conducted for low temperatures ($T < 40$ °C).

- **(Choi and Nešić [202])**: This study is focused on corrosion measurement in X65 carbon steel samples. The corrosion rate tests were conducted either by maintaining a constant temperature and varying pressures, or by maintaining constant pressure while changing temperatures.
- **(Zhang *et al.* [203])**: Various types of steel samples were utilized in the study, which included carbon steel that is martensitic, a pipeline X65 steel, and three corrosion-resistant alloys (CRA) that contain chromium. However, only the corrosion rate results for the carbon steel were used in the modeling process to maintain consistency, since incorporating other corrosion rate measurements would impact the resulting model. The experimental corrosion rate results were obtained for temperatures ranging from 50 to 130 °C and a pressure range of 9.5 to 23.3 MPa.
- **(Cui *et al.* [204])** : Samples of P110, N80, and J55 carbon steels were used in this experimental study.

A summary of the variable ranges is mentioned in Table 6.1.

Table 6.1 Statistics of the CO₂ corrosion data

Variable	Range	Mean
Temperature (°C)	24-150	80.25
CO ₂ Partial Pressure (MPa)	3.5-23.3	13.17
Velocity (m/s)	0-4	2
pH	3.1-6	3.96
Corrosion Rate (mm/year)	0.9-19	10.78

Abbas *et al.* [160] performed a weighted principal component analysis on the dataset to assess how well the principal components explain the variation in the data. Their analysis indicated that the first two principal components accounted for 81.5% of the cumulative variation in the dataset, which is a sufficient amount to explain the majority of the variation.

6.2.3 Development of corrosion model

In complete accordance with Abbas *et al.* [160], the data collected in the last step is partitioned into training and test sets (see Appendix B). This way, it is possible to properly compare the newly developed GEP formula with the NN-based model of Abbas *et al.* [160]. The training dataset is fed into a GEP model with the setting mentioned in Table 6.2. Subsequently, the process of selection, replication, mutation, inversion, transposition, and recombination are repeated until the stopping criterion (i.e., R² in predicting test dataset) is

fulfilled (Fig. 6.1). The expression tree of the developed GEP model is depicted in Fig. 6.2. Nevertheless, for the ease of use, its corresponding C++ code is provided in Appendix A. The

Table 6.2 GEP settings for the calculation of corrosion rate

Number of chromosomes	30	Head size	6
Linking function		Fitness function	R2
IS Transposition	0.00546	RIS Transposition	0.00546
One-point Recombination	0.00277	Two-point Recombination	0.00277
Constants per gene	10	Range of constants	-10 to +10
Number of genes	6	Inversion	0.00546
Mutation	0.00138	Gene Transposition	0.00277

accuracy of suggested GEP equations in predicting target values (test dataset) is elaborately discussed in the next sections.

6.3 Results and discussion

6.3.1 Prediction accuracy

Abbas *et al.* [160] evaluated the accuracy of their derived NN model by predicting a test corrosion dataset in the temperature range of 40 °C to 140 °C. The predicted values of the NN model, the newly-developed GEP equation, and the experimental test dataset are displayed in Fig. 6.3. Although this figure can be helpful in evaluating the effect of temperature on the corrosion rate, it may not conclusively indicate which mathematical model performs better in predicting the target experimental values. Thus, in Fig. 6.4 and Fig. 6.5, the corresponding absolute and relative errors in predicting the corrosion rate are presented. Fig. 6.4 indicates that utilizing the NN model leads to a notable absolute error in calculating the corrosion rate at low temperatures (i.e., 40 °C and 50 °C). At temperatures of 60°C, 80°C, and 130°C, the absolute error of the GEP equation is slightly larger than that of the neural network model. Nonetheless, the average absolute error of 1.25 *mm* demonstrates the superior performance of the GEP function compared to the NN model, which has an average absolute error of 1.77 *mm*. The distinction between these two mathematical models becomes more apparent when evaluating the relative error (Fig. 6.5). The average relative errors of the NN and GEP models in predicting the test dataset are 38% and 21%, respectively. The smaller value of corrosion rate and high absolute error of the NN model at low temperatures (Fig. 6.4, 40 °C) results in very high relative error (Fig. 6.5, 40 °C, 140% error). The NN model well fits the CO₂ corrosion test dataset, as shown by the R²-coefficient of 0.91 in Fig. 6.6a. However, the GEP model greatly enhances the prediction accuracy, achieving an R² value of 0.99 (Fig. 6.6b).

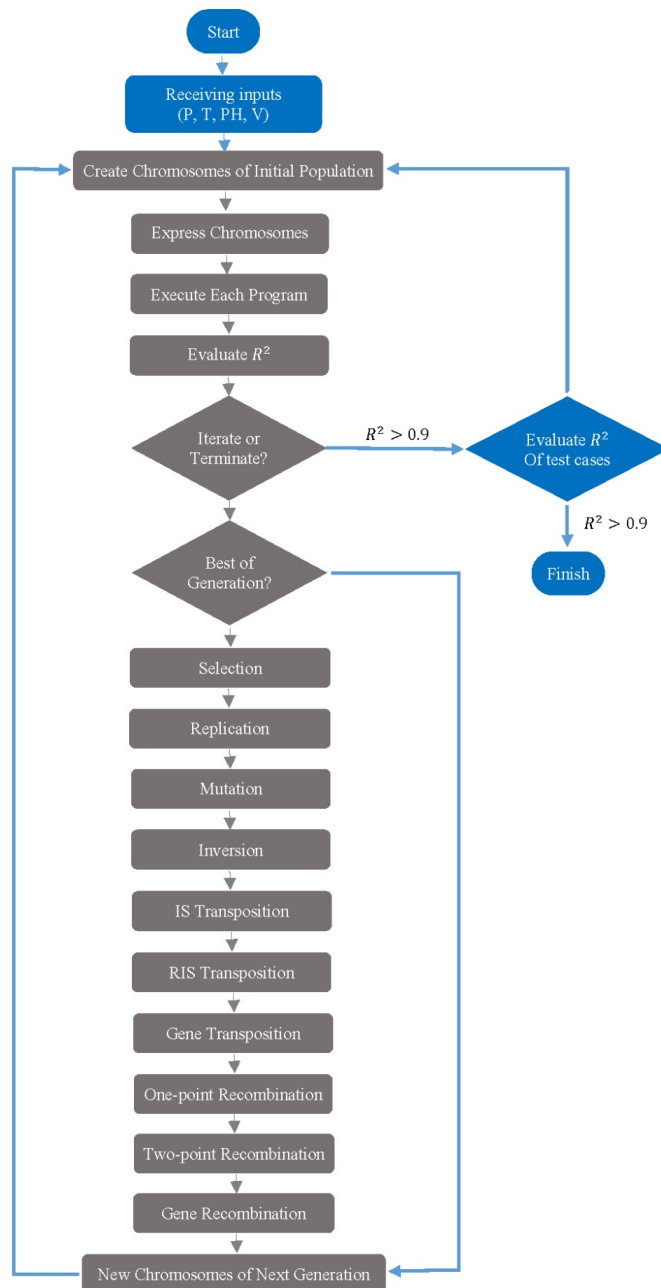
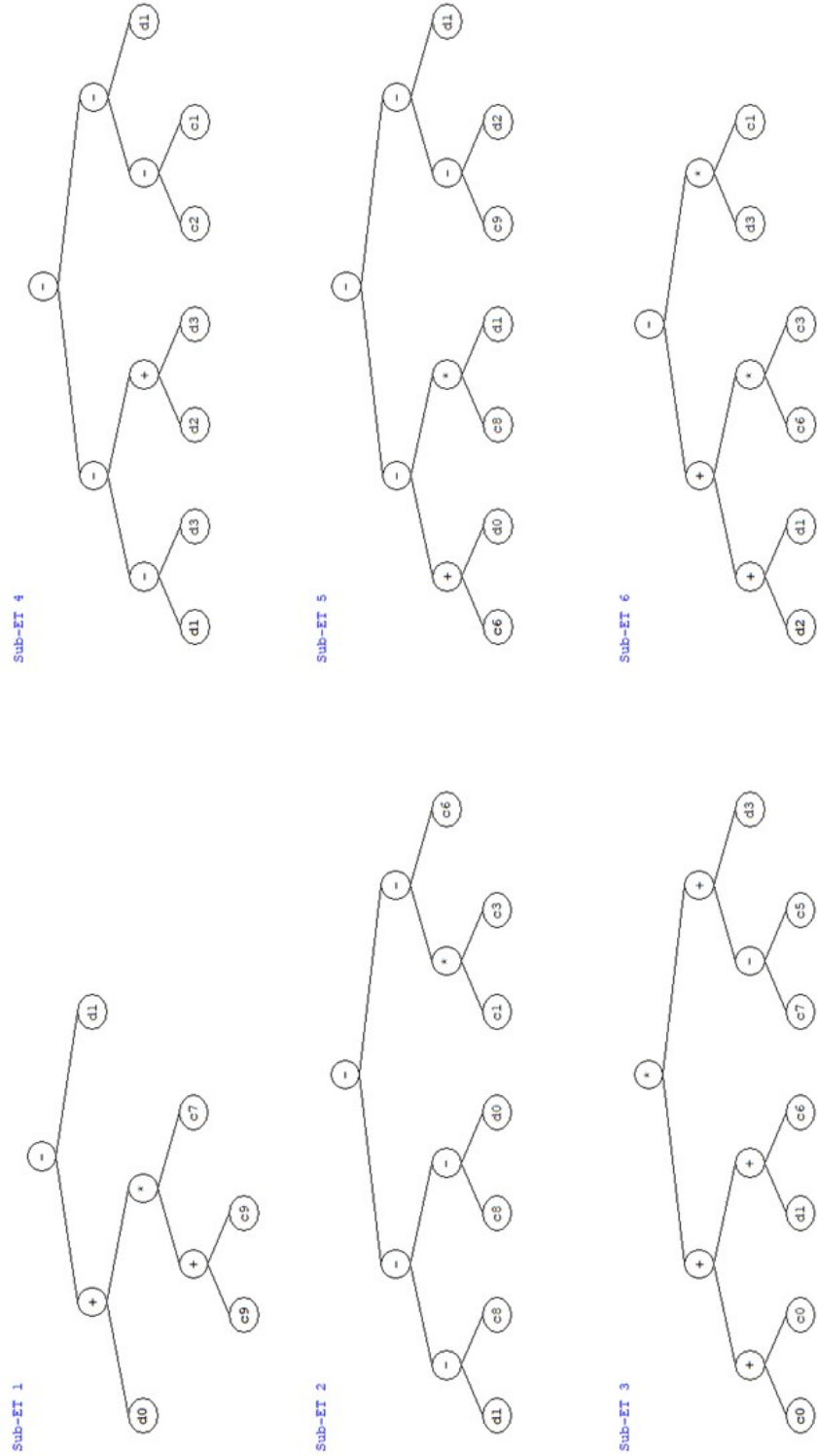


Fig. 6.1 The flowchart of gene expression algorithm. Pressure, temperature, pH, and velocity are assumed inputs, while the R-squared in calculating corrosion rate is considered as a fitness function.

Fig. 6.2 Generated expression tree for the GEP corrosion model. It is constructed from a set of genes, which are the building blocks of the program. These genes are represented as strings of characters, and they encode the operators and operands that will be used to construct the tree.



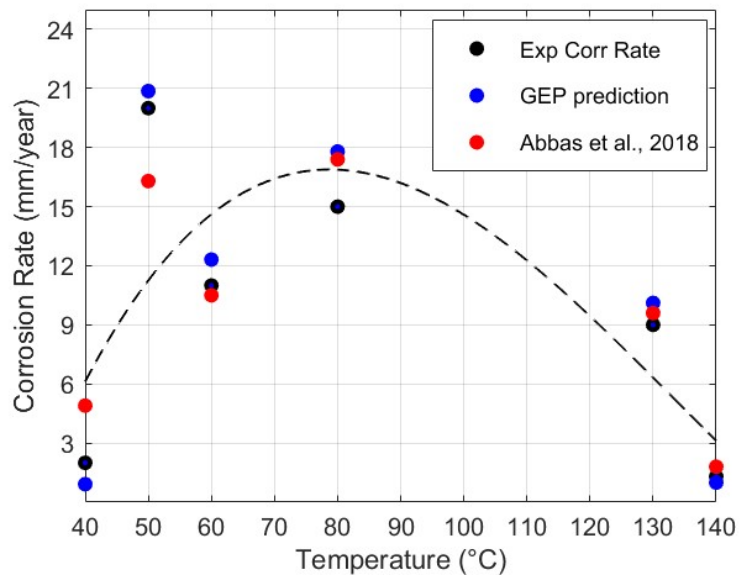


Fig. 6.3 Comparing the corrosion rates predicted by mathematical models with the experimental test dataset.

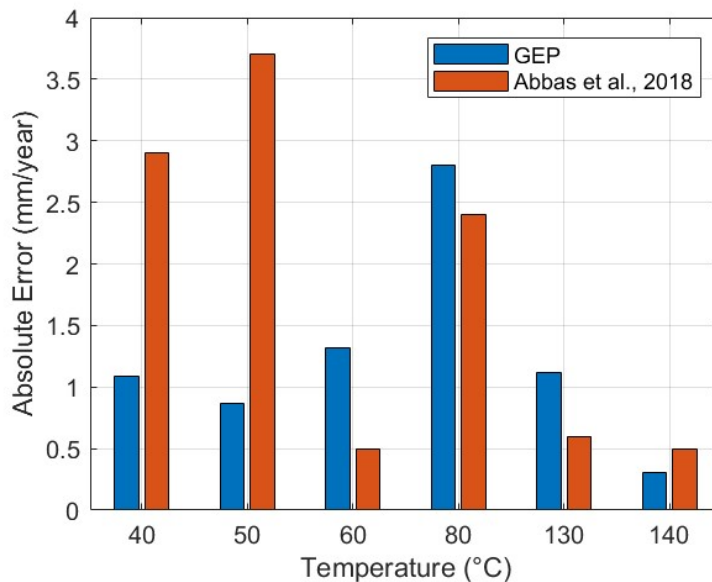


Fig. 6.4 The absolute error of GEP and NN models in predicting test dataset.

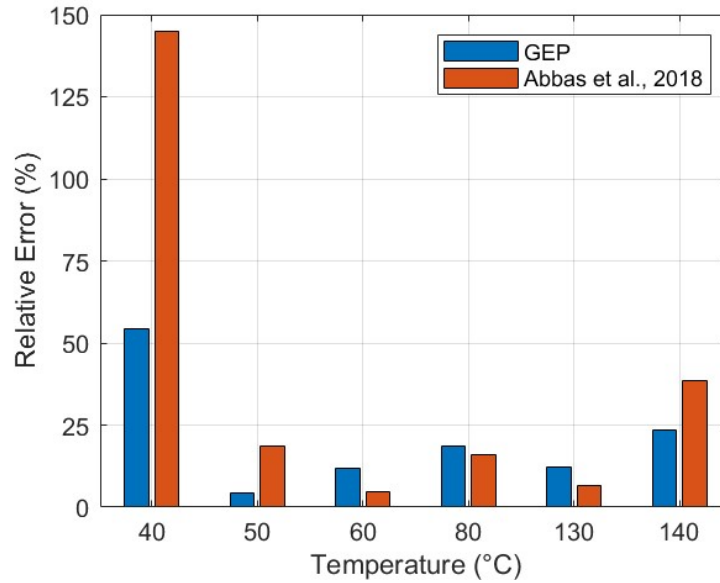


Fig. 6.5 The relative error of GEP and NN models in predicting test dataset.

To the best of our knowledge, the high level of accuracy achieved in predicting experimental corrosion data using the GEP model has not been previously reported in the literature.

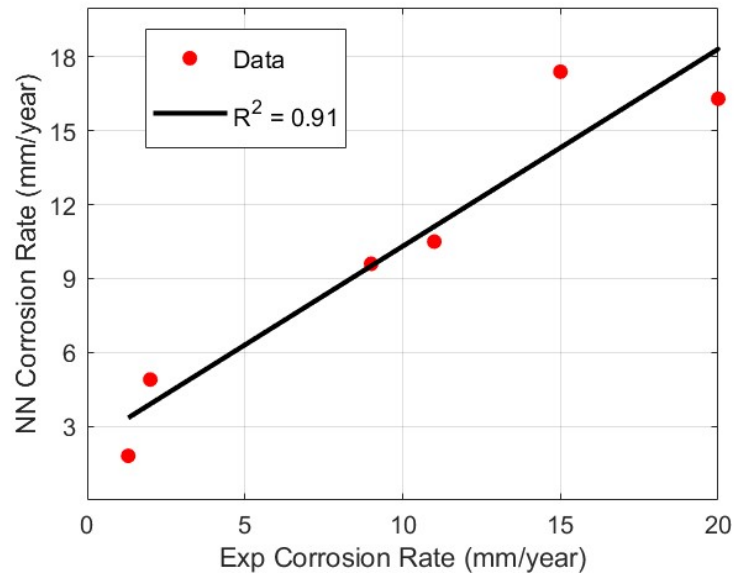
6.3.2 Relevant parameters

• Temperature

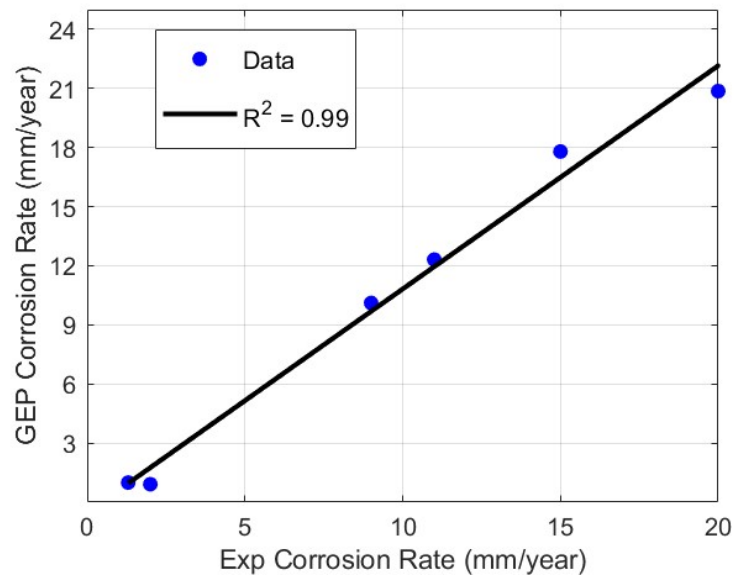
The corrosion rate-temperature profile for all the experimental data points is illustrated in Fig. 6.7. Data points with identical temperatures were plotted using the median corrosion rate value. The classic peak of CO₂ corrosion rate as a function of temperature is represented by a polynomial curve fit. The increase in corrosion rates within the temperature range of 20 °C to 80 °C is caused by accelerating chemical and electrochemical reactions. However, a further rise in temperature reduces carbonates solubility, increases the chance of precipitation, and creates a corrosion-protective layer on the metal. Moreover, increasing the temperature leads to a reduction in the amount of dissolved CO₂ in the aqueous phase, known as the carbonate/temperature dissolution effect. As a result, the concentration of carbonic acid decreases, making the aquatic environment less corrosive. The peak temperature for corrosion is case specific and will be further discussed in the next section.

• pH

The corrosion rate is affected by the acidity or basicity of the solution, which alters the electrochemical reactions taking place at the metal surface. At lower pH values (acidic conditions), the rate of CO₂-induced corrosion is typically higher. This is because the



(a)



(b)

Fig. 6.6 Calculated corrosion rates by mathematical models against experimental data.

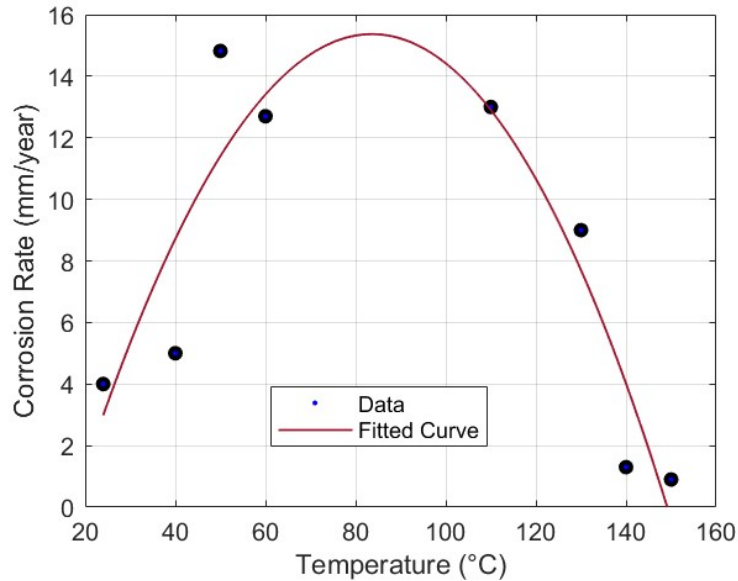


Fig. 6.7 Experimental corrosion rate versus temperature plot for all the training/test datasets.

acid reacts with the metal, forming iron ions, which are then dissolved in the aqueous phase. In contrast, higher pH values typically result in a lower corrosion rate as there are fewer hydrogen ions available to react with the metal surface. This can establish a proper environment for forming of a protective film of compounds like iron carbonate (FeCO_3) or iron hydroxide ($\text{Fe}(\text{OH})_2$) on the metal surface. The resulting film can help slow down the corrosion process (i.e., passivation process).

The behavior of the developed GEP model in predicting corrosion rate at different pressures, temperatures, and (pH)s is depicted in Fig. 6.8. As shown, there is an increase in corrosion rates as the pH decreases, which is consistent with the trend observed for CO_2 corrosion rate versus pH in low-pressure systems ($P < 2\text{MPa}$). It is also clear that at a specific range of temperatures, the corrosion rate is larger (represented by yellow semi-oval shapes). This general trend aligns with the findings of the previous section that there is a higher risk of corrosion within a specific temperature range. However, this temperature domain is sensitive to various factors, including pressure, pH, and other variables.

• CO_2 partial pressure

The corrosion rate of carbon steel in CO_2 -containing environments exhibits a non-linear relationship with the partial pressure of CO_2 . Even a slight variation in the CO_2 partial pressure can have a substantial effect on the corrosion rate. An increase in CO_2 partial pressure enhances its solubility in the aqueous phase, leading to changes in the corrosion rate through two distinct mechanisms. Firstly, it increases the production of hydrogen at

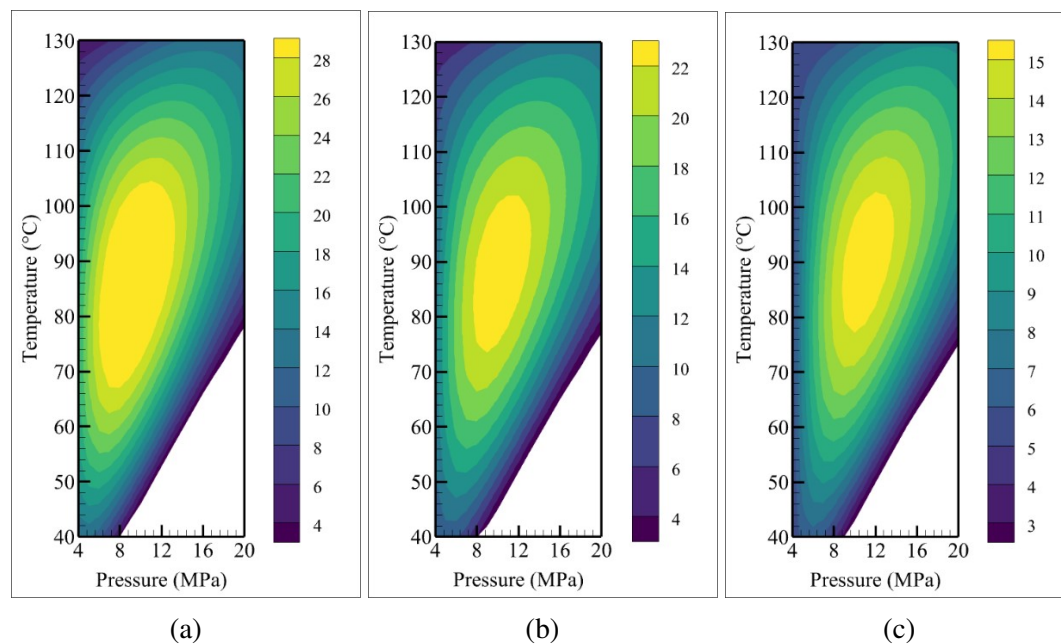


Fig. 6.8 Calculated corrosion rates by the developed GEP model for a) pH=4.5 b) pH=5.5 c) pH=6.5

the cathode, and secondly, it promotes the formation of carbonate-oxide films on the metal surface. The corrosion rate is ultimately determined by the relative efficiency of these two processes.

A rise in CO₂ partial pressure results in an increase in the concentration of H₂CO₃, which in turn leads to an acceleration of the redox half-reaction $2\text{H}_2\text{CO}_3 + 2\text{e} \rightarrow \text{H}_2 + 2\text{HCO}_3^-$. However, when conditions are favorable for the formation of iron carbonate (FeCO₃) or other corrosion products, a higher CO₂ partial pressure along with a high pH can lead to an increased formation of the protective layer. This layer acts as a barrier that restricts the diffusion of CO₂ and other corrosive species to the metal surface. It's worth noting that if the CO₂ partial pressure exceeds a certain threshold, the protective layer may become unstable and start to dissolve. This can lead to an increase in the corrosion rate once again. Fig. 6.9 demonstrates the non-linear effect of CO₂ partial pressure on corrosion rate, which reflects the complex interplay between the formation of protective layers and the dissolution of these layers under varying CO₂ partial pressure conditions.

6.4 Conclusion

The primary objective of this study is to quantify high-pressure CO₂-induced corrosion in wellbores, which is an essential factor endangering the longevity of geothermal systems.

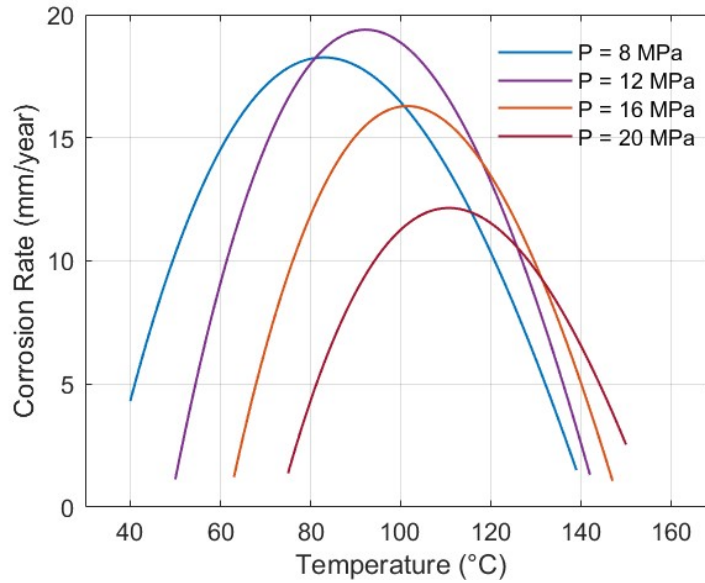


Fig. 6.9 Pressure impact on the corrosion rate [$P = 10 \text{ MPa}$, $U = 2 \text{ m/s}$]

Our findings could be of great interest to the geothermal community since most existing corrosion models have focused primarily on low-pressure CO_2 corrosion ($P_{\text{CO}_2} < 20 \text{ bar}$). However, in geothermal projects, particularly in the context of carbon capture and storage (CCS) applications, the CO_2 partial pressure can be significantly higher. To our knowledge, the machine learning-based corrosion model proposed by Abbas *et al.* [160] provides the best fitting on the available experimental data on high-pressure CO_2 corrosion. Nevertheless, the R^2 -coefficient of 0.91 and average relative error of $\approx 38\%$ in the prediction of corrosion rate (the experimental test dataset) motivated us to further work on their collected dataset and improve the corrosion prediction accuracy by implementing an alternative AI technique. Gene expression programming is the machine learning method employed by the current study to develop the corrosion model. Some important points regarding the developed GEP model and its predicted corrosion rates are listed below:

- The GPG formula proposed in this study exhibits a significantly higher prediction accuracy compared to the NN model developed by Abbas *et al.* [160]. Table 6.3 presents a brief comparison of these two models.
- Chemical and electrochemical reaction rates, carbonates solubility, CO_2 dissolution in the aqueous phase, and generation of the corrosion-protective layer are the main factors controlling the corrosion variation at different temperatures. The alteration of high-pressure GEP-predicted corrosion rate as a function of temperature is similar to its known temperature-dependent trend at low pressures. The success of the developed

Table 6.3 Comparing the accuracy of mathematical models in predicting experimental test dataset

Criterion	GEP	NN
R ² -coefficient	0.99	0.91
Average relative error	21%	38%
Average absolute error	1.25 mm/year	1.77 mm/year

GEP model goes beyond accurately estimating corrosion data. It also precisely predicts the trend of corrosion as a function of input parameters such as partial pressure, temperature, pH, and velocity. The predicted behavior of the model is in good agreement with the observed pattern of experimental data at high pressures.

- Unlike neural networks, gene expression programming is capable of generating an explicit formula that can be easily implemented in various software and codes. For ease of use, the developed GEP function is provided as a simple C++ code in Appendix A.
- It is crucial to note that the developed model is valid only for CO₂-induced carbon steel corrosion. For more information about steel types refer to section (6.2.2 Data collection).

Acknowledgment

The study is part of the subtopic "Geoenergy" in the program "MTET - Materials and Technologies for the Energy Transition" of the Helmholtz Association.

Chapter 7

Conclusions

Geothermal energy is a clean, renewable energy source that can reduce our dependence on fossil fuels and lower CO₂ emissions. By tapping into the Earth's energy, we can work towards a sustainable energy future and mitigate the effects of climate change. Wellbores are critical components of geothermal systems that are drilled into the Earth's crust to access hot water and steam, which can be used to generate electricity or heat buildings. The design, construction, and maintenance of these wells are essential factors in the efficiency and reliability of geothermal systems, and well-designed and maintained wellbores can maximize the flow of geothermal fluids and ensure the long-term sustainability of the geothermal resource.

Numerical modeling is crucial in optimizing the functionality of geothermal wellbores due to the complexity of simulating various physical phenomena, such as gas and salt transport, thermal interactions between the wellbore and reservoir, flow regime triggering, and the complex geometries and trajectories of the wellbore. To simulate these phenomena with precision, mathematical equations and numerical methods are necessary, and the accuracy and efficiency of these techniques can significantly affect the computational complexity and accuracy of the final results. The primary objectives of the current study are to develop a robust numerical tool to comprehensively understand non-isothermal, multiphase, and multicomponent flow in geothermal wellbores and to utilize the gained knowledge to design innovative geothermal frameworks that prioritize wellbore integrity and optimize energy absorption through closed-loop systems. The study aims to improve the efficiency and productivity of geothermal systems resulting in cost savings and enhanced sustainability.

7.1 Major findings of the research

As previously discussed, designing wellbores with good thermal performance and integrity necessitates developing a robust numerical tool to accurately predict the system's behavior under various scenarios. Hence, one of the primary objectives of this study is to develop a fast, accurate, user-friendly, and extendable wellbore simulator capable of handling a wide range of geothermal problems. To achieve this objective, an open-source finite element platform called MOOSE is used to incorporate a fully coupled system of continuity, momentum, energy, and transport equations, as well as advanced equations of state. The object-oriented nature of the developed wellbore simulator (MOSKITO) provides a friendly environment for both users and developers and makes it easy to further develop it and include other complex phenomena. MOSKITO can easily simulate steady-state and transient problems in wellbores with complicated trajectories, casing programs, and configurations (e.g., U-shape, coaxial, multilateral, etc.). Two methods can be used to describe the lateral heat exchange between the wellbore and reservoir. The first method (stand-alone mode) involves using a semi-empirical approach to calculate the heat exchange rate based on the temperature difference between the working fluid and formation, time, and thermophysical properties of the fluid, casing, cement layer, and formation. The second method involves coupling the heat exchange model with a reservoir simulator.

Coupling the 1D modeling on fluid flow in the wellbore to the semi-empirical radial heat model can considerably increase the computation speed. Nonetheless, the significant computational expenses associated with calculating properties of two-phase multicomponent fluids remain a significant challenge that we must address. Therefore, Chapter 3 of this thesis focuses on developing a rapid equation of state for computing properties of geofluids. Determination of the composition of the aqueous and non-aqueous medium is essential for computing two-phase mixtures properties. However, the two commonly used thermodynamic models for computing gas components' solubility in the aqueous phase - the fugacity-fugacity and fugacity-activity models - are highly iterative. As an example, when using the Fugacity-activity algorithm, the fluid temperature and gas component equilibrium constants must be initially guessed, and the Rachford-Rice equation, compressibility factor, and enthalpy should be calculated iteratively. To bypass the need for iterations, we opted to use a machine learning technique called Gene Expression Programming (GEP), which can generate highly accurate explicit formulas for computing target outputs. This innovative equation of state (called GENEOS) is developed with several key factors in mind, including accuracy, computation speed, applicability, and transparency. By utilizing the new GEP functions of GENEOS, fluid temperature can be predicted for 1,000,000 arbitrary sets of pressure, enthalpy, and two-phase composition with an average relative error of only 0.6%. Additionally, when the

GEP functions are used as an initial guess in the F-A algorithm, the error is reduced to zero after the first iteration. One of the significant advantages of GENEOS is its computational efficiency, which reduces EOS-related computational costs by 90%. The equation of state is highly applicable to geothermal applications, including the nine primary components relevant to these fields, such as H₂O, CO₂, CH₄, N₂, H₂S, NaCl, KCl, CaCl₂, and MgCl₂. GENEOS can be used in standalone mode or coupled with any other modeling platform. Moreover, GENEOS is transparent, with all new GEP equations presented as simple C++ codes in Appendix A and implemented equations for other properties and corresponding references clearly addressed in the context of this thesis. Coupling GENEOS to other conservation equations in MOSKITO resulted in fast and accurate modeling of two-phase multicomponent flows in geothermal wellbores.

The developed numerical tool is subsequently used to model the thermal performance of closed-loop deep geothermal (CDG) systems comprising two vertical wellbores connected to each other through a long horizontal extension. This novel geothermal framework is designed to sustainably produce a significant amount of thermal power by mitigating the typical risks associated with open systems, such as subsurface water contamination and potential seismic activity. An intriguing aspect of CDG systems is their ability to operate using the thermosiphon effect. This effect is triggered by the density difference between the injection and horizontal wellbore, which creates a pressure gradient that is sufficient for spontaneous fluid circulation within the system, without requiring any external pumping. Therefore, the study elaborated in Chapter 4 focuses on quantifying thermosiphon flow in CDG systems. The evaluation of the thermosiphon flow rate, generated under various pressure losses at surface facilities, indicates that it is sufficient for producing a significant amount of thermal power with a reasonable extraction temperature. Furthermore, the assessment revealed that this flow rate remains stable for at least one century. Extensive investigations are also conducted to analyze the extraction stability over time. It is found that the extraction temperature can be stabilized by controlling the energy absorption/loss in different sections of CDG systems at lower flow rates. Although the designed CDG system can generate thermal power exceeding 2 MW, the drilling cost for a 12 km total wellbore length may pose a risk to its economic viability. Our primary suggestion for improving power generation per meter of deep closed-loop installations is to operate with multilateral CDG systems. This is discussed in a separate study in chapter 5 of this thesis.

A multilateral closed deep geothermal (MCDG) system is a complex system consisting of several vertical injection wellbores connected through doglegs at a particular depth. The parallel wellbores must be positioned far enough apart to prevent thermal interaction. The injected fluids from the vertical wellbores are initially collected at the doglegs and then

redistributed through horizontal wellbores. Finally, the total injected fluid is extracted through a single production wellbore. To assess the performance of MCDG systems, 160 scenarios were analyzed by varying the system configuration, such as the number of wellbores and flow rate. Through stochastic analysis, it was found that the long-term performance of MCDG systems can be predicted based on their short-term behavior. For instance, the extraction temperature after 30 years of operation can be determined as a function of the extraction temperature after the first year. Remarkably, this correlation is independent of the number of wellbores and flow rate. The extraction temperature and power generation per meter of the system are then used as criteria to filter successful MCDG systems in the subsequent step. One of the key findings of this study is the identification of successful MCDG systems based on a specific relationship between the total flow rate and the number of injection and horizontal wellbores. This result is highly important for the future design of high-performance MCDG systems.

The final study in this Ph.D. project is dedicated to the mathematical prediction of CO₂-induced corrosion in geothermal wellbores. This topic has captured our attention as corrosion poses a significant threat to the wellbore integrity. Upon reviewing the existing literature on corrosion, it is apparent that the majority of corrosion models are only applicable up to a CO₂ partial pressure of 20 bar, rendering them unsuitable for use in deep geothermal systems. Therefore, we decided to develop a machine learning-based model that can accurately fit available experimental data on high-pressure CO₂-induced corrosion. The developed model takes pressure, temperature, pH (or composition), and fluid velocity as input and calculates the corrosion rate accordingly. The developed corrosion model demonstrates a high level of precision, as evidenced by the R² coefficient of 0.99 and an average absolute error of 1.25 *mm/year* in predicting the experimental test dataset.

7.2 Outlook

Although the primary focus of the current study is to evaluate the thermal performance of closed-loop deep geothermal systems, it is essential to conduct a techno-economic assessment (TEA) to determine the feasibility and economic viability of such projects. By assessing the capital costs, operating costs, and potential revenue streams, TEA provides a comprehensive understanding of the financial aspects of closed-loop deep geothermal systems. Additionally, evaluating the drilling risks associated with these systems is important in ensuring that the drilling process is safe and effective. This includes assessing potential geological hazards, the suitability of drilling equipment, and the environmental impact of drilling operations. By conducting thorough TEA and drilling risk evaluations, stakeholders can make informed

decisions about the viability and potential risks associated with closed-loop deep geothermal systems, ultimately helping to drive the adoption of sustainable energy solutions.

The mathematical description of corrosion impact on mineral precipitation in geothermal wellbores is another interesting topic for future studies. Corrosion can create surface irregularities and roughness, which can serve as nucleation sites for mineral precipitation. The types of minerals that form can vary depending on the specific corrosion environment and the composition of the geothermal fluid. For example, corrosion in the presence of dissolved silica can lead to the formation of silica-rich mineral deposits such as quartz, chalcedony, and amorphous silica. On the other hand, corrosion in the presence of sulfates can lead to the formation of sulfates such as gypsum and anhydrite. However, in some cases, corrosion can also inhibit mineral precipitation by disrupting the chemical balance needed for precipitation to occur. Therefore, the impact of corrosion on mineral precipitation is complex and dependent on multiple factors, including the composition of the geothermal fluid, the temperature, and the corrosion environment.

References

- [1] NASA. Global surface temperature. Available at <https://climate.nasa.gov/vital-signs/global-temperature/>, 2023.
- [2] NOAA. Global monitoring laboratory - carbon cycle greenhouse gases. Available at <https://gml.noaa.gov/ccgg/trends/data.html>, 2022.
- [3] Saif Al Ghafri, Geoffrey C. Maitland, and J. P. Martin Trusler. Densities of aqueous mgcl_2 (aq), cacl_2 (aq), ki (aq), nacl (aq), kcl (aq), alcl_3 (aq), and $(0.964 \text{ nacl} + 0.136 \text{ kcl})$ (aq) at temperatures between (283 and 472) k, pressures up to 68.5 mpa, and molalities up to 6 mol·kg⁻¹. *Journal of Chemical & Engineering Data*, 57(4):1288–1304, 2012.
- [4] Marc Laliberté. Model for calculating the viscosity of aqueous solutions. *Journal of Chemical & Engineering Data*, 52(2):321–335, 2007.
- [5] Lala A. Akhmedova-Azizova and Ilmutdin M. Abdulagatov. Thermal conductivity of aqueous cacl_2 solutions at high temperatures and high pressures. *Journal of Solution Chemistry*, 43(3):421–444, 2014.
- [6] NCEI. Annual 2022 global climate report. Available at <https://www.ncei.noaa.gov/access/monitoring/monthly-report/global/202213>, 2023.
- [7] IEA. International energy agency. Available at <https://www.iea.org/>, 2022.
- [8] ThinkGeoEnergy. Thinkgeoenergy's top 10 geothermal countries 2022 – power generation capacity (mw). Available at <https://www.thinkgeoenergy.com/thinkgeoenergys-top-10-geothermal-countries-2022-power-generation-capacity-mw/>, 2022.
- [9] Gabriel Plascencia, Lamberto Díaz–Damacillo, and Minerva Robles-Agudo. On the estimation of the friction factor: a review of recent approaches. *SN Applied Sciences*, 2(2), jan 2020.
- [10] Shuxin Huang. Reading the moody chart with a linear interpolation method. *Scientific Reports*, 12(1), apr 2022.
- [11] John D. Valiantzas. Explicit power formula for the darcy–weisbach pipe flow equation: Application in optimal pipeline design. *Journal of Irrigation and Drainage Engineering*, 134(4):454–461, aug 2008.
- [12] T. K. Serghides. Estimate friction factor accurately. *Chemical Engineering*, 91:63–64, 1984.

- [13] H. Shi, J. A. Holmes, L. J. Durlofsky, K. Aziz, L. R. Diaz, B. Alkaya, and G. Oddie. Drift-flux modeling of two-phase flow in wellbores. *SPE Journal*, 10(01):24–33, mar 2005.
- [14] H. Shi, J. A. Holmes, L. R. Diaz, L. J. Durlofsky, and K. Aziz. Drift-flux parameters for three-phase steady-state flow in wellbores. *SPE Journal*, 10(02):130–137, jun 2005.
- [15] A. R. Hasan, C. S. Kabir, and M. Sayarpour. A basic approach to wellbore two-phase flow modeling. In *All Days*. SPE, nov 2007.
- [16] H. J. Ramey. Wellbore heat transmission. *Journal of Petroleum Technology*, 14(04):427–435, 1962.
- [17] G. P. Willhite. Over-all heat transfer coefficients in steam and hot water injection wells. *Journal of Petroleum Technology*, 19(05):607–615, 1967.
- [18] D. Dropkin and E. Somerscales. Heat transfer by natural convection in liquids confined by two parallel plates which are inclined at various angles with respect to the horizontal. *Journal of Heat Transfer*, 87(1):77–82, feb 1965.
- [19] Nicolas Spycher and Karsten Pruess. Co₂-h₂o mixtures in the geological sequestration of co₂. ii. partitioning in chloride brines at 12–100°C and up to 600 bar. *Geochimica et Cosmochimica Acta*, 69(13):3309–3320, 2005.
- [20] Nikolay N. Akinfiev and Laryyn W. Diamond. Thermodynamic description of aqueous nonelectrolytes at infinite dilution over a wide range of state parameters. *Geochimica et Cosmochimica Acta*, 67(4):613–629, 2003.
- [21] Mohsen Zirrahi, Reza Azin, Hassan Hassanzadeh, and Mahmood Moshfeghian. Mutual solubility of ch₄, co₂, h₂s, and their mixtures in brine under subsurface disposal conditions. *Fluid Phase Equilibria*, 324:80–93, 2012.
- [22] John W. Lund and Aniko N. Toth. Direct utilization of geothermal energy 2020 worldwide review. *Geothermics*, 90:101915, 2021.
- [23] Khaled Salhein, C. J. Kobus, and Mohamed Zohdy. Forecasting installation capacity for the top 10 countries utilizing geothermal energy by 2030. *Thermo*, 2(4):334–351, 2022.
- [24] William T. Stringfellow and Patrick F. Dobson. Technology for the recovery of lithium from geothermal brines. *Energies*, 14(20):6805, 2021.
- [25] Ju Miao, Kaiyu Zhao, Feng Guo, Lina Xu, Yingchun Xie, and Tianlong Deng. Novel lis-doped mixed matrix membrane absorbent with high structural stability for sustainable lithium recovery from geothermal water. *Desalination*, 527:115570, 2022.
- [26] Yiqun Zhang, Chao Yu, Gensheng Li, Xiaofeng Guo, Gaosheng Wang, Yu Shi, Chi Peng, and Yawen Tan. Performance analysis of a downhole coaxial heat exchanger geothermal system with various working fluids. *Applied Thermal Engineering*, 163:114317, 2019.

- [27] Richardson M. Abraham-A, Fabio Taioli, and Anthony I. Nzekwu. Physical properties of sandstone reservoirs: Implication for fluid mobility. *Energy Geoscience*, 3(4):349–359, 2022.
- [28] Bin Yuan, Weiqiang Luo, Bihua Xu, and Hongfei Fan. A prediction model for carbonation depth of cement sheath of carbon capture utilization and storage (ccus) wells. *Journal of Natural Gas Science and Engineering*, 108:104842, 2022.
- [29] Thomas M.P. Ratouis, Sandra Ó. Snæbjörnsdóttir, Martin J. Voigt, Bergur Sigfússon, Gunnar Gunnarsson, Edda S. Aradóttir, and Vala Hjörleifsdóttir. Carbfix 2: A transport model of long-term co₂ and h₂s injection into basaltic rocks at hellisheidi, sw-iceland. *International Journal of Greenhouse Gas Control*, 114:103586, 2022.
- [30] Anna Khaghani, Abhijit Date, and Aliakbar Akbarzadeh. Sustainable removal of non-condensable gases from geothermal waters. *Renewable and Sustainable Energy Reviews*, 21:204–214, 2013.
- [31] Siyuan Chen, Jiangfeng Liu, Qi Zhang, Fei Teng, and Benjamin C. McLellan. A critical review on deployment planning and risk analysis of carbon capture, utilization, and storage (ccus) toward carbon neutrality. *Renewable and Sustainable Energy Reviews*, 167:112537, 2022.
- [32] Danchen Li, Soheil Saraji, Zunsheng Jiao, and Ye Zhang. Co₂ injection strategies for enhanced oil recovery and geological sequestration in a tight reservoir: An experimental study. *Fuel*, 284:119013, 2021.
- [33] Osama Massarweh and Ahmad S. Abushaikha. A review of recent developments in co₂ mobility control in enhanced oil recovery. *Petroleum*, 8(3):291–317, 2022.
- [34] Ingrid Stober and Kurt Bucher. Geothermal systems in high-enthalpy regions. In Ingrid Stober and Kurt Bucher, editors, *Geothermal Energy*, pages 227–256. Springer International Publishing, Cham, 2021.
- [35] Stefan Finsterle, Eric L Sonnenthal, and Nicolas Spycher. Advances in subsurface modeling using the tough suite of simulators. *Computers & Geosciences*, 65:2–12, 2014.
- [36] Karsten Pruess. *ECO2N: A TOUGH2 fluid property module for mixtures of water, NaCl, and CO₂*. Lawrence Berkeley National Laboratory Berkeley, CA, 2005.
- [37] Lehua Pan, Nicolas Spycher, Christine Doughty, and Karsten Pruess. Eco2n v2. 0: A tough2 fluid property module for mixtures of water, nacl, and co₂. *Scientific report LBNL-6930E*, 2015.
- [38] Curtis M Oldenburg, George J Moridis, Nicholas Spycher, and Karsten Pruess. Eos7c version 1.0: Tough2 module for carbon dioxide or nitrogen innatural gas (methane) reservoirs. Technical report, Lawrence Berkeley National Lab.(LBNL), Berkeley, CA (United States), 2004.
- [39] Karsten Pruess and Alfredo Battistelli. Tmvoc, a numerical simulator for three-phase non-isothermal flows of multicomponent hydrocarbon mixtures in saturated-unsaturated heterogeneous media. 2002.

- [40] Alfredo Battistelli and Marica Marcolini. Tmgas: A new tough2 eos module for the numerical simulation of gas mixtures injection in geological structures. *International Journal of Greenhouse Gas Control*, 3(4):481–493, 2009.
- [41] Alfredo Battistelli, Claudio Calore, and Karsten Pruess. The simulator tough2/ewasg for modelling geothermal reservoirs with brines and non-condensable gas. *Geothermics*, 26(4):437–464, 1997.
- [42] Zhenhao Duan and Rui Sun. An improved model calculating co₂ solubility in pure water and aqueous nacl solutions from 273 to 533 k and from 0 to 2000 bar. *Chemical Geology*, 193(3-4):257–271, 2003.
- [43] Zhenhao Duan, Rui Sun, Chen Zhu, and I-Ming Chou. An improved model for the calculation of co₂ solubility in aqueous solutions containing na⁺, k⁺, ca²⁺, mg²⁺, cl⁻, and so₄²⁻. *Marine Chemistry*, 98(2-4):131–139, 2006.
- [44] Shu-Xin Hou, Geoffrey C. Maitland, and J. Martin P. Trusler. Measurement and modeling of the phase behavior of the (carbon dioxide+water) mixture at temperatures from 298.15k to 448.15k. *The Journal of Supercritical Fluids*, 73:87–96, 2013.
- [45] Shide Mao, Dehui Zhang, Yongquan Li, and Ningqiang Liu. An improved model for calculating co₂ solubility in aqueous nacl solutions and the application to co₂-h₂o-nacl fluid inclusions. *Chemical Geology*, 347:43–58, 2013.
- [46] Nicolas Spycher and Karsten Pruess. A phase-partitioning model for co₂-brine mixtures at elevated temperatures and pressures: Application to co₂-enhanced geothermal systems. *Transport in Porous Media*, 82(1):173–196, 2010.
- [47] Nicolas Spycher, Karsten Pruess, and Jonathan Ennis-King. Co₂-h₂o mixtures in the geological sequestration of co₂. i. assessment and calculation of mutual solubilities from 12 to 100°c and up to 600 bar. *Geochimica et Cosmochimica Acta*, 67(16):3015–3031, 2003.
- [48] Wei Yan, Shengli Huang, and Erling H. Stenby. Measurement and modeling of co₂ solubility in nacl brine and co₂-saturated nacl brine density. *International Journal of Greenhouse Gas Control*, 5(6):1460–1477, 2011.
- [49] Haining Zhao, Mark V. Fedkin, Robert M. Dilmore, and Serguei N. Lvov. Carbon dioxide solubility in aqueous solutions of sodium chloride at geological conditions: Experimental results at 323.15, 373.15, and 423.15 k and 150 bar and modeling up to 573.15 k and 2000 bar. *Geochimica et Cosmochimica Acta*, 149:165–189, 2015.
- [50] Zhenhao Duan, Rui Sun, Rong Liu, and Chen Zhu. Accurate thermodynamic model for the calculation of h₂s solubility in pure water and brines. *Energy & Fuels*, 21(4):2056–2065, 2007.
- [51] Zhenhao Duan and Shide Mao. A thermodynamic model for calculating methane solubility, density and gas phase composition of methane-bearing aqueous fluids from 273 to 523k and from 1 to 2000bar. *Geochimica et Cosmochimica Acta*, 70(13):3369–3386, 2006.

- [52] Zaman Ziabakhsh-Ganji and Henk Kooi. An equation of state for thermodynamic equilibrium of gas mixtures and brines to allow simulation of the effects of impurities in subsurface CO_2 storage. *International Journal of Greenhouse Gas Control*, 11:S21–S34, 2012.
- [53] C.A.J. Appelo, D. L. Parkhurst, and V.E.A. Post. Equations for calculating hydrogeochemical reactions of minerals and gases such as CO_2 at high pressures and temperatures. *Geochimica et Cosmochimica Acta*, 125:49–67, 2014.
- [54] Henning Francke, Matthias Kraume, and Ali Saadat. Thermal–hydraulic measurements and modelling of the brine circuit in a geothermal well. *Environmental Earth Sciences*, 70(8):3481–3495, 2013.
- [55] Shide Mao and Zhenhao Duan. A thermodynamic model for calculating nitrogen solubility, gas phase composition and density of the N_2 – H_2O – NaCl system. *Fluid Phase Equilibria*, 248(2):103–114, 2006.
- [56] Mohsen Zirrahi, Reza Azin, Hassan Hassanzadeh, and Mahmood Moshfeghian. Prediction of water content of sour and acid gases. *Fluid Phase Equilibria*, 299(2):171–179, 2010.
- [57] Babak Shabani and Javier Vilcáez. Prediction of CO_2 – CH_4 – H_2S – N_2 gas mixtures solubility in brine using a non-iterative fugacity-activity model relevant to CO_2 -meor. *Journal of Petroleum Science and Engineering*, 150:162–179, 2017.
- [58] Jun Li, Lingli Wei, and Xiaochun Li. An improved cubic model for the mutual solubilities of CO_2 – CH_4 – H_2S –brine systems to high temperature, pressure and salinity. *Applied Geochemistry*, 54:1–12, 2015.
- [59] Jun Li, Lingli Wei, and Xiaochun Li. Modeling of CO_2 – CH_4 – H_2S –brine based on cubic eos and fugacity-activity approach and their comparisons. *Energy Procedia*, 63:3598–3607, 2014.
- [60] H. Li and J. Yan. Evaluating cubic equations of state for calculation of vapor–liquid equilibrium of CO_2 and CO_2 -mixtures for CO_2 capture and storage processes. *Applied Energy*, 86(6):826–836, 2009.
- [61] Rana A. Fine and Frank J. Millero. Compressibility of water as a function of temperature and pressure. *The Journal of Chemical Physics*, 59(10):5529–5536, 1973.
- [62] Kenneth S. Pitzer. Thermodynamics of electrolytes. i. theoretical basis and general equations. *The Journal of Physical Chemistry*, 77(2):268–277, 1973.
- [63] Cândida Ferreira. Gene expression programming in problem solving. In Rajkumar Roy, Mario Köppen, Seppo Ovaska, Takeshi Furuhashi, and Frank Hoffmann, editors, *Soft Computing and Industry*, pages 635–653. Springer London, London, 2002.
- [64] Shuhua Gao, Andrew Morgan, and Ting M. ShuhuaGao/geppy: Release 0.1 of geppy, 2020.

- [65] C. O. POPIEL and J. WOJTKOWIAK. Simple formulas for thermophysical properties of liquid water for heat transfer calculations (from 0°C to 150°C). *Heat Transfer Engineering*, 19(3):87–101, 1998.
- [66] Thomas Driesner. The system h₂o–nacl. part ii: Correlations for molar volume, enthalpy, and isobaric heat capacity from 0 to 1000°C, 1 to 5000bar, and 0 to 1 xnacl. *Geochimica et Cosmochimica Acta*, 71(20):4902–4919, 2007.
- [67] Yodha Yudhistra Nusiaputra. *Coupled Hydraulic, Thermal and Chemical Simulations for Geothermal Installations*. PhD thesis, Dissertation, Karlsruhe, Karlsruher Institut für Technologie (KIT), 2017, 2017.
- [68] Ding-Yu Peng and Donald B. Robinson. A new two-constant equation of state. *Industrial & Engineering Chemistry Fundamentals*, 15(1):59–64, 1976.
- [69] Lehua Pan, Nicolas Spycher, Christine Doughty, and Karsten Pruess. Eco2n v2.0: A tough2 fluid property module for modeling co₂-h₂o-nacl systems to elevated temperatures of up to 300°C. *Greenhouse Gases: Science and Technology*, 7(2):313–327, 2017.
- [70] Wolfgang Wagner and Hans-Joachim Kretzschmar. *International Steam Tables*. Springer Berlin Heidelberg, Berlin, Heidelberg, 2008.
- [71] Peter J. Linstrom and William G. Mallard. The nist chemistry webbook: A chemical data resource on the internet. *Journal of Chemical & Engineering Data*, 46(5):1059–1063, 2001.
- [72] Babak Shabani and Javier Vilcáez. Toughreact-co2bio – a new module to simulate geological carbon storage under biotic conditions (part 1): The multiphase flow of co₂-ch₄-h₂-h₂s gas mixtures. *Journal of Natural Gas Science and Engineering*, 63:85–94, 2019.
- [73] A. Fenghour, William A. Wakeham, and V. Vesovic. The viscosity of carbon dioxide. *Journal of Physical and Chemical Reference Data*, 27(1):31–44, 1998.
- [74] V. Vesovic, W. A. Wakeham, G. A. Olchoway, J. V. Sengers, J. T. R. Watson, and J. Millat. The transport properties of carbon dioxide. *Journal of Physical and Chemical Reference Data*, 19(3):763–808, 1990.
- [75] Makita Tadashi, Tanaka Yoshiyuki, and Nagashima Akira. Evaluation and correlation of viscosity data : the most probable values of the viscosity of gaseous methane. *The Review of Physical Chemistry of Japan*, 43, 1973.
- [76] K. Stephan, R. Krauss, and A. Laesecke. Viscosity and thermal conductivity of nitrogen for a wide range of fluid states. *Journal of Physical and Chemical Reference Data*, 16(4):993–1023, 1987.
- [77] Binod R. Giri, Robert A. Marriott, and Pierre Blais. H₂s viscosities and densities at high-temperatures and pressures. In Ying Wu, John J. Carroll, and Weiyao Zhu, editors, *Sour Gas and Related Technologies*, volume 66, pages 37–47. Wiley, 2012.

- [78] C. R. Wilke. A viscosity equation for gas mixtures. *The Journal of Chemical Physics*, 18(4):517–519, 1950.
- [79] Laurel A. Watts. Electrolytes. properties of solutions. methods for calculation of multicomponent systems and experimental data on thermal conductivity and surface tension. by g. g. asejev. begell house, inc., new york. 1998. 611 pp. \$275.50. isbn 1-56700-106-8. *Journal of Chemical & Engineering Data*, 44(6):1435, 1999.
- [80] Ali Akbar Amooey. A simple correlation to predict thermal conductivity of supercritical carbon dioxide. *The Journal of Supercritical Fluids*, 86:1–3, 2014.
- [81] R. C. Prasad, J. E. S. Venart, and N. Mani. Thermal conductivity of methane and ethane. In T. Ashworth and David R. Smith, editors, *Thermal Conductivity 18*, pages 81–91. Springer US, Boston, MA, 1985.
- [82] E. W. Lemmon and R. T. Jacobsen. Viscosity and thermal conductivity equations for nitrogen, oxygen, argon, and air. *International Journal of Thermophysics*, 25(1):21–69, 2004.
- [83] Bruce E. Poling, J. M. Prausnitz, and John P. O’Connell. *The properties of gases and liquids*. McGraw-Hill, New York, 5th ed. edition, 2007.
- [84] Cody J. Permann, Derek R. Gaston, David Andrs, Robert W. Carlsen, Fande Kong, Alexander D. Lindsay, Jason M. Miller, John W. Peterson, Andrew E. Slaughter, Roy H. Stogner, and Richard C. Martineau. Moose: Enabling massively parallel multiphysics simulation. *SoftwareX*, 11(10):100430, 2020.
- [85] Morteza Esmaeilpour, Maziar Gholami Korzani, and Thomas Kohl. Impact of thermosiphoning on long-term behavior of closed-loop deep geothermal systems for sustainable energy exploitation. *Renewable Energy*, 194:1247–1260, 2022.
- [86] Morteza Esmaeilpour, Maziar Gholami Korzani, and Thomas Kohl. *Performance Analyses of Deep Closed-loop U-shaped Heat Exchanger System with a Long Horizontal Extension: 46th Workshop on Geothermal Reservoir Engineering*. Stanford University, Stanford, California. 2021.
- [87] Morteza Esmaeilpour, Maziar Gholami Korzani, and Thomas Kohl. *Evaluation of the Advantages of Multilateral Closed Deep Geothermal Frameworks over Conventional Geothermal Systems: 47th Workshop on Geothermal Reservoir Engineering*. Stanford University, Stanford, California. 2022.
- [88] Morteza Esmaeilpour, Maziar Gholami Korzani, and Thomas Kohl. Stochastic performance assessment on long-term behavior of multilateral closed deep geothermal systems. *Renewable Energy*, 2023.
- [89] S. Eyerer, C. Schiffechner, S. Hofbauer, W. Bauer, C. Wieland, and H. Spliethoff. Combined heat and power from hydrothermal geothermal resources in germany: An assessment of the potential. *Renewable and Sustainable Energy Reviews*, 120:109661, 2020.

- [90] Maziar Gholami Korzani, Sebastian Held, and Thomas Kohl. Numerical based filtering concept for feasibility evaluation and reservoir performance enhancement of hydrothermal doublet systems. *Journal of Petroleum Science and Engineering*, 190:106803, 2020.
- [91] Alessandro Santilano, Eugenio Trumpy, Gianluca Gola, Assunta Donato, Davide Scrocca, Federica Ferrarini, Francesco Brozzetti, Rita de Nardis, Giusy Lavecchia, and Adele Manzella. A methodology for assessing the favourability of geopressured-geothermal systems in sedimentary basin plays: A case study in abruzzo (italy). *Geofluids*, 2019:1–28, 2019.
- [92] Robert Egert, Maziar Gholami Korzani, Sebastian Held, and Thomas Kohl. Implications on large-scale flow of the fractured eggs reservoir soultz inferred from hydraulic data and tracer experiments. *Geothermics*, 84:101749, 2020.
- [93] Songyan Li, Yifan Wang, and Kaiqiang Zhang. Exergy analysis of heat extraction from hot dry rock by enclosed water recycling in a horizontal well. *Geothermics*, 86:101867, 2020.
- [94] Anna Jentsch, Egbert Jolie, David G. Jones, Helen Taylor-Curran, Loïc Peiffer, Martin Zimmer, and Bob Lister. Magmatic volatiles to assess permeable volcano-tectonic structures in the los humeros geothermal field, mexico. *Journal of Volcanology and Geothermal Research*, 394:106820, 2020.
- [95] Javad Nouraliee, Davar Ebrahimi, Ali Dashti, Maziar Gholami Korzani, and Sepehr Sangin. Appraising mahallat geothermal region using thermal surveying data accompanied by the geological, geochemical and gravity analyses. *Scientific reports*, 11(1):12190, 2021.
- [96] Robert Egert, Fabian Nitschke, Maziar Gholami Korzani, and Thomas Kohl. Stochastic 3d navier–stokes flow in self–affine fracture geometries controlled by anisotropy and channeling. *Geophysical Research Letters*, 48(9), 2021.
- [97] Quan Gan and Qinghua Lei. Induced fault reactivation by thermal perturbation in enhanced geothermal systems. *Geothermics*, 86:101814, 2020.
- [98] Graciela Jharap, Laura P. van Leeuwen, Robert Mout, Wouter E. van der Zee, Femke M. Roos, and Annemarie G. Muntendam-Bos. Ensuring safe growth of the geothermal energy sector in the netherlands by proactively addressing risks and hazards. *Netherlands Journal of Geosciences*, 99, 2020.
- [99] Kai Stricker, Jens C. Grimmer, Robert Egert, Judith Bremer, Maziar Gholami Korzani, Eva Schill, and Thomas Kohl. The potential of depleted oil reservoirs for high-temperature storage systems. *Energies*, 13(24):6510, 2020.
- [100] Zhenjun Ma, Lei Xia, Xuemei Gong, Georgios Kokogiannakis, Shugang Wang, and Xinlei Zhou. Recent advances and development in optimal design and control of ground source heat pump systems. *Renewable and Sustainable Energy Reviews*, 131:110001, 2020.

- [101] Debasree Roy, Tanusree Chakraborty, Dipanjan Basu, and Bishwajit Bhattacharjee. Feasibility and performance of ground source heat pump systems for commercial applications in tropical and subtropical climates. *Renewable Energy*, 152:467–483, 2020.
- [102] L. Rybach and T. Kohl. *The geothermal heat pump boom in Switzerland and its background*. In: *Proceedings of International Geothermal Congress*. Reykjavik, Iceland, 2003.
- [103] Xianzhi Song, Yu Shi, Gensheng Li, Ruiyue Yang, Zhengming Xu, Rui Zheng, Gaosheng Wang, and Zehao Lyu. Heat extraction performance simulation for various configurations of a downhole heat exchanger geothermal system. *Energy*, 141:1489–1503, 2017.
- [104] S. Signorelli, T. Kohl, and L. Rybach. *Sustainability of Production from Borehole Heat Exchanger Fields*. In: *Proceedings of World Geothermal Congress*. Antalya, Turkey, 2005.
- [105] Yu Shi, Xianzhi Song, Gensheng Li, Ruixia Li, Yiqun Zhang, Gaosheng Wang, Rui Zheng, and Zehao Lyu. Numerical investigation on heat extraction performance of a downhole heat exchanger geothermal system. *Applied Thermal Engineering*, 134:513–526, 2018.
- [106] Gaosheng Wang, Xianzhi Song, Yu Shi, Ruiyue Yang, Feixue Yulong, Rui Zheng, and Jiacheng Li. Heat extraction analysis of a novel multilateral-well coaxial closed-loop geothermal system. *Renewable Energy*, 163:974–986, 2021.
- [107] Cristina Sáez Blázquez, Arturo Farfán Martín, Ignacio Martín Nieto, Pedro Carrasco García, Luis Santiago Sánchez Pérez, and Diego González-Aguilera. Analysis and study of different grouting materials in vertical geothermal closed-loop systems. *Renewable Energy*, 114:1189–1200, 2017.
- [108] Adel Eswiasi and Phalguni Mukhopadhyaya. Critical review on efficiency of ground heat exchangers in heat pump systems. *Clean Technologies*, 2(2):204–224, 2020.
- [109] Satish Kumar and K. Murugesan. Optimization of geothermal interaction of a double u-tube borehole heat exchanger for space heating and cooling applications using taguchi method and utility concept. *Geothermics*, 83:101723, 2020.
- [110] Burkhard Sanner. *Summary of EGC 2019 Country Update Reports on Geothermal Energy in Europe*. In: *proceedings of European Geothermal Congress*. Den Haag, Netherlands, 2019.
- [111] Martin Kaltschmitt, Ernst Huenges, Helmut Wolff, Jörg Baumgärtner, Peer Hoth, Martin Kayser, Burkhardt Sanner, Kuno Schallenberg, Reinhard Jung, Traugott Scheytt, and Rainer Lux. *Energy from geothermal energy*. Springer spectrum, 1 edition, 1999.
- [112] Robert A. Caulk and Ingrid Tomac. Reuse of abandoned oil and gas wells for geothermal energy production. *Renewable Energy*, 112:388–397, 2017.
- [113] Yong-Le Nian and Wen-Long Cheng. Evaluation of geothermal heating from abandoned oil wells. *Energy*, 142:592–607, 2018.

- [114] Mohamad Kharseh, Mohammed Al-Khawaja, and Ferri Hassani. Optimal utilization of geothermal heat from abandoned oil wells for power generation. *Applied Thermal Engineering*, 153:536–542, 2019.
- [115] T. Kohl, M. Salton, and L. Rybach. *Data analysis of the deep borehole heat exchanger plant Weissbad (Switzerland)*. In: *Proceedings of World Geothermal Congress*. Kyushu-Tohoku, Japan, 2000.
- [116] Thomas Kohl, Renzo Brenni, and Walter Eugster. System performance of a deep borehole heat exchanger. *Geothermics*, 31(6):687–708, 2002.
- [117] Yibin Huang, Yanjun Zhang, Yangyang Xie, Yu Zhang, Xuefeng Gao, and Jingchen Ma. Long-term thermal performance analysis of deep coaxial borehole heat exchanger based on field test. *Journal of Cleaner Production*, 278:123396, 2021.
- [118] Esa Dube Kerme and Alan S. Fung. Comprehensive simulation based thermal performance comparison between single and double u-tube borehole heat exchanger and sensitivity analysis. *Energy and Buildings*, 241:110876, 2021.
- [119] Elias M. Salilih, Nidal H. Abu-Hamdeh, and Hakan F. Oztop. Analysis of double u-tube ground heat exchanger for renewable energy applications with two-region simulation model by combining analytical and numerical techniques. *International Communications in Heat and Mass Transfer*, 123:105144, 2021.
- [120] N. Jamshidi and A. Mosaffa. Investigating the effects of geometric parameters on finned conical helical geothermal heat exchanger and its energy extraction capability. *Geothermics*, 76:177–189, 2018.
- [121] Hossein Javadi, Seyed Soheil Mousavi Ajarostaghi, Mohsen Pourfallah, and Mohammad Zaboli. Performance analysis of helical ground heat exchangers with different configurations. *Applied Thermal Engineering*, 154:24–36, 2019.
- [122] Jeffrey D. Templeton, Seyed Ali Ghoreishi-Madiseh, Ferri P. Hassani, Agus P. Sasmito, and Jundika C. Kurnia. Numerical and experimental study of transient conjugate heat transfer in helical closed-loop geothermal heat exchangers for application of thermal energy storage in backfilled mine stopes. *International Journal of Energy Research*, 44(12):9609–9616, 2020.
- [123] Hossein Javadi, Seyed Soheil Mousavi Ajarostaghi, Marc A. Rosen, and Mohsen Pourfallah. Performance of ground heat exchangers: A comprehensive review of recent advances. *Energy*, 178:207–233, 2019.
- [124] Salaheldin Elkatatny, Hany Gamal, Abdulmalek Ahmed, Pranjal Sarmah, Shiv Sangaru, and Maryam Alohaly. A novel solution for severe loss prevention while drilling deep wells. *Sustainability*, 12(4):1339, 2020.
- [125] Edoardo Rossi, Shahin Jamali, Volker Wittig, Martin O. Saar, and Philipp Rudolf von Rohr. A combined thermo-mechanical drilling technology for deep geothermal and hard rock reservoirs. *Geothermics*, 85:101771, 2020.

- [126] Edoardo Rossi, Shahin Jamali, Martin O. Saar, and Philipp Rudolf von Rohr. Field test of a combined thermo-mechanical drilling technology. mode i: Thermal spallation drilling. *Journal of Petroleum Science and Engineering*, 190:107005, 2020.
- [127] Edoardo Rossi, Shahin Jamali, Dennis Schwarz, Martin O. Saar, and Philipp Rudolf von Rohr. Field test of a combined thermo-mechanical drilling technology. mode ii: Flame-assisted rotary drilling. *Journal of Petroleum Science and Engineering*, 190:106880, 2020.
- [128] Jia Wang, Fabian Nitschke, Maziar Gholami Korzani, and Thomas Kohl. Temperature log simulations in high-enthalpy boreholes. *Geothermal Energy*, 7(1), 2019.
- [129] Eavor – the first truly scalable form of clean baseload power, 10/4/2021.
- [130] Andres Budiono, Suyitno Suyitno, Imron Rosyadi, Afif Faishal, and Albert Xaverio Ilyas. A systematic review of the design and heat transfer performance of enhanced closed-loop geothermal systems. *Energies*, 15(3):742, 2022.
- [131] Xianzhi Song, Yu Shi, Gensheng Li, Ruiyue Yang, Gaosheng Wang, Rui Zheng, Jiacheng Li, and Zehao Lyu. Numerical simulation of heat extraction performance in enhanced geothermal system with multilateral wells. *Applied Energy*, 218:325–337, 2018.
- [132] Fengrui Sun, Yuedong Yao, Guozhen Li, and Xiangfang Li. Geothermal energy development by circulating co₂ in a u-shaped closed loop geothermal system. *Energy Conversion and Management*, 174:971–982, 2018.
- [133] Xiaohui Sun, Zhiyuan Wang, Youqiang Liao, Baojiang Sun, and Yonghai Gao. Geothermal energy production utilizing a u-shaped well in combination with supercritical co₂ circulation. *Applied Thermal Engineering*, 151:523–535, 2019.
- [134] Wanju Yuan, Zhuoheng Chen, Stephen E. Grasby, and Edward Little. Closed-loop geothermal energy recovery from deep high enthalpy systems. *Renewable Energy*, 177:976–991, 2021.
- [135] Ali Ghavidel, Robert Gracie, and Maurice B. Dusseault. Transient heat transfer in a horizontal well in hot dry rock – model, solution, and response surfaces for practical inputs. *Applied Thermal Engineering*, 195:117158, 2021.
- [136] AmirHossein Fallah, Qifan Gu, Dongmei Chen, Pradeepkumar Ashok, Eric van Oort, and Michael Holmes. Globally scalable geothermal energy production through managed pressure operation control of deep closed-loop well systems. *Energy Conversion and Management*, 236:114056, 2021.
- [137] Xiong Zhang. Numerical study of geothermal district heating from a ground heat exchanger coupled with a heat pump system. *Applied Thermal Engineering*, 185:116335, 2021.
- [138] Yuzhu Chen, Jun Wang, and Peter D. Lund. Sustainability evaluation and sensitivity analysis of district heating systems coupled to geothermal and solar resources. *Energy Conversion and Management*, 220:113084, 2020.

- [139] Morteza Esmaeilpour and Maziar Gholami Korzani. Enhancement of immiscible two-phase displacement flow by introducing nanoparticles and employing electro- and magneto-hydrodynamics. *Journal of Petroleum Science and Engineering*, 196:108044, 2021.
- [140] Morteza Esmaeilpour and Maziar Gholami Korzani. Analyzing impacts of interfacial instabilities on the sweeping power of newtonian fluids to immiscibly displace power-law materials. *Processes*, 9(5):742, 2021.
- [141] Maziar Gholami Korzani, Fabian Nitschke, Sebastian Held, and Thomas Kohl. The development of a fully coupled wellbore-reservoir simulator for geothermal application. *Geothermal Resources Council Transactions*, 43:927–936, 2019.
- [142] Derek Gaston, Chris Newman, Glen Hansen, and Damien Lebrun-Grandié. Moose: A parallel computational framework for coupled systems of nonlinear equations. *Nuclear Engineering and Design*, 239(10):1768–1778, 2009.
- [143] S. Livescu, L. J. Durlofsky, K. Aziz, and J. C. Ginestra. A fully-coupled thermal multiphase wellbore flow model for use in reservoir simulation. *Journal of Petroleum Science and Engineering*, 71(3-4):138–146, 2010.
- [144] M. L. Huber, R. A. Perkins, A. Laesecke, D. G. Friend, J. V. Sengers, M. J. Assael, I. N. Metaxa, E. Vogel, R. Mareš, and K. Miyagawa. New international formulation for the viscosity of h₂o. *Journal of Physical and Chemical Reference Data*, 38(2):101–125, 2009.
- [145] S. Phillips, A. Igbene, j. Fair, H. Ozbek, and M. Tavana. *A Technical Databook for Geothermal Energy Utilization*. Lawrence Berkeley National Laboratory, 1981.
- [146] I. E. Idelchik. *Handbook of hydraulic resistance*. New York, 3 edition, 1996.
- [147] Hwei Tang, Boyue Xu, A. Rashid Hasan, Zhuang Sun, and John Killough. Modeling wellbore heat exchangers: Fully numerical to fully analytical solutions. *Renewable Energy*, 133:1124–1135, 2019.
- [148] Julian Formhals, Frederik Feike, Hoofar Hemmatabady, Bastian Welsch, and Ingo Sass. Strategies for a transition towards a solar district heating grid with integrated seasonal geothermal energy storage. *Energy*, 228:120662, 2021.
- [149] Christoph Clauser and Markus Ewert. The renewables cost challenge: Levelized cost of geothermal electric energy compared to other sources of primary energy – review and case study. *Renewable and Sustainable Energy Reviews*, 82:3683–3693, 2018.
- [150] Emmanuel Gaucher, Martin Schoenball, Oliver Heidbach, Arno Zang, Peter A. Fokker, Jan-Diederik van Wees, and Thomas Kohl. Induced seismicity in geothermal reservoirs: A review of forecasting approaches. *Renewable and Sustainable Energy Reviews*, 52:1473–1490, 2015.
- [151] Amalsh Dhar, M. Anne Naeth, P. Devereaux Jennings, and Mohamed Gamal El-Din. Geothermal energy resources: potential environmental impact and land reclamation. *Environmental Reviews*, 28(4):415–427, 2020.

- [152] Tharaka Dilanka Rathnaweera, Wei Wu, Yinlin Ji, and Ranjith Pathegama Gamage. Understanding injection-induced seismicity in enhanced geothermal systems: From the coupled thermo-hydro-mechanical-chemical process to anthropogenic earthquake prediction. *Earth-Science Reviews*, 205:103182, 2020.
- [153] Yu Shi, Xianzhi Song, Gaosheng Wang, John McLennan, Bryan Forbes, Xiaojiang Li, and Jiacheng Li. Study on wellbore fluid flow and heat transfer of a multilateral-well co2 enhanced geothermal system. *Applied Energy*, 249:14–27, 2019.
- [154] Xuefeng Gao, Yanjun Zhang, Yibin Huang, Yongjie Ma, Yi Zhao, and Qiangbin Liu. Study on heat extraction considering the number and orientation of multilateral wells in a complex fractured geothermal reservoir. *Renewable Energy*, 177:833–852, 2021.
- [155] Guofeng Song, Xianzhi Song, Gensheng Li, Yu Shi, Gaosheng Wang, Jiayan Ji, Fuqiang Xu, and Zihao Song. An integrated multi-objective optimization method to improve the performance of multilateral-well geothermal system. *Renewable Energy*, 172:1233–1249, 2021.
- [156] Gaosheng Wang, Xianzhi Song, Yu Shi, Feixue Yulong, Ruiyue Yang, and Jiacheng Li. Comparison of production characteristics of various coaxial closed-loop geothermal systems. *Energy Conversion and Management*, 225:113437, 2020.
- [157] M. J. Assael, S. A. Monogenidou, M. L. Huber, R. A. Perkins, and J. V. Sengers. New international formulation for the viscosity of heavy water. *Journal of Physical and Chemical Reference Data*, 50(3):033102, 2021.
- [158] Abdur Rehman Mazhar, Shuli Liu, and Ashish Shukla. A state of art review on the district heating systems. *Renewable and Sustainable Energy Reviews*, 96:420–439, nov 2018.
- [159] DOE. U.s. department of energy. Available at <https://www.energy.gov/>, 2022.
- [160] Muhammad Hashim Abbas, Rosemary Norman, and Alasdair Charles. Neural network modelling of high pressure co2 corrosion in pipeline steels. *Process Safety and Environmental Protection*, 119:36–45, 2018.
- [161] Satya Widya Yudha, Benny Tjahjono, and Philip Longhurst. Sustainable transition from fossil fuel to geothermal energy: A multi-level perspective approach. *Energies*, 15(19):7435, 2022.
- [162] Jun He, Lin Chen, and Yanjing Su. Role of mn addition on the general corrosion and pitting corrosion behavior of 13cr stainless steel. *Anti-Corrosion Methods and Materials*, 69(1):94–103, 2022.
- [163] Liang Wei, Yong Liu, Qian Li, and Y. Frank Cheng. Effect of roughness on general corrosion and pitting of (fecocrni)0.89(wc)0.11 high-entropy alloy composite in 3.5 wt.% nacl solution. *Corrosion Science*, 146:44–57, 2019.
- [164] K.V Akpanyung and R.T Loto. Pitting corrosion evaluation: a review. *Journal of Physics: Conference Series*, 1378(2):022088, 2019.

- [165] Siavash Jafarzadeh, Ziguang Chen, and Florin Bobaru. Computational modeling of pitting corrosion. *Corrosion Reviews*, 37(5):419–439, 2019.
- [166] Heng Chen, Zhaochong Lv, Lin Lu, Yunhua Huang, and Xiaogang Li. Correlation of micro-galvanic corrosion behavior with corrosion rate in the initial corrosion process of dual phase steel. *Journal of Materials Research and Technology*, 15:3310–3320, 2021.
- [167] Xin Chen, Maxim Gussev, Magdalena Balonis, Mathieu Bauchy, and Gaurav Sant. Emergence of micro-galvanic corrosion in plastically deformed austenitic stainless steels. *Materials & Design*, 203:109614, 2021.
- [168] Yunze Xu, Qiliang Zhang, Qipiao Zhou, Shan Gao, Bin Wang, Xiaona Wang, and Yi Huang. Flow accelerated corrosion and erosion–corrosion behavior of marine carbon steel in natural seawater. *npj Materials Degradation*, 5(1), 2021.
- [169] Li Zeng, Geng Chen, and Hanxin Chen. Comparative study on flow-accelerated corrosion and erosion–corrosion at a 90° carbon steel bend. *Materials*, 13(7):1780, 2020.
- [170] Renshi Zheng, Xiaoyu Zhao, Leilei Dong, Gang Liu, Yi Huang, and Yunze Xu. On the cavitation erosion-corrosion of pipeline steel at different locations of venturi pipe. *Engineering Failure Analysis*, 138:106333, 2022.
- [171] N. Mundhenk, S. Carrero, K. G. Knauss, R. Wonneberger, A. Undisz, and Y. Wu. Kinetic and thermodynamic analysis of high-temperature co₂ corrosion of carbon steel in simulated geothermal nacl fluids. *Corrosion Science*, 171:108597, 2020.
- [172] Xiaoqi Yue, Lei Zhang, Lei Ma, Minxu Lu, Anne Neville, and Yong Hua. Influence of a small velocity variation on the evolution of the corrosion products and corrosion behaviour of super 13cr ss in a geothermal co₂ containing environment. *Corrosion Science*, 178:108983, 2021.
- [173] Bernardus F.M. Pots, editor. *Prediction of Corrosion Rates of the Main Corrosion Mechanisms in Upstream Applications*, volume All Days of NACE CORROSION, 2005.
- [174] Bernardus F.M. Pots, Sergio D. Kapusta, Randy C. John, M.J.J. Simon Thomas, Ian J. Rippon, T. S. Whitham, and Magdy Girgis, editors. *Improvements on de Waard-Milliams Corrosion Prediction and Applications to Corrosion Management*, volume All Days of NACE CORROSION, 2002.
- [175] Rolf Nyborg. Co₂ corrosion models for oil and gas production systems. *Corrosion*, 2010.
- [176] Srdjan Nesic, Rolf Nyborg, Aage Stangeland, and Magnus Nordsveen, editors. *Mechanistic Modeling for CO₂ Corrosion with Protective Iron Carbonate Films*, volume All Days of NACE CORROSION, 2001.
- [177] Bill Hedges, Yuhua Sun, Richard Chapman, Donald Harrop, and Imran Mohammed, editors. *A Prophetic CO₂ Corrosion Tool - But When is it to be Believed?*, volume All Days of NACE CORROSION, 2005.

- [178] Srdjan Nesic, Shihuai Wang, Jiyong Cai, and Ying Xiao, editors. *Integrated CO₂ Corrosion - Multiphase Flow Model*, volume All Days of SPE International Oilfield Corrosion Conference and Exhibition, 2004.
- [179] Srdjan Nesic, Jiyong Cai, and Kun-Lin Lee, editors. *A Multiphase Flow and Internal Corrosion Prediction Model for Mild Steel Pipelines*, volume All Days of NACE CORROSION, 2005.
- [180] Anne Marie Halvorsen and Terje Sontvedt, editors. *CO₂ Corrosion Model for Carbon Steel Including Wall Shear Stress Model for Multiphase Flow and Limits for Production Rate to Avoid Mesa Attack*, volume All Days of NACE CORROSION, 1999.
- [181] Stein Olsen, Anne Marie Halvorsen, Per G. Lunde, and Rolf Nyborg, editors. *CO₂ Corrosion Prediction Model - Basic Principles*, volume All Days of NACE CORROSION, 2005.
- [182] C. de Waard, U. Lotz, and D. E. Milliams. Predictive model for CO₂ corrosion engineering in wet natural gas pipelines. *Corrosion*, 47(12):976–985, 1991.
- [183] Stein Olsen, editor. *CO₂ Corrosion Prediction by Use of the NORSOK M-506 Model - Guidelines and Limitations*, volume All Days of NACE CORROSION, 2003.
- [184] Rolf Nyborg, editor. *CO₂ Corrosion Models For Oil And Gas Production Systems*, volume All Days of NACE CORROSION, 2010.
- [185] Muhammad Hashim Abbas. *Modelling CO₂ corrosion of pipeline steels*. PhD thesis, Newcastle University, 2016.
- [186] C. de Waard and D. E. Milliams. Carbonic acid corrosion of steel. *Corrosion*, 31(5):177–181, 1975.
- [187] C. de Waard, U. Lotz, and A. Dugstad. Influence of liquid flow velocity on CO₂ corrosion: A semi-empirical model. 1995.
- [188] S. Nesic, J. Postlethwaite, and S. Olsen. An electrochemical model for prediction of corrosion of mild steel in aqueous carbon dioxide solutions. *Corrosion*, 52(4):280–294, 1996.
- [189] Srdjan Nešić, Hui Li, Dusan Sormaz, and Jing Huang. A free open source mechanistic model for prediction of mild steel corrosion. 2008.
- [190] Jim Y.F. Yam and Tommy W.S. Chow. A weight initialization method for improving training speed in feedforward neural network. *Neurocomputing*, 30(1-4):219–232, 2000.
- [191] Deepak Ghimire, Dayoung Kil, and Seong-heum Kim. A survey on efficient convolutional neural networks and hardware acceleration. *Electronics*, 11(6):945, 2022.
- [192] A. V. L. N. Sujith, R. Swathi, R. Venkatasubramanian, Nookala Venu, S. Hemalatha, Tony George, A. Hemlathadhevi, P. Madhu, Alagar Karthick, M. Muhibbullah, and Sameh M. Osman. Integrating nanomaterial and high-performance fuzzy-based machine learning approach for green energy conversion. *Journal of Nanomaterials*, 2022:1–11, 2022.

- [193] Li Liu and Fanzhang Li. A survey on dynamic fuzzy machine learning. *ACM Computing Surveys*, 55(7):1–42, 2023.
- [194] Jireh Yi-Le Chan, Steven Mun Hong Leow, Khean Thye Bea, Wai Khuen Cheng, Seuk Wai Phoong, Zeng-Wei Hong, and Yen-Lin Chen. Mitigating the multicollinearity problem and its machine learning approach: A review. *Mathematics*, 10(8):1283, 2022.
- [195] Abhinav Kumar Singh, Pankaj Kumar, Rawshan Ali, Nadhir Al-Ansari, Dinesh Kumar Vishwakarma, Kuldeep Singh Kushwaha, Kanhu Charan Panda, Atish Sagar, Ehsan Mirzania, Ahmed Elbeltagi, Alban Kuriqi, and Salim Heddami. An integrated statistical-machine learning approach for runoff prediction. *Sustainability*, 14(13):8209, 2022.
- [196] Changqi Luo, Behrooz Keshtegar, Shun Peng Zhu, Osman Taylan, and Xiao-Peng Niu. Hybrid enhanced monte carlo simulation coupled with advanced machine learning approach for accurate and efficient structural reliability analysis. *Computer Methods in Applied Mechanics and Engineering*, 388:114218, 2022.
- [197] Denny Thaler, Leonard Elezaj, Franz Bamer, and Bernd Markert. Training data selection for machine learning-enhanced monte carlo simulations in structural dynamics. *Applied Sciences*, 12(2):581, 2022.
- [198] Liang Gao, Mi Xiao, Xinyu Shao, Ping Jiang, Li Nie, and Haobo Qiu. Analysis of gene expression programming for approximation in engineering design. *Structural and Multidisciplinary Optimization*, 46(3):399–413, 2012.
- [199] Jinghui Zhong, Liang Feng, and Yew-Soon Ong. Gene expression programming: A survey [review article]. *IEEE Computational Intelligence Magazine*, 12(3):54–72, 2017.
- [200] Cândida Ferreira. *Gene expression programming: mathematical modeling by an artificial intelligence*. Springer, 2006.
- [201] Sven M. Hesjevik, Stein Olsen, and Marion Seiersten, editors. *Corrosion at High CO₂ Pressure*, volume All Days of NACE CORROSION, 2003.
- [202] Yoon-Seok Choi and Srdjan Nešić, editors. *Corrosion Behavior Of Carbon Steel In Supercritical CO₂-Water Environments*, volume All Days of NACE CORROSION, 2009.
- [203] Y. Zhang, K. Gao, G. Schmitt, and R. H. Hausler. Modeling steel corrosion under supercritical co₂ conditions. *Materials and Corrosion*, 64(6):478–485, 2013.
- [204] Z. D. Cui, S. L. Wu, S. L. Zhu, and X. J. Yang. Study on corrosion properties of pipelines in simulated produced water saturated with supercritical co₂. *Applied Surface Science*, 252(6):2368–2374, 2006.

Appendix A

C++ Codes

In the functions below: $d[0]$ = pressure (Pa), $d[1]$ = Enthalpy ($MJ\ kg^{-1}$), $d[2]$ = MF_{CH_4} , $d[3]$ = MF_{CO_2} , $d[4]$ = MF_{N_2} , $d[5]$ = MF_{H_2S} , $d[6]$ = MF_{NaCl} , $d[7]$ = MF_{KCl} , $d[8]$ = MF_{CaCl_2} , $d[9]$ = MF_{MgCl_2} . (MF = mole fraction in the two-phase mixture)

Listing A.1 Temperature/enthalpy (pressure > 10 MPa)

```
1 double gepModel(double d[])
2 {
3     const double G1C1 = 20468.3987895087;
4     const double G1C8 = -0.632584680896207;
5     const double G1C4 = -0.126694048571721;
6     const double G1C0 = -2.34224648339043;
7     const double G2C6 = -4.6741958733112;
8     const double G2C5 = 26.4014636827949;
9     const double G2C1 = 21.0155662431996;
10    const double G3C6 = 1.38009587889663;
11    const double G3C7 = 11.0276506089214;
12    const double G4C0 = 6.40107789479513;
13    const double G4C7 = -15.3514731948368;
14
15    double y = 0.0;
16
17    y = ((d[10]+((d[2]*G1C8)+(d[7]*G1C4)))*(((d[1]+G1C0)+d[3])*(G1C1+d[0])));
18    y /= (((d[1]+d[7])+(d[7]+d[7]))*((G2C5+G2C1)*d[8]))+((d[8]+G2C6)+d[6]));
19    y /= (d[0]+((((d[9]*G3C7)*d[0])*(d[2]*G3C6))*((d[9]+d[1])+(d[3]+d[6]))));
20    y /= (d[1]*((d[1]+(((d[10]*G4C7)*d[10])*(G4C0+d[1])))+d[2]));
21
22    return -0.00080765*y + 0.0005711;
23 }
```

Listing A.2 Temperature/enthalpy (pressure < 10 MPa)

```
1 double gepModel(double d[])
2 {
3     const double G1C1 = -32318.1483269907;
4     const double G1C8 = -13.8547740182964;
5     const double G1C7 = -3.88915202762322;
6     const double G2C3 = 6.31536021447302;
7     const double G2C5 = 4.0254239988184;
8     const double G2C2 = -1.73940616972321;
9     const double G3C4 = 7.38868080049002;
10    const double G3C2 = 6.19566639338576;
11    const double G3C8 = 5.98974791711173;
12    const double G3C0 = -5.72206137923993;
13    const double G4C2 = 2.98313090164621;
14
15    double y = 0.0;
16
17    y = (((d[4]+(G1C8*d[8]))+((G1C7+d[3])+d[3]))*((G1C1+d[2])+(d[2]*d[0])));
18    y /=
19    (((((d[6]+d[6])*d[3]+d[1]))*((d[2]*d[2])*G2C3))+((d[4]+G2C5)+(d[7]*G2C2)));
20    y /= (d[0]+(((G3C4+G3C2)*d[0])*((G3C8+G3C0)+d[3]))*d[9]);
21    y /= (((((d[2]*d[5])+d[8])*d[8]*G4C2))+d[1])*(d[1]+d[2]));
22
23    return -0.00027023*y + 0.00050106;
}
```

In the functions below: $d[0]$ = pressure (Pa), $d[1]$ = Enthalpy ($MJ\ kg^{-1}$), $d[2]$ = MF_{CH_4} , $d[3]$ = MF_{CO_2} , $d[4]$ = MF_{N_2} , $d[5]$ = MF_{H_2S} , $d[6]$ = MF_{NaCl} , $d[7]$ = MF_{KCl} , $d[8]$ = MF_{CaCl_2} , $d[9]$ = MF_{MgCl_2} . (MF = mole fraction in the two-phase mixture)

Listing A.3 Equilibrium constant of methane

```

1 double gepModel(double d[])
2 {
3     const double G2C5 = 2.22339771721549;
4     const double G2C6 = -2.14637233854183;
5     const double G3C1 = -1.07790690658374;
6     const double G4C2 = -0.794709937672379;
7     const double G4C4 = 9.25857853236488;
8     const double G4C9 = 3.02574550033259;
9     const double G5C8 = -7.32716149082919;
10    const double G5C7 = -4.92416150395215;
11    const double G6C2 = -1.10201172067956e-03;
12    const double G6C8 = -0.146189368197262;
13    const double G7C8 = -9.06125064851833;
14    const double G7C0 = -0.732014600985748;
15    const double G8C8 = -0.419130189333237;
16    const double G8C6 = -57.7562791833247;
17    const double G8C3 = 11.7499738632408;
18
19    double y = 0.0;
20
21    y = -(pow(exp((d[8]*exp(pow((d[2]+(-(d[3]))),3))),2)));
22    y /= (pow((((((d[7]+G2C6)/2.0)+d[5])/2.0)
23    +((d[3]+G2C6)-G2C5)/2.0),3)+sqrt(d[0]));
24    y /= ((G3C1+exp(d[8]))/2.0);
25    y /= ((d[9]*sqrt((((G4C9-d[2])*d[0])+pow(G4C4,2))))-pow(G4C2,2));
26    y /= ((d[0]*G5C8)+exp(((1.0/(((d[4]+d[1])/2.0))
27    +((((G5C7+d[2])/2.0)+d[6])/2.0)))));
28    y /= pow(-((((G6C2+((G6C8+d[10])/2.0))/2.0))),3);
29    y /=
30    (((sqrt(d[2])+((G7C8+G7C8)*(d[9]+d[10]))) + exp((pow(G7C0,3)-d[5])))/2.0);
31    y /=
32    (((((((d[9]+G8C8)+(1.0))/2.0)-(1.0/(((d[1]+G8C3)/2.0))))+G8C8)/2.0)+d[7]);
33
34    return 0.040489*y + 98.83;

```

Listing A.4 Equilibrium constant of carbon dioxide

```

1 double gepModel(double d[])
2 {
3     const double G1C5 = -4.37535902279733;
4     const double G1C9 = 7.77214880825221;
5     const double G2C5 = -5.47728293710135;
6     const double G3C1 = -1.0671278375179;
7     const double G3C5 = 2.79641102328562;
8     const double G4C2 = -0.785190099381902;
9     const double G5C6 = -8.36603900265511;
10    const double G5C7 = 0.728626256797193;
11    const double G5C9 = -1.60924100466933;
12    const double G6C8 = -1.47651261879235;
13    const double G7C5 = -5.13412884914701;
14    const double G7C3 = 4.56887319587694;
15    const double G7C0 = -3.8067540910062;
16    const double G8C8 = -0.418711059143904;
17    const double G8C1 = 7.49136353832348;
18
19    double y = 0.0;
20
21    y =
22    (((((d[1]+d[0])+(d[0]+G1C9))/2.0)-G1C5)+(((d[0]-d[2])-d[6])+sqrt(d[9])));
23    y /=
24    (d[7]+((((G2C5+d[5])-(d[4]+d[4]))+sqrt(d[9]))+exp((d[4]+d[5])))/2.0));
25    y /= (((1.0)+d[9])+G3C1);
26    y /= ((pow(((d[9]+G4C2)/2.0),3)+((((d[8]+d[7])/2.0)+(d[7]+d[8]))/2.0
27    +pow(d[7],2)))/2.0);
28    y /= (((exp((1.0))+((0.0)+G5C7)/2.0)/2.0)*d[0])+(1.0/(G5C6))/2.0);
29    y /= (((((G6C8+((d[5]+d[6])/2.0))/2.0)+(d[10]+d[10])/2.0)+(d[9]
30    +((d[4]+d[10])/2.0))/2.0);
31    y /= (((exp(d[9])*G7C3)+exp(G7C0))+(G7C5+(d[8]+d[8])))/2.0+d[10];
32    y /=
33    (((((1.0/(((G8C1+((1.0/(G8C8))+(0.0))/2.0))/2.0))+G8C8)/2.0+d[10])/2.0);
34
35    return 0.0000295*y + 10.24;
36 }

```

Listing A.5 Equilibrium constant of nitrogen

```
1 double gepModel(double d[])
2 {
3     const double G2C5 = 1.67885372478408;
4     const double G2C6 = -7.45217217976714;
5     const double G3C1 = -1.07682899967716;
6     const double G4C2 = -0.794497735526597;
7     const double G4C4 = 9.17515873978827;
8     const double G5C4 = -6.81051781670583;
9     const double G5C8 = -7.32642877468011;
10    const double G6C2 = -1.36023620908092e-03;
11    const double G6C8 = -0.145897135650236;
12    const double G7C4 = -7.68247756264025;
13    const double G7C7 = -9.76255287331767;
14    const double G7C0 = -0.885736781455088;
15    const double G8C8 = -0.423744812717796;
16    const double G8C3 = 11.8556061282713;
17
18    double y = 0.0;
19
20    y = exp((pow(exp(d[7]),3)+exp(((exp(-(d[9])))+d[7])/2.0)))));
21    y /= ((pow((((sqrt(d[8])+d[5])/2.0)+((G2C6/G2C5)/G2C5))/2.0),3)
22    +sqrt(d[9]))/2.0);
23    y /= ((G3C1+exp(d[8]))/2.0);
24    y /= ((sqrt((((d[6]*d[1])/d[2])+pow(G4C4,2)))*d[9]-pow(G4C2,2)));
25    y /= (((G5C4*d[0])+(-(d[5]+d[5]))+(1.0/(((d[1]+G5C8)/2.0)))))/2.0);
26    y /= pow(-(((G6C2+(G6C8+d[10]))/2.0)),3);
27    y /= ((sqrt(d[2])+((G7C4+G7C7)*(d[9]+d[10])))+exp(((G7C0-d[3])-d[7])));
28    y /=
29    (((G8C8+(((G8C8+d[9])+(1.0))/2.0)-(1.0/(((d[1]+G8C3)/2.0)))))/2.0+d[7]);
30
31    return 0.0000105*y + 82.87;
32 }
```

Listing A.6 Equilibrium constant of hydrogen sulfide

```

1 double gepModel(double d[])
2 {
3     const double G1C7 = 3.33536790063173;
4     const double G1C6 = 5.94302407910398;
5     const double G2C0 = -7.01362340355867;
6     const double G3C0 = 4.18216557671013;
7     const double G3C2 = -7.15920981856555;
8     const double G3C8 = 4.65926084170049;
9     const double G4C1 = -0.759923389690848;
10    const double G4C7 = 7.49086935868265;
11    const double G4C3 = 8.43005236884671;
12    const double G4C5 = -9.50941801202429;
13    const double G5C4 = 0.936272689231344;
14    const double G6C6 = 8.64558854945524;
15    const double G6C8 = -0.144408844877855;
16    const double G7C7 = 4.36078981902524;
17    const double G7C8 = -10.6495893859506;
18    const double G8C1 = 6.26367671004059;
19
20    double y = 0.0;
21
22    y = exp((((G1C7+sqrt(d[8]))/2.0)+exp((((G1C6+d[7])/2.0)+d[8]))));
23    y /= (exp(((d[6]+(d[2]-((d[0]*d[6])+G2C0)/2.0))/2.0))+sqrt(d[0]));
24    y /=
25    (((((G3C0-G3C2)*(d[9]+d[7]))+((G3C8+d[6])+(d[7]+G3C2))/2.0))/2.0)+d[10]);
26    y /= ((d[9]*(((d[6]+G4C7)+((G4C3+G4C5)/2.0))+d[0]*d[6])))-pow(G4C1,2));
27    y /= (d[9]-d[0]/sqrt((pow(((d[5]/d[0])+G5C4),3)-d[5]))));
28    y /= ((1.0/(G6C6))*pow((((d[10]*exp((d[4]+d[6])))+G6C8)/2.0),3));
29    y /= (((1.0)+((d[2]+G7C8)*(d[9]+d[10])))/2.0)/exp(((d[9]*d[4])*d[1]));
30    y /= (1.0/((((G8C1+(((d[1]+d[0])/2.0)+(1.0/(d[1])))/2.0))/2.0)
31    -((-d[0])+d[6]));
32    return 3.07E-13*y + 2.98;
33 }

```

Listing A.7 corrosion rate

```
1 double gepModel(double t, double p, double u, double ph, double & crr)
2 {
3     double d[4];
4
5     d[0] = t;
6     d[1] = p;
7     d[2] = u;
8     d[3] = ph;
9
10    const double G1C7 = -6.37490076288078;
11    const double G1C9 = 9.71954790027811;
12    const double G2C6 = -22.4713541949907;
13    const double G2C8 = 112.371930589555;
14    const double G2C1 = 16.9811572846352;
15    const double G2C3 = 7.47999511703848;
16    const double G3C0 = 12.3071233835765;
17    const double G3C6 = -58.1855518566808;
18    const double G3C7 = -4.79938154426978;
19    const double G3C5 = 2.20796920024472;
20    const double G4C2 = 7.59265536537209;
21    const double G4C1 = 10.6737329569532;
22    const double G5C6 = -5.9717883032398;
23    const double G5C8 = 4.35994554792827;
24    const double G5C9 = 8.28125857955026;
25    const double G6C1 = 3.41839318569503;
26    const double G6C6 = -3.72394969086718;
27    const double G6C3 = 7.62807399214605;
28
29    double y = 0.0;
30    y = ((d[0]+((G1C9+G1C9)*G1C7))-d[1]);
31    y *= (((d[1]-G2C8)-(G2C8-d[0]))-((G2C1*G2C3)-G2C6));
32    y *= (((G3C0+G3C0)+(d[1]+G3C6))*((G3C7-G3C5)+d[3]));
33    y *= (((d[1]-d[3])-(d[2]+d[3]))-((G4C2-G4C1)-d[1]));
34    y *= (((G5C6+d[0])-(G5C8*d[1]))-((G5C9-d[2])-d[1]));
35    y *= (((d[2]+d[1])+(G6C6*G6C3))-(d[3]*G6C1));
36
37    crr = - 0.00000013*y + 508.116;
38    return crr/100;
39 }
```


Appendix B

Training and test datasets for the corrosion model

Table B.1 Training Dataset.

T (°C)	(MPa)	U (m/s)	pH	Corr. Rate (mm/year)	Source
24	3.5	0	3.1	4	Hesjevik <i>et al.</i> [201]
40	5.8	0	3.4	8	Hesjevik <i>et al.</i> [201]
50	4	0	3.25	18	Choi and Nesic [202]
50	8	0	3.14	19	Choi and Nesic [202]
50	9.5	4	5.1	9	Zhang <i>et al.</i> [203]
50	9.5	0	5.1	8.1	Zhang <i>et al.</i> [203]
60	12.1	4	3.1	15	Zhang <i>et al.</i> [203]
60	12.1	4	4.08	12	Zhang <i>et al.</i> [203]
60	12.1	0	4.08	10.5	Zhang <i>et al.</i> [203]
80	15.4	4	4	15	Zhang <i>et al.</i> [203]
110	20.3	4	4	13	Zhang <i>et al.</i> [203]
110	20.3	4	4	13	Zhang <i>et al.</i> [203]
130	23.3	4	3.2	9	Zhang <i>et al.</i> [203]
130	23.3	4	3.9	9	Zhang <i>et al.</i> [203]
130	23.3	0	3.9	9	Zhang <i>et al.</i> [203]
150	8.27	0	6	0.9	Cui <i>et al.</i> [204]

Table B.2 Test Dataset.

T (°C)	(MPa)	U (m/s)	pH	Corr. Rate (mm/year)	Source
40	8.5	0	3.4	2	Hesjevik <i>et al.</i> [201]
50	6	0	3.18	20	Choi and Nesic [202]
60	12.1	0	3.1	11	Zhang <i>et al.</i> [203]
80	15.4	4	3.12	15	Zhang <i>et al.</i> [203]
130	23.3	0	3.2	9	Zhang <i>et al.</i> [203]
140	8.27	0	5	1.3	Cui <i>et al.</i> [204]

Appendix C

Immiscible displacement flows

Immiscible displacement flow occurs when two fluids that are not miscible, or cannot mix, come into contact and one displaces the other. In geothermal wellbores, this phenomenon can happen when a drilling fluid is used that is immiscible with the formation fluids. For instance, oil-based drilling fluids are commonly used in geothermal wells, and they are not miscible with water-based formation fluids. When the drilling fluid is pumped down the wellbore, it displaces the formation fluids, creating a flow path for the drilling fluid. This process helps to maintain wellbore stability and prevent the influx of formation fluids into the wellbore during drilling operations. However, it can also create challenges when it comes to well completion and production, as the immiscible drilling fluid can leave behind a residual film on the wellbore surface that can impede fluid flow and heat transfer. Proper management of immiscible displacement flow is crucial to ensure the efficient operation of geothermal wells. Electro-hydrodynamic and magneto-hydrodynamic effects can have a significant impact on immiscible displacement flows. These effects involve the interaction between fluids and electric or magnetic fields, and they can alter the behavior of the fluids in the displacement process. For example, electro-hydrodynamic effects can induce electric fields that cause changes in the interfacial tension between the two fluids, which can affect displacement efficiency. Similarly, magneto-hydrodynamic effects can create magnetic fields that induce fluid motion, which can alter flow patterns and displacement behavior. Understanding and accounting for these effects is important for accurately modeling immiscible displacement flows in geothermal wellbores and other applications. During this Ph.D. project, two papers were published that focused on these topics.

Journal of Petroleum Science and Engineering 196 (2021) 108044



Contents lists available at ScienceDirect

Journal of Petroleum Science and Engineering

journal homepage: <http://www.elsevier.com/locate/petrol>



Enhancement of immiscible two-phase displacement flow by introducing nanoparticles and employing electro- and magneto-hydrodynamics

Morteza Esmailpour^{*}, Maziar Gholami Korzani

Department of Civil Engineering, Geo and Environmental Sciences, Karlsruhe Institute of Technology, 76131 Karlsruhe, Germany

ARTICLE INFO

Keywords:
 Lattice Boltzmann method
 He-Chen-Zhang method
 Non-Newtonian fluid displacement
 Magneto-hydrodynamics
 Electro-hydrodynamics
 Nanoparticles

ABSTRACT

In this study, two-component displacement of a time-dependent non-Newtonian fluid by a Newtonian fluid in a two-dimensional inclined channel is simulated. Using a special multi-component model of the lattice Boltzmann method that is called He-Chen-Zhang, made it possible to do the simulations for non-uniform density and very high viscosity ratios. The main focus of this study is altering the flow pattern and displacement efficiency by Applying Electro- and magneto-hydrodynamic fields, using added nanoparticles and heating the channel walls. Displacement efficiency in different cross-sections, thickness of the static wall layer at the top and bottom of the channel, development of interfacial instabilities, magnitude of generated forces and, temperature distribution in the simulation environment are analyzed comprehensively to fully control the fingering structure. Investigation of injected fluid movement in the other one and displacement efficiency showed that enhancement in the power of the electric field is associated with displacement efficiency alteration in various longitudinal sections of the channel. However, removing the residual layer at the top and bottom of the fingering structure doesn't cause the total efficiency of displacement (M_t) to change significantly since the axial motion of the invading fluid is weakened. In contrast, applying magnetic field, increasing the Hartmann number and changing the rotation angle of the coordinate system (to 180), enhances the axial velocity and displacing ability of this fluid. Furthermore, for $Ha = 10$ and $\theta = 0$, with the transverse velocity rising, displacement efficiency for longitudinal sections close to the channel axis decreases and the occurrence of interfacial instabilities is inevitable.

Article

Analyzing Impacts of Interfacial Instabilities on the Sweeping Power of Newtonian Fluids to Immiscibly Displace Power-Law Materials

Morteza Esmailpour *  and Maziar Gholami Korzani 

Department of Civil Engineering, Geo and Environmental Sciences, Karlsruhe Institute of Technology, 76131 Karlsruhe, Germany; m.gholami@kit.edu

* Correspondence: morteza.esmailpour@kit.edu

Abstract: Injection of Newtonian fluids to displace pseudoplastic and dilatant fluids, governed by the power-law viscosity relationship, is common in many industrial processes. In these applications, changing the viscosity of the displaced fluid through velocity alteration can regulate interfacial instabilities, displacement efficiency, the thickness of the static wall layer, and the injected fluid's tendency to move toward particular parts of the channel. The dynamic behavior of the fluid–fluid interface in the case of immiscibility is highly complicated and complex. In this study, a code was developed that utilizes a multi-component model of the lattice Boltzmann method to decrease the computational cost and accurately model these problems. Accordingly, a 2D inclined channel, filled with a stagnant incompressible Newtonian fluid in the initial section followed by a power-law material, was modeled for numerous scenarios. In conclusion, the results indicate that reducing the power-law index can regulate interfacial instabilities leading to dynamic deformation of static wall layers at the top and the bottom of the channel. However, it does not guarantee a reduction in the thickness of these layers, which is crucial to improve displacement efficiency. The impacts of the compatibility factor and power-law index variations on the filling pattern and finger structure were intensively evaluated.

Keywords: lattice Boltzmann method; multi-component flow; He–Chen–Zhang method; power-law non-Newtonian fluid; displacement flow



Citation: Esmailpour, M.; Gholami Korzani, M. Analyzing Impacts of Interfacial Instabilities on the Sweeping Power of Newtonian Fluids to Immiscibly Displace Power-Law Materials. *Processes* **2021**, *9*, 742. <https://doi.org/10.3390/pr9050742>

